Fibre Optic Pressure Sensors in Healthcare Applications

by

Chalani Lakshani Abeywardena,

Thesis submitted to the University of Nottingham

for the degree of Doctor of Philosophy

April, 2020

University of Nottingham

UK | CHINA | MALAYSIA

Table of Content

Abstract

This PhD thesis provides an extensive description of the development of two fibre optic pressure sensors for applications in health care: (i) a miniature fibre optic Fabry–Perot pressure sensor for fluid pressure measurements in invasive blood pressure monitoring and; (ii) a highly sensitive fibre Bragg grating sensor for contact/interface pressure measurement.

The fibre optic Fabry-Perot pressure sensor has a diameter of 125 µm and is created by forming a cavity at the tip of a single-mode optical fibre. Parylene films were used as the pressure-sensitive diaphragm. The performance of three sensors with different aspect ratios has been investigated. The pressure sensing range of ~10 kPa (diastolic pressure)- ~15 kPa (systolic pressure) was targeted; sensor with the cavity of 70 µm in diameter and cavity length of 87 µm is able to sense within a range of 0- 18 kPa with an average sensitivity of 0.12 nm/kPa and response time of 3 seconds. The temperature sensitivity of 0.084 nm/°C was observed. Hysteresis and wavelength drift were observed for the sensors, which may be due to the permeability of the Parylene film to the air. Solutions for reducing hysteresis, wavelength drift and temperature cross-sensitivity are discussed in detail.

Fibre Bragg grating (FBG) sensor technology is an ideal candidate for contact pressure measurement in compression therapy, pressure ulcer or prosthetics due to its many advantages such as conforming to body parts, small size, biocompatibility and multiplexing capabilities. A successful mathematical model for an FBG contact pressure sensor for healthcare applications has been presented and experimentally validated. The model has been compared with previous studies reported in the literature and takes into account birefringence. The highest sensitivity was achieved for the disc shape with a sensitivity of 0.8719 nm/MPa for a diameter of 5.5 mm, thickness of 1 mm and Young's modulus of 20 MPa. This sensor was comprised of a 3 mm long FBG

centrally located in the patch. This is a pressure sensitivity of ~270 times increase when compared with a bare FBG reported in the literature. Birefringence effect was observed for the disk patch for pressures larger than 2.6 MPa.

Even though FBGs provide high sensitivity in contact pressure sensing in healthcare, the potential applications are limited by the size and cost of commercially available FBG interrogators. A successful first attempt towards the development of a single channel compact FBG interrogation was accomplished. The system consists of a three-section distributed Bragg Reflector (DBR) tuneable laser, microcontroller unit, precision 5 channel current driver IC, photodiode circuit and a temperature controller IC. The tuneable laser was calibrated within 1535-1544 nm wavelength range to produce three current–wavelength lookup tables for wavelength resolution of 1 nm, 0.1 nm, 0.01 nm which is dependent on the current resolution. Future work includes adding power circuitry, a photodiode circuit and a feedback circuit to minimize power fluctuations. The system was tested compared to the commercial Smartscope FBG interrogator.

Author's Publications

Journal Articles:

Chalani L. Abeywardena,Frederique J. Vanheusden, Kate F. Walker, Richard Arm ,Qimei Zhang ,'Fetal Movement Counting Using Optical Fibre Sensors' , https://doi.org/10.3390/s21010048

Conferences:

Poster presentation on 'Development of an optical fibre Fabry-Perot pressure sensor for biomedical applications using Focused Ion Beam technology' at 15th conference on Optics Within Life Sciences (OWLS) held in, Western Australia, (November 2018)

Acknowledgement

My deep sense of gratitude and appreciation goes first to my PhD supervisors Dr. Stephen Bull, Dr. Sergiy Korposh and Dr. Ricardo Correia for the continuous support, guidance and courage you have given me throughout my PhD journey. All of your thoughtfulness, patience and expertise supervision strengthen me always during my research and writing up period.

I would also like to thank my internal assessor Professor Stephen Morgan. Your critical comments and advices during the annual reviews always helped me to enhance the quality of my research work.

I would also like to thank Prof, Lee from the University of Kitakyushu, Japan for providing the necessary Parylene films for the experiments. I would like to thank Dr. Christopher Parmenter from the Nanoscale and Microscale Research Centre for all the training and support provided during the FIB micromachining of the sensors. I am grateful to Dr Yaping Zhang from the University of Nottingham, Ningbo, China for providing the 3 sectional tunable laser required for the project. I would also like to thank Dr. Qimei Zhang for conducting the experiments in chapter 4.

I would also like to thank my colleagues from the 10th floor of the Tower building. Thank you all for your kind words, support and affection. You all made my PhD journey more enjoyable one.

I would also like to the thank Mark and John from the 8th floor Technician office. Thanks for supporting me when it was needed.

My most special thanks go to the love of my life Thiwanka, my loving son Thivein, my loving mother, loving father and dear sisters. You were my strength always. Without your support, love, care, encouragement and patience this journey will not be the same. Thank you all again.

Chapter 1

Fibre Optical Pressure Sensors, Overview and Thesis Outline

1.1 Introduction to fibre optical pressure sensors

The history of optical fibre sensors dates back to the mid-1960, where the first photonic sensor for measuring displacement based on a bifurcated fibre bundle was patented [1]. One half of the bundle was used to illuminate a surface and the other half of the bundle was used to collect the reflected light from the surface. Since then, optical fibre sensor technology has evolved and become established over a half a century. Over that period, fibre optic sensing (FOS) has progressed in its ability for the measurement of a wide range of measurands including strain, pressure, temperature, vibration, chemicals, viscosity, acceleration, rotation, magnetic field, light level, radiation, and hence established itself in applications including healthcare, structural health monitoring, aerospace, smart textiles, environmental, chemical sensing, military, inertial navigation systems, industrial systems and many more.

This thesis focuses on the biomedical applications of FOS and therefore the discussion on applications and sensor performance will be limited to the biomedical applications of FOS. Recent developments in the biomedical field have been driven by healthcare trends such as minimally invasive surgery, miniaturization of the medical devices, automation and the use of robotics in surgery and medical procedures [2], wearable sensors and smart textiles [3]. As a result, there is a huge demand for biocompatible sensors based on FOS technology. Due to their unique properties and characteristics such as immunity to electromagnetic interference, light weight and bio compatibility, FOS have made remarkable progress and more importantly can be used simultaneously with technologies such as Magnetic Resonance Imaging [4], and optical coherence tomography [5] .

A sensor is a device that can measure biological, chemical and physical parameters safely and reliably [6]. For example, a sensor can tell if the fetus in the womb is healthy [7], measure blood pressure or glucose levels [8], check the level of healing of a wound [9] or measure temperature of the body [10] providing many advantages over other commercial bio sensing technologies. FOS are immune to electrical noise [11]. The light weight, flexible nature, along with the small diameter, allows them to be used for most of the invasive and *in vivo* medical applications, for example in catheters or endoscopic tools [12]. Typically the diameter of a single mode optical fibre is 125 µm. Nevertheless with the necessary fibre protections such as fibre jackets and polyacrylate coating, the diameter would be 250 µm. Generally, OFS are made from silica glass (SiO_2), fused silica or fused quartz. SiO_2 is an inert compound which is very stable and thus unreactive with most of the substances [13] except hydrofluoric acid and some alkaline materials [14],[15]. Hence OFS sensors are biocompatible and non-toxic which make them an ideal candidate for the biomedical sensors to be used for minimally invasive surgeries or therapies. They also can be sterilised with the standard sterilisation procedures [5]. A futher major advantage of OFS is that they are thin and flexible. Consequently, they are easier to adhere to bones and biological tissues and therefore OFS sensors have been developed to measure the deformation of bones due to strain [16]. Additionally FOS provide the ability to measure multiple parameters simultaneously using one single optical fibre [17],[18]. This is very advantageous in bio medical sensing as this will give multiple information using one single sensor.

1.2 Aims and Objectives

This thesis discusses extensively the development of two fibre optic pressure sensing technologies for application in healthcare. Fabry- Perot interferometric fibre optic pressure sensors and fibre Bragg grating pressure sensors were studied. The aim of the research can be broadly divided into three major objectives as follows.

1. Development of a miniature fibre optic Fabry-Perot interferometric pressure sensor for minimally invasive medical applications.
2. Mathematical modelling of the Fibre Bragg Grating (FBG) pressure sensor response for an FBG embedded in a polymer patch with the aim to optimising the design parameters (Young's modulus, size , shape) to enhance the sensitivity for contact pressure measurement applications in health care.
3. Design and development of a miniature FBG interrogator.

1.3 Motivation and Novelty

This thesis includes mainly three major pieces of research as described in section 1.2. The significance and novelty of each is described below.

1.3.1 Development of a miniature fibre optic Fabry-Perot pressure sensor

Pressure is an important parameter that should be measured accurately and precisely, in many different healthcare situations [19]–[22]. The human and animal organism is composed of a complex combination of bones, joints and muscles. Each part of the body experiences different pressure ranges in its normal physiological state. Clausen and Glott [23] suggest dividing the pressures in the body into three domains, namely, lower pressure domain (capillary, brain, urinary, bladder and muscular compartments), medium pressure domain (circulatory system including heart) and high pressure domain (load bearing structures like hips and knees). The pressure range can vary depending on the physiological state or the condition of the body. Variable ranges of pressure in the body cavities for normal and abnormal physiological conditions are detailed in reference [24]. The sensor developed in this work has the ability to cover a maximum pressure range of 0-80 kPa. Therefore it is suitable for the targeted application disussed in chapter 2, table 2.1. For example, left ventricular pressure usually lies within a range of 0- 13 kPa, but in an abnormal condition from the minimum limit can reach up to ~ -0.13 kPa

and the maximum limit can reach up to 40 kPa. Deviation of pressure from its normal range can cause body injuries or even death in critical situations. For example, raised blood pressure is the major cause of death in the world, being responsible for 60% of strokes and 50% of coronary heart disease [25]. Low blood pressure can also cause serious problems. A study shows that when the mean arterial blood pressure is lower than 7.33 kPa (55 mmHg), even for a short time, it can cause acute kidney injury and myocardial injury [26]. Regular measurement of blood pressure levels accurately and precisely can prevent such situations. Accuracy in terms of sensor requirement often depends on the area of interest. In case of blood pressure monitoring for every 2.6 kPa increase in systolic pressure or 1.3kPa increase in diastolic pressure the mortality from ischemic heart disease or heart stroke doubles[27]. For this application, an accuracy of the pressure sensor of 0.5 kPa would be required. However, according to the American National Standard Institute, pressure transducers should hold accuracy of ±0.1kPa in the range of -4kPa -6.7kPa and ±0.4kPa in the range of 6.7kPa-40kPa [28]. Blood pressure measurment using the non-invasive oscillometric method is an old and common technique using a sphygmomanometer cuff with an electronic pressure transducer [29]. Although modern arm non-invasive blood pressure (BP) devices provide accurate and precise measurement of mean BP these devices are not reliable in acute conditions and may not provide reliable information about cardiac functions [30]–[32]. Pulmonary artery cauterization (PAC) is a well-known invasive method and is viewed as being the gold standard despite limitations such as ruptures in the pulmonary artery caused by the insertion of catheter and catheter related complications such as sepsis [33]. The minimally invasive methods of blood pressure monitoring, such as arterial cannulation provide accurate measurements when compared with the cuff method and are advantageous in conditions like severe hypotension and severe trauma [34]. It has been shown that invasive methods provide more accurate blood pressure monitoring when compared with non-invasive methods, especially in acute and critical care settings [32]. Kizilova showed that many commercially available non-invasive arterial pressure monitoring technologies fail to satisfy the AAMI

(Association for the Advancement of Medical Instrumentation) standards, especially for patients with cardiovascular disease, obesity and faint pulse [35]. Therefore, invasive techniques for pressure measurement in healthcare play a more important role in critical conditions, providing the facility for accurate and continuous measurements. When it comes to the minimally invasive techniques, optical fibre pressure sensors have become increasingly popular and are widely researched for medical applications. There are various pressure sensors used in healthcare, such as Micro Electro Mechanical Systems (MEMS) [36] and arterial catheters connected to external transducers [37][38][39]. The most common intra-arterial measuring system consists of a fluid column directly connecting the arterial system to the pressure transducer [40]. The pressure waveform of the arterial pulse is transmitted via the column of fluid to the pressure transducer where it is converted into an electrical signal. However, fluid filled systems suffer from a number of drawbacks, includes damping of the signal, which is the reduction of the amplitude of the oscillation due to the friction in the fluid pathway. Other factors that impact on the performance include formation of bubbles and clots and kinks in the cannula or tubing [40]. However, fibre optic in situ measurement sensors could be the solution to most of these issues and replace fluid filled invasive pressure measurement systems [41]. Early development of FOS pressure sensors for pressure measurement in healthcare is described in the work [42]–[44]. These works are based on single fibre oriented to a distal reflective mirror and based on two or more fibre optic systems. In this research, one of the objectives is to design and develop a miniature fibre optic Fabry-Perot tip pressure sensor for minimally invasive medical applications. Parylene self-supporting films were used for the first time to create the pressure sensitive OFS. The maximum diameter of the sensor will be 250 µm including fibre protection jacket and biocompatiable coatings discussed in chapter 3. The proposed sensor will be made with all biocompatible material and hence has great potential for application as an implantable pressure sensor in acute and critical conditions, where non-invasive techniques are less suitable. The key advantage of the proposed method is ease of fabrication, but there is a need to improve the

reproducibility. The development of the sensor, results and future potential are thoroughly described in chapter 3.

1.3.2 Development of a mathematical model for a highly sensitive FBG pressure sensor embedded in a polymer patch

Accurate contact pressure measurement is very important in avoiding pressure injuries caused by being in prolonged contact with mattresses, wheelchairs and prostheses, or through using devices such in dwelling catheters. In the UK, the average daily costs of treating a pressure ulcer are estimated to range from £43 to £374 and the mean healing cost per patient ranges from £1,214 to £14,108, depending on the ulcer category [45]. The monitoring of contact pressure can help avoid tissue injury by alerting clinicians when it is too high or when there has been prolonged contact.

Another healthcare challenge where contact pressure measurement is important is in compression bandaging where it is necessary to obtain and maintain a desired sub bandage pressure during its application and wear. Venous leg ulcers (VLU) are a major cause of morbidity and affect up to 3% of the adult population in the United States and Europe [46]. A study has shown that 87% of VLU patients are prescribed a recognised compression bandage treatment and 52% of them were healed [47]. The mainstay of treatment for established venous insufficiency includes the use of compression to apply external pressure to the lower extremities with the aim of improving venous function [48]. Compression therapy is a very important treatment for certain medical conditions such as chronic wounds, lymphedema, and venous leg ulcers. Accurate contact pressure measurement is very important in compression therapy in order to prevent either the inefficiency of the treatment by not applying a sufficient pressure level or any potential tissue damage by applying pressure over the desirable limits [49], [50].

Fibre optic Bragg sensors are an ideal candidate for this application as they satisfy most of the characteristics for an ideal sensor for interface pressure measurements in healthcare described by Partsch H et al. [51]. Some of these

include easy to wear during contact pressure measurements and a conformity to the limb during the application.

A potential highly sensitive FBG contact pressure sensor has been proposed based on the design by Correia R et al. [52], [53]. Although bare FBGs are sensitive to strain and temperature they are less sensitive to pressure [52], [53]. The sensitivity could be increased by embedding the FBG embedded in a polymer patch. The polymer patch improves the sensitivity of the pressure sensor by transferring the transverse pressure loading into axial strain. However, the sensitivity of the FBG sensor is heavily dependent on the shape, size and the material stiffness of the polymer patch. Therefore, an accurate simulation of the sensor is important to this optimise performance.

Although there are some reports of numerical simulation of FBGs using integrating finite element analysis and the transfer matrix method [54]–[56], the use of these techniques is limited by the fact that they are only developed for a particular application and the simulation code is not provided. Moreover, these models do not account for the non-uniform behaviour of the FBG grating due to the transverse stresses. Therefore, the necessity for a novel mathematical model for the sensor arises. A mathematical model based on finite element analysis and transfer matrix theory was developed to take into account the non uniform behaviour of a FBG due to the transverse stresses and the baseline theory is explained in chapter 2 in detail. The finite element analysis, simulation methodology, experimental validation and the concluded optimised parameters for highest sensitivity are extensively discussed in chapter 4.

1.3.3 Development of a miniature FBG interrogator for the FBG pressure sensor for contact pressure measurement in healthcare

Although there are many advantages of FBG sensors for use in healthcare applications, their use is limited by the size and the cost of the FBG techniques available commercially. The average cost of a commercially available FBG interrogator is about £5000. Moreover, for an application similar to sub

bandage pressure measurement as described in section 1.3.2, the size of the FBG interrogator is important as it should be light-weight and wearable. Hence the main objective of this part of the research was to develop a novel miniature FBG interrogator system for the use of FBG sensors in contact pressure measurement in healthcare. Early work related to the FBG interrogators using tunable lasers reported in [57], [58]. This miniature system is based on a three section tunable laser due to the availability of the device and its advantages, including the orders of magnitude improvement in the output power, as well as reduction in the laser linewidth and hence higher resolution it offers compared to the other techniques such as interferometers, edge filters and tunable filters (chapter 5, section 5.2). The underlying theory, development method, results and future potential are discussed in chapter 5. The development method is unique and consists of a LabVIEW software user interface for constant control and for plotting the results. A small and precise current controlling chip used first time in with a microcontroller to make the system compact. The size of the 5 channel current controlling IC is 5mmx5mm. The system comprises a micro-controller unit for controlling the injection current to the tuneable laser during wavelength scanning and to detect the response from the FBG sensor. A high efficiency thermoelectric cooler (TEC) controller chip is used as the temperature controlling unit. The size of the PCB design in the current design is 8cmx 6cm. The small sizes of the ICs used in the design miniaturize the system immensely when compared with the commercially available interrogators using the same tuneable laser technique such as Smartscan by Smart Fibers.

1.4 Structure of the Thesis

This thesis comprises 6 Chapters.

Chapter 1 introduces the optical fibre pressure sensing technology, the thesis aim and objectives along with the novelty of the research work followed by a description of the structure of the thesis.

Chapter 2 includes an extensive literature review related to fibre optic Fabry-Perot pressure sensing technology and FBG pressure sensing technology, including the approaches detailed in the literature and commercially available instruments. Proposed research methods are introduced with the explanation of relevant background theory.

Chapter 3 describes the research work related to the development of the miniature fibre optic pressure sensor. Research methods, results and conclusions are discussed in detail, along with a discussion of the future potential.

Chapter 4 explains the mathematical modelling of an FBG embedded in a polymer patch layer. A detailed explanation of the mathematical modelling methods and experimental validation is presented. The optimisation of the parameters of the patch sensor is presented.

Chapter 5 describes the theoretical background and produces review of the currently available FBG interrogation techniques. This is followed by a description of the proposed design, software and hardware development and its future potential.

Chapter 6 presents the conclusions and suggesttion of future work of the PhD.

Chapter 2

Background information and Literature Review

2.1 Introduction

This chapter includes the necessary background information, the underlying theory related to the presented research and a literature review. Section 2.2 discusses the working principles of optical fibres by explaining the underlying theoretical concepts of wave-guiding in optical fibres. This is followed by section 2.3 which describes fibre optic interferometry. In section 2.4 fluid pressure measurement in healthcare using FP interferometry is discussed by describing the background information. Section 2.5 is focused on explaining the background information and underlying theory of FBG pressure sensors. This section also details the motivation behind the FBG mathematical modelling.

2.2 Working principles of optical fibres

The basic structure of an optical fibre is shown in figure 2.1. Conventional fibre optic cable consists of a core which is glass/plastic of uniform refractive index, and a cladding, which is glass/plastic of slightly lower refractive index than the core. The optical fibre has a jacket that protects it from mechanical and environmental influence. The diameters of the core, cladding and the jacket can vary widely. For example, most commonly, single mode optical fibre is composed of a core of 9 µm diameter, cladding of 125 µm diameter and jacket with 250 µm diameter.

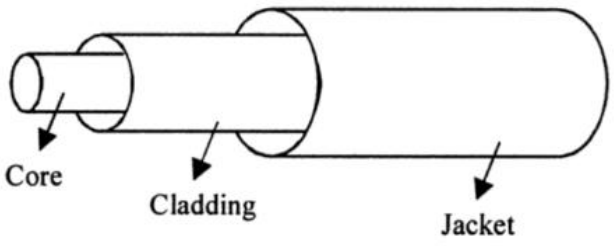

Figure 2.1: Geometry of an optical fibre

Light propagation along an optical fibre can be described using two theories. Ray theory gives a clear physical picture of the light propagation along the fibre and uses a geometrical approach. The other technique is called mode theory, which uses electromagnetic concepts in explaining the light propagation along the fibre.

2.2.1 Ray optic concepts

Figure 2.2. Illustrates the propagation of light rays inside an optical fibre. The propagation of light along the optical fibre can be explained using total internal reflection. When a light ray travels from a high refractive index medium to a low refractive index medium, the light ray refracts away from the normal at the interface between two media. That is, the angle of refraction is greater than the angle of incidence. As the angle of incidence becomes higher than an angle called 'critical angle' the light will be totally internally reflected. At the critical angle the ray is travelling at an angle of refraction of $\frac{\pi}{2}$.

According to this when a light ray is launched into an optical fibre at an angle which is greater than the critical angle at the core-cladding interface, the ray will undergo total internal reflection. This is because the refractive index of the core is higher than the refractive index of the cladding. The ray would undergo multiple total internal reflections and get trapped within the optical fibre before it leaves the optical fibre through the other end.

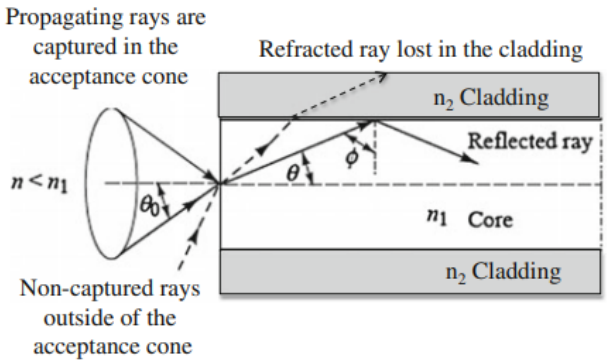

Figure 2.2: Propagation of rays in an optical fibre [59]

Applying the Snell's law at the core-cladding interface at the critical angle θ_c , $n_1 \sin\theta_c = n_2 \sin\frac{\pi}{2}$ one can obtain the equation 2.1 [59].

$$\theta_C = sin^{-1}\left(\frac{n_2}{n_1}\right) \quad 2.1$$

The rays entering the fibre at an angle less than the critical angle will be refracted out of the core and will be lost in the cladding. By applying Snell's law to the air-fibre interface one can determine the maximum angle of entrance (θ_0) which satisfies the above conditions for total internal reflection. This maximum angle is called the 'acceptance angle (θ_A)'. Therefore due to the cylindrical symmetry θ_A forms an acceptance cone. The numerical aperture (NA) of a fibre can be given as [59].

$$NA = n\ sin\,\theta_A = n_1\,sin\,\theta_c = \sqrt{n_1^2 - n_2^2} \quad 2.2$$

The NA is a very important parameter of an optical fibre, which indicates the light gathering ability of a fibre.

2.2.2 Modal theory concepts

Light is an electromagnetic wave and can be mathematically interpreted using Maxwell's equations. The four Maxwell equations for an electromagnetic wave travelling in an optical fibre can be given as follows [60].

$$\nabla \times \vec{E} = -\frac{\overrightarrow{\partial B}}{\partial t} \quad 2.3$$

$$\nabla \times \vec{B} = \mu\vec{J} + \mu\varepsilon\frac{\overrightarrow{\partial E}}{\partial t} = \mu\varepsilon\frac{\overrightarrow{\partial E}}{\partial t} \quad 2.4$$

$$\nabla.\vec{E} = \frac{\rho}{\varepsilon} = 0 \quad 2.5$$

$$\nabla.\vec{B} = 0 \quad 2.6$$

Where $\vec{E}$ is the electric field, $\vec{B}$ is the magnetic field, ρ is the charge density, $\vec{J}$ is the current density, ε is the electric permittivity and μ is the permeability of the medium. Since there are no free electric carriers or currents in an optical fibre $\rho = 0$ and $\vec{J} = 0$. The electric field can be related to the electric flux density ($\vec{D}$) as in equation 2.7 and the magnetic field can be related to the magnetic flux density ($\vec{H}$) as in equation 2.8 [61].

$$\vec{D} = \varepsilon\vec{E} \quad 2.7$$

$$\vec{B} = \overrightarrow{\mu H} \qquad 2.8$$

The electromagnetic wave equation describes the propagation of light within an optical fibre. The wave equation is derived by taking the curl of equations 2.3 and 2.4 and using relevant mathematical identities. It can be written as.

$$\nabla \times \left(\nabla \times \vec{E}\right) = \nabla \cdot \left(\nabla \cdot \vec{E}\right) - \nabla^2 \vec{E} = -\frac{\partial(\nabla \times \vec{B})}{\partial t} \qquad 2.9$$

Substituting equations 2.4 and 2.5 in equation 2.9, the wave equation can be obtained

$$\nabla^2 \vec{E} - \mu\varepsilon \frac{\partial^2 \vec{E}}{\partial t^2} = 0 \qquad 2.10$$

The magnetic field can also be derived using the same methods and can be given

$$\nabla^2 \vec{H} - \mu\varepsilon \frac{\partial^2 \vec{H}}{\partial t^2} = 0 \qquad 2.11$$

Using $\frac{\partial}{\partial t} = i\omega$, equations 2.10 and 2.11 can be re-written as in equations 2.12 and 2.13 [62],

$$\nabla^2 \vec{E} + k^2 \vec{E} = 0 \qquad 2.12$$

$$\nabla^2 \vec{H} + k^2 \vec{H} = 0 \qquad 2.13$$

Where $\mathrm{k} = \omega\sqrt{\mu\varepsilon} = \frac{\omega^2}{c^2} n^2 = k_0^2 n^2$ is the wave number, n is the refractive index of the propagating medium and $\nabla^2 = \frac{\partial^2}{\partial \mathrm{x}^2} + \frac{\partial^2}{\partial \mathrm{y}^2} + \frac{\partial^2}{\partial \mathrm{z}^2}$.

In order to understand the wave propagation in optical fibres which are axially symmetric, it is worth writing the wave equations using cylindrical coordinates (r,ϕ, z) to find the appropriate solutions.

The axis of wave propagation can be considered as the z direction and hence the wave equation can be written as [63].

$$\frac{\partial^2 \vec{E}}{\partial r^2} + \frac{1}{r}\frac{\partial \vec{E}}{\partial r} + \frac{1}{r^2}\frac{\partial^2 \vec{E}}{\partial \emptyset^2} + \frac{\partial^2 \vec{E}}{\partial z^2} = \mu\varepsilon \frac{\partial^2 \vec{E}}{\partial t^2} \qquad 2.14$$

This is true for the magnetic field as well. The following facts are true for both the electric and magnetic fields and, for simplicity, only the electric field is considered.

$\overrightarrow{\mathrm{E}_z}$ can be regarded as the longitudinal component (along the axis of the fibre/wave propagation) of $\vec{\mathrm{E}}_{(r,\phi,z,t)}$ and $\overrightarrow{\mathrm{E}_r}$ and $\overrightarrow{\mathrm{E}_\phi}$ are dependent on $\overrightarrow{\mathrm{E}_z}$. These are called transverse components and can be related to the longitudinal component as follows [64] .

$$\overrightarrow{E_r} = \frac{-j}{q^2}\left\{\beta \frac{\partial E_z}{\partial r} + \frac{\mu\omega}{r} \frac{\partial H_z}{\partial \emptyset}\right\} \quad 2.15$$

$$\overrightarrow{E_\emptyset} = \frac{-j}{q^2}\left\{\beta \frac{\partial E_z}{\partial \emptyset} - \mu\omega \frac{\partial H_z}{\partial r}\right\} \quad 2.16$$

Where $q^2 = \omega^2\mu\varepsilon - \beta^2$ (β is the propagation constant along the axis of the fibre). The wave equation of the optical fibre can be written as

$$\frac{\partial^2\overrightarrow{E_z}}{\partial r^2} + \frac{1}{r}\frac{\partial\overrightarrow{E_z}}{\partial r} + \frac{1}{r^2}\frac{\partial^2\overrightarrow{E_z}}{\partial \emptyset^2} + \frac{\partial^2\overrightarrow{E_z}}{\partial z^2} = \mu\varepsilon \frac{\partial^2\overrightarrow{E_z}}{\partial t^2} \quad 2.17$$

Applying the separation of variables method, the solutions of equation 2.17 can be found. After applying boundary conditions this can be presented as two Bessel function solutions.

For the core,

$$E_{z1} = A\, J_v\,(\kappa r) e^{iv\emptyset}\, e^{-i\beta z} \quad 2.18$$

$$H_{z1} = B\, J_v\,(\kappa r) e^{iv\emptyset}\, e^{-i\beta z} \quad 2.19$$

Where $\kappa^2 = (n_{core}k_0)^2 - \beta^2$ and $v = 0,1,2\ldots$ J_v represents the Bessel functions of first kind and order v, A and B are arbitrary constants.

For the cladding,

$$E_{z2} = CK_v(\gamma r) e^{iv\emptyset}\, e^{-i\beta z} \quad 2.20$$

$$H_{z2} = DK_v\,(\gamma r) e^{iv\emptyset}\, e^{-i\beta z} \quad 2.21$$

Where $-\gamma^2 = (n_{cladding}k_0)^2 - \beta^2$ and $v = 0,1,2\ldots$ K_v represents the modified Bessel function of second kind and order v, C and D are arbitrary constants.

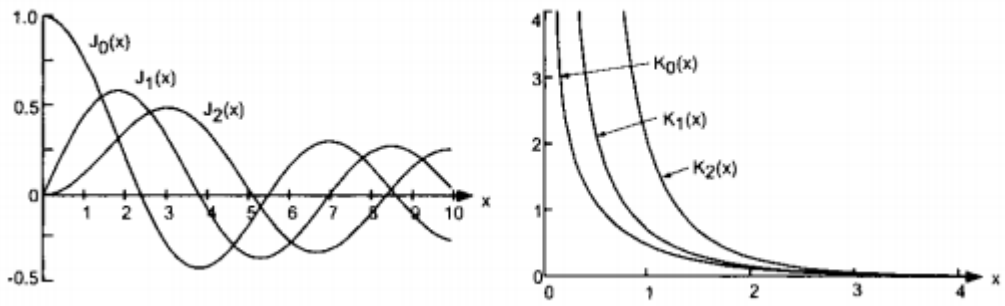

Figure 2.3: The first three Bessel functions of first kind (J_v) and second kind (K_v) [65]

The tangential components, equations 2.15 and 2.16, can be obtained using the equations 2.20 and 2.21 by applying the boundary conditions at core and cladding interface for continuity ($\overrightarrow{\mathrm{E}_{\emptyset 1}} = \overrightarrow{\mathrm{E}_{\emptyset 2}}$, $\overrightarrow{\mathrm{H}_{\emptyset 1}} = \overrightarrow{\mathrm{H}_{\emptyset 2}}$, $\overrightarrow{\mathrm{E}_{r1}} = \overrightarrow{\mathrm{E}_{r2}}$, $\overrightarrow{\mathrm{H}_{r1}} = \overrightarrow{\mathrm{H}_{r2}}$). Hence the characteristic equation of optical fibre can be deduced to be equation 2.22 [64], where 'a' is the core radius.

$$\frac{\beta^2 v^2}{a^2}\left(\frac{1}{\kappa^2}+\frac{1}{\gamma^2}\right)^2 = \left(\frac{J_v'(\kappa a)}{\kappa J_v(\kappa a)}+\frac{K_v'(\gamma a)}{\gamma K_v(\gamma a)}\right)\left(\frac{(n_{core}k_0)^2 J_v'(\kappa a)}{\kappa J_v(\kappa a)}+\frac{(n_{cladding}k_0)^2 K_v'(\gamma a)}{\gamma K_v(\gamma a)}\right) \qquad 2.22$$

The V number of an optical fibre can be defined as

$$V^2 = (\kappa a)^2 + (\gamma a)^2 \qquad 2.23$$

Where $V = k_0 a\sqrt{{n_{core}}^2 - {n_{cladding}}^2} = \frac{2\pi}{\lambda}.a.\sqrt{{n_{core}}^2 - {n_{cladding}}^2}$ 2.24

The solutions to the characteristic equation for a mode show that corresponding to each solution there exists a mode that can propagate along the optical fibre. However, the cut-off frequency of the mode determines its ability to propgate along the fibre. Only if the frequency of a certain mode is higher than the cut-off frequency, can the corresponding mode propagate within the fibre. Cut-off frequency is proportional to the V number (equation 2.24).

2.2.3 Fibre modes

According to equation 2.22 a mode can be characterised by the value of v. When $v = 0$ one term of equation 2.22 should be equal to zero. This will result in two different types of modes. TE_{0m} modes where Ez = 0, or TM_{0m} modes where Hz = 0 and m is a non-zero integer. These TE/TM modes do not have Ø dependence and hence the field is symetrical about the axis of the optical fibre [64].

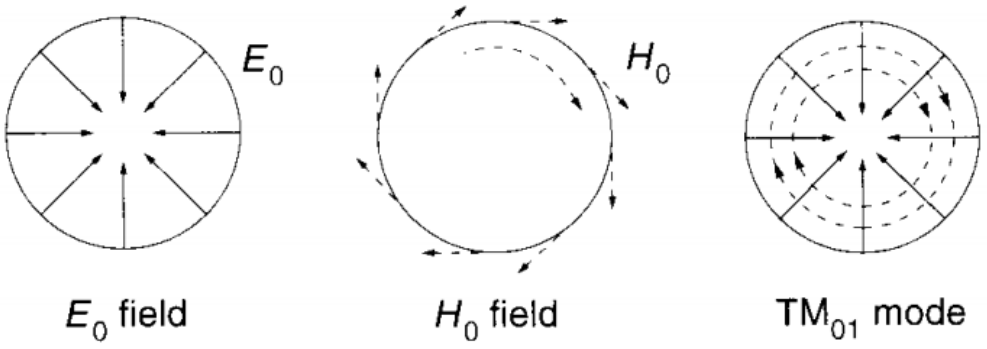

Figure 2.4:TM_{01} mode representation [66]

When $v \neq 0$, the modes have both $E_z \neq 0$ and $H_z \neq 0$ and are called hybrid modes. Hybrid modes can be either EH_{vm} or HE_{vm} depending on what component is dominant.

Realistically, in a step-index fibre the core refractive index is very similar to cladding refractive index. The difference is of the order of 10^{-3} [67] and hence the refractive indices can be considered to be equal using weakly guide approximations. This simplifies the characteristic equations and is used to introduce the concept of linearly polarised modes of the optical fibre.

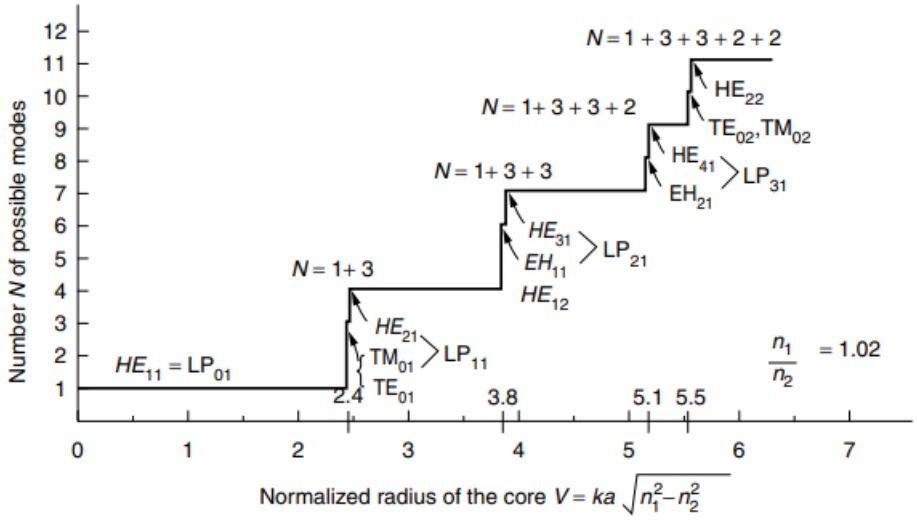

Figure 2.5: Number of possible modes in a step index fibre as a function of normalised radius of the core [66]

As it was mentioned earlier, the V number determines the mode propagation characteristics and cut-off frequency. The lowest order mode that can propagate in an optical fibre is the HE_{11} mode which is the linear polarised mode LP_{01} as shown in figure 2.5.

In single mode fibres, the V number is lower than 2.4, and hence only the lowest mode HE_{11} can propagate. Multimode fibres have a V number higher than 2.4 and can excite multiple modes. According to equation 2.23 to satisfy the single mode requirement, $\left(\frac{a}{\lambda}\right) \approx 4$. For example, for the communication window at 1550 nm, the core radius should be at least 6 μm. Hence, the core diameter of single mode fibres are less than those of multimode fibres.

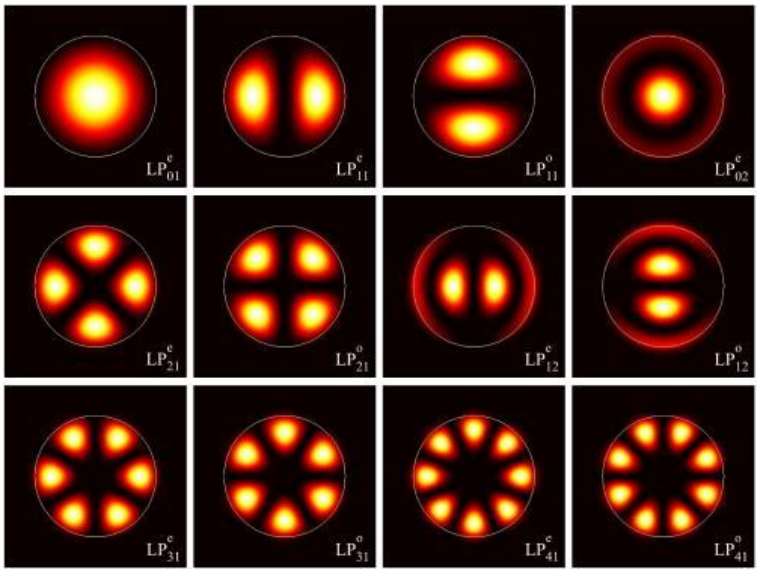

Figure 2.6: Intensity distribution of linearly polarised modes of optical fibre [68]

Figure 2.6 shows a typical example of the intensity distribution of the linearly polarised modes of an optical fibre. One thing that should be noted is for the HE_{11} / LP_{01} mode, most of the optical power is confined in the core of the fibre and less power in the cladding. This is one advantage of single mode optical fibres when compared with multimode fibres. Since a single mode optical fibre carries only one mode that is confined very well in the fibre, the mode suffers less dispersion, and can be propagated over longer distances for communication without attenuation.

2.2.4 Birefringence of optical fibres

Linearly polarised modes were derived by making two assumptions: the weakly guided approximation and the circular symmetry of the modes. However, when the radial symmetry of an optical fibre is broken, this may lead to an anisotropic distribution of the refractive index in the fibre. This will introduce birefringence characteristics to the optical fibre. In a single mode fibre, the HE_{11} mode consists of two orthogonally polarised modes. If the fibre is circular symmetric, the two modes will propagate at the same speed. However if the fibre is not circular symmetric, these two modes will propagate at slightly different speeds. This will result in the output signal of the light being split into two components

that are slightly delayed with respect to each other [69]. This phenomena is called the birefringence of the optical fibre.

This asymmetry may result from either intrinsic birefringence or induced birefringence. Intrinsic birefringence may be introduced during the manufacturing process and is a permanent feature of the fibre. This can be a noncircular core giving rise to geometrical birefringence, or a circular core with a non-symmetrical stress field in the fibre cross section, creating stress birefringence. Examples are bow-tie Hi-Bi fibres and PANDA Hi-Bi fibres [70].

Induced/extrinsic birefringence is produced when a fibre undergoes elastic stresses resulting from external forces such as hydrostatic pressure, longitudinal strain as a result of transverse loading on the fibre, squeezing, twisting or bending etc. This is further described in section 2.5 with respect to the related work.

2.3 Fibre optic interferometry

In this section of the thesis the background related to Fabry-Perot interferometry is discussed.

Generally, optical interferometry techniques use the interference of two or multiple light beams from the same light source, or the propagation of light through space or dielectric media such as glass waveguides with different optical paths. As a result the light intensity varies periodically as a function of the optical path difference between the beams [71]. This wavelength-dependent intensity modulation is caused by the optical phase difference between beams of interference. These periodic changes in the intensity are often called the interference pattern or interference fringes. The wavelength changes in the optical path difference on the scale of the output from the light source can introduce a measurable change in the interference pattern [72]. When the interference beam is in phase, maxima are formed and when they are out of phase minima are formed in the interference pattern. To setup a stable interference pattern two important conditions should be met. The light

source should be a coherent source that produces identical waves with a constant phase difference and waves should be monochromatic.

With the development of fibre optic technology, optical interferometry was greatly advanced from the classical bulk optics [73]. Fibre optic interferometry has been exploited in many applications such as temperature [74], pressure, strain [75] and acoustic measurements [76]. Figure 2.7 shows four main configurations of fibre optic interferometric techniques.

The coherence length of narrow bandwidth light sources like lasers are greater than the optical path difference of the interferometer. Because of the periodic nature of the interference fringe pattern, the measurement due to the optical path length difference, may suffer from 2π phase ambiguity [77]. Hence, light sources with narrow line bandwidth do not produce absolute data. Resolving this issue will add extra complexity to the system. This can be resolved by employing light sources with short coherence length like tungsten light sources. In wide bandwidth interferometers, the fringes are narrowly located in the zero path length difference region [78]. Therefore, the phase can be determined without ambiguity by measuring the fringe peak.

The fibre optic Mach Zehnder interferometer uses two fibre optical paths one connected with the sensor, and the other standing as the reference, Figure 2.7(a). The light in the reference arm and the sample arm are directed to a splitter/combiner and the light interference is measured by a detector. Any change in the optical path length of the sensor arm due to the physical changes in the sensor will be detected as a shift in the interference pattern [79].

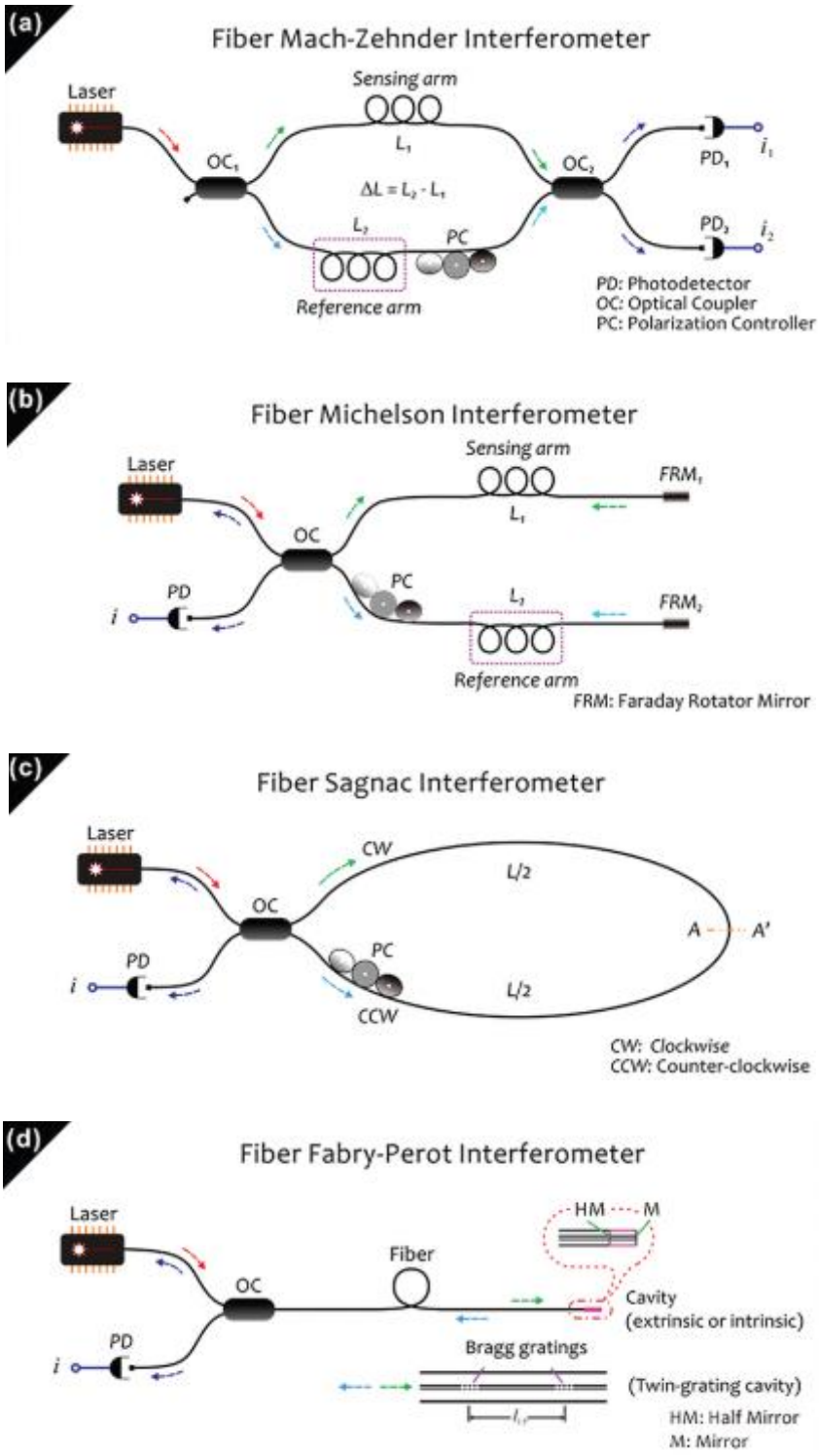

Figure 2.7: Configuration of main fibre optic interferometric techniques (a) Mach-Zehnder interferometer (b) Michelson interferometer (c) Sagnac interferometer (d) Fabry-Perot interferometer [72]

The Michelson interferometer is similar to the Mach Zehnder interferometer except that the light from the sensor arm and the reference arm are reflected

back to the coupler, where they are combined and directed to the detector as seen in the figure 2.7 (b). In the Sagnac interferometer the incident light is split into two beams and these two beams travel in opposite angular directions as can be seen in figure 2.7 (c). After completing a trajectory the light beams will recombine at the point it split. When the external measurand disturbs the fibre close to one end of the loop a phase shift occurs and an interference shift happens [72][79].

Figure 2.7 (d) represents the schematic of a fibre optic Fabry Perot interferometer. The working principles are explained, extensively along with their applications in the next section 2.4.

2.4 Fibre sensing technology, fluid pressure sensing and application of fibre optic Fabry –Perot pressure sensors in healthcare

Fibre optic sensing technology used in fluid pressure sensing and contact pressure sensing in healthcare applications is extensively discussed below.

2.4.1 Fluid pressure sensing in health care

Fluid pressure is the force per unit area exerted by a fluid acting perpendicular to any surface it contacts. Fluid can be in the form of a gas or liquid [80]. Fluid pressure sensing plays a vital role in healthcare. For example, intra-arterial blood (IBP) pressure monitoring is one of the techniques commonly used in intensive care units and that is often used in operating theatres. This is done by inserting a catheter (a thin hollow tube which is inserted into a large blood vessel) into a suitable artery and then displaying the measured pressure waveform on a monitor [81]. The pressure waveform of the arterial pulse is transmitted via the column of fluid to the pressure transducer where it is converted into an electrical signal. This technique has many advantages where conventional a sphygmomanometer cannot be used, for example, when BP pressure is measured in shocked patients [82]. Moreover, it avoids the trauma caused by repeated cuff inflations, significant for patients who are likely to

need close blood pressure monitoring for a long period of time. Another example are pressure measurements done during cardiac catheterization. Cardiac catheterization is a procedure to examine how well the heart is working. [83]. The pressures measured during cardiac catheterisation are the mean pulmonary artery pressure (mPAP) and the mean right arterial pressure (mRAP) [84]. Other fluid pressure measurements examples include those undertaken in endoscopic tools to measure the pressure in esophagus or intravariceal pressure [85], respiratory pressure measurements, which involve the measurement of the pressure of air expelled from the lungs, and in therapeutic equipment such as nebulizers, ventilators and laparoscopic devices, where gastrointestinal internal pressure should be measured [86].

In most of the above illustrated situations, invasive pressure measurements are involved and it is of great importance in medical diagnostics. Most of the invasive pressure measurements are done indirectly through a fluid line, where pressure is transmitted from the organ to a remote transducer using a fluid filled catheter [87]. This method has several drawbacks. This method is highly affected by the movement of a patient and therefore throughout the measurement the patients should stay still, which is not very practical.

Direct measurement of the pressure during invasive pressure measurements have many more advantages over indirect measurements, such as higher accuracy, immunity to motion and patient's movements and high response time.

Various aspects should be considered when designing a system for invasive direct pressure measurements. The key considerations are biocompatibility, inertness, and the size of the sensor. This will allow minimally invasive procedures which will be beneficial for the patient as well as the therapist/ physician causing less trauma to the muscles, less bleeding, less scarring, less pain and thus reduced use of narcotics, less effects on the immune system, less trauma to organs and fewer cuts [88].

Within the context of this research, the targeted applications are listed in table 2.1. The measurement standards including required pressure range, pressure resolution and sampling frequency for different potential applications in invasive pressure sensing are detailed in table 2.1.

Table 2.1: Targeted applications of the FP sensor along with the required standards

Area	Body part	Min. pressure	Max. pressure	Pressure resolution	Sampling frequency	Reference
Cardiology (BP monitoring)	Heart, Arteries, Veins	-4 kPa	40 kPa	0.013 kPa	200 Hz	AAMI BP22[89]
Urology (Cystometry)	Bladder, Abdomen	0 Pa	25 kPa	0.050 kPa	10 Hz	[90]–[92]
Neurology (Intracranial pressure monitoring)	Brain, Skull, Dural Tissue	0 Pa	13.3 kPa	0.260 kPa	-	[93], [94]
Gastroenterology	Stomach. Colon	0 Pa	13.3 kPa	-	8Hz	[95], [96]
Opthalmology	Eyes	0 Pa	8 kPa	0.013 kPa	100 Hz	[97], [98]

2.4.2 Fibre optic Fabry-Perot pressure for invasive medical applications; advantages over other techniques

Conventional pressure measuring methods involve piezo-resistive or capacitive techniques, strain gauges and solid state sensing methods. They represent robust, highly tested, mature technologies offering precise measurements and competitive prices [13]. However, the main drawbacks of these technologies includes long-term drifts, electrical shock hazard, fragility and costliness [99].

Fibre optic pressure sensors are a very good candidates for invasive pressure measurements. They have many advantages over the conventional pressure sensing methods used for invasive medical applications. Optical fibres are made of amorphous silica (SiO_2). Most of the times this is an chemically inert and biocompatible compound [100],[13]. By selecting biocompatible fibre coatings and biocompatible diaphragms the requirement for inertness is maintained.

Moreover, fibre optics can be used under sterilisation or high levels of disinfection to eliminate all the microorganisms that might be on the surface of the optical fibre [101][102], hence minimising the risk of infections associated with invasive procedures. Optical fibres are thin and flexible. However, optical fibres should be encapsulated within layers of biocompatible and sterilisable layers in order to protect them from mechanical abrasion. These coatings are made of polymeric materials such as acrylate, polyimide, silicone, metallic coatings such as aluminium, tin gold, indium and inorganic coatings such as oxides, carbides, nitrides and carbon [103]. Thus a carefully designed fibre optical sensor is an ideal candidate for invasive biomedical applications.

Along with the advantages that have been discussed in chapter 1, which are common to almost all fibre optic sensors, there are more benefits of selecting Fabry Perot techniques for pressure sensing in invasive medical applications. The fibre optic Fabry- Perot technique provides the highest design flexibility

(for choosing different cavity sizes, different diaphragms to alter the sensitivity) and sensitivity among other fibre optic pressure sensing methods [104]. Moreover, it can fabricate the most miniaturised versions of the pressure sensors among other fibre optic pressure sensing techniques.

2.4.3 Fibre optic FP pressure sensors-how it works?

A Fabry-Perot interferometer (FPI) is formed by making a cavity between two reflective mirrors. Figure 2.8 shows the basic structure of a Fabry-Perot interferometer. M1 and M2 are two mirrors with reflectivities r1 and r2 respectively. 'n' is the refractive index of the medium of the cavity. The reflectance 'R' of the interferometer can be given using the following equation [105].

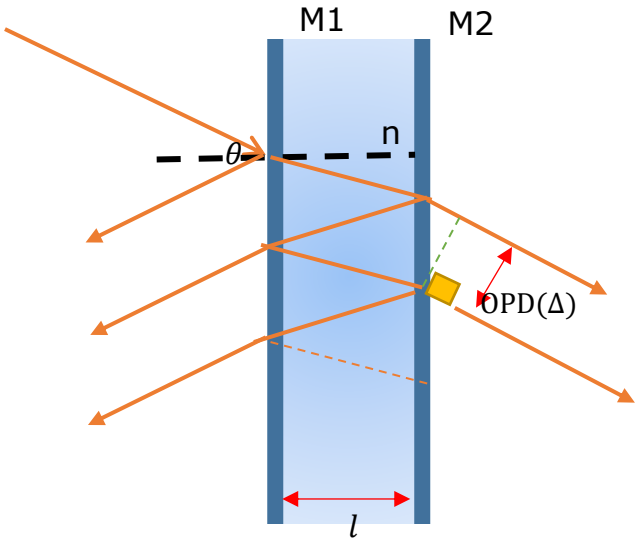

Figure 2.8: basic structure of Fabry-Perot interferometer, l is the cavity length, Δ is the optical path difference, n is the refractive index of the cavity medium. M1 and M2 are the two parallel reflection surfaces

$$R = \frac{r_1+r_2+2\sqrt{r_1 r_2}\cos\emptyset}{1+r_1 r_2+2\sqrt{r_1 r_2}\cos\emptyset} \qquad 2.25$$

Where $\emptyset$ is the propagation phase shift in the interferometer, λ is the free space wavelength, R is the ratio of the intensity reflected by the FPI to the incident intensity. The propagation phase shift is given by

$$\emptyset = \frac{2\pi}{\lambda}.\Delta \qquad 2.26$$

Where, Δ is the optical path difference (OPD) can be given as follows

$$\Delta = 2 * n * l * cos\theta \qquad 2.27$$

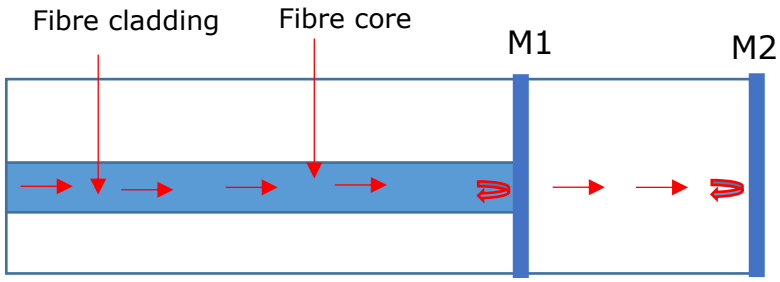

Figure 2.9: Fibre Fabry-Perot Interferometer, M1 and M2 are the reflection interfaces

For a single mode fibre, it can be assumed as that the light is incident normal to the mirror

$$\Delta = 2 * n * l * 1 \qquad 2.28$$

Hence the propagation phase shift can be written as

$$\emptyset = \frac{4\pi nl}{\lambda} \qquad 2.29$$

For the above equation 2.25, normal incidence reflectivity (r) can be given using equation 2.30

$$r = \left[\frac{n1-n2}{n1+n2}\right]^2 \qquad 2.30$$

'n_1' is the refractive index of the incidence medium and 'n_2' is the refractive index of the transmitted medium.

Figure 2.10 shows the simulated reflection spectrum based on equation 2.25, of a fibre Fabry-Perot sensor using equation 2.30, where it was assumed that the Fabry-Perot cavity length was 20 µm and that the cavity medium was air during the simulations. It is also assumed that there are no losses due to absorption or scattering. As the wavelength increases, the frequency of the intereference decreases and hence the period between the fringes increases.

Figure 2.11 shows simulated reflection spectra of fibre Fabry-Perot sensors with different cavity lengths. By changing the cavity length, one can observe a wavelength shift. If the end mirror of the fibre Fabry-Perot sensor is made from a deflecting diaphragm the cavity length could be changed accordingly. According to equation 2.25, pressure which perturbs the OPD within a range of 0- λ/2 can be detected. Beyond this range, 2π ambiguity will start to show up.

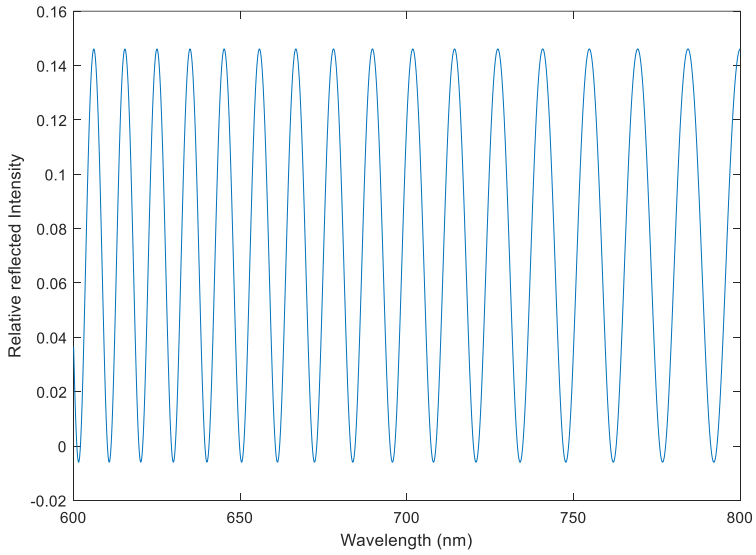

Figure 2.10: Simulated reflection spectrum of a Fabry-Perot for normal incidence when cavity length 20 μm

According to equation 2.25, intensity maxima occur when

$$R_{max}\ cos\left(\frac{4\pi nl}{\lambda}\right) = 0 = cos(m * 2\pi)\,; m \in \mathbb{Z} \qquad 2.31$$

Therefore,

$$l = \frac{m * \lambda}{2} \qquad 2.32$$

(n=1 for air cavity)

For small deflections, the shift of a given reflectance maximum is linear with the shift in the cavity length

$$dL = \frac{2}{m} d\lambda_m \qquad 2.33$$

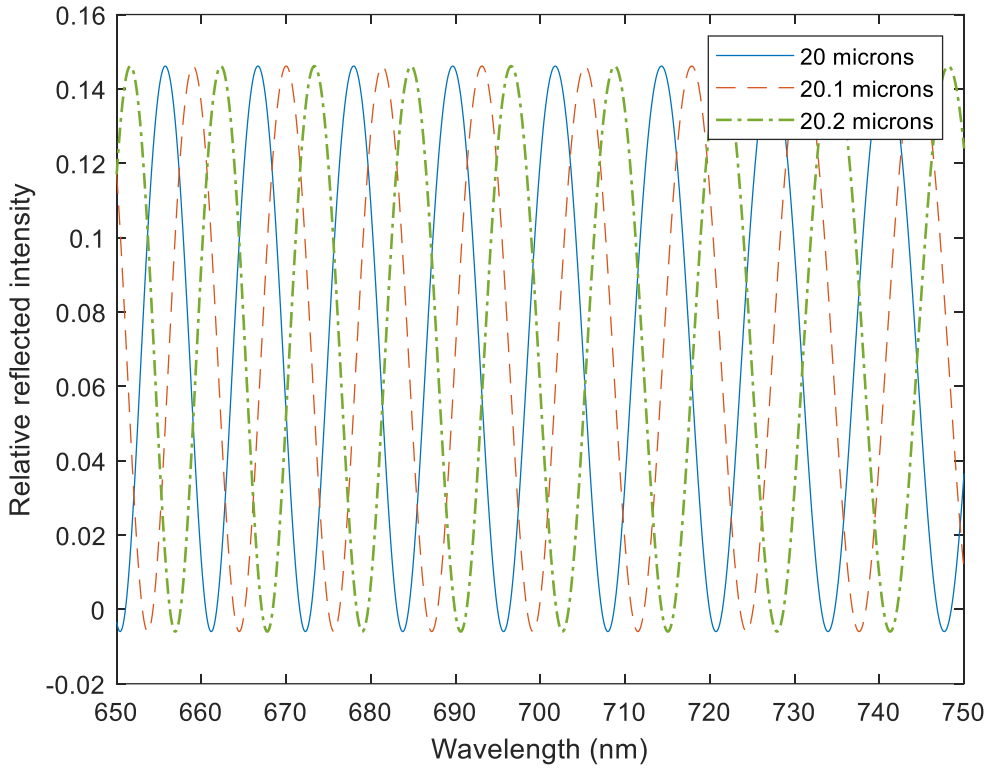

Figure 2.11: Simulated reflection spectrum of a Fabry-Perot interferometer for normal incidence when the cavity length changes (20, 20.1, 20.2 μm)

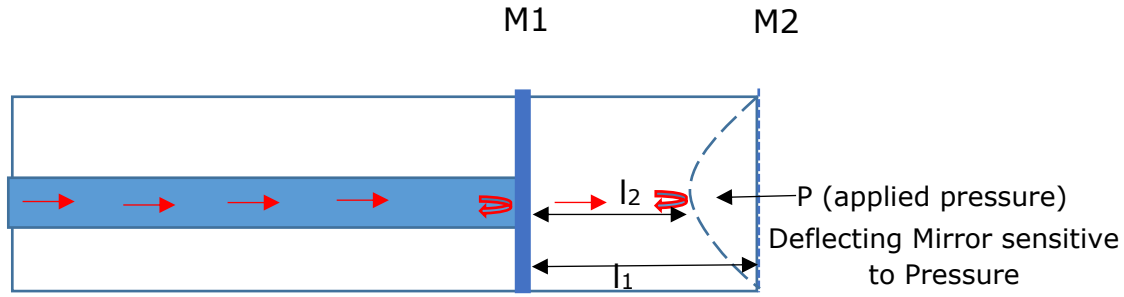

Figure 2.12: Schematic of a fibre Fabry-Perot tip pressure sensor, P is the applied pressure, l_1 is the initial cavity length before application of the pressure, l_2 is the cavity length after applying the pressure P. M1 formed by a fibre-air interface and M2 is air-film interface

Figure 2.12 shows a schematic of a fibre Fabry-Perot pressure sensitive interferometer. As the pressure is applied, mirror M2 will deflect and the cavity length will change accordingly. According to above figure 2.11, as the cavity length changes, wavelength maxima and minima of the reflection spectrum

also shift. Therefore by using a pressure sensitive mirror a fibre Fabry-Perot interferometer pressure sensor can be made.

2.4.4 Theoretical analysis of the sensitivity of the elastic diaphragm to the applied pressure

The sensitivity of the fibre optic Fabry-Perot pressure sensor depends on the rate of cavity length changes with respect to the applied pressure. The following section describes, in theory, how much deflection the flexible membrane should undergo according to the applied pressure and hence allows the theoretical sensitivity of the fibre optic Fabry-Perot pressure sensor to be calculated.

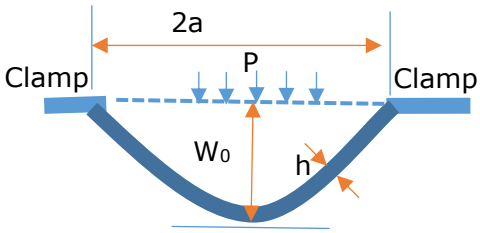

Figure 2.13: Schematic diagram of a circular membrane of a radius 'a' deformed by a uniform pressure 'P', and the deflection at the centre of the memebrane is 'w0',and the thickness of the membrane is 'h'

The sensitivity of the pressure sensor is given by

$$\frac{deflection\ of\ the\ membrane}{change\ of\ the\ pressure} = Sensitivity \qquad 2.34$$

$$\frac{\Delta W_0}{\Delta P} = Sensitivity \qquad 2.35$$

The behaviour of a circular membrane under uniform pressure was first solved by Hencky [106], [107]. This solution was modified to include the initial tension of the membrane by Campbell [108].

The centre deflection of the circular membrane of radius 'a' and a thickness 'h' under uniform pressure for small initial tension such as the conditions given in [108] can be given by,

$$W_0 = 0.653a\left(\frac{Pa}{Eh}\right)^{\frac{1}{3}} \qquad 2.36$$

Where E = Young's modulus.

For large intital tension or small applied pressure such as the conditions given in [108], the centre deflection can be given by,

$$W_0 \approx \frac{a}{4}\left(\frac{Pa}{\sigma h}\right) \qquad 2.37$$

Where σ = initial stress

2.4.4.1 Wavelength sensitivity of the diaphragm to pressure for small initial tension

Using equation 2.36, the sensitivity in the terms of diaphragm deflection with applied pressure for a membrane with a small initial tension is

$$\frac{dW_0}{dP} = 0.2176\, a\left(\frac{a}{Eh}\right)^{\frac{1}{3}} .\ (P)^{-\frac{2}{3}} \qquad 2.38$$

In the FP interferometer, deflection of the diaphragm can be related to the cavity length as $\Delta W_0 = \Delta L$

The cavity length and the wavelength of the mth reflection maximum can be written as,

$$\frac{\Delta L}{L} = \frac{\Delta \lambda_m}{\lambda_m} \qquad 2.\ 39$$

Thus, equation 2.38 can be written as,

$$\frac{\Delta \lambda_m}{\Delta P} \cong\ 0.2176\, a\left(\frac{a}{Eh}\right)^{\frac{1}{3}} .\ (P)^{-\frac{2}{3}} .\ \frac{\lambda_m}{L} \qquad 2.\ 40$$

The wavelength change due to the pressure change can therefore be represented by equation 2.40

According to the above equation the wavelength sensitivity of the diaphragm is a function of pressure.

The FP interferometer's wavelength sensitivity for pressure range 0-15 kPa can be plotted for a diaphragm diameter of 21 µm and a cavity length of 10 µm as shown in figure 2.14 . These values were considered because sensor 01 (cavity diameter 21 µm and cavity length ~10 µm) described in chapter 3 has

approximately these dimensions. The Young's modulus of the film is 4600 MPa and the thickness of the film is 200 nm. The wavelength maximum is assumed to be 740 nm.

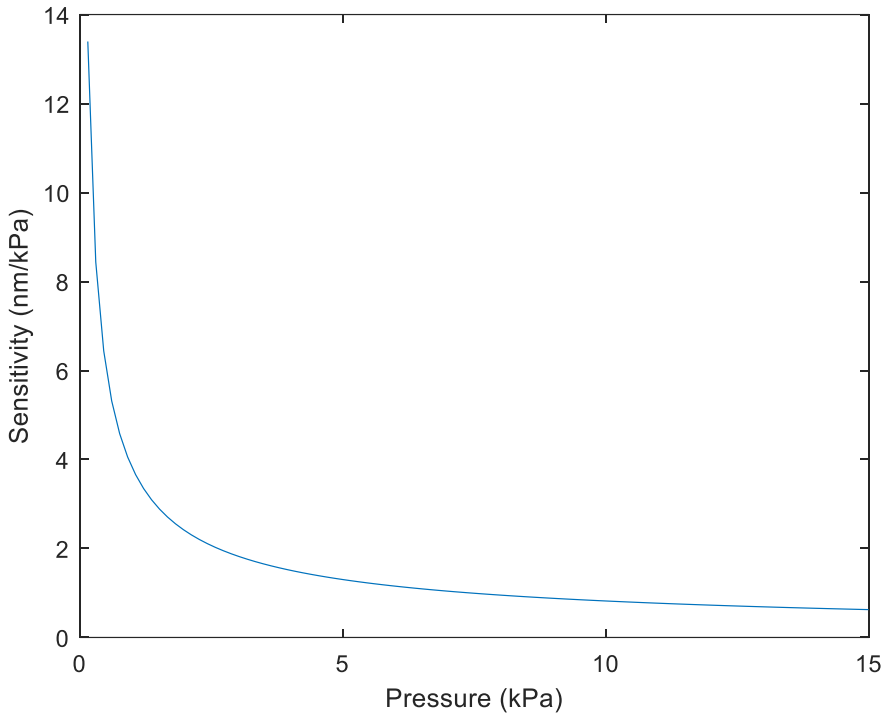

Figure 2.14: FP interferometer wavelength sensitivity as a function of pressure for diaphragms with smaller initial tension

According to figure 2.14 it is clear that as the applied pressure increases the sensitivity of the FP interferometer decreases for the case where the diaphragm has zero or small initial tension. This is similar to the situation where the Parylene film is attached to the fibre tip loosely.

2.4.4.2 Wavelength sensitivity of the diaphragm to pressure for larger initial tension

In a similar manner to the derivation in section 2.4.4.1, using equation 2.37 it can be shown that for a diaphragm with a larger initial tension, the wavelength change due to the pressure change is,

$$\frac{\Delta\lambda_m}{\Delta P} \cong \frac{1}{4}\left(\frac{a^2}{\sigma h}\right).\ \frac{\lambda_m}{L} \qquad 2.41$$

According to equation 2.41 it is clear that for a diaphragm that is under a significant initial tension, the sensitivity is not dependent on the applied pressure. In this situation, the sensitivity is directly proportional to the square of the diaphragm's radius and inversely proportional to the initial stress.

The sensitivity of the FP interferometer can be plotted against the initial stress for the following conditions: diaphragm diameter of 21 µm, cavity length of 10 µm, Young's modulus of the film of 4600 MPa and film thickness of 200 nm. The wavelength maximum is assumed to be 740 nm.

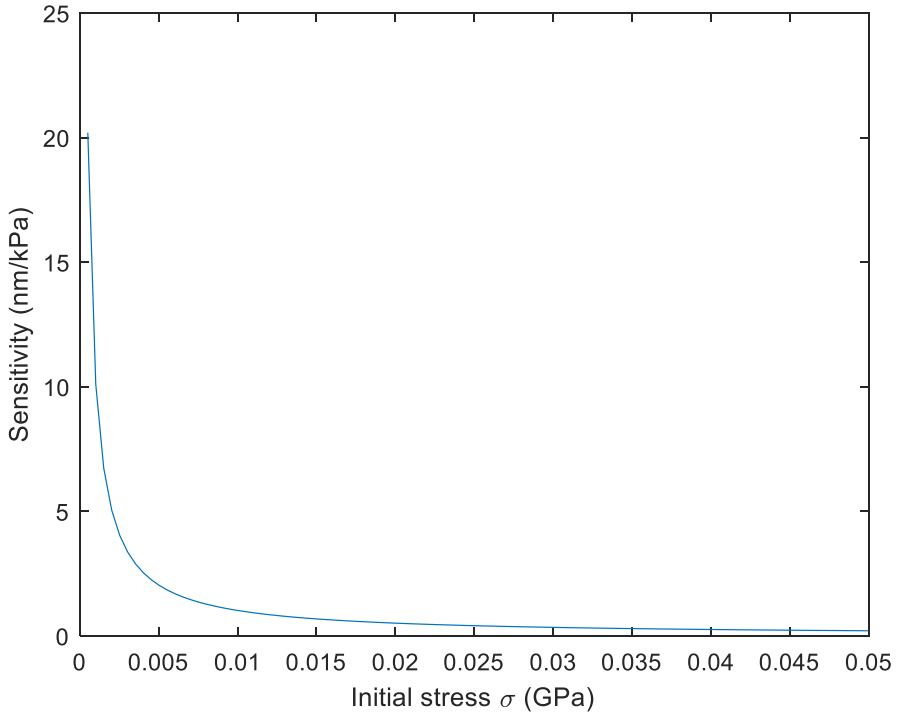

Figure 2.15: FP interferometer wavelength sensitivity as a function of initial stress for diaphragms with larger initial tension

By applying a pre-tension to the diaphragm a linear change of the wavelength to the pressure could be observed.

2.4.5 Literature review on fibre optic FP pressure sensors

This section will review commercially available Fabry-Perot pressure sensors used in biomedical applications and provide a detailed review of the miniature Fabry Perot pressure sensors reported in the literature. It will detail how the sensors are fabricated, their sensitivities and what diaphragm materials are used.

Table 2.2 presents the commercially available fibre optic Fabry-Perot pressure sensors. Although the number of companies producing miniature fibre optic Fabry-Perot sensors is not large, the technique is widely used and is suitable for minimally invasive medical procedures, as discussed previously.

The pressure sensors from FISO technology use a drum like structure that is attached to the tip of the fibre to act as the pressure transducer [109]. This structure consists of a flexible membrane and a vacuum cavity. The bottom of the cavity which is the tip of the optical fibre, and the flexible membrane acts as the two reflective mirrors for the Fabry-Perot structure. This flexible membrane is pressure sensitive and changes the cavity length with respect to the applied pressure. FOP-M offers miniature sensors (~ OD 0.25- 0.5 mm) manufactured using well established photolithographic techniques [110]. Hence, this flexible membrane is made of a thin silicon layer. The company claim that they have manufactured the world's smallest pressure sensor FOP-F125, in their published journal article [104]. However, at the time of writing it is not available on the market. FOP-F125 is made from all glass, even the diaphragm, providing more flexibility than silicon. The cavity is carved at the tip of the fibre using patented technologies [111][112].

RJC enterprises manufacture patented miniature pressure sensors expoiting multimode fibre optic Fabry-Perot techniques. They use an LED to interrogate the optical cavity with an emission bandwidth of about 60nm [113]. The reflectance of the emission wavelength varies uniquely with the optical cavity length. The reflectance change occurring between a maximum and a minimum within a single reflectance cycle and the sensor response is linear over a very

short range. The sensor consists of a glass optical fibre and a glass substrate attached to it which forms the Fabry Perot cavity structure. The pressure sensing diaphragm is a silicon membrane. The cavity has thickness of 1.4-1.7 µm and a 200 µm diameter. The cavity is etched using Hydrofluoric acid. The bottom surface of the cavity is coated with titanium dioxide. The prepared silicon wafer film is then attached to the cavity permanently and hermetically using a bonding technique called 'anodic bonding'.

A miniature fibre optic Fabry Perot pressure sensor using three different fibre types of SM fibre, graded index multimode fibre (62.5/125 µm) and step index multimode fibre (105/125 µm) has been proposed by Zhu Y et al. [114]. The SM fibre is spliced to a 105 µm core diameter fibre and cleaved to create a thin layer (~ 10 – 15 µm) of 105 µm fibre on top of the SM fibre. This thin layer of fibre acts as the etch limiting layer. The 62.5 µm fibre is then spliced to it and cleaved at a certain length (~ 20 – 30 µm). Then this is immersed in Hydrofluoric acid. Since the etching rates for doped and undoped cores are different, the etching process will stop at the barrier layer. Once the cavity is created, a length of 105 µm fibre is spliced once again using a special set of splicing parameters in order to prevent the structure deforming. These splicing parameters are described in chapter 3. Afterwards this fibre is cleaved by leaving a layer of 105 µm fibre. In order to reduce the thickness of this layer, which will ultimately act as the diaphragm, etching is performed. The pressure range gives 137-1310 kPa with a sensitivity of 0.043 nm/kPa with an excellent repeatability.

Wang X. et al. [115] proposed a miniature fibre tip pressure sensor for biomedical applications. This sensor is comprised of a single mode fibre spliced with a hollow fibre. The detailed information of the fabrication is not presented. However the claimed tested pressure range is 1034.2 mmHg (137.88 kPa) - 1551.3 mmHg (206.82 kPa) and sensitivity is 0.039 nm/mmHg. This is a sensitivity of 0.299 nm/kPa.

Guo F. presented a fibre tip Fabry-Perot interferometric sensor based on a thin silver film [115]. The silver thin film is prepared using vapour deposition techniques. The cavity is formed at the tip of the fibre using two different

methods. The first involves inserting the fibre into a micro tube which has an inner diameter of 150 µm and an outer diameter of 365 µm. Under the microscope the fibre is pushed carefully into the tube until the required cavity length is achieved. The other method involves splicing a micro tube to the fibre and then cleaving it. The silver film is then attached to the fibre cavity using UV Epoxy under the microscope. The obtained sensitivity is 1.6 nm/kPa, over a pressure range of 0-344 kPa . However this sensor suffers from drift in the baseline with time.

Chen L H et al. proposed a fibre optic FP pressure sensor based on a Chitosan diaphragm [116]. Chitosan is a material which is biodegradable and provides elastic properties. The proposed sensor has outer diameter of 125 µm and inner diameter of 75 µm. The thickness of the diaphragm is 1.5 µm. SMF28 single mode fibre was first cleaved to make a perpendicular surface and then spliced with hollow core fibre to form a cavity. Then the hollow core fibre was cleaved at the desired cavity length. The film was deposited using the dip coating technique. The sensitivity obtained was 0.4336 µm/kPa. This technique suffers from air permeability of the diaphragm. However, the paper claims that, since the cavity is smaller than the diaphragm size, it is expected to be insensitive to the background pressure drift while maintaining its sensitivity.

Table 2.2: Commercialised fibre optic Fabry- Perot pressure sensors available on the market

Company and Product	**Specifications**				**Applications**	**Reference**
	Dimension	**Resolution**	**Pressure range**	**Speed**		
Opsense OPP-M25	0.2mm OD	66 Pa	-6.66 kPa to 40 kPa	250 Hz	Intravascular blood pressure Urodynamic Intra cranial pressure Intra uterine pressure Intra ocular	[117]
FISO FOP-M200-NS	0.2mm/0.225mm/0.272mm/0.307mm OD	40 Pa	-40 kPa to 40 kPa	250 Hz	Cardiovascular: arterial BP, LV pressure Urology: bladder/ureter pressure Endoscopy Spine/Bones: Intradiscal pressure Neuroscience: intracranial pressure	[118]

Endosense PN-004075 PN-00465	Tip electrode: 3.5mm		0-70grams		Force sensor at distal catheter tip Contact force ablation catheter: treatment of cardiac arrhythmias ,	[119]
RJC Enterprises , LLC Model 60 Model 62 Model 40	0.508mm, 0.324mm, 0.273mm OD	<13 Pa	66kPa to 133 kPa	1 kHz	Medical applications Intracranial pressure Vascular pressure applications	[120][113]

Wu J. et al. [121] reported a fibre optic Fabry Perot sensor probe (dimensions: ~ 100 micron OD) fabricated by an in house developed 3D micro printing setup for highly localised pressure measurements. The reported sensitivity is 2.9 nm/MPa for a pressure range of 0-700 kPa. SU8 diaphragm is directly printed on the end face of a standard single mode fibre to form a sealed FP cavity. Hill G. C. et al. [122] reported a fibre optic FP pressure sensor for invasive biomedical applications based on SU8 biocompatible polymer. The sensor head diameter was 300 µm. The reported sensitivity is in the range of 13.5- 21.02 nm/kPa (1.8-2.8 nm/Hgmm). However, this sensor suffers from sensitivity and linearity degradation with time and the large coefficient of thermal expansion of SU8 polymer affects the cavity length of the polymer.

Katsumata T. et al. [123] proposed an ultra-miniature pressure sensor for invasive blood pressure measurements using catheters. The outer diameter of the sensor is 125 µm. An SiO_2 diaphragm is manufactured by the wafer deposition technique and the cavity is formed by attaching polymide spacers between the film and the tip of the fibre. Micromachining techniques are used to fabricate the sensor. The intensity modulation technique has been used to integrate the cavity.

Other miniature fibre optic Fabry Perot pressure sensors designed for invasive medical therapies which are available in literature are summarized in table 2.3. Among these available technologies, this PhD research work attempts to discuss and develop a novel miniature fibre optic Fabry Perot interferometric sensor with a head diameter of 125 µm using all biocompatible materials and a unique method (focused ion beam technology), for application in invasive pressure monitoring in healthcare.The targeted applications are included in table 2.1.

2.4.6 Proposed fibre optic Fabry- Perot sensor

One of the main objectives of this PhD is to develop a novel miniature fibre optic pressure sensor for invasive biomedical applications.

A simple schematic of the sensor is shown in figure 2.16.

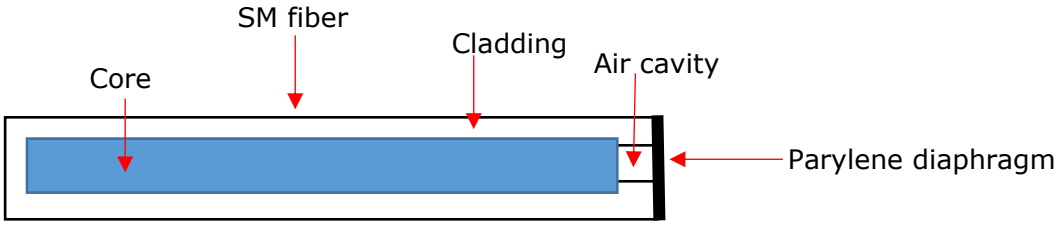

Figure 2.16: Simple schematic of the proposed fibre optic Fabry-Perot pressure sensor

The proposed sensor has a maximum sensor diameter of 125 µm. Two fabrication methods were proposed for cavity formation. The first method is to inscribe the cavity at the tip of the SM fibre using focused ion beam micromachining technology. The second method of the cavity formation involves splicing the SM fibre to a capillary fibre tube and cleaving it to make a micro air cavity. Splicing a capillary tube to an optical fibre is a cost effective and simple method when compared with the FIB method. The details of the methods are described in Chapter 3. Parylene-C vapour deposited polymer is used as the pressure sensitive diaphragm at the end of the optical cavity. Since Parylene and silica are biocompatible materials this is an ideal candidate for invasive biomedical applications. Zhou M. et al. [124] presented an implantable pressure sensor fabricated for left ventricular assist devices (LVDA) based on a Parylene diaphragm with a silicon mirror at the centre. However, the design is used for the sensing element of the inlet area of about 36mm^2 of the LVDA device and use a complex fabrication mechanism.

Table 2.3: Summary of fibre optic Fabry-Perot sensors for medical applications available in literature

Sensor	Description of fabrication and dimensions and notes	Sensitivity and range	References
A Novel MEMS Pressure Sensor Fabricated on an Optical Fibre	200 µm diameter, silicone diaphragm (7 µm) bonded anodically to the tip of the fibre cavity. Air cavity (0.6 µm) created using photolithographic patterning and chemical etching.	0.115 mV/ kPa, 0-551 kPa	[125]
Miniature Fibre Optic Pressure Sensor for Medical Applications	125 µm diameter, diaphragm thickness of 4 µm, cavity length of 80µm, cavity is formed by splicing SM fibre with MM fibre and chemically etching. Polymer diaphragm is attached to the tip of the cavity by dipping in the polymer solution and drying	~0.067 nm/kPa 0-40 kPa	[126][127]
Compressible fibre optic micro-Fabry-Pérot cavity with ultra-high-pressure sensitivity	125 µm diameter, cavity is formed by immersing a single mode fibre spliced with silica tube into a liquid to form a microbubble. Diaphragm free method. One reflector is the silica-air interface, and the other reflector is air-liquid interface. Main drawbacks in this method are in each use the sensor should be calibrated, the sensor should be always positioned vertically to the liquid, stabilisation problems of the air bubble.	>15 nm/kPa	[128]
Miniature all-glass robust pressure sensor	125 µm diameter, a cavity is micro machined at the tip of a sensor forming fibre using chemical etching techniques, cavity side is fusion-spliced to the lead fibre, sensor forming fibre is cleaved near the splice by visually inspection under a microscope and polished.	>10 nm/kPa (~0-25 kPa)	[129]
All-fibre high-sensitivity pressure sensor with SiO2 diaphragm	125 µm diameter, SM fibre spiced with MM fibre and MM fibre is chemically etched to form the cavity, another SM fibre is spliced at the end of the cavity to form the diaphragm and polished to form a thin diaphragm.	1.1 rad/40 kPa diaphragm deflection 3.4 nm /kPa (0-40 kPa)	[130]

2.4.7 Parylene-C films as the pressure sensitive diaphragm

Parylene C (poly (dichloro-p-xylylene)) is a polymeric material commonly used as a substrate or encapsulation material for many kinds of biomedical micro devices [131].

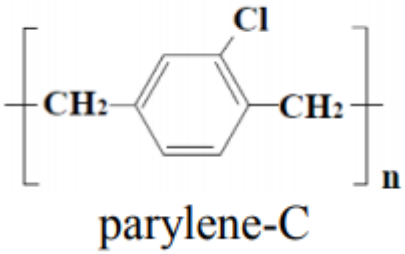

Figure 2.17:Chemical molecular structure of parylene-C [132]

Parylene is an FDA approved biocompatible material with the highest U.S. Pharmacopeia class VI approval and is considered to be material suitable for long term medical implantation [133]. Moreover it is extremely stable chemically and biologically and is resistant to high temperatures and to corrosive gases. These characteristics make parylene an ideal candidate for invasive biomedical processes. Parylene has been widely used as a coating material for implantable biomedical devices [134], surgical instruments, mandrels and medical devices and medical electronics [135],[136]. The mean Young's modulus of parylene-C lies in 1.3 GPa- 3.5 GPa range [137] and it can bear up to 200% elongation before it breaks [138]. According to equations 2.36 and 2.37, although the large Young's modulus reduces the deflection in respect to applied pressure, the sensitivity can be increased by using a thin membrane (~100nm) as the sensitivity is inversely proportional to the thickness of the diaphragm. Consequently, due to the above discussed characteristics of parylene-C it is a suitable candidate for the pressure sensitive diaphragm for invasive biomedical applications.

2.4.7.1 Self –supporting Parylene-C chemical vapour deposition

Parylene-C thin films are produced by using a method called chemical vapour deposition (CVD). The mechanism of CVD can be described as follows, based on references [132] and [139]. Parylene-C films are grown as vapour deposits, molecule by molecule in a room temperature vacuum chamber, on a sacrificial layer. The parylene-C CVD process starts with a granular form of Parylene, dimer paracyclophane (di-poly-chloro-p-xylylene or DPX-C). In the first step, the solid is converted to its gas phase by a process called 'sublimation', where the temperature is maintained at 110-150 °C and the pressure is 1 mbar. In the second step, the vapour is pyrolyzed (decomposed using high temperatures) in the temperature zone of 650-690 °C and at a pressure of 0.5 mbar. This results in an intermediate monomeric form of the dimer molecule. In the final step, the monomer gas interacts with substrate surface and forms a polymer film. The vacuum process removes impurities and moisture and provides an even thickness in deposition. This process is explained in figure 2.18.

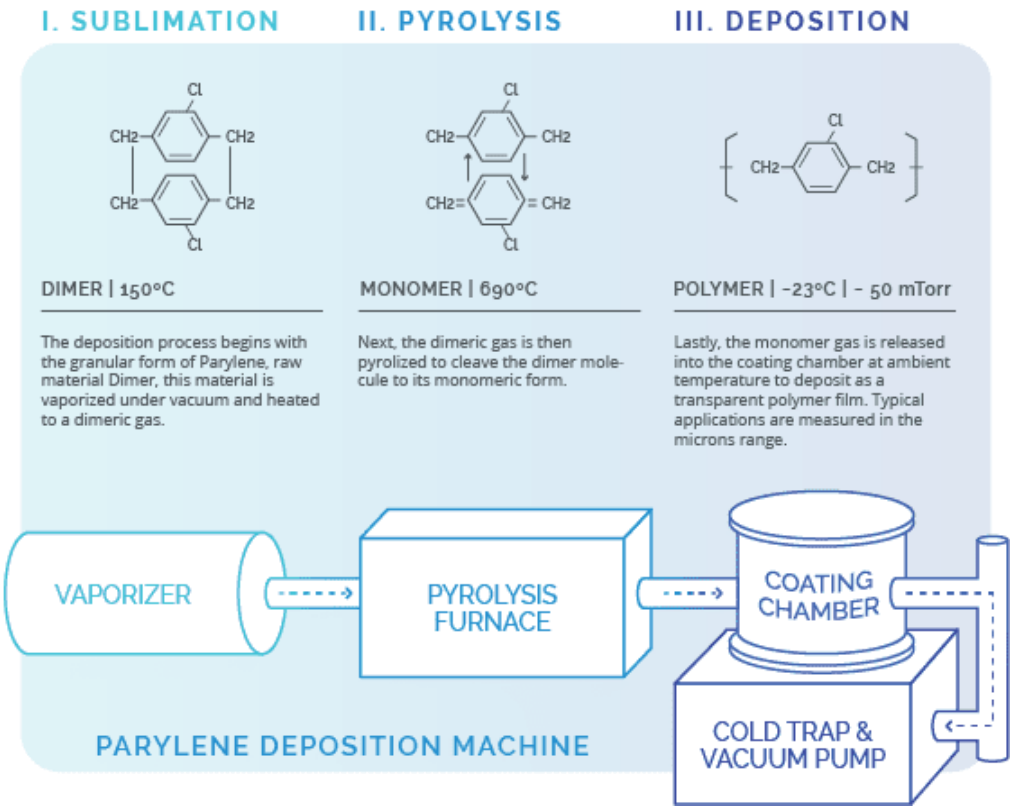

Figure 2.18:Parylene-C chemical vapour deposition method [140]

2.5 Fibre Bragg grating (FBG) pressure sensors and software simulation of the FBG reflected spectrum

In this section, the discussion will divert to the explanation of FBG pressure sensors for contact pressure measurement in healthcare. The working principles, sensor design and applications are all detailed in the following section.

2.5.1 Fibre Bragg grating pressure sensors: working principles

An FBG consists of a periodic modulation of the refractive index of the core of a single mode optical fibre. These periodic modulations form a grating structure inside the fibre. As the light is guided inside the optical fibre, it undergoes a Fresnel reflection at each of the grating planes, where there is a refractive index change. This light progressively becomes out of phase except for at the Bragg wavelength, which satisfies the Bragg condition. The light at the Bragg wavelength constructively interferes to produce a peak in the reflection spectrum. The Bragg condition is given by equation 2.42 [141]. λ_B is the Bragg wavelength, n_{eff} is the effective refractive index of the fibre core. Λ is the grating period.

$$\lambda_B = 2n_{eff}\Lambda \tag{2.42}$$

An FBG reflects a very narrow bandwidth of wavelengths, as shown in figure 2.19.

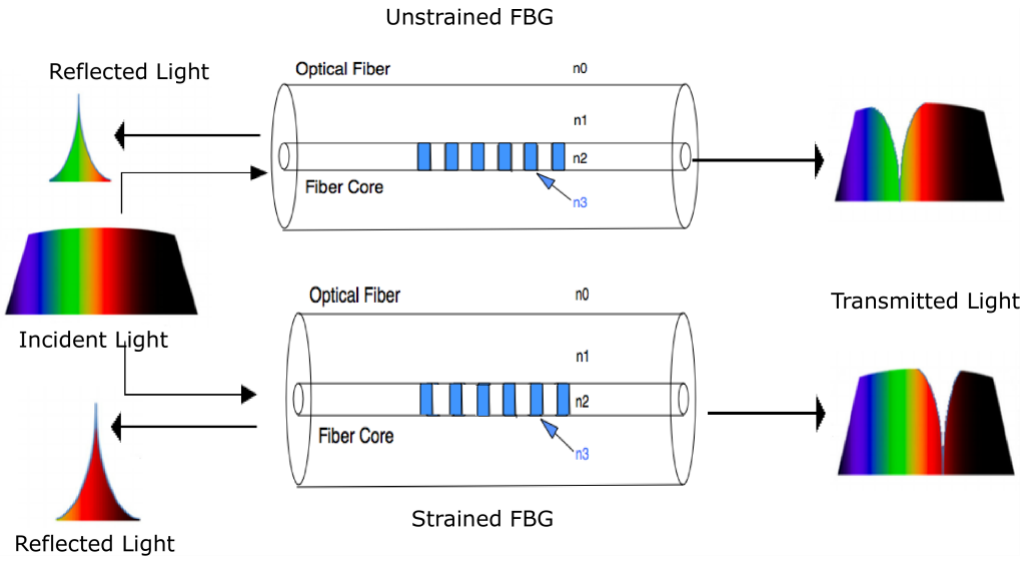

Figure 2.19: working principle of FBG and strain response, top figure show the unstrained FBG and bottom figure shows strained FBG. An increase in the periodicity of the FBG is visible after application of strain to the FBG. Wavelength shift in the reflected peak and the transmitted valley is visible with respected to the unstrained spectra

The Bragg wavelength is sensitive to temperature and strain. The centre wavelength of the reflected light depends on the effective refractive index and grating period. The Bragg wavelength shift due to temperature and strain change is given by equation 2.43 [141]

$$\Delta\lambda_B = 2\left[\Lambda\frac{\partial n_{eff}}{\partial l} + n_{eff}\frac{\partial \Lambda}{\partial l}\right]\Delta l + 2\left[\Lambda\frac{\partial n_{eff}}{\partial T} + n_{eff}\frac{\partial \Lambda}{\partial T}\right]\Delta T \qquad 2.43$$

Strain effect — Temperature effect

As the temperature changes, the Bragg wavelength will be changed due to the thermo-optic effect that modifies the effective refractive index of the fibre and due to the alteration in the grating period that occurs due to the thermal expansion of the fibre. When the FBG is strained, it causes a change in the grating period and also a change in the effective refractive index of the fundamental mode via the photo-elastic effect [142].

The strain term shown in 2.43 can be written as,

$$\Delta\lambda_B = \lambda_B \left[1 - \frac{{n_{eff}}^2}{2} [p_{12} - \nu(p_{11} + p_{12})\right] \varepsilon_z = \lambda_B (1 - p_e)\, \varepsilon_z$$

2.44

Where p_{11} and p_{12} are the components of strain optic tensor, ν is Poisson's ratio and ε_z is the strain. FBGs fabricated in typical germanosilicate fibre exhibit a 1.2 pm shift at 1550 nm centre wavelength for 1 micro strain applied to the FBG [143].

2.5.2 Coupled mode theory and transfer matrix method

The spectral response of FBGs can be calculated using couple mode equations and the transfer matrix method. The transfer matrix method is an approximation based method and models the non uniform grating properties as a piecewise constant function and reduces the calculation of the grating spectral response to a single response matrix [144].

FBGs are able to couple light from the propagating core guided mode into the counter propagating core guided modes. This causes loss dips in the transmission spectrum and peaks in the reflection spectrum [145]. Using couple mode theory, the electric fields of the backward and forward propagating waves can be given using the following equations [141]

$$E_a(x,t) = A(x)exp[i(\omega t - \beta x)] \quad 2.45$$

$$E_b(x,t) = B(x)exp[i(\omega t + \beta x)] \quad 2.46$$

Where β is the propagation constant. The complex amplitudes $A(x)$ and $B(x)$ can be given by the following two coupled mode equations.

$$\frac{dA(x)}{dx} = i\kappa B(x)exp\,[-i2(\Delta\beta)x] \quad 2.47$$

$$\frac{dB(x)}{dx} = -i\kappa^* A(x)exp\,[i2(\Delta\beta)x] \quad 2.48$$

Where β is the propagation constant and is given by $\frac{2\pi n_0}{\lambda}$, $\beta_0 = \pi/\Lambda$ and Λ is the grating period. $\Delta\beta = \beta - \beta_0$ is the differential propagation constant. κ is the coupling coefficient, which is given by

$$\kappa = \pi * m * \overline{\delta n_{eff}}/\lambda \qquad 2.49$$

where m is the striate visibility for a single mode FBG.

The detuning $\Delta\beta$, which is dependant on z, can be defined as [146] .

$$\Delta\beta = \beta - \frac{\pi}{\Lambda} \qquad 2.50$$

$$\Delta\beta = 2\pi n_0 \left(\frac{1}{\lambda} - \frac{1}{\lambda_D}\right) + \frac{2\pi}{\lambda}\overline{\delta n_{eff}} \qquad 2.51$$

λ_D is the 'design wavelength' for Bragg reflectance by a weak grating where ($\Delta n \rightarrow 0$) and can be given by $\lambda_D = 2\, n_0 \Lambda$. $\overline{\delta n_{eff}}$ is the 'dc' index change, spatially averaged over the grating period.

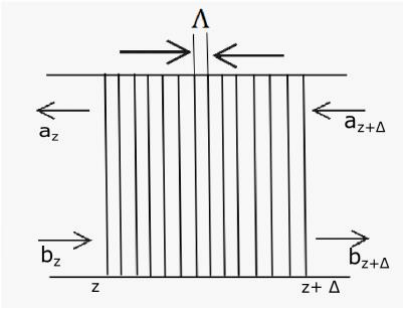

Figure 2.20: Transfer matrix method, Λ is the grating period, a_z is the backward output reflected wave, $b_{z+\Delta}$ is the forward transmitted wave

The perturbation of the refractive index can be described using following formula

$$\delta n_{eff}(z) = \overline{\delta n_{eff(z)}}\left\{1 + \nu \cos\left[\frac{2\pi}{\Lambda} z + \phi(z)\right]\right\} \qquad 2.52$$

Where $\phi(z)$ is the grating chirp, which for a uniform grating $\phi(z)$ = 0. In the transfer matrix method, the grating is divided into N uniform sections of length Δ = L/N.

The transfer matrix relation can then be given for the sections at z and z+Δ. The backward output reflected wave a_z and the forward output transmitted wave $b_{z+}\Delta$ can be expressed using a transfer matrix, as shown in equation 2.53 [147].

$$\begin{bmatrix} a_{z+\Delta} \\ b_{z+\Delta} \end{bmatrix} = \begin{bmatrix} cosh(\gamma\Delta) - i\frac{\Delta\beta}{\gamma}sinh\,(\gamma\Delta) & -\frac{\kappa}{\gamma}sinh\,(\gamma\Delta) \\ i\frac{\kappa}{\gamma}sinh\,(\gamma\Delta) & cosh(\gamma\Delta) + i\frac{\Delta\beta}{\gamma}sinh\,(\gamma\Delta) \end{bmatrix} \cdot \begin{bmatrix} a_z \\ b_z \end{bmatrix} \quad 2.53$$

$$\gamma = \sqrt{\kappa^2 - \Delta\beta^2} \quad 2.54$$

Connecting all the fields' together equation 2.53 can be modified to become

$$\begin{bmatrix} a_L \\ b_L \end{bmatrix} = T. \begin{bmatrix} a_0 \\ b_0 \end{bmatrix} \quad 2.55$$

Where $T = T_N * T_{N-1} * \ldots\ldots * T_i * \ldots . * T_1$

T will have dimensions 2x2. Therefore T can be written as

$$T = \begin{bmatrix} T_{11} & T_{12} \\ T_{21} & T_{22} \end{bmatrix} \quad 2.56$$

$$T_i = \begin{bmatrix} cosh(\gamma l_i) - i\frac{\Delta\beta}{\gamma}sinh\,(\gamma l_i) & -\frac{\kappa}{\gamma}sinh\,(\gamma l_i) \\ i\frac{\kappa}{\gamma}sinh\,(\gamma l_i) & cosh(\gamma l_i) + i\frac{\Delta\beta}{\gamma}sinh\,(\gamma l_i) \end{bmatrix} \quad 2.57$$

The reflection coefficient is calculated by,

$$R(\lambda) = \left|\frac{T_{21}(\lambda)}{T_{11}(\lambda)}\right|^2 \quad 2.58$$

Simulation results for the FBG generated using the above formule are given in figure 2.21. The central wavelength of the FBG is 1534.75 nm, the length of the FBG is 3mm and its period is 0.5178 µm.

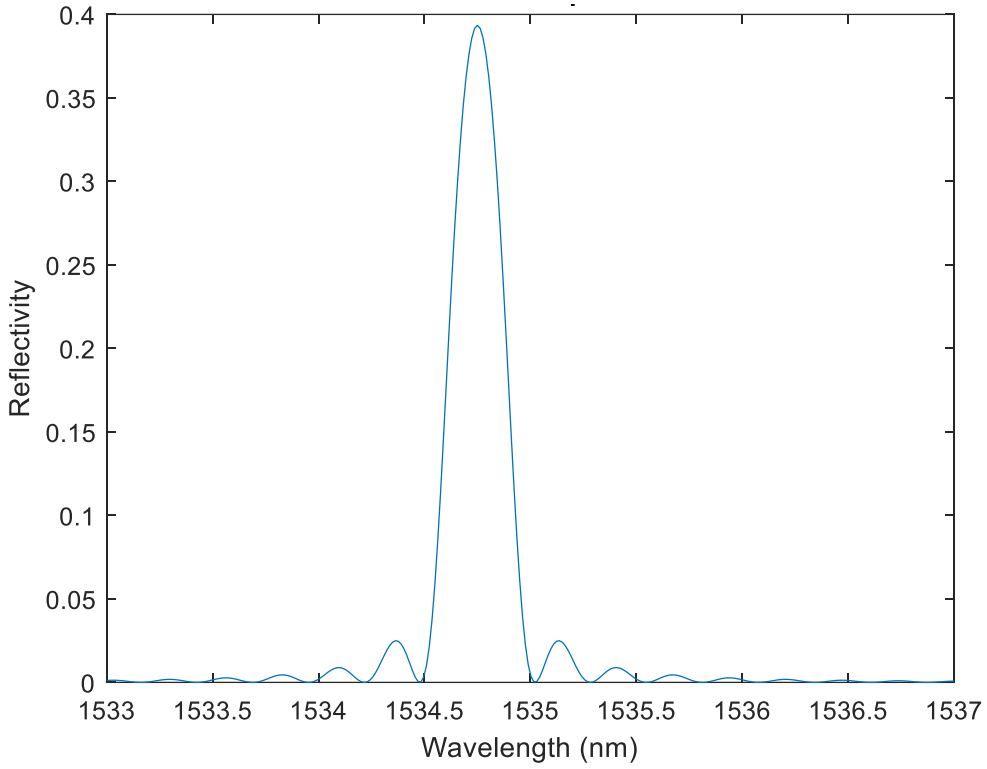

Figure 2.21: Simulated reflection spectrum of FBG using the Transfer matrix method

2.5.3 Response of a non-uniform strain field

According to Peters K. et al. [148], an applied strain induces a change in both grating period and the mean index. These two effects can be linearly superimposed at least for a piecewise continuous strain field because it is locally uniform. The two effects can be included by applying an effective strain $(1 - p_e)\varepsilon_{zz\,(z)}$ to the grating period, where the $\varepsilon_{zz\,(z)}$ strain variation is along the z direction. p_e is the photoelastic coefficient. Thus for a non-uniformly loaded grating, the grating period can be written as in equation 2.59.

$$\Lambda(z) = \Lambda_0\,[1 + (1 - p_e)\varepsilon_{zz}(z)] \qquad 2.59$$

The effective mode index can be written as

$$\delta n_{eff}(z) = \overline{\delta n_{eff}}\left\{1 + \varsigma\, cos\left[\frac{2\pi}{\Lambda_0\,[1+(1-p_e)\varepsilon_{zz}(z)]}z\right]\right\} \qquad 2.60$$

Where ς is the fringe visibility. $\varsigma \approx 1$ for a conventional single mode fibre [149],[150].

The bandwidth of an FBG in its free state is the full width at half maximum (FWHM) and can be given using equation 2.61 [151],[152]

$$\overline{\lambda_0} \approx \overline{\lambda_{FWHM}} = \lambda_b s \left[\left(\frac{\delta n_{eff}}{2n_{core}}\right)^2 + \left(\frac{\Lambda}{L}\right)^2\right]^{1/2} \qquad 2.61$$

Where s ≈ 1 for strong gratings with near 100% reflectivity and s ≈ 0.5 for weak gratings. n_{core} is the unexposed core refractive index.

2.5.4 Birefringence/signal anomalies of FBGs to Transverse loading conditions

The refractive index of an optical fibre depends on the applied perturbations. The refractive index changes caused by applied loads are called photo-elastic phenomena [153]. When an FBG experiences a transverse loading it may exhibit birefringence effects. This may cause a splitting of the FBG Bragg peak into two peaks. This is illustrated in figure 2.22. Birefringence is a condition where two orthogonal components of the optical fibre cross section have different indices of refraction [154]. When an FBG is under a transverse loading, the refractive index will increase in the compressed side and the index of refraction will decrease in the orthogonal direction. The compressed direction is called the slow axis, whilst the orthogonal axis is called the fast axis. In any un-deformed FBG, the refractive index to be assumed is uniform across the core cross section at any location along the fibre axis. When a transverse load is applied on the FBG, the core cross section of the FBG will deform into an elliptical shape with a compressive force acting on the short axis. This is illustrated in figure 2.23.

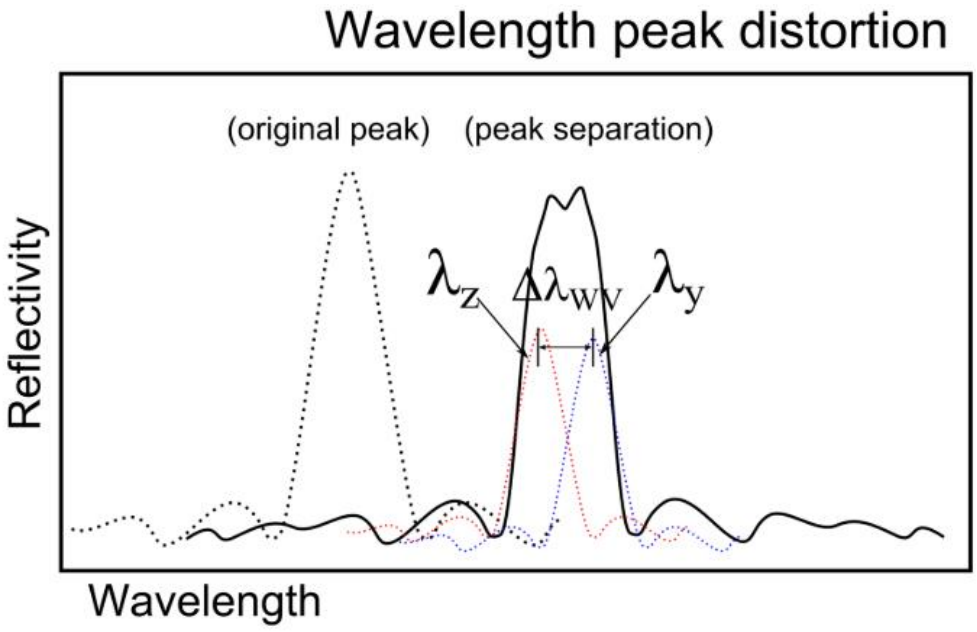

Figure 2.22: FBG response under a transverse load. Birefringent effect [152]

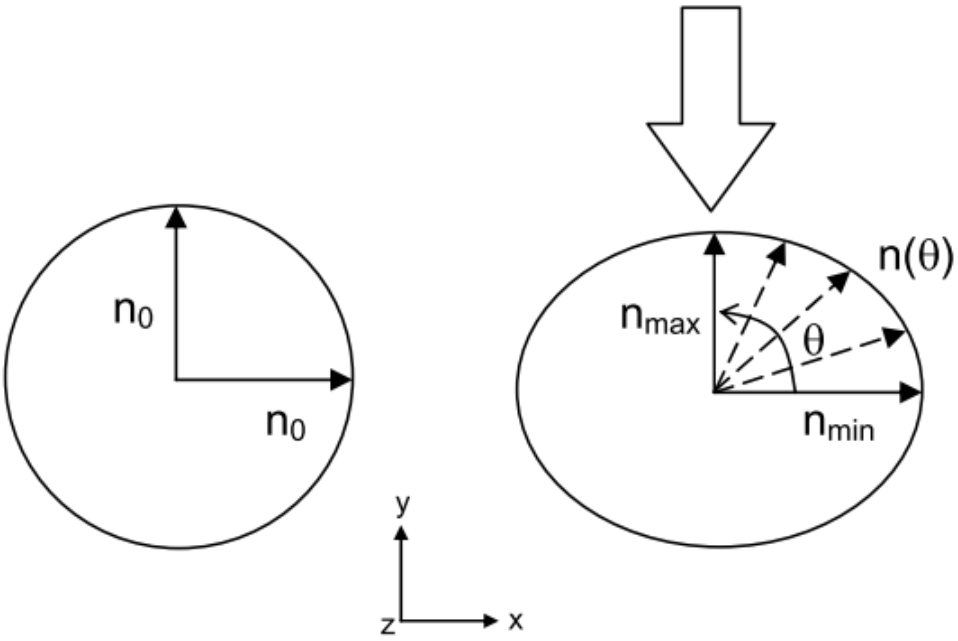

Figure 2.23: Loading effects on refractive index [154]

Birefringence happens as a result of photo elasticity in the fibre. The stresses that are acting in the FBG change the index of refraction. Photo elasticity caused refractive index changes in the x and y polarisation axis are expressed in equations 2.63 and 2.64 [153], [155]. 'σ' indicates the stresses.

$$(\Delta n_{eff})_x = -\frac{(n_{eff})^3}{2E} \times \{(p_{11} - 2\nu p_{12})\sigma_x + [(1-\nu)p_{12} - \nu p_{11}] \times [\sigma_y + \sigma_z]\}$$

2. 62

$$(\Delta n_{eff})_y = -\frac{(n_{eff})^3}{2E} \times \{(p_{11} - 2\nu p_{12})\sigma_y + [(1-\nu)p_{12} - \nu p_{11}] \times [\sigma_x + \sigma_z]\}$$

2. 63

The corresponding Bragg wavelength changes can be given using the following equations 2.65 and 2.66 [153], [155].

$$(\Delta \boldsymbol{\lambda_B})_x = -\frac{(n_{eff})^3 \Lambda_{B,0}}{E} \times \{(p_{11} - 2\nu p_{12})\sigma_x + [(1-\nu)p_{12} - \nu p_{11}] \times [\sigma_y + \sigma_z]\} + 2\frac{n_{eff}\Lambda_{B,0}}{E} \times \{\sigma_z - \nu[\sigma_x + \sigma_y]\}$$

2. 64

$$(\Delta \boldsymbol{\lambda_B})_y = -\frac{(n_{eff})^3 \Lambda_{B,0}}{E} \times \{(p_{11} - 2\nu p_{12})\sigma_y + [(1-\nu)p_{12} - \nu p_{11}] \times [\sigma_x + \sigma_z]\} + 2\frac{n_{eff}\Lambda_{B,0}}{E} \times \{\sigma_z - \nu[\sigma_x + \sigma_y]\}$$

2. 65

The first terms of equations 2.65 and 2.66 are different and correspond to the effect of transverse applied loads and the second terms of these equations are identical and correspond to the Bragg reflection wavelength changes of the FBG induced by the longitudinal strain. The change in the FWHM of the reflected peak due to the transverse loading can be given as follows.

$$\Delta\lambda'_{wv} = 2\Lambda \left|\Delta n_{effx} - \Delta n_{effy}\right|$$

2. 66

$$\Delta\lambda''_{wv} = \frac{\Lambda n_0^3}{E_f}\left[(1+v_f)(p_{12}-p_{11})\right]\left|\sigma_x - \sigma_y\right|$$

2. 67

The total width variation due to the non-uniform behaviour and transverse loading can be calculated by adding $\Delta\lambda'_{wv}$ and $\Delta\lambda''_{wv}$.

Hence the total width variation of the reflected peak can be given as,

$$\Delta\lambda_{WV} = \Delta\lambda'_{wv} + \Delta\lambda''_{wv}$$

2. 68

The wavelength shift can be given using the following formula

$$\Delta\lambda_b = \lambda_b * (1 - p_e) * (average\ (\varepsilon_{zz}(z)) \quad 2.\ 69$$

Where λ_b is the design wavelength of the FBG.

Since the gratings seen by the orthogonal polarisation states are independent, the total reflectivity can be deduced by adding the weighted reflectivity along each of the polarisation states. The reflectivity weights along two different polarisation states are defined by the intensity fractions present in each direction. Therefore, the total reflectivity can be given as [156],

$$R = p_x^2 R_x + p_y^2 R_y \quad 2.\ 70$$

$\boldsymbol{p_x}$ and $\boldsymbol{p_y}$ are the amplitude components along the x and y axes where

$p_x^2 + p_y^2 = 1$.

2.5.5 FBGs for contact/interface pressure measurements in healthcare

Accurate contact pressure measurement is very important in avoiding pressure injuries caused by being in prolonged contact with mattresses, wheelchairs and prostheses, or through using devices such in dwelling catheters and compression therapy bandages.

According to the World Union of Wound Healing Societies (WUWHS) consensus document for compression in venous leg ulcers [157], bandage systems and compression garments are graded according to the level of compression they produce. WUWHS suggest 4 different levels of pressure applied to the limb: Mild (< 20 mmHg≈ 2.66 kPa), moderate (≥ 20-40 mmHg≈ 2.66 -5.33 kPa), strong (≥ 40-60 mmHg≈ 5.33-7.99 kPa) and very strong (>60 mmHg≈ 7.99 kPa).

Compression bandaging is an important treatment method for certain medical conditions such as wounds, lymphedema, venous leg ulcers and varicose veins, deep vein thrombosis, venous insufficiencies and pulmonary embolism [158],[159]. Depending on the medical condition, the amount of pressure needed to be applied by the compression bandaging may change. For example, light compression (1.9-2.3 kPa) is used for the management of early varices and

varicose at the ankle while moderate compression of (2.4-3.2 kPa) is used at the ankle for the treatment of ulcers. Strong compression (3.3 – 4.7 kPa) is used at the ankle for post thrombotic venous insufficiency and the management of venous leg ulcers [160][161]. In the case of venous leg ulcers or varicose vein treatments, the aim of the use of compression bandaging is the reduction of venous hypertension caused by vulvar insufficiency [162]. Application of external compression by means of a bandage will ultimately increase the velocity of blood flow within the veins by providing support to the muscles. However, reaching and maintaining the desired pressure is difficult when applying the compression bandage. Compression bandages can be harmful if not applied properly due to the high tension and pressure applied. For example, a compression pressure in excess of 4 kPa may decrease venous blood velocity and produce tissue damage over bony prominences when applied for long periods [163],[49],[50].

Thorough assessment, including the magnitude, distribution and duration of pressure, limb radius and layers of bandage, is required for compression bandaging therapy. Issues related to compression bandaging are still debatable such as the level of pressure required and the actual level of compression achieved during the bandage application [164].

Sub-bandage pressure can be defined as the pressure accomplished beneath the bandage during its application and while wearing the bandage. Sub-bandage pressure can be predicted using equation 2.72 [164]. This is based on the formula described for the pressure exerted on a curved surface by Pierre Simon de Laplace and Thomas Young in 1805 [165],[166].

$$Sub - bandage\ pressure = \frac{No.of\ bandage\ layers \times Tension\ of\ bandage}{Circumference\ of\ limb \times Width\ of\ badage} \quad 2.71$$

However, the reliability of equation 2.72 is still controversial due to the complexity of the human limb and the long-term drift of the sub-bandage pressure [167],[168]. Therefore it is important to measure the sub-bandage

pressure regularly and there is a necessity for a reliable sensor for sub-bandage pressure measurements.

Prosthetics is also another healthcare field where interface pressure measurement techniques are deployed widely. The pressure measurement at the interface between the stump and the prosthetic socket can provide valuable information in the process of prosthetic socket fabrication, modification and fit [169]. The prime objective of any prosthesis is to provide function in a comfortable manner. However, comfort of the prosthesis is dependent on the pressure between the socket and the residual limb [170]. Depending on the type of socket, the interface pressure range between the residual limb and the socket may differ widely. For example Moo et al. [171] discuss interface pressure profile analysis of two types of sockets, namely the patellar tendon bearing (PTB) socket and the hydrostatic socket. According to the study, the anterior pressure profile of the PTB socket exhibits a pressure range of 50-90 kPa, whereas the posterior PTB socket exhibits peak pressure of up to 210- 230 kPa. As Quesada et al. [172] note in their study of analysis of below knee PTB prosthesis, pressure peaks can go up to 800 kPa for hard sockets.

There is a wide variety of commercially available pressure sensors, including pneumatic, piezo electric, resistive, strain gauge and capacitive sensors. The main limitations of these sensors are that they are bulky when compared with fibre optic sensors. Some of the available contact pressure measurement techniques are discussed in detail in section 2.8.

The FBG is one of the most attractive solutions for sub-bandage pressure measurements among all other technologies, because of the small size, flexibility, immunity to electromagnetic interference, bio-compatibility, and wavelength encoding ability. Although FBGs are sensitive to strain and temperature, FBGs are less sensitive to pressure, with a bare FBG exhibiting a sensitivity of about 3.04×10^{-3} nm/MPa [173]. Nevertheless, FBGs could be engineered in a way that the pressure can be transduced to axial strain to increase its sensitivity to pressure.

2.5.6. Available techniques for contact pressure measurements in healthcare

The characteristics of an ideal sensor for sub-bandage pressure measurements were summarised by Partsch H. et.al [51]; a suitable sensor should be flexible, small in size, durable, reliable, offer variable sensor sizes, be thin, accurate, insensitive to temperature and strain, with low hysteresis, a linear response and a high sampling rate.

Barbenel J et al. [160] developed a device for measuring soft tissue interface pressure. The device consists of a sensor cell of a diameter of 28mm, tubing of 1m length and a commercially available electro pneumatic sensor cell (by Tally group limited, Medical equipment division, Hants, UK,). The transducer is a piezo resistive pressure sensitive device whose output voltage is proportional to the applied pressure. The device has a dynamic range of 0-5kPa, has a linear pressure sensitivity and is robust. However, it suffers from bulkiness and low flexibility. The sensor cell, tubing and transducer are filled with vegetable oil, which may cause problems during motion and is not suitable for use in dynamic studies due to the hydrostatic pressure variation as the sensor moves vertically relative to the transducer.

Steinberg M et al. [163] presented a method for the measurement of sub-bandage pressure using an electro pneumatic sensor. Electro pneumatic sensors transform displacement or proximity into change in air pressure. This sensor consists of a polyurethane disc with a diameter of 2.8cm and profile 0.5mm, to which a 1m length of pipe is attached. An electronic circuit is used to calculate the pressure. The maximum sampling rate achieved was 2.9 Hz. The main drawback of this sensor is that it suffers from hysteresis.

Ferguson-Pell et al. [174] evaluated a sensor which is commercially available for low interface pressure measurements. The sensor namely ‘Flexiforce’ developed by Tekscan, is designed for the measurement of the low interface pressure between skin and the support surface, for example in pressure garments. The sensor uses an ink whose electrical resistance is changed with

the force applied. The main drawbacks of the sensor are that it is only suitable for static measurements, and it is less conforming to the curvature of the limb.

Wang et al. [167] describes an fibre optical force sensor consisting of two arrays of FBGs entwined in a double helix form. Two optical fibres are contacted and entwined into a double helix form by pitch matching the spatial separations of the FBGs. Due to the double helix structure, when a force is applied, one FBG experiences a compression while the other experiences an elongation. The degree of differential Bragg wavelength shift is used to determine the applied force. The double helix structure is advantageous because any temperature fluctuation causes a common mode variation which is independent of the force induced differential wavelength shift. Thus, this sensor array is immune to temperature variations and capable of real time distributed sensing of sub-bandage pressure.

2.5.7 FBG sensor for the contact pressure measurements

Correia R. et al. [53],[175] presented a pressure measuring system using a FBG embedded in an epoxy patch. This epoxy cube transduces the external pressure into strain on the FBG. The deformation of the epoxy cube in response to the transverse load results in an axial strain across the FBG.

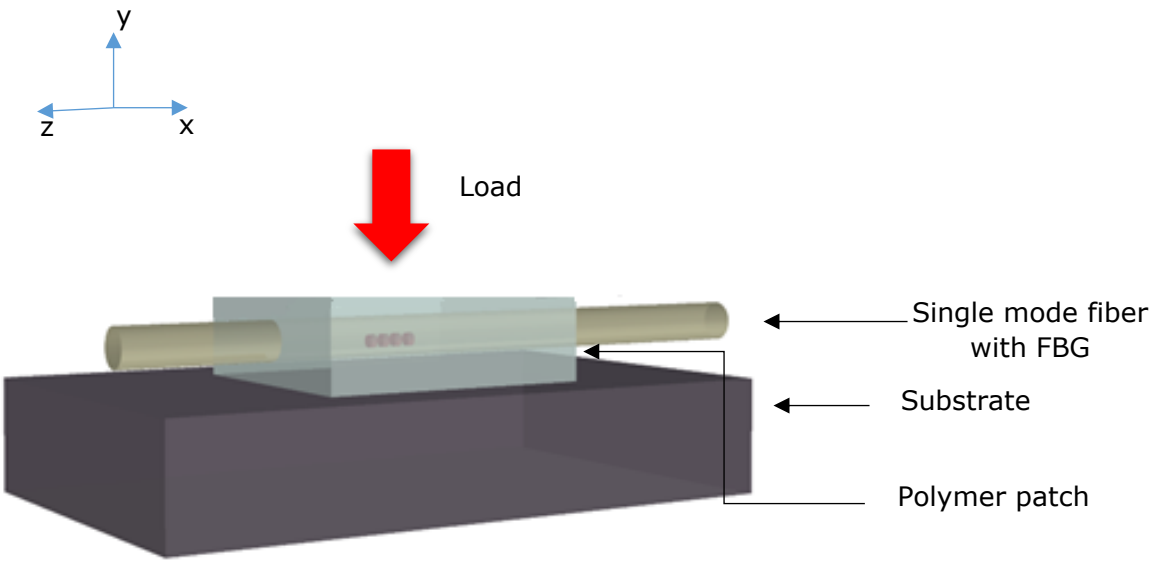

Figure 2.24: Schematic of the FBG sensor design for contact pressure measurements

This phenomena has been used to measure the contact pressure between an endotracheal tube cuff and the trachea [52]. The sensitivity reported was $2.1x10^{-2}$ nm/kPa, increasing the pressure sensitivity of the FBG by a factor of 15 when compared with a bare FBG. According to the study, measurements made using a commercial manometer agreed well with the FBG contact pressure measurements.

This method has many advantages such as small dimensions and lightweight (because the FBG itself is about 3mm length and the patches are less than about 6mm long and 3mm wide). Moreover, these sensors provide a lot of flexibility over other methods in contact pressure measurements due to the flexible nature of optical fibres. Several FBGs can be placed in a single fibre due to the multiplexing capabilities of FBGs and hence can do multiplex point sensing during contact pressure measurements and also allow compensation for strain and temperature. Moreover, this sensor offers the robustness required for contact pressure measurements.

2.5.8 Why a mathematical model for the FBG sensor?

The technique described in section 2.5.7 is a suitable technique for contact pressure measurements. However, one of the important phases before the design and fabrication of the sensor is to optimise the design parameters of the sensor. Although the initial patch design was cube shaped as described in [53] [175], it is important to investigate the optimum dimensions and shape of the patch to optimise its performance for the specific application. Moreover, there is an impact of the material properties of the patch upon the sensitivity of the device. By selecting the material carefully the sensor could be designed for different sensitivities and pressure ranges, depending on the application. This is one of the key characteristics that should be expected from an ideal contact pressure measurement sensor, as described by Partsch. H et al. [51].

The output reflection spectrum from the FBG is dependent on the stress/strain field profile acting along the FBG. However, the stress/strain exerted on the FBG is dependent on how the patch deforms due to the transverse loading. The patch deformation is dependent on the material it has been made of, and on its design.

An accurate simulation would enable the optimisation process. This PhD aims to develop an accurate virtual simulation of the FBG sensor by developing a mathematical model. Finite element analysis is used to simulate the stress/strain field along the FBG due to the transverse loading. The Transfer matrix method, described in section 2.6, is used to simulate the FBG reflected spectrum output corresponding to the applied transverse load.

Hu H. et al. [54] presented a FBG simulation for real time evaluation of transverse cracking in cross-ply laminates. A MATLAB code exploiting the Transfer matrix method was developed for the purposes of FBG simulation. Hassoon O. et al. [55] developed a numerical simulation of an FBG for modeI delamination detection to determine the material strength. Again a MATLAB code was used to simulate the reflected spectrum. In both cases the authors do not provide the code/algorithm, and also their analyses are limited by their

specific application. Pereira G. et al. [56] developed an FBG signal simulation tool for finite element method models. This tool provides the facility to simulate FBG response independently of the structure, loading or type of application. Moreover, this is a free to download software. This provides three different simulations; longitudinal uniform strain, longitudinal non uniform strain and transverse stress. Since the working principles of the FBG sensor described in section 2.5.6 are based on the application of transverse loading it is important to look at the resultant transverse stresses and the non-uniform strain experienced by the FBG. When examining the python code of the algorithm and then after assessing it was found that, for transverse stresses, the software does not consider the non-uniformity of the grating. Instead it uses an average strain value which may not produce an accurate approximation for the non-uniform conditions. For example, figure 2.25 shows a situation where the fibre experiences non uniform strain due to the transversely applied loading. This situation can be found in a compression bandage, in which average value of the strain is not a good approximation through out every section of the transfer matrix. In another example, the software produced unrealistic results. Although the input file had zero strain along all the directions of the fibre the simulation showed a shift in the reflected spectrum as shown in figure 2.26.

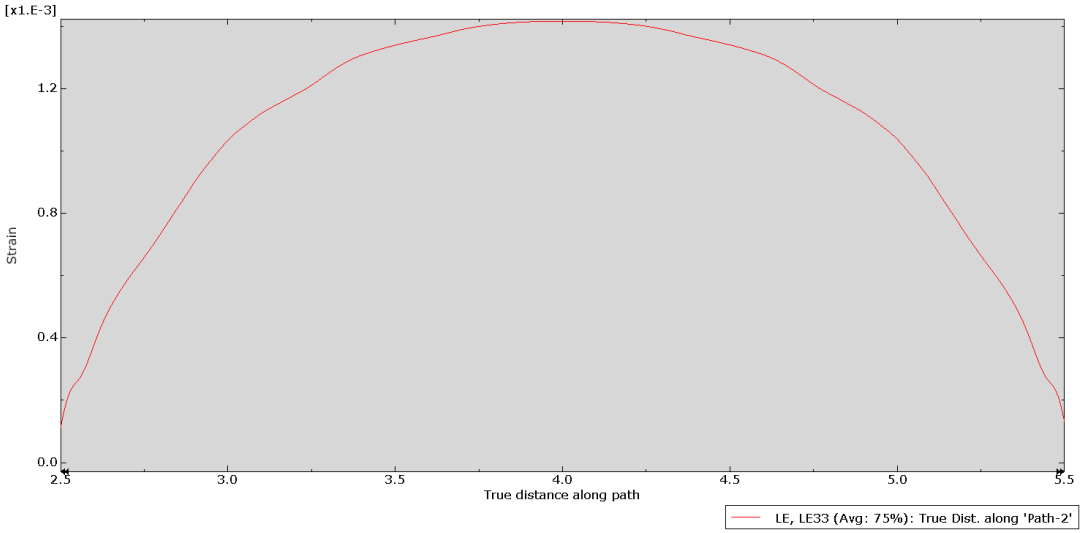

Figure 2.25: Non-uniform strain profile along the fibre axis of 3mm FBG

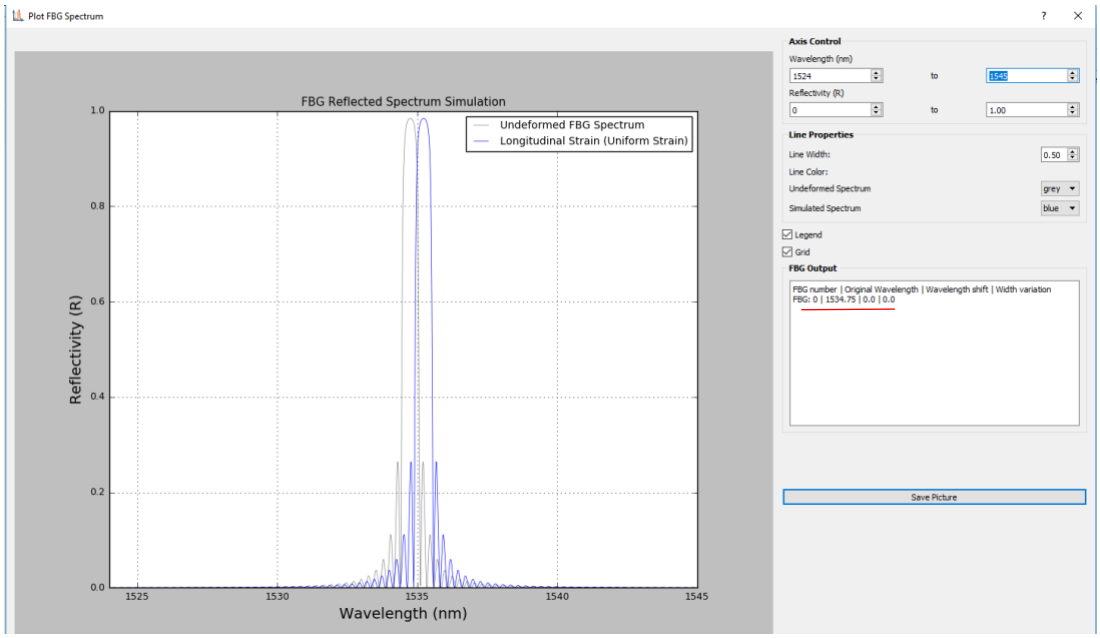

Figure 2.26: FBG-SiMul 1.0 software produced results for zero strain

2.6 Summary

Pressure measurement in healthcare can be divided into two types. Fluid pressure measurements (invasive blood pressure, urethral pressure) and contact pressure measurements (prosthetics, pressure ulcers, compression therapy). In this chapter, two main fibre optic sensing techniques for addressing these two types of measurements have been discussed. These two techniques are fibre optic Fabry-Perot interferometric sensing and fibre Bragg grating based sensing, respectively. Theoretical models for both sensor technologies were presented and discussed. An extensive literature review was presented for both of the techniques by comparing all currently available techniques, both as reported in literature and commercially.

Chapter 3

Fabrication of a miniature Fibre Optic Fabry-Perot Pressure Sensor and its Characterisation

3.1 Introduction

In this chapter, section 3.2 describes the fabrication methods used for the fibre optic Fabry-Perot pressure sensor. Pressure sensor fabrication is conducted in two stages. The first stage involves the formation of the cavity at the tip of the single mode fibre while the second stage is the application of the film/diaphragm to the tip of the fibre. Two different methods of cavity formation and two different methods of diaphragm application are explained. Section 3.3 describes the experimental setup established for the calibration of the pressure sensors and which was used to gather the results obtained in section 3.4. Section 3.5 contains the discussion, conclusion and future work.

3.2 Fabrication Methodology

3.2.1 Focused ion beam milling

In the first stages of the sensor development, Focused Ion Beam (FIB) milling techniques were used as the cavity formation technique. FIB provides the most precise, mask-less micro/nano fabrication tools [176]. FIB is becoming a popular micro/nano fabrication tool in the field of engineering.

3.2.1.1 FIB technology applications

The focused ion beam technique uses a highly focused Gallium ion beam column (Ga+) beam to mill and image a sample inside a vacuum chamber. The spot size, which is typically less than 10nm provides high precision in micro and nano fabrication [177]. Most of the FIB systems integrate an electron beam column at an angle of 52° to the ion column. This is shown in figure 3.1. The electron beam is used for sample imaging during or after the FIB processing. Electron beam is also used for depositing extra material [178]. FIB enables mainly 4 processes which are milling, deposition, imaging and etching. FIB

milling is a process of material removal from the target specimen. The milling of the material occurs through a process called sputtering. This is a mechanism where incident ions transfer momentum to the substrate and release atoms through cascade collisions [179]. The efficiency of FIB milling is evaluated by the sputtering efficiency and is given by equation 3.1

$$\gamma = \Lambda F_D(E_0) \qquad 3.1$$

Where γ is the mean number of atoms sputtered or emitted / incoming ions, Λ contains the material properties of the sample such as surface binding energy and the range of displaced target atoms, and $F_D(E_0)$ is the density of the transferred energy within the surface. $F_D(E_0)$ depends on the type (atomic number, mass number) energy, and the direction of the incident particle as well as on the type of the target atoms (atomic number, mass number) [178].

γ is an important characteristic in an FIB system, and it increases with E_0. After 30 keV γ stays constant and this is the reason most FIB systems use 30 keV as the beam voltage.

FIB techniques have been used in a number of fibre optical applications including the fabrication of long period gratings [180], [181], tapering and micromachining tips [182], [183], and for the milling of side holes on fibres [184].[185]. The FIB based Fabry-Perot tip sensor created here is a novel approach and has not been reported in the literature before.

3.2.1.2 FIB milling procedure:

The FIB Quanta 200 3D was used as the FIB machine during the experiments. This system is a FIB/SEM workstation, which provides range of capabilities not possible with separate FIB and SEM tools. For example, real-time cross-section images and videos with the electron beam during FIB milling, focused electron beam charge neutralisation during FIB milling and high resolution elemental micro analysis of defect cross sections are all possible [186]. The following section describes the FIB milling procedure used in the experiments.

The fibre (single mode silica optical fibre 780HP, Thorlabs) was first cleaned using isopropanol (C_3H_8O). Then it was cleaved using a precision fibre cleaver (VF-15H precision fibre cleaver, INNO instruments) to achieve a flat surface at the tip of the fibre. Next, the fibres were coated using a platinum coater. Platinum coating is an important part of the procedure. During the FIB milling/sputtering process as explained above, excess charge may build-up on the surface of the material during the ion bombardment process. This may cause a random deflection of the incident ion beam over time. Therefore, platinum coating prior to the FIB /SEM application will reduce drifting and protect the sample from the ion beam during the process. Platinum has higher conductivity and contrast in electron microscopy [187]. This fibre was then mounted on a 45° angled stub, after securing on a rotational stage. Then the stage is rotated towards the ion beam so that the fibre tip is directly facing the ion beam. Next, the system was pumped until a vacuum was achieved inside the chamber. Typically, the pressure inside the chamber is $\sim 10^{-5}$ Pa in the high vacuum mode. The next step is to set the sample height to the 'eucentric height'. The ion and electron beams should coincide at one particular place in order to do the milling correctly. The two beams will coincide at the 'eucentric height' position. This is shown in figure 3.1. The electron beam remains vertical, and the Ion beam is located at an angle of 52^0 to the electron beam. Because a 45° angled stub is used at the stage, this should be tilted by a tilt 7^0 in order to make the plane of the sample perpendicular to the ion beam column. The eucentric height should be set to 15mm for the electron beam and 30mm for the ion beam. This is shown in figure 3.1.

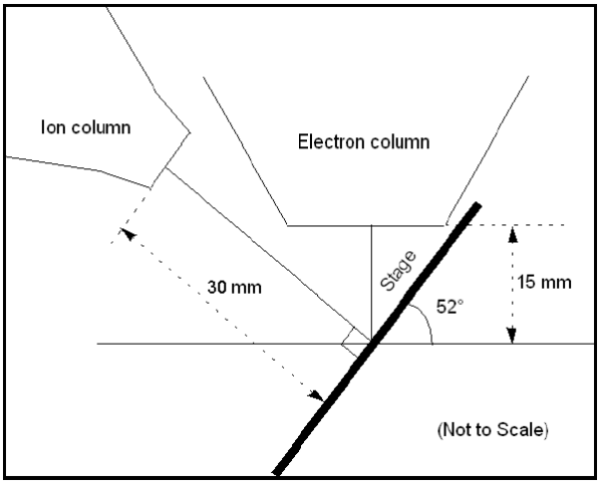

Figure 3.1: Schematic of ion beam and electron beam coincidence at 'eucentric height' [188]

For the milling purposes, a voltage of 30kV is used as the ion beam accelerating voltage as the manual suggests. The reason was discussed in section 3.2.1.1. The electron beam accelerating voltage was selected to be 10kV.

The electron beam image and the ion beam image were consecutively used to focus on the sample and when these positions coincided, the distance is set to be the free working distance by pressing 'Link Z to FWD'. The electron beam view and the ion beam view of the fibre tip are shown in figure 3.2

The next step is the patterning process. This is the process of milling a pattern into the sample surface with the ion beam. Firstly, platinum was deposited on the fibre tip. This prevents any drift and damage of the sample. Because platinum is a conducting material, it can stop charge building up on the sample surface by conducting it to the ground. The fibre tip after the deposition of the platinum layer of 1 micron thickness is shown in figure 3.2. The beam current used for the platinum deposition was 0.5nA and, to deposit a 24micron diameter and 1 micron thick layer of platinum, it took approximately 13 minutes. Figure 3.3 shows the fibre tip after deposition of platinum. The two different figures correspond to the electron beam image and ion beam image, respectively.

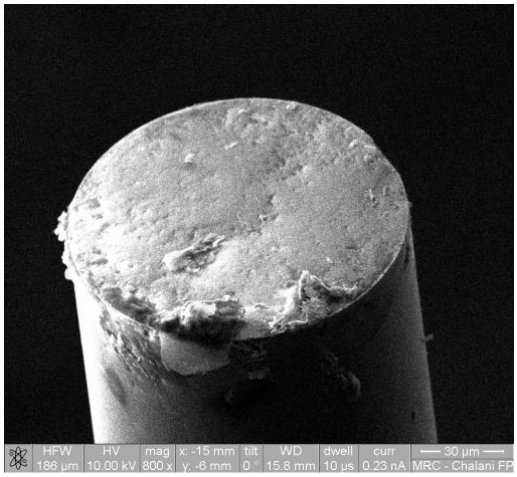

(a)

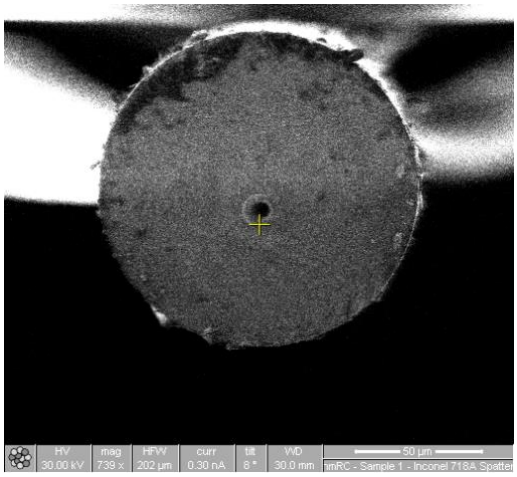

(b)

Figure 3.2: (a) Electron beam image of the fibre tip, magnification x739, scale bar 30 um (b) ion beam image of the fibre tip, magnification x5000, scale bar 50 um

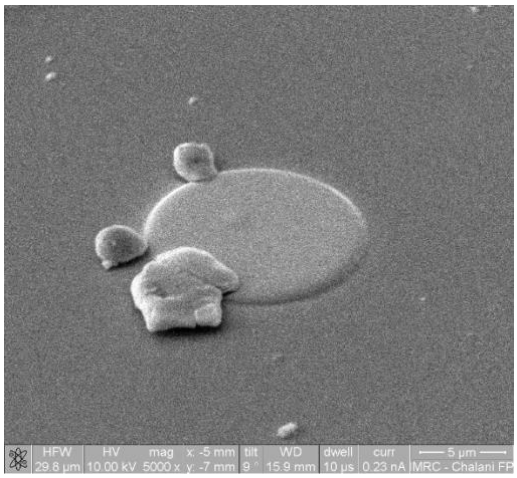

Figure 3.3: Deposition of platinum layer of 1 µm thickness at the tip of the fibre, magnification x5000, scale bar 5 um

Once the platinum layer was deposited, the milling pattern was created and the milling started. The milling profile was kept as a cylindrical shape at the centre of the fibre tip. Figure 3.4 shows the cavity milled using an ion beam current of 5nA. It took 49 minutes to mill a 21 µm diameter and 9 µm deep cavity. Table 3.1 shows the milling times taken for different cavity volumes.

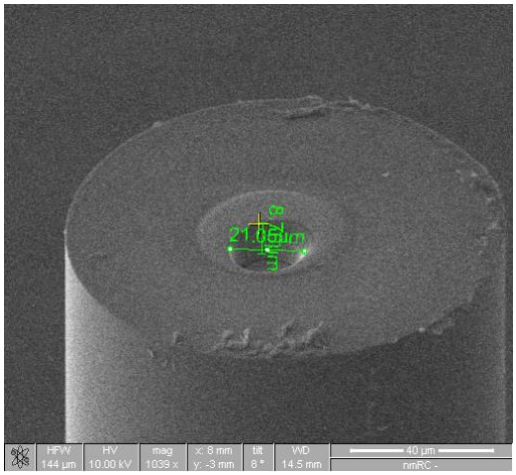

Figure 3.4: Cavity inscribed at the tip of the optical fibre (diameter= 21 µm, cavity length ~9µm), magnification x1039, scale bar 40 um

Table 3.1: Milling time for different milling currents and different cavity volumes

Cavity Diameter(μm), length(μm)	Milling volume μm^3 ($\pi . \frac{diameter^2}{2} . length$)	Milling current(nA) (acc. Voltage=30 kV)	Milling time(min)
6 , 7	120.09	0.3	73
5 , 8	86.54	0.5	35
7 , 9	162.94	1	40
7 , 10	163.94	3	14
12 , 8	460.34	5	14
16 , 8	812.25	5	25
18 , 9	1026.87	5	33
20 , 9	1265.64	5	49

According to table 3.1 it is clear that milling time is a function of milling volume. As the milling volume increases milling time increases whereas when milling current increases, the milling time decreases. However as the milling current

is increased the re-deposition of the material is increased significantly as will be discussed later.

3.2.1.3 Application of the diaphragm:

The Parylene-C films used for the experiments were provided by the Faculty of Environmental Engineering and Graduate School of Environmental Engineering, The University of Kitakyushu, Japan. Background information and advantages of use of Parylene-C films as a pressure sensitive diaphragm and thin films manufacturing procedure were discussed in chapter 2, section 2.4.6. These films had been deposited using chemical vapour deposition (CVD) on glass substrates coated with a sacrificial layer. They can be peeled off from the substrates in order to obtain self-supporting membranes for easy application onto the tip of the fibre. To dissolve the sacrificial layer, the substrates with parylene thin films were soaked in ethanol for 24 hours, after which the film was easily peeled off from the substrate. A parylene film floating in ethanol is shown in figure 3.5. The thicknesses of parylene films were 200nm as confirmed by the quartz crystal microbalance measurements at the University of Kitakyushu, Japan.

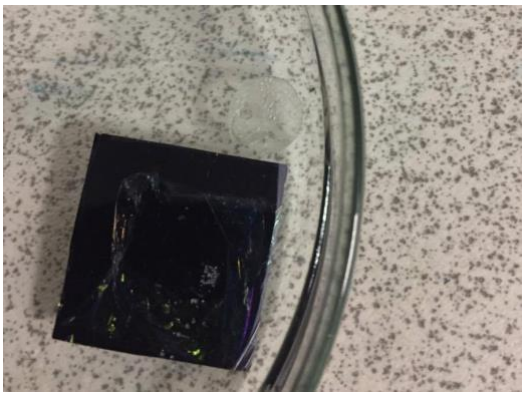

Figure 3.5: Detachment of the films from the substrate by soaking in ethanol

Then the film was attached to a washer as shown in figure 3.6.

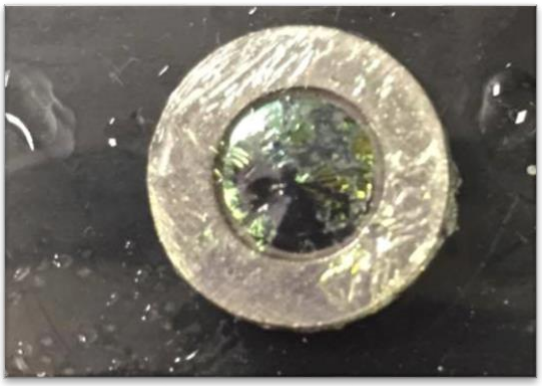

Figure 3.6: Attachment of the Parylene-C film to a metal washer

The film was deposited on to the tip of the fibre using the setup shown in figure 3.7. The idea of this method is to use the self-supporting properties of the Parylene films to make the attachment between the film and the fibre tip. The fibre with the FIB created cavity was setup on the micro stage, as shown in figure 3.7. Such that the fibre could be moved forwards/ backwards in μm steps. The washer with the Parylene film was kept stationary. As the fibre approached the film, the film would be attached to the fibre tip and detach from the rest of the film.

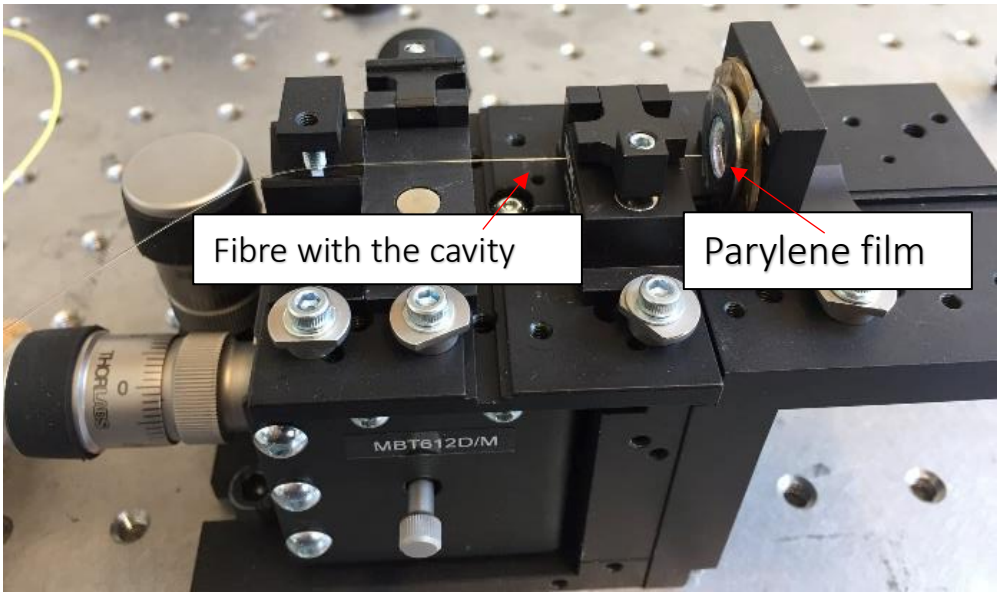

Figure 3.7: Attachment of the film to the tip of the fibre using a micro stage

Once the film is attached, the fibre optic Fabry-Perot pressure sensor is ready for testing.

3.2.2 Splicing with fibre capillary tubing

This section will describe the method of creating the cavity of a fibre Fabry-Perot pressure sensor by splicing fibre capillary tubing to the tip of the fibre.

3.2.2.1 Splicing Procedure:

A single mode(SM) optical fibre with an operating wavelength range of 780-970nm, by HP 'Thorlabs' and the fibre capillary TSP075150 flexible fused silica capillary by 'CM scientific' were used for Fabry-Perot sensor fabrication. This capillary has an inner diameter of 75 µm and outer diameter of 150 µm, which includes a polyimide coating of 12 µm thickness. The polyimide coating should be removed in order to successfully splice the capillary to the SM fibre. The polyimide coating could be removed by holding the capillary in an open flame. This is an easy, quick and effective way of removing polyimide. In this way polyimide will carbonize and flake off. Isopropanol was used to remove the residual carbonized flakes from the capillary.

For splicing purposes, a Fujikura FSM 100MP fibre splicer was used. This splicer provides standard splicing modes for single mode-single mode (SM-SM) fibre splicing. However, it does not provide any standard automated mode for the SM-capillary spicing. If the standard SM-SM is used for this purpose one can observe that the capillary tubing may undergo a deformation at the splicing point as shown in figure 3.8. Therefore it is crucial to establish the correct splicing parameters in order to prevent deformation of the capillary tubing at the splicing point. The parameters that may affect the deformation are identified as the main arc power, pre-fusion power and gap set position of the two fibres. A comparison between the standard and adjusted splicing parameters is listed in table 3.2.

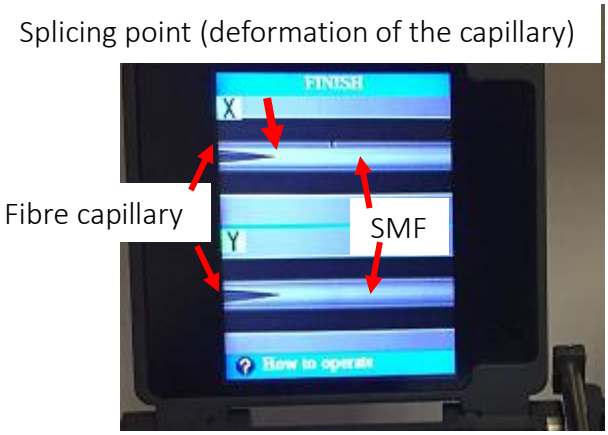

Figure 3.8: Using standard SM-SM for splicing result in a deformation of capillary

Table 3.2: Parameters for SM-Capillary splicing, STD(Standard power 250 bits)

Parameter	SM-SM mode	SM-Capillary
Main Arc power	Standard (STD)	STD -216bit
Perfusion power	Standard (STD)	STD -85bit
Gap set position	Centre	L-15 micrometre (15 microns left from the centre)

After using the settings described in table 3.2 the splicing point was achieved without any deformation and it is shown in the figure 3.9

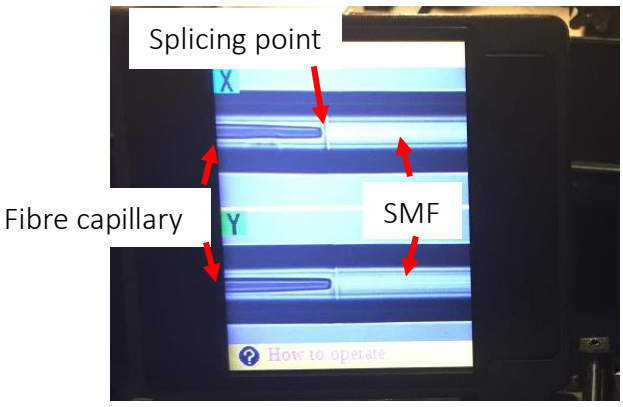

Figure 3.9: SM-Capillary mode for splicing

The next step is to cleave the capillary to the required cavity length. The main challenge in cleaving is to achieve a cavity length of µm range. To assist with

precise cleaving the process was conducted using a microscope to view this fibre. First, the splicing point was coincided with the cleaver blade by viewing it through the microscope. Then the fibre was withdrawn to the length of the cavity from the cleaver blade position using the micro stage. Finally the cleaving was done. The setup is shown in figure 3.10.

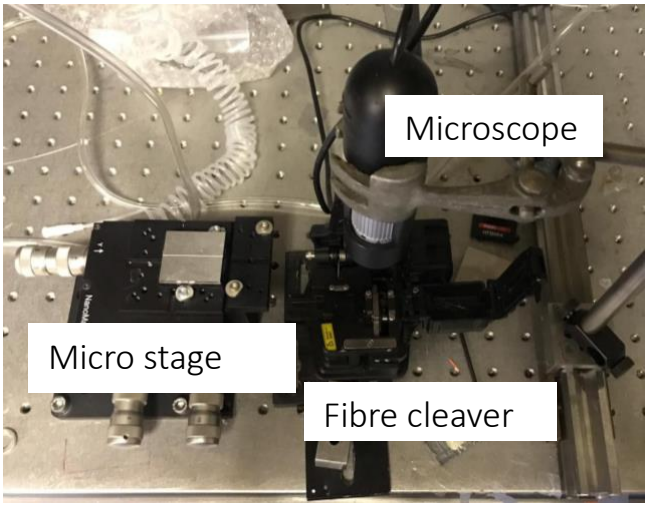

Figure 3.10: Fibre cleaving setup

Figure 3.11 shows the microscopic image of the fibre optic Fabry-Perot cavity after cleaving.

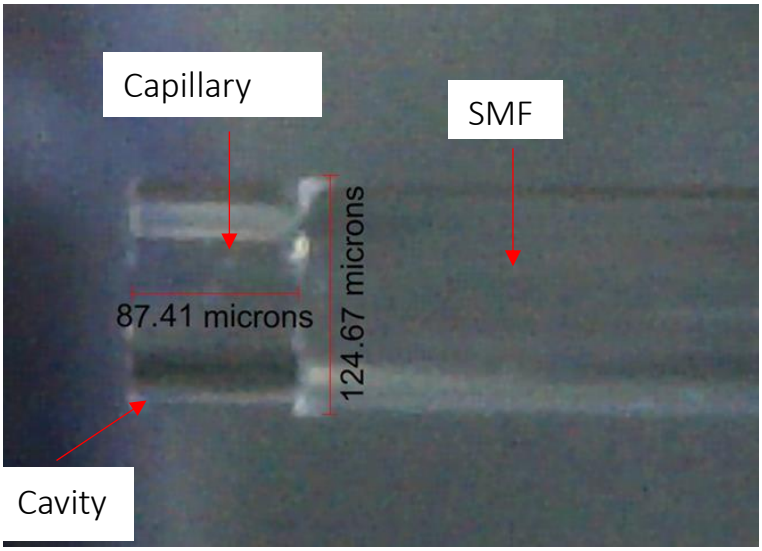

Figure 3.11: Microscopic image of the fibre Fabry-Perot cavity

3.2.2.2 Application of the Diaphragm:

The parylene film was attached to the end of the FP cavity as shown in figure 3.12. The fibre with the cavity was gently tipped towards the Parylene film which is floating on the liquid. Once its attached to the tip the fibre was taken out from the liquid and kept vertical. This will allow the film to be stretched and attached to the tip firmly as the film dries due to electrostatic interaction.

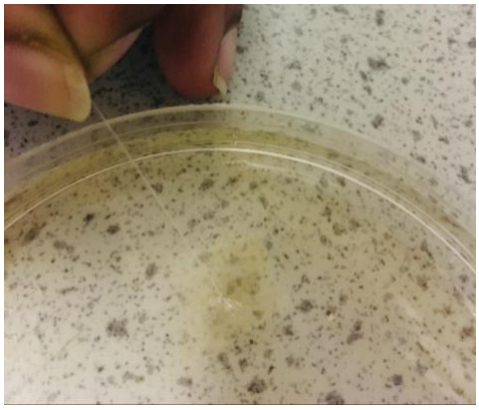

Figure 3.12: Application of the Parylene- C film

Figure 3.13 shows the fibre optic Fabry-Perot sensor ready for testing after the attachment and drying of the Parylene diaphragm.

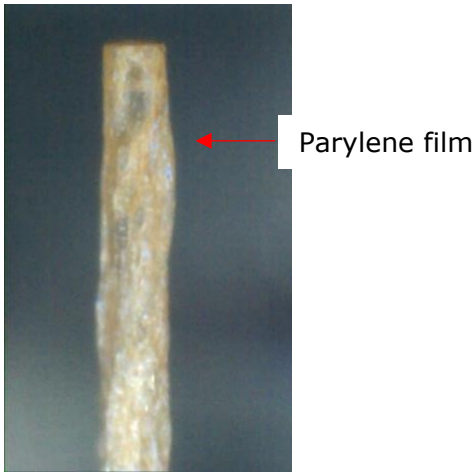

Figure 3.13: The fibre optic Fabry-Perot sensor after applying the Parylene-C diaphragm

3.3 Experimental setup and signal processing techniques

Figure 3.14 shows the experimental setup used for testing and calibration of the pressure sensor. A pressure pump was used to control the pressure inside the pressure chamber. The system is sealed and the pressure change due to the infusion/withdraw of the air was monitored by the commercial 'Extech HD 750' differential pressure manometer or the Integrated Silicon pressure sensor MPX4250. These two devices offer two dfifferent pressure ranges.

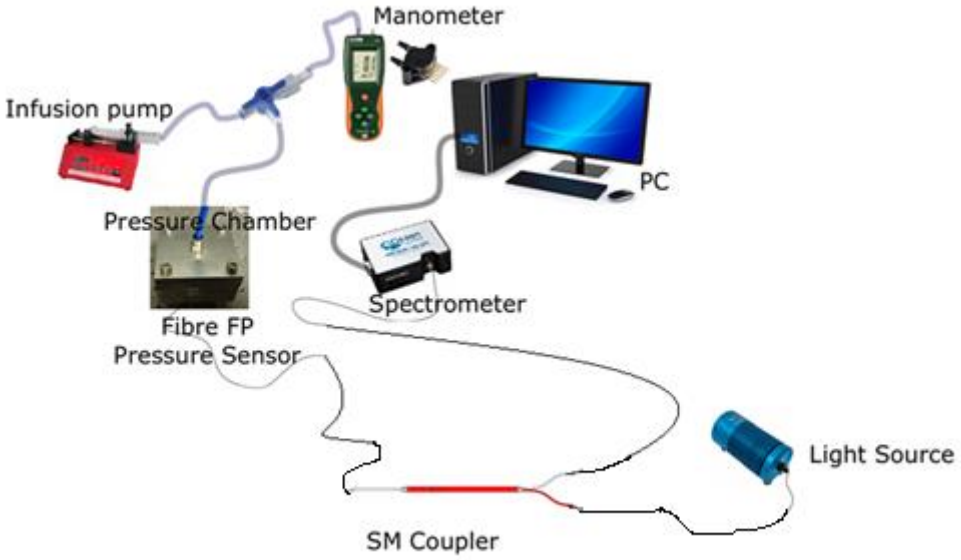

Figure 3.14: Experiment Setup for testing and calibration of the fibre FP pressure

The Extech 750HD comes with a user friendly software interface that allows the user to visualise and save the data in real-time. The Extech 750HD by Extech has a pressure limit of 5psi (~34 kPa). The MPX 4250 pressure sensor by freescale semiconductors was used with a DAQ board by National Instruments and LabVIEW interface, which was used for recording and visualising the voltage output related to the applied pressure. The maximum measurable pressure is 250 kPa for the MPX 4250.

A halogen broadband light source was used for sensor interrogation, since it provides a wide bandwidth (wavelength range of about 300-2400nm). The reflection interference fringe pattern was captured using an Ocean Optics USB 2000 spectrometer, which was connected to the computer. The software interface provided by the spectrometer is easy to use and allows the

visualisation and saving of the spectra with desired spectral sampling frequency.

Figure 3.15 shows an example of the reflection spectrum observed for a sensor before and after the application of parylene film. The cavity related to the spectrum is shown in figure 3.15 (a) with a cavity length of 62.64 µm. The Blue line shows the baseline before the application of the film. The shape of the baseline is due to the dark current. The red line graph shows the spectrum after the application of film. The baseline reflection spectrum turns into an interference fringe pattern due to the application of the film to the tip of the cavity, which acts as a mirror.

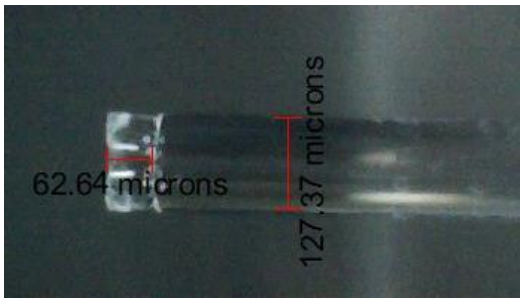

(a)

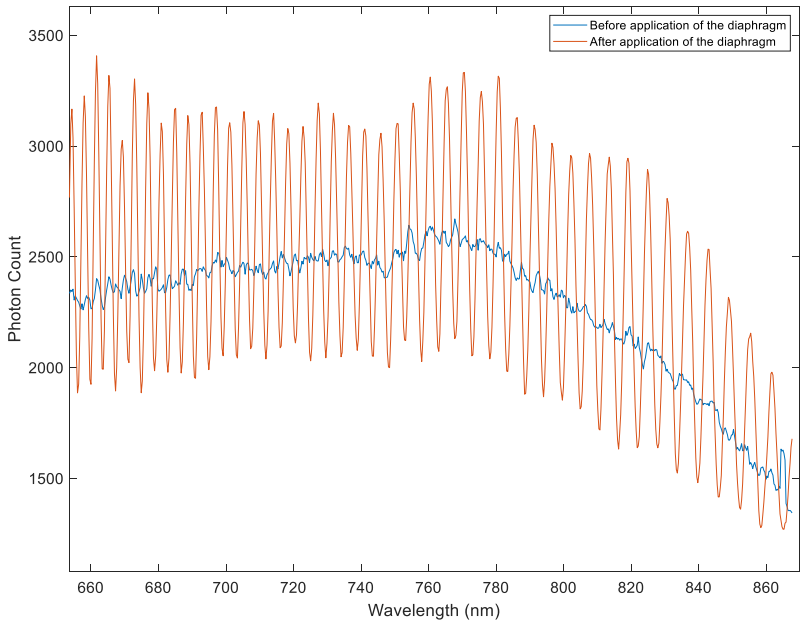

(b)

Figure 3.15: (a) image of the fibre tip, showing the dimensions of the cavity (b) The reflection spectrum of the FP pressure sensor recorded before (blue) and after application of the Parylene-C diaphragm(red)

The pressure in the chamber is measured and recorded with its time stamp. The wavelength spectrum is also recorded with its time stamp. A Labview based software is then used to analyse the spectrum. The peak detection virtual instrument (VI), provided with LabView, was included in the program to detect the peak. The VI fits a polynomial to the data to identify the wavelengths of the peaks. Data is synchronized with their time stamps. For the peaks, the wavelength shift over the time is extracted. Then, for a selected wavelength, the pressure and the wavelength change were plotted against time. In this way, the pressure sensitivity of the FP pressure sensor is obtained in terms of wavelength change per unit pressure change.

According to figure 3.15, the cavity length can be approximated using the mathematical equations discussed in chapter 2 for fibre Fabry-Perot interferometry. For the cavity length 62.64 μm, the simulated interference fringe pattern (using the mathematical model detailed in chapter 2) was plotted for the wavelength range of 660 nm – 860 nm. The number of fringes obtained is 44 whereas the experimentally observed number of fringes is 42. Therefore the uncertainty is 4% for the cavity length measurement.

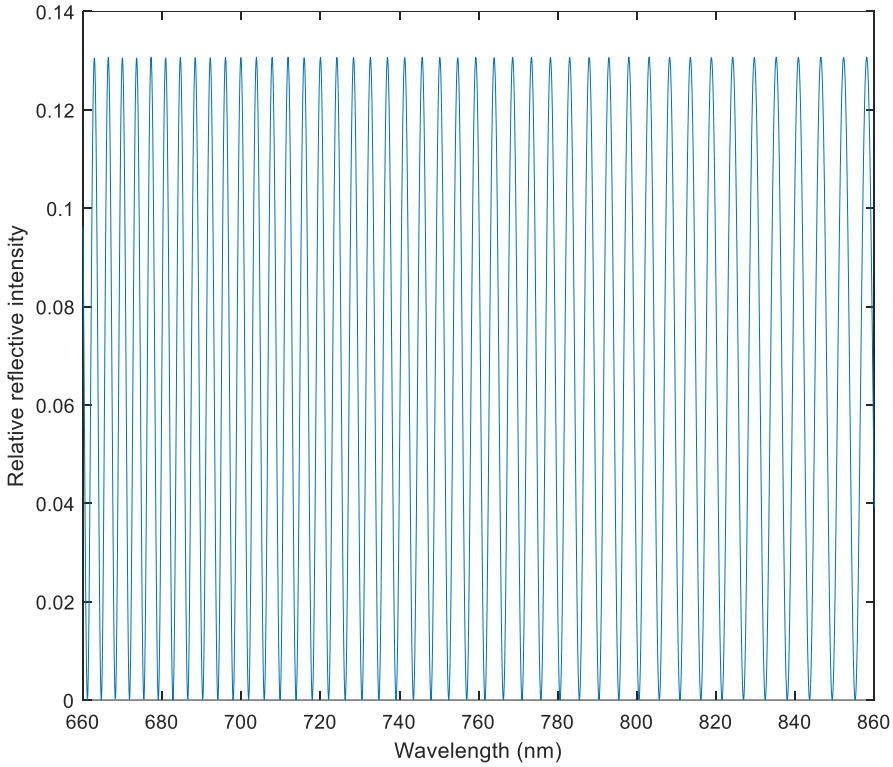

Figure 3.16: Simulated reflection spectrum of fibre optic Fabry-Perot sensor for a cavity length of 62.64 μm

3.4 Results

3.4.1 Sensor 1 -FIB based sensor

This section will discuss the results for the sensor with cavity fabricated using the approach detailed in 3.2.1.1 and the diaphragm applied using the method described in section 3.2.1.3. The cavity length is 8.7± 2 μm. Diameter of cavity is 21±1 μm.

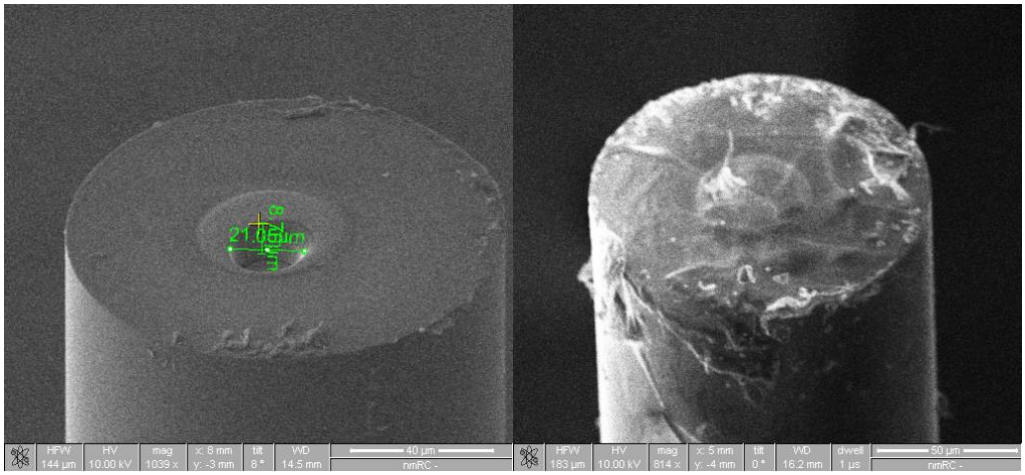

(a) (b)

Figure 3.17: FIB images of the sensor (a) fibre Fabry-Perot cavity fabricated using FIB milling, maginification x1039,scale bar 40 µm (b) Fibre Fabry-Perot sensor with the parylene film, magnification x814, scale bar 50 µm

Figure 3.17(a) shows the fibre optic FP cavity and figure 3.15(b) shows the FIB image of the fibre optic FP pressure sensor after depositing the parylene diaphragm.

Once the diaphragm is applied, an interference fringe pattern can be observed. The interference fringe pattern is shown in figure 3.18. The pressure and the wavelength changes were plotted against time and are shown in figure 3.20. In this plot, the red curve represents the wavelength behaviour of the spectrum peak, initially at 734 nm (in figure 3.18) in response to pressure change. The simulated spectrum for the cavity length 8.7 µm is shown in figure 3.19. The uncertainty in the measurement showed 30% with respect to the number of fringes obtained The fringes observed in figure 3.18 have more structure when compared to the fringes obtained in figure 3.15. This structure has contributed significantly to the error indicated above. The structure may be a result of the length of the cavity being so small and it not acting as a two beam interferometer.

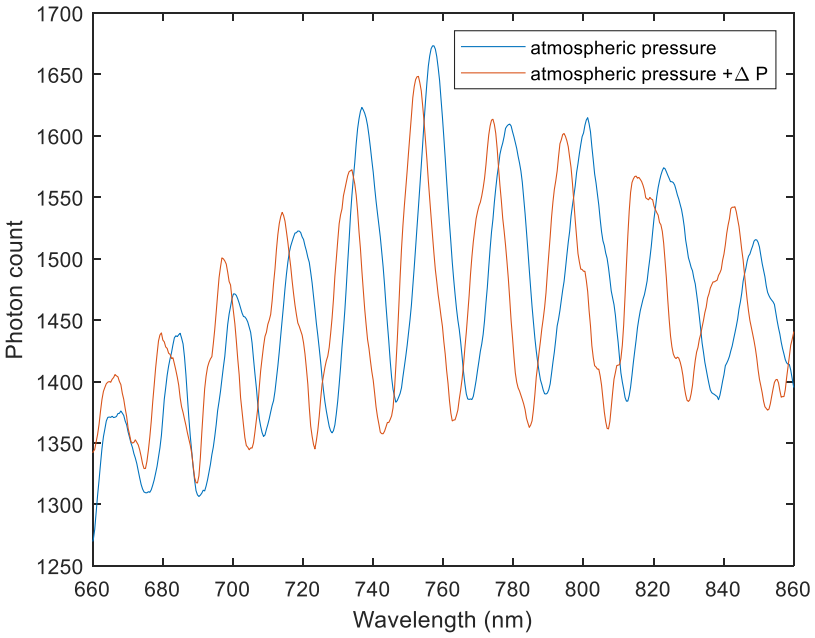

Figure 3.18: The interference fringe pattern of sensor 1. The blue curve corresponds to the fringe pattern when the sensor is kept under normal atmospheric pressure and the red line indicates the shift of the wavelength when the pressure decreased by ΔP =15 kPa

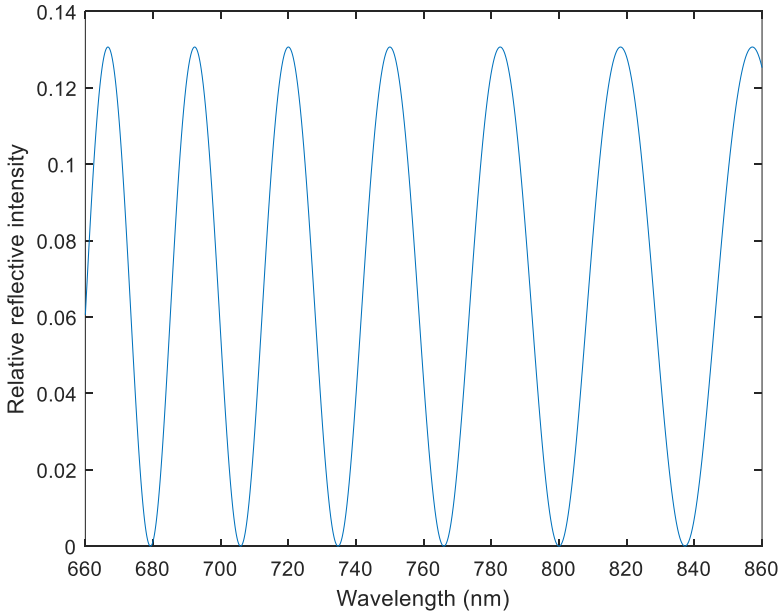

Figure 3.19: Simulated FP sensor interference fringe pattern for 660-860 nm wavelength window obtained for a cavity length of 8.7 μm

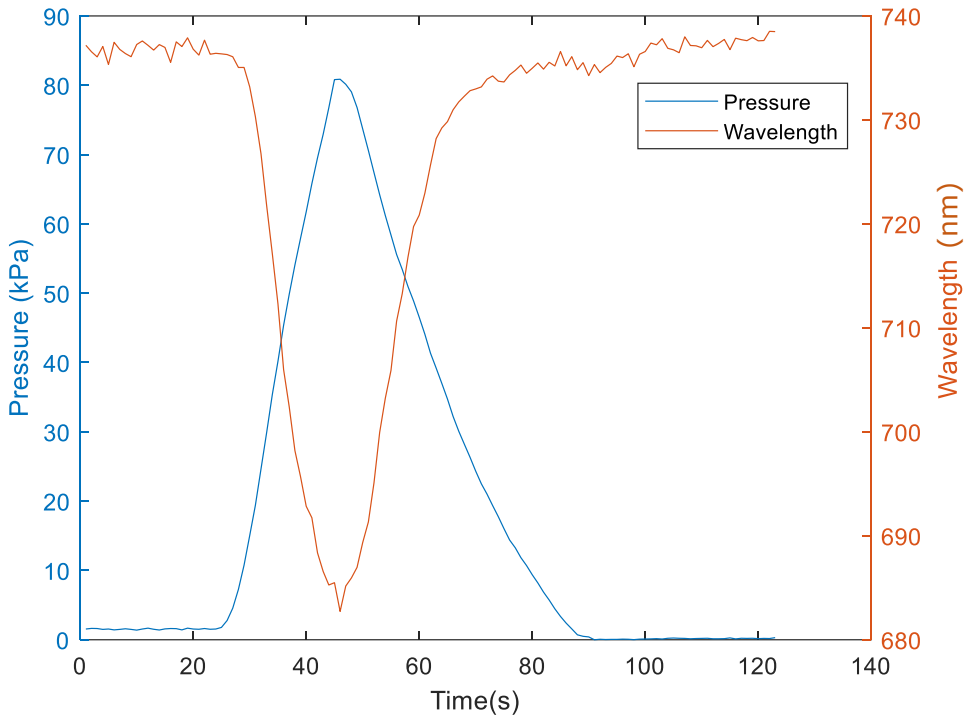

Figure 3.20: The pressure and wavelength change with the time. The blue curve represents the pressure response with the time and the red curve shows the wavelength change of the peak at 734 nm with time

By observing figure 3.21 it is noted that the measured wavelength change of the peak was noisy when the pressure was <10 kPa. The pressure and wavelength data for pressures <10 kPa are plotted and illustrated in figure 3.21 for increasing pressure (blue) and decreasing pressure (red).

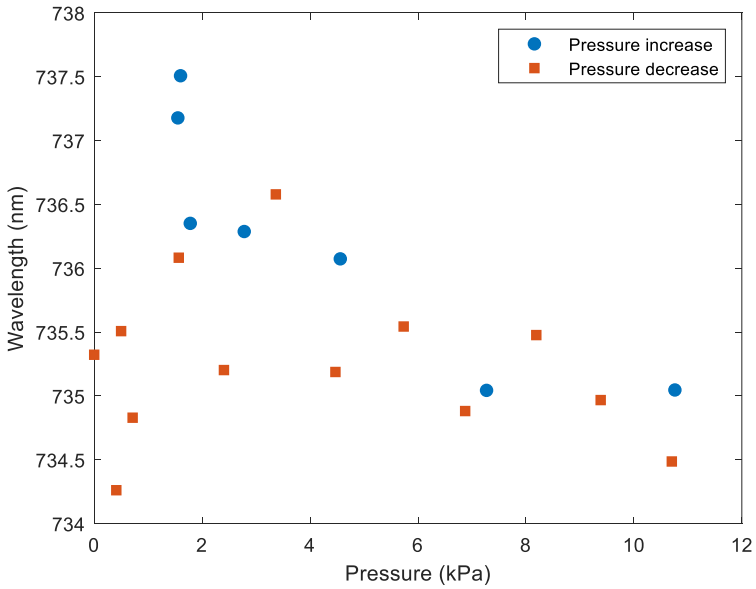

Figure 3.21: Pressure data against the wavelength data plotted for pressure less than 10 kPa

Below 10 kPa, the relationship between pressure and wavelength is not clear. This may be because the film is not under a pretension before applying the pressure. Therefore, at lower pressure, the film is not behaving linearly with pressure. The relative wavelength change with pressure change, within the range 10-80 kPa, is plotted and illustrated in figure 3.22 for a pressure increase and pressure decrease cycle. This was plotted using the synchronous pressure and wavelength data. For each pressure related peak, the wavelength shift was plotted. The drift in the zero measurement is due to the measurement uncertainty coming from the viscoelastic nature of the film and film permeability which will be dicussed in detail in section 3.5. This drift in the zero measurement is a problem in data reproducibility. It can be also noted that pressure increase and pressure decrease follow two different paths and show hysteresis. The anaomaly circled on figure 3.22 due to a sudden change in the air flow into the pressure chamber due to friction of the syringe pump. The behaviour of figure 3.22, could be related to equation 2.40, in chapter 2. In chapter 2, it was discussed that for smaller pre-tension, sensitivity of the sensor is a function of pressure. As pressure increases, wavelength sensitivity is decreased.

The calibration curve with the standard deviations, were plotted based on 10 repeated measurements. One measurement is one pressure cycle from 0-80 kPa. Figure 3.23 shows a linear fit to the data obtained for increasing the pressure over the range 10-80 kPa. It indicates a correlation coefficient of about 0.98 for the linear fit. The average sensitivity for a pressure cycle can be given as 0.57 nm/kPa with a root mean squared error of 2.081 nm/kPa. For the same data, a quadratic function was fitted to check the correlation as shown in figure 3.24. Figure 3.25 shows the linear calibration curves plotted for decreasing pressure and figure 3.26 shows the quadratic calibration curve fitted for the same data.

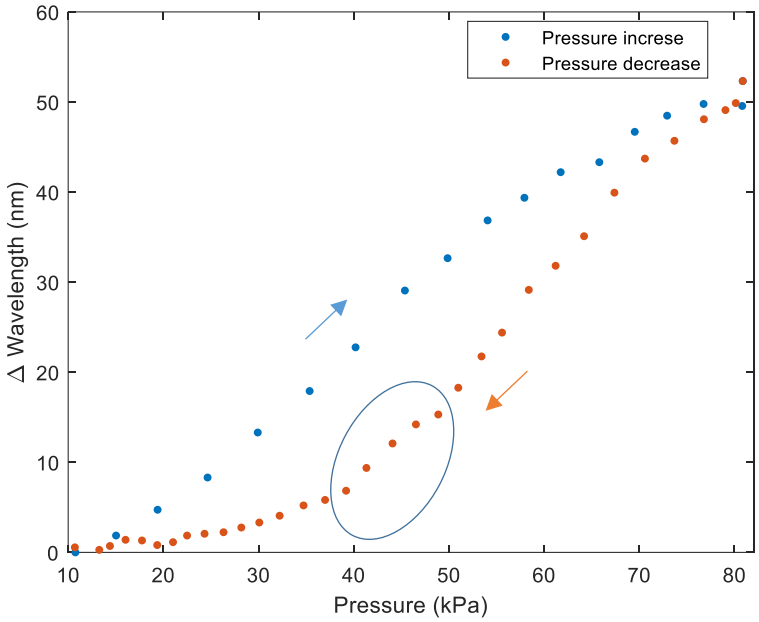

Figure 3.22: Pressure data against the wavelength change data plotted for pressure range 10 kPa- 80 kPa. Blue curve for pressure increase and red curve for pressure decrease

The qaudratic fit offers higher precision over the linear fit resulting in a higher coefficient of correlation of 0.99. Root mean square error was reduced to 1.18 nm/kPa when using the quadratic fit. Moreover, the second derivative of the quadratic fit provides information about the direction of the pressure application (increasing or decreasing).

For the decrease of pressure, a sensitivity of 0.62 nm/kPa was observed with a root mean square error of 3.74nm/kPa (figure 3.25). However, the quadratic fit reduced the root mean square error to 1.906nm/kPa for the same decreasing pressure data (figure 3.27).

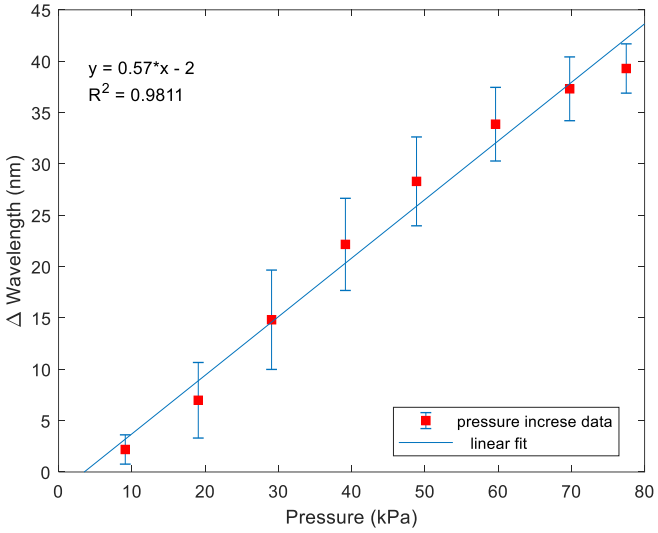

Figure 3.23: Linear calibration curve fitting for pressure increase

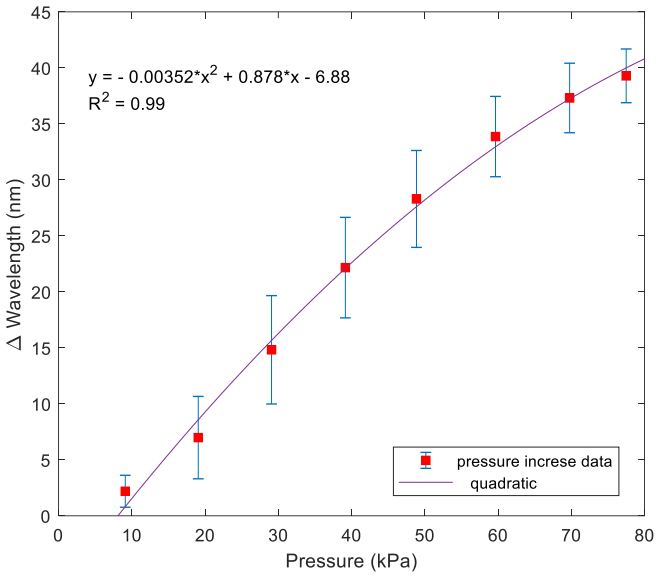

Figure 3.24: Quadratic calibration curve fitting for pressure increase

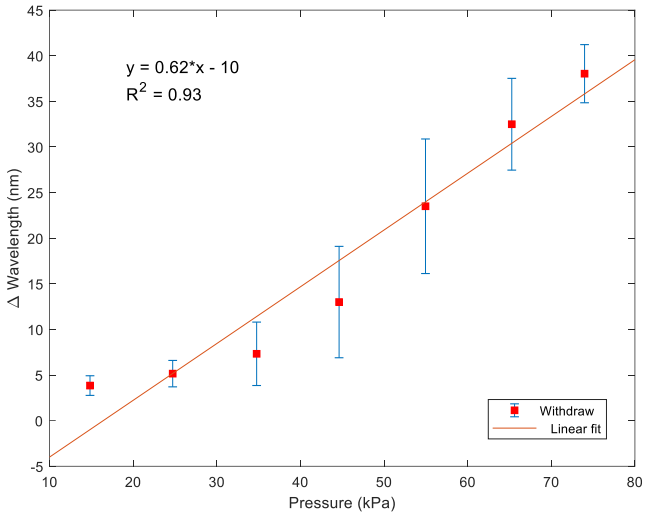

Figure 3.25: Linear calibration curve fitting for pressure decrease

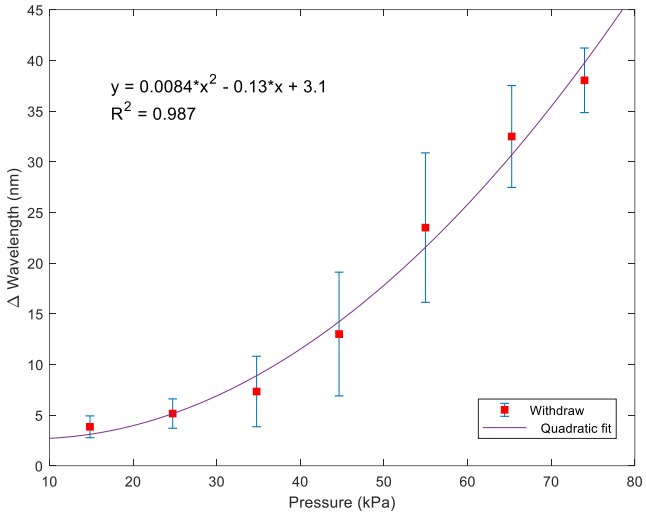

Figure 3.26: Quadratic calibration curve fitting for pressure decrease

3.4.2 Sensor 2- Capillary tube based sensor, applying the film using the movable stage

This section will discuss the results obtained from Sensor 2. Sensor 2 was made with the Fabry-Perot cavity splicing method described in section 3.2.2 and the diaphragm application method described in section 3.2.1.3. Figure 3.28 shows the microscope image of the fabricated FP sensor. The cavity length is ~84.58 μm and the diameter is 70 μm.

Figure 3.28 shows the interference fringe pattern obtained for the sensor. In the wavelength window of 720nm-740nm 7 fringes could be observed. The simulted interference fringe pattern obtained for a cavity length of 84.58 μm is shown in figure 3.29. The uncertainty in the number of fringes can be given as 22%. Therefore the cavity length can be given as 84.58 μm ± 18 μm. The uncertainty due to the limited wavelength resolution (figure 3.28) is minimised by using the LabVIEW peak detection function that fits a quadratic polynomial to the spectrometer data.

Figure 3.30 presents four examples of pressure and wavelength behaviour of the sensor with time. These figures provide good indication of the sensors' behaviour to different functions of pressure. Moreover, it is noticeable that the drift in the wavelength response is quite significant when the pressure is increased slowly than when the pressure increased faster. When air is infused to the pressure chamber, the film tends to oscillate due to the wind and the FP tip orientation against the wind flow results in these fluctuations. When the air is infused at a slower rate, this drift is significant. It is also visible that the pressure drops below and wavelength rises above the starting values due to air leakage that may present in the pressure chamber.

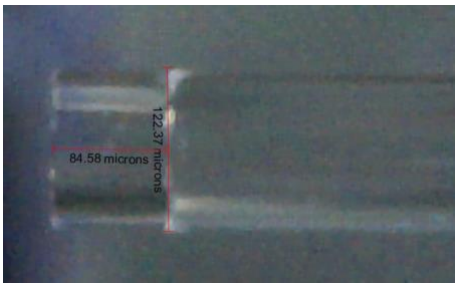

(a)

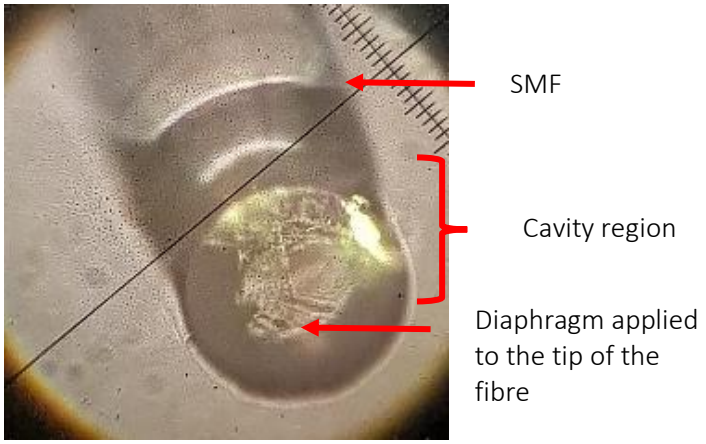

(b)

Figure 3.27: (a) Microscopic image of the fibre sensor 2 with cavity length of 84 μm (b) transmission microscopic image of the fibre tip of the sensor with the film

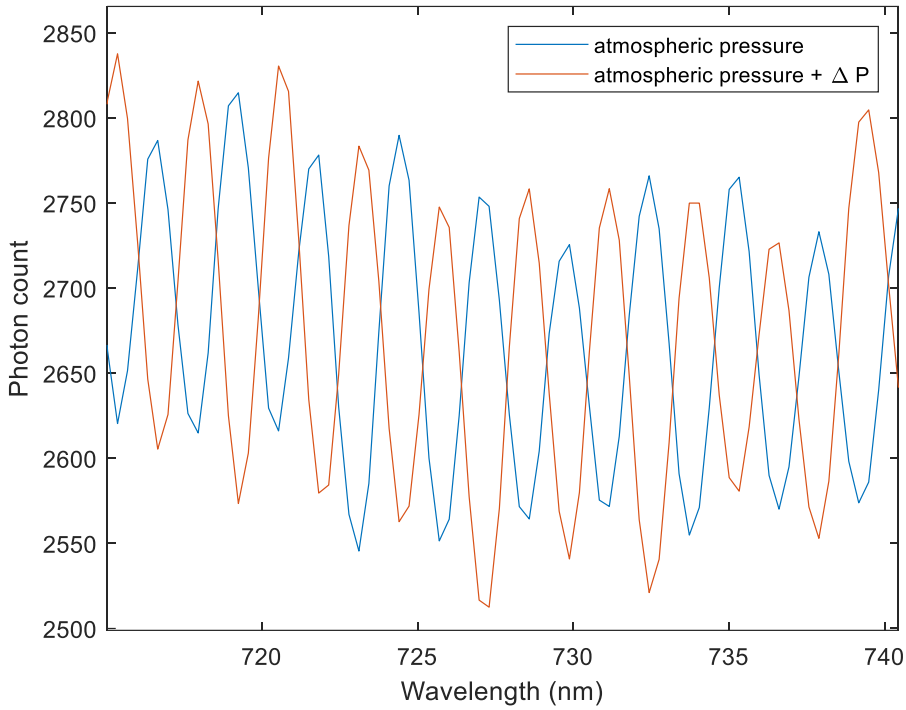

Figure 3.28: The interference fringe pattern of sensor 2. The blue curve corresponds to the fringe pattern when the sensor is kept under atmospheric pressure, while the red line indicates the shift of the wavelength when pressure decreased by 0.8kPa is applied

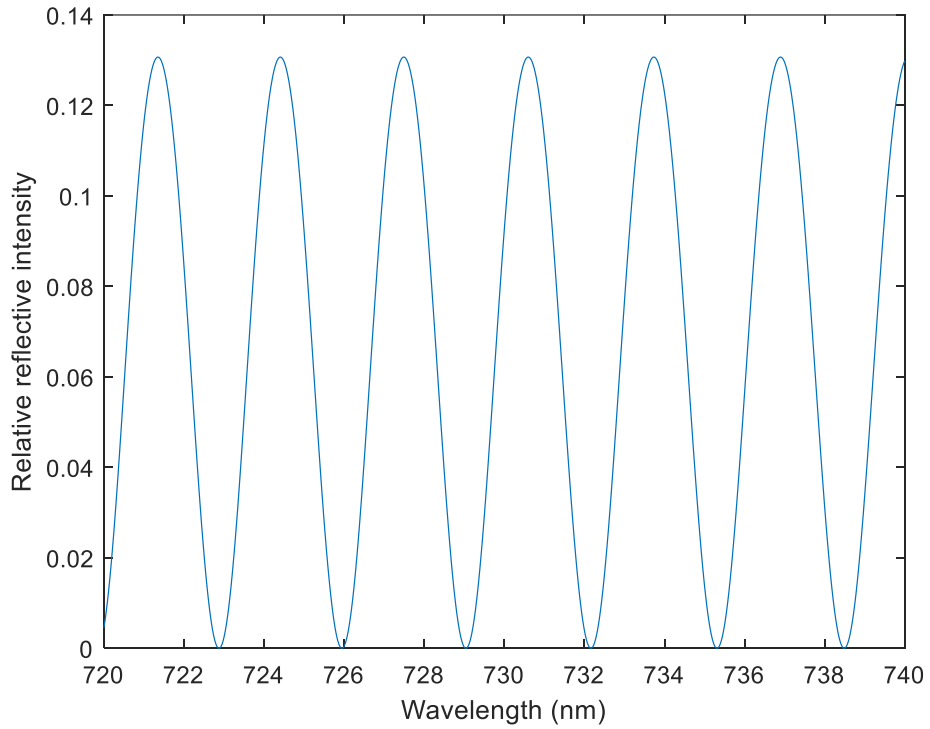

Figure 3.29: Simulated FP sensor interference fringe pattern for 720-740 nm wavelength window obtained for a cavity length of 84.58 μm

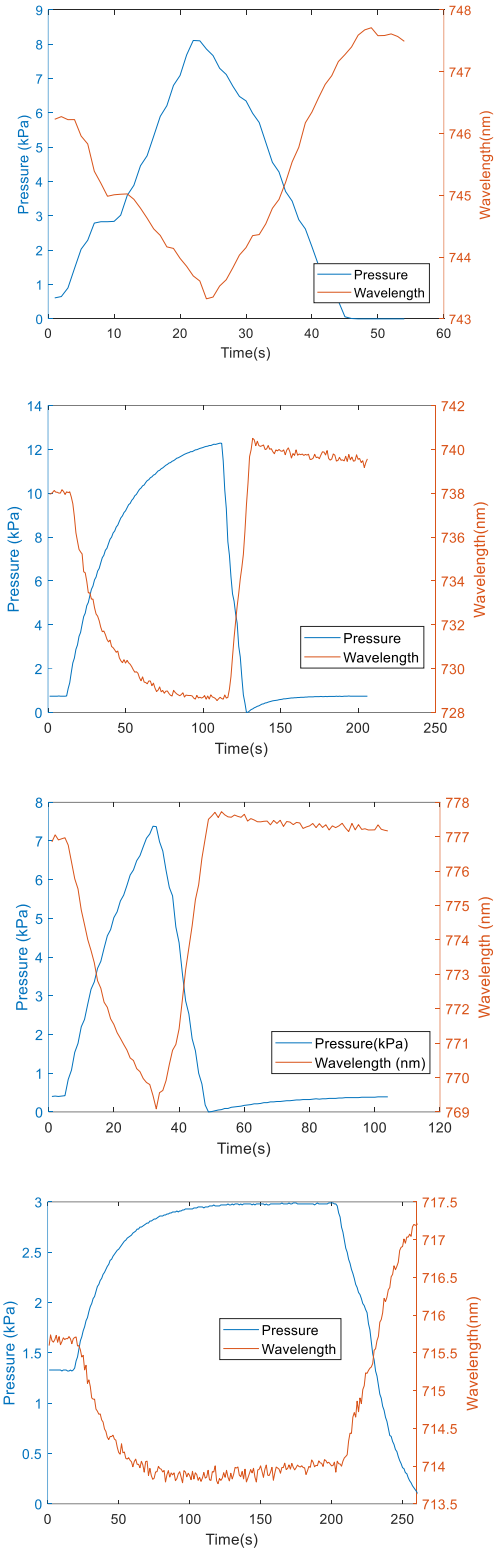

Figure 3.30: Four examples of pressure and wavelength changes with time for sensor 2, pressure was changed as four different functions of time

It can be seen that the wavelength change of a particular fringe is a function of pressure. Figures 3.31 and 3.32 show the calibration curves for the pressure increase and pressure decrease data. These calibration data were determined

from 10 repeats. The data shows a good linear response with a correlation coefficient of 0.9. The sensitivity to pressure increase is 0.86 nm/kPa, with a root mean square error of 0.3 nm/kPa and to pressure decrease it is 1.2 nm/kPa with a root mean square error of 0.9 nm/kPa. At a pressure of 12 kPa, the centre deflection of the film can be calculated using equation 2.36 as 23.8 µm.

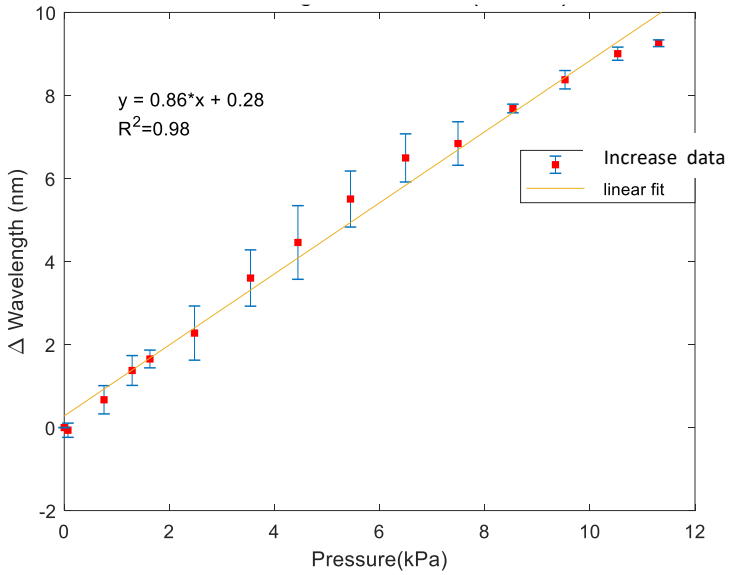

Figure 3.31: Calibration curve for the wavelength and pressure data for the pressure increase

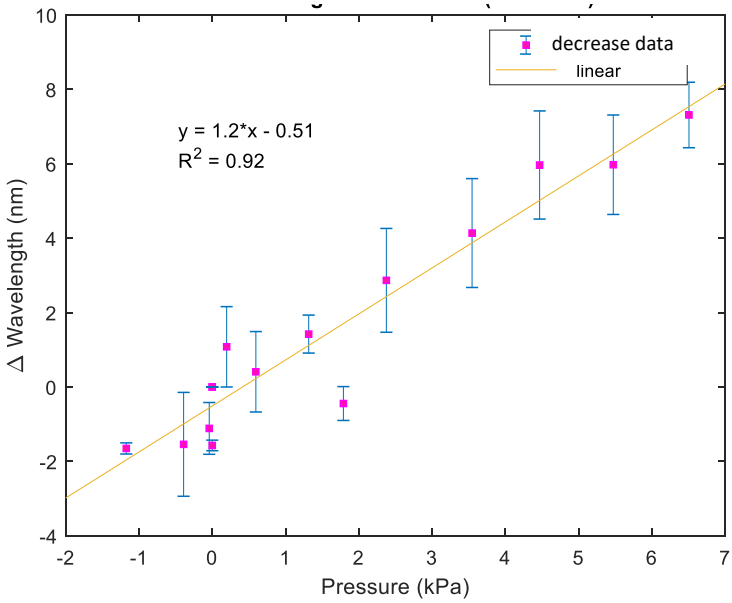

Figure 3.32: Calibration curve for the wavelength and pressure data for withdraw of air

The larger negative values in pressure and wavelength seen in figure 3.32 indicates the air leaking of the pressure chamber.

3.4.3 Sensor 3- Capillary tube based sensor and applying the wet film to the tip

The results described in this section are for the sensor made using the cavity splicing method described in section 3.2.2.1 and the film deposition method described in section 3.2.2.2 (applying the wet film to the tip and drying it out). Figure 3.33 shows the microscope view of the optical cavity of the sensor with cavity length of 87.41 µm. Figure 3.34 shows the reflection spectrum of the interference fringe pattern of the FP sensor. Figure 3.35 shows the baseline test done for the sensor without applying any pressure load. This test was done to ensure whether there is significant drift in the wavelengths before application of any pressure. A number of peaks were selected and their peak wavelengths were plotted against time. The baseline was showing a maximum deviation of ± 0.1 nm without applying any pressure. This concludes that no external variables are affecting the wavelength changes of the sensor other than the variable changes induced by the pressure difference.

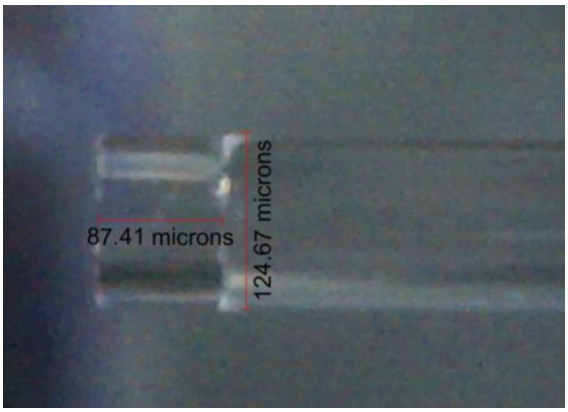

Figure 3.33: Microscopic image of the fibre sensor 3 with cavity length of 87 µm

Figure 3.36 presents four examples of pressure and wavelength changes with time. The drift in the pressure is due to the air leak in the pressure chamber/ at the connectors. The noise and the drift in the wavelength is caused by the

pressure drift mentioned above and air penetration through the film is discussed in section 3.5 in detail. This drift is a problem in reproducibility of the measurments. This could be overcome by using a stable film. Figure 3.37 shows the wavelength shift for the pressure range of 0- ~20 kPa for one pressure cycle. Figure 3.40 and figure 3.41 show the calibration curves for the pressure increase and pressure decrease data. These data were plotted for 10 repetitions.

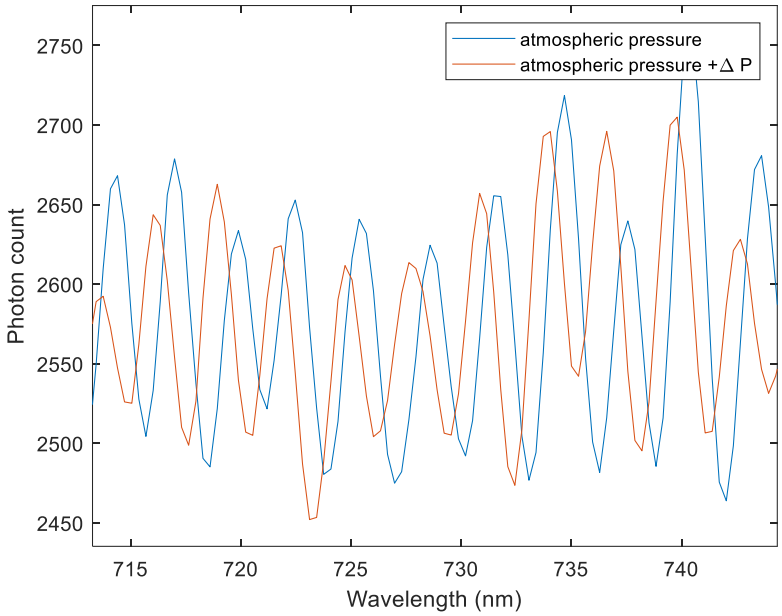

Figure 3.34: Interference fringe pattern of the FP sensor 3

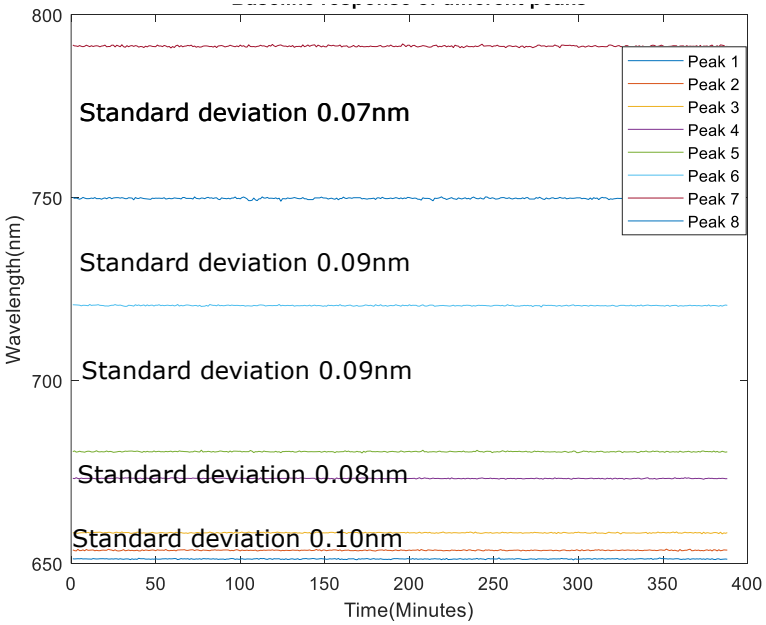

Figure 3.35: Baseline experiment when no pressure applied

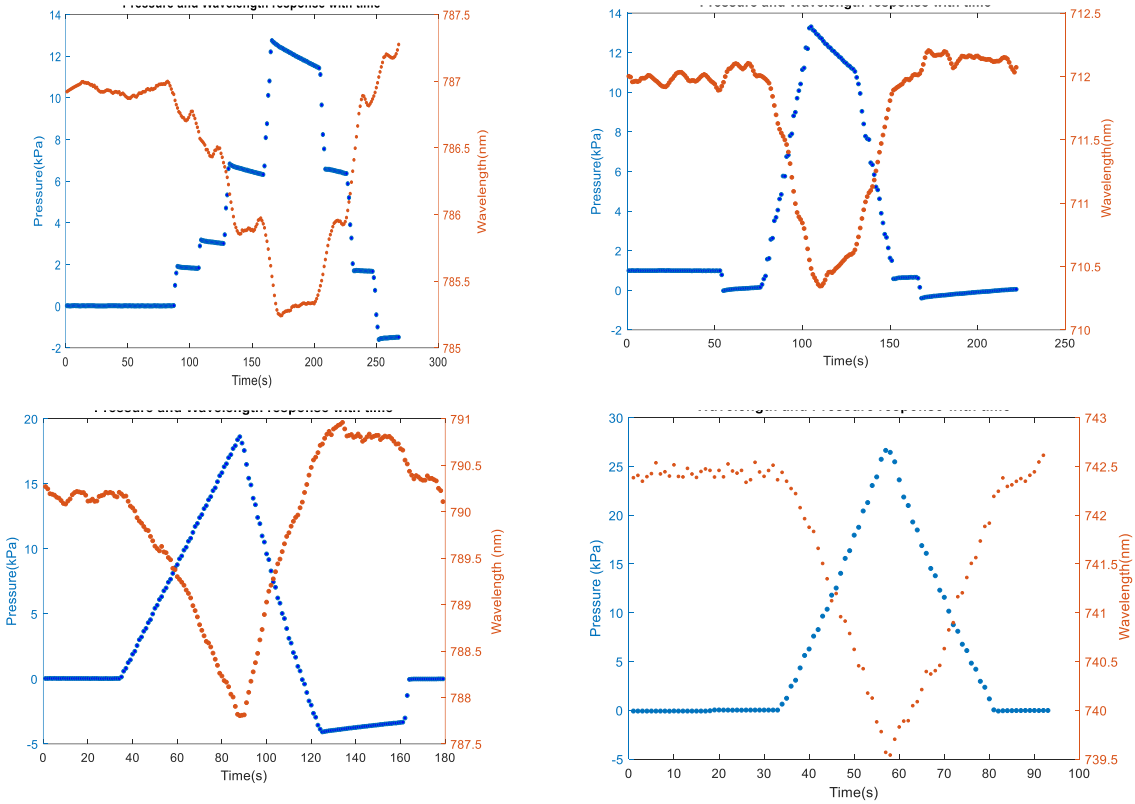

Figure 3.36: Pressure and wavelength changes with time for sensor 3, pressure was changed as four different functions of time

According to the figures 3.37 and 3.38 it is clear that the sensors have a linear response to the pressure and shows a linear correlation coefficient ~0.98. However, the sensor performace is limited by the drift, as shown in figure 3.39. The sensitivity for increasing pressure was 0.11 nm/kPa with a root mean square error of 0.0706nm/kPa over a range of 0-16 kPa. The sensitivity for decreasing pressure was 0.13 nm/kPa with a root mean square error of 0.1434nm/kPa.

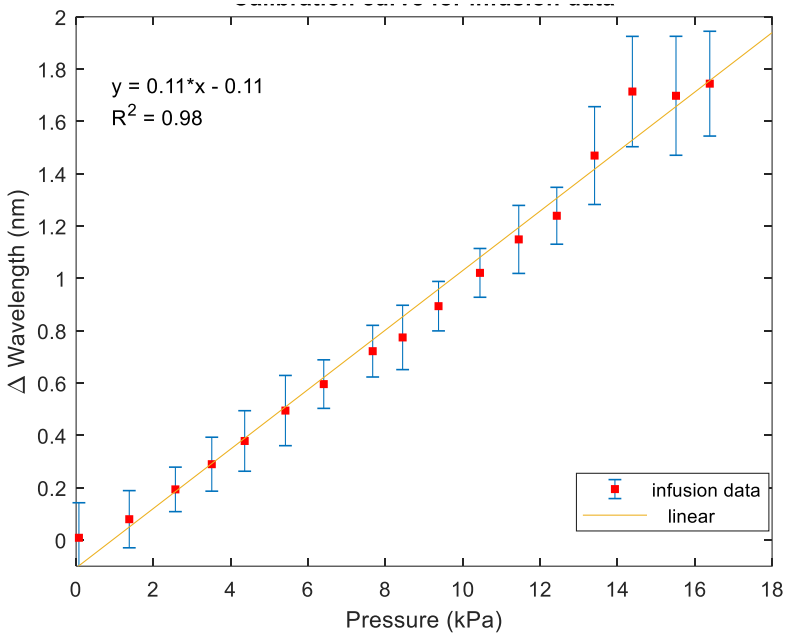

Figure 3.37: Calibration curve for the pressure increase data

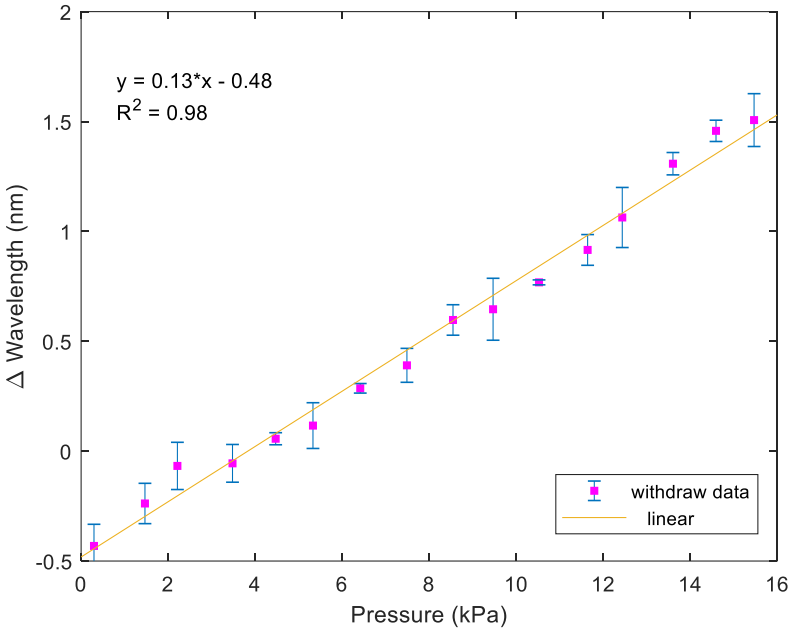

Figure 3.38: Calibration curve for the pressure decrease data

3.4.3.1 Step Response and time response

Figure 3.39 shows the step pressure response of the FP pressure sensor. This test was conducted over a time period of about half an hour.

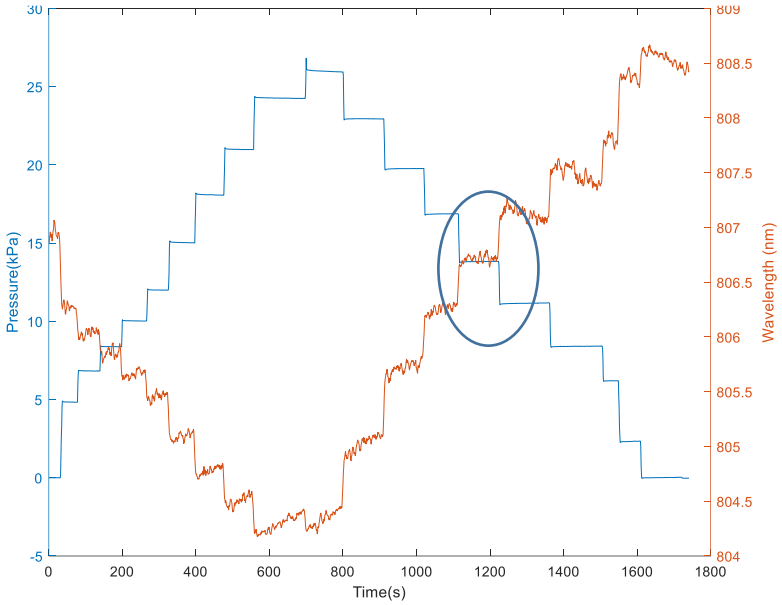

Figure 3.39: Step pressure response of the FP sensor, circled region is plotted below for time response calculation

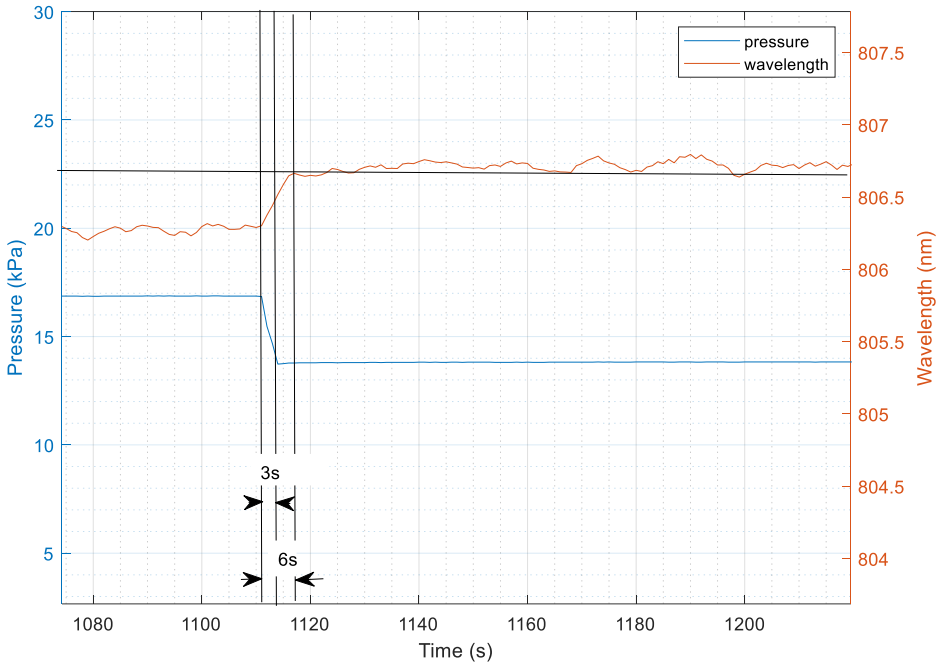

Figure 3.40: Response time of the wavelength to the pressure for a pressure step change. This graph is the magnified section of circled section of figure 3.39

The circled section of figure 3.39 was plotted again as figure 3.40 to calculate the response time for the sensor. As pressure increased through a step index within 3s, the wavelength increases the step change taking 6 seconds. Therefore the time response for the sensor can be given as 3s. Frequency response is hence 0.3Hz.

The calibration curve for the above step changes were plotted for the pressure increase and decrease on the same graph, as shown in figure 3.41. A noticeable increase in the hysteresis can be observed during the step response. The increase pressure showed 0.10 nm/kPa where decrease/withdraw pressure showed 0.16 nm/kPa. The possible reasons for the behaviour are discussed in section 3.5.

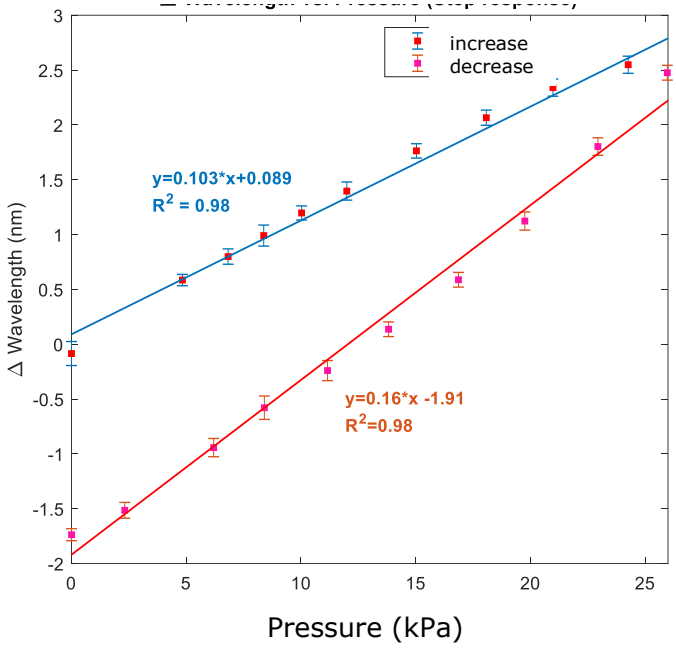

Figure 3.41: Calibration curves for the step response

3.4.3.2 Temperature Response

The temperature may affect the sensor response in two ways. As the temperature increases due to the thermal expansion of the silica fibre the cavity length may change. This change will introduce a wavelength shift. The second reason is as that the temperature increases, the air trapped in the cavity may undergo a volume increase due to the internal kinetic energy increment caused by the temperature increment. Therefore the temperature response of the sensor was investigated using the setup described figure 3.42. The FP sensor was inserted inside the oven. The temperature inside the oven was measured using a BME 280 temperature, pressure and humidity sensor. This was connected to a computer, as shown in figure 3.42. The reflection spectrum of the FP sensor was recorded and observed using an Ocean Optics spectrometer connected to the computer. The sensor was illuminated using a halogen light source.

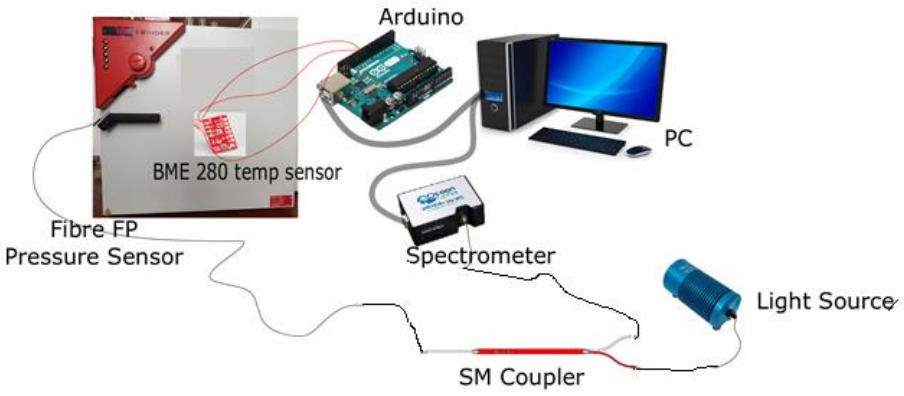

Figure 3.42: Experimental setup for temperature measurements

Figure 3.43 shows the temperature response curve plotted for the FP sensor. According to the figure there is a sensitivity of about 0.08 nm/^{0}C.

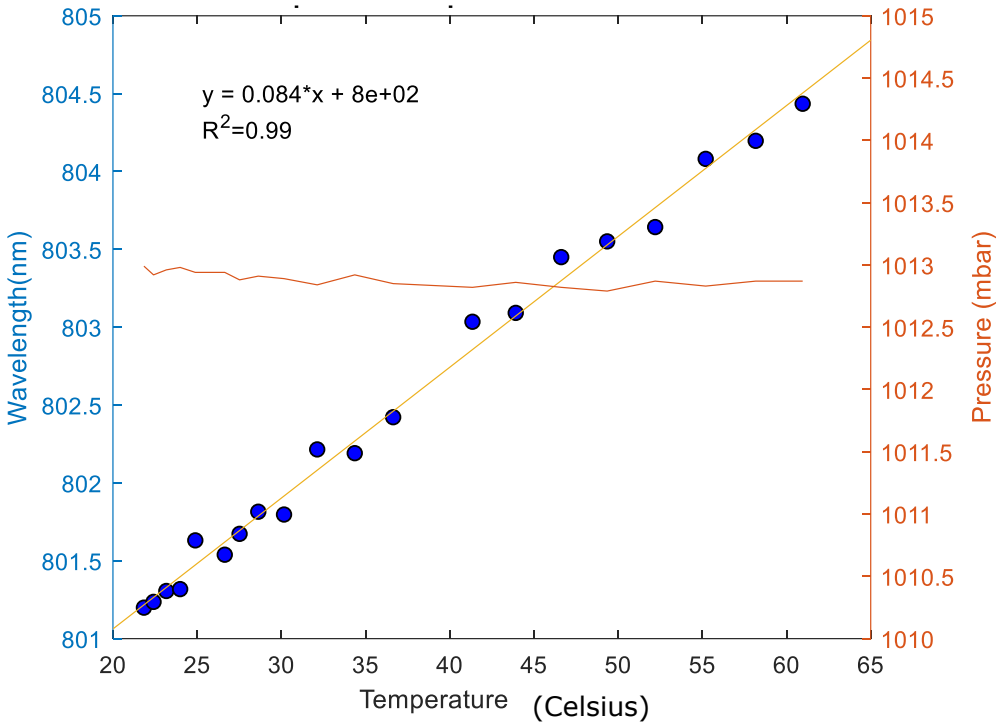

Figure 3.43: Wavelength and pressure as a function temperature

With this result it is clear that wavelength change of the FP sensor is not only a function of pressure, but it is a function of both temperature and pressure. The temperature sensitivity of the sensor is significant figure when compared with the sensitivities of the three sensors described above. If the measurements are done in a temperature static environment this may not affect the pressure measurements, however when there are dynamic temperature changes this

may give inaccurate pressure measurements. Therefore temperature compensation methods should be identified. This is discussed in detail in section 3.5.

3.5 Discussion, Conclusions and future works

Three implementation methods of a miniature fibre optic pressure sensor for air/fluid pressure sensing in invasive medical applications were demonstrated. The limitations of the sensor and future work is detailed in this section.

Sensor 1 where the cavity was formed using FIB and Sensor 2 where the cavity was formed using capillary tube both exhibit hysteresis. A possible reason could be the weak bond between the pressure sensitive diaphragm and the fibre tip. This will result in a negligible initial stress on the film. In chapter 2, equation 2.36 and 2.38 dicussed the sensitivity and the deflection of the film with negligible initial stress. According to these equations the sensitivity is a function of pressure and sensitivity drops as the pressure increases. This was observed for the calibration curves of sensor 1 and 2. The film attachment method used in these sensors may suffer from certain limitations. Although Parylene films are self-supporting, over the time of use the film may loosen its attachment to the fibre tip and this may cause air leakage from and out of the FP cavity and therefore may lose their performance. But the attachment method used in fabricating the sensor 3 is quite promising. As the film dries the edges will be sealed therefore making a good attachment and providing a durability to the film attachment.

The cavity inscription method used for the sensor 1 using FIB is a promising method. Nevertheless, there is a compromise between the milling time and the quality of the cavity. To mill a cavity of 21 μm diameter and ~9 μm depth, takes around 49 minutes (Table 3.1), using a high current of 5nA. For one sensor this is excessive amount of time and associated cost. As the milling current increases, the milling time can be reduced by compromising on the quality of the cavity. Figure 3.44 shows the cavity after making a cross-section. This cavity was milled by setting the cavity length to 8 μm. The diameter of the cavity was

set to 7 µm. As the figure shows, when milling small diameter cavities, there is redeposition of the material. This is a common issue which has been reported previously and relates to the milling of silicon based samples [189], [190]. During the experiments based on cavity based on FIB, this was a limitation. Some of the sensors did not produce fringes after application of the film. Compared to the cavity dimensions this redeposition may cause scattering of light. This issue can be eliminated by increasing the diameter of the cavity, which will increase the required milling time.

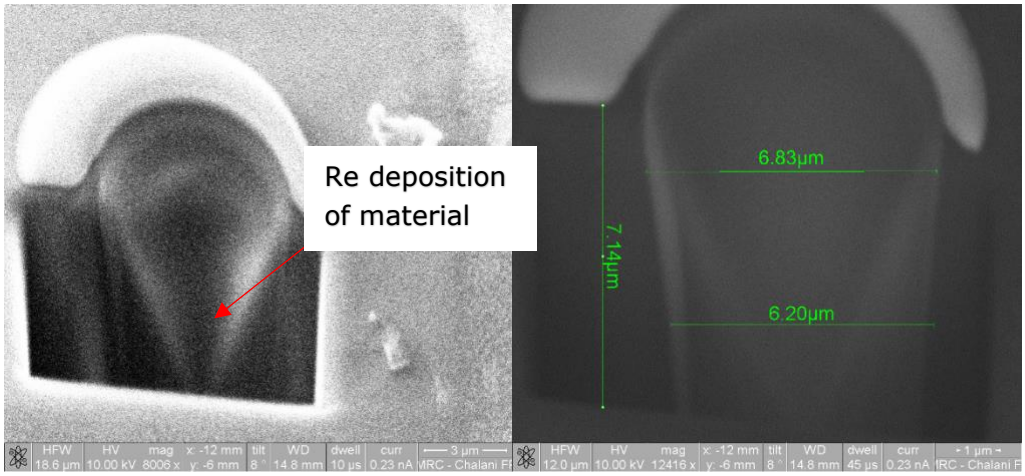

(a) (b)

Figure 3.44: SEM cross sectional view of the cavity,a) without measurements of the cavity, scale bar of 3um b) with measurements of the cavity, scale bar of 1um

For smaller cavity lengths it was observed there is a structure added to the fringe pattern (figure 3.18). Another example is given in figure 3.45, observed for a FP cavity made with the FIB technique.

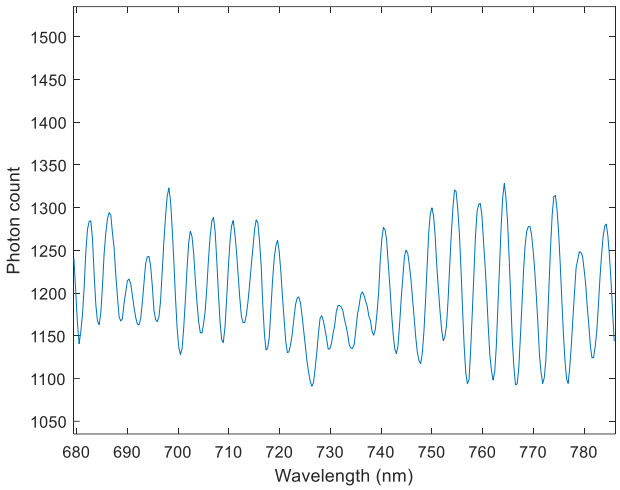

Figure 3.45: Interference fringe pattern observed with envelopes for FP cavity formed using FIB

For all the sensors, noise in the wavelength response may be due to a couple of reasons. In these experiments the fibre tip in the chamber sits horizontally and the air flows into the chamber vertically, this may introduce vibrations in the sensor and hence wavelength oscillations. As will be explained in the subsequent section, air diffusion continously through the film due to the air permeability, will also cause noise and drift in the wavelength response.

3.5.1 Hysteresis of the pressure sensor

The hysteresis of a sensor can be described as the maximum difference in output at any measured value within the sensor's specified range when approaching the point first with increasing and then with decreasing the input parameter [191]. This phenomenon causes instrument performance to vary depending on the direction of the applied input signal. In general, a commercial sensor's accuracy is a function of hysteresis, linearity and repeatability as defined in International Electrotechnical Commission standards IEC 61298-2 [192],[193],[194]. The hysteresis of a pressure sensor can be in two forms: mechanical hysteresis and temperature hysteresis [195]. Mechanical hysteresis is the output deviation at a certain input pressure when the input is first approached by increasing and then decreasing pressure. Temperature hysteresis is the output deviation at a certain input pressure before and after a temperature cycle. However, hysteresis is not generally described as two

different components for a device but as the total hysteresis [196]. This hysteresis behaviour can be realted to the viscoelasticity (viscous and eleastic properties) properties [197] of the parylene film. Viscoelasticity is the property of material that exhibits both viscous and elastic characteristic when undergoing deformation. Applied stress results in an instantaneous elastic strain followed by a viscous, time dependent strain. Unlike in purely elastic material, when a viscoelastic material is loaded some of the energy is dissipated as heat. Therefore, when the load is removed, viscoelastic materials possess a hysteresis.

One study has been reported in the literature [198] where hysteresis was studied specifically for optically-addressed diaphragm pressure sensors. The sensor used in that study was a ferrule based, single mode fibre optic Fabry-Perot pressure sensor. The application area for this sensor was the measurement of the pressure in wind tunnel experiments and therefore aluminium and copper foil diaphragms of thickness of 38 μm and 12 μm were employed. This study of the hysteresis effects considered the diaphragm material, diaphragm bonding material, attachment to the ferrule and the properties of the air confined in the cavity. Mechanical hysteresis, which is inherent to the diaphragm material, contributes to the total hysteresis significantly. This study also concluded that the diaphragm bonding with no edge support (film is not supported at the edges) has lower hysteresis behaviour when compared with an edge supported diaphragm. The study concluded that the air confined in the cavity does not make a significant contribution to the hysteresis observed during quasi static pressure but it may effect at high temperatures and high frequencies or at subatomic pressure due to the diaphragm deflecting outwards, resulting in problems such as diaphragm buckling and loss of reflected power.

The hysteresis error with respect to the sensors described in this thesis can be approximated using the following explanation. The maximum deviation with respect to the measurable full range is considered as the hysteresis error. This can be given as in equation 3.2 [199].

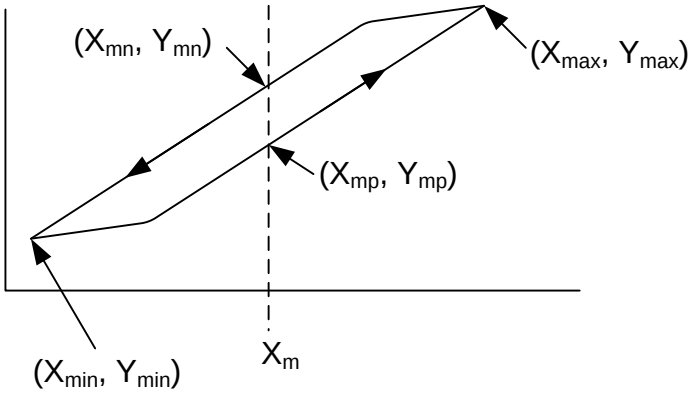

Figure 3.46: Hysteresis calculations [199]

$$Hysteresis\% = \left| \frac{\left(Y_{mn} - Y_{mp}\right)}{\left(Y_{\max} - Y_{\min}\right)} \right| \times 100\% \qquad 3.2$$

Hysteresis was observed for all of the sensors. Table 3.3 shows the hysteresis calculations for the optical fibre pressure sensors.

Table 3.3: Hysteresis calculation comparison table

Sensor	Hysteresis calculation	Hysteresis (%)
01 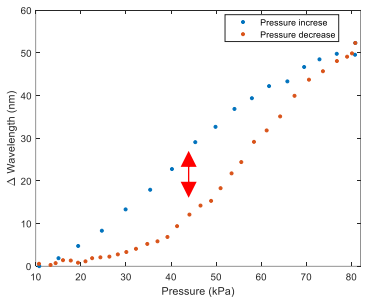	$\frac{28-12}{50} \times 100\%$	32%
02 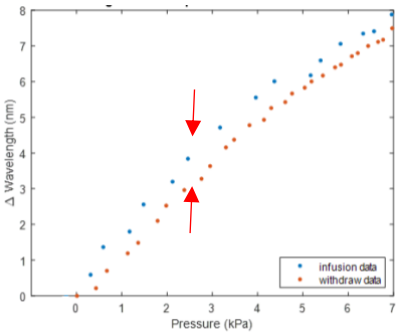	$\frac{4.2-3.2}{8} \times 100\%$	12.5%

03 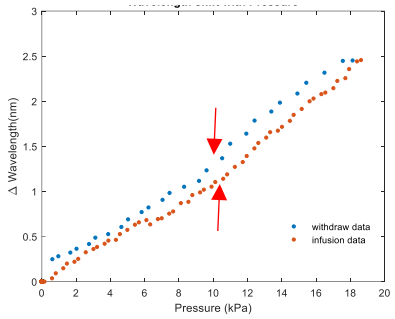	$\frac{1.4 - 1.1}{2.5} \times 100\%$	12%

Sensor 3 has been tested for dynamic and static pressure response as discussed in the results section 3.4.3. Therefore, the errors of the static and dynamic response were calculated with respect to their calibration curves as shown in figure 3.47 and figure 3.48.

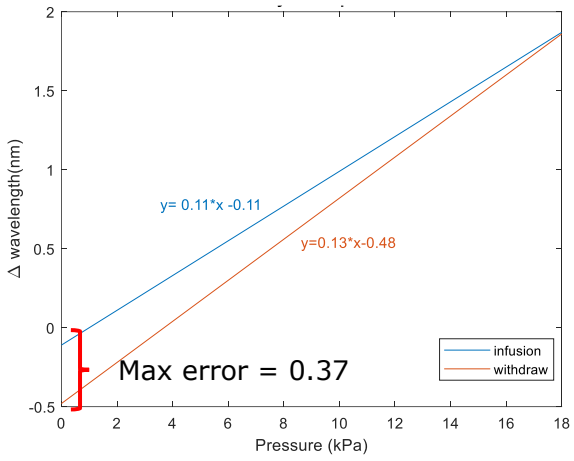

Figure 3.47: calibration curve for dynamic pressure measurements

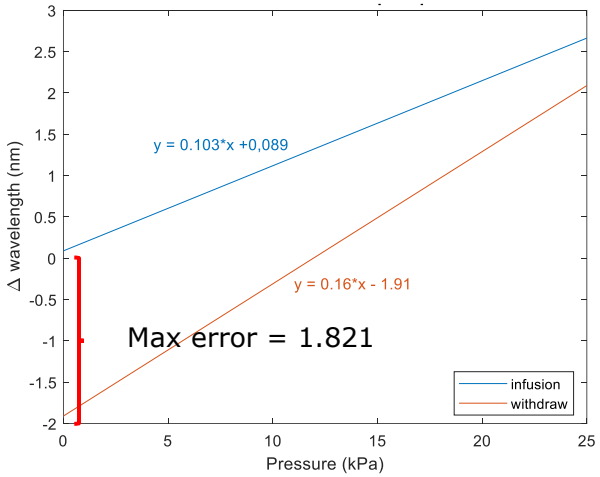

Figure 3.48: calibration curve for step pressure measurements

The percentage error for the dynamic response = 15.74% and the percentage error for the step response = 1.821/4.57 × 100% = 40%. These results show that error percentage increases as the time bandwidth of the experiment increases. The above numbers conclude that the sensor experiences more hysteresis when the measurements are done for long periods of time. This may be due to that the differential pressure between the air cavity and the applied pressure is decreasing over time. One possibility is the film air permeability. The air permeability/gas permeability of a polymeric film can be defined as in equation 3.3 [200]

$$Gas\ permeability = \frac{amount\ of\ gas \times thickness\ of\ membrane}{membrane\ area \times time \times differential\ pressure\ of\ gas} \qquad 3.\ 3$$

Gas permeability is a constant for a specific material and describes the material property that defines the penetration of gas through a solid membrane. According to ISO 15105-1:2007 international standards [201]; coefficient of the gas permeability is the volume of gas passing through a plastic material of unit thickness, per unit area and unit time under unit partial-pressure difference between the two sides of the material. As the thickness of the membrane decreases the amount of gas penetrating through the membrane increases when the membrane area, time and differential pressure of gas are kept constant. Moreover, the amount of gas penetrating through the film also increases as the differential pressure, time and membrane area increases. Gas permeability values of Parylene C films are provided in table 3.4 [202]

Table 3.4: Gas permeability values for Parylene C

Gas	Permeability of Parylene C (cc*mm)/(m^2 *day*atm)
Nitrogen (N_2)	0.4 at 25^0C
Oxygen (O_2)	2.8 at 25^0C
Carbon Dioxide (CO_2)	3.0 at 25^0C
Hydrogen (H_2)	43.3 at 25^0C

In accordance with equation 3.3, since the thickness of the film is in the nm range the volume of the gas penetrating will increase by a factor of 10^6. Moreover, as the time bandwidth increases more gas will penetrate through the film. This explains the reason of the increment of the hysteresis error during long periods of pressure measurements. For N_2 at 25 ^{0}C, for a differential pressure of 27 kPa, over the time of the experiment (900 seconds), with a parylene C film with 200 nm thickness, and the effective radius of 35 µm, the amount of gas that penetrates can be calculated using equation 3.3. This will result in an air penetration of 23 $\mu m^3/s$. Every second this air penetration causes the wavelength to drift and also introduces noise due to the fluctuations of the mebrane.

One solution is to increase the film thickness considerably in order to prevent the gas escaping through the film during the long time of the testing. Nevertheless, it should be also noted that there is a compromise between the film thickness and the sensitivity as described in chapter 2.

The use of polymer materials in food packaging is one of the largest growing market area and uses various methods to prevent the air permeability in the food packaging. In contrast to glass or metal packaging, packages made with polymer materials are permeable to air at different degrees depending on the material properties. In order to reduce the rates of diffusion of gasses through membranes, protective layers of metal foils are laminated on the films or films are metalized by vacuum sputtering [203]. The deposition of amorphous silicon oxide and other ceramics, or nanocomposites on polymer films are also reported [204]. These methods could also be adopted in order to reduce the air permeability of the Parylene films, in order to achieve the future potential, for the targeted applications.

This is a very important factor to be considered in the development of the miniature FP pressure sensor for the context of invasive medical treatments. The measurement could be any gas, blood or any other liquid and according to Choudhury R.et al. [205] a material that is permeable to air is usually permeable to water/liquid, in either the vapour or the liquid phase.

3.5.2 Temperature effect and compensation

The temperature sensitivity observed for the sensor was 0.08 nm/°C. Temperature compensation methods should be identified in order to obtain the sensors full potential. Temperature self-compensation by integrating FBGs into the FP pressure sensor is reported in literature [206]. This is done by multiplexing the FBG signal and FP signals.

Another possibility reported in the literature is the creation two hybrid cavities to compensate for the temperature [207],[208]. This method will introduce two frequency components (one is an envelope of the other) to the net interference fringe pattern in which each frequency corresponds to a pressure or temperature. Using frequency domain signal analysis methods, temperature and pressure can be retrieved separately. However, there are limitations in this method as the elastic properties of the film are dependent on the temperature.

In conclusion, the potential of a miniature, biocompatible fibre optic Fabry – Perot pressure sensor with a sensor head diameter of 125 µm and a response time of 3 second has been achieved for invasive healthcare applications. However, the requirements for the targeted applications (chapter 2, table 2.1), requires higher sampling frequency and this sensor performance is not meeting the required sampling rates. For example, in cardiology the required standard sampling frequency is 200 Hz, and in urology it is 10 Hz. However, when compared with the commercial techniques in table 2.2, this is the smallest diameter sensor among them all. The pressure ranges and the sensitivity described in table 3.3 offered by these sensors are most suitable for health care intracranial pressure measurements [209] and arterial blood pressure monitoring in critical care [210],[211]. However, to achieve its full potential it is important to address the above discussed future work.

Chapter 4

Highly sensitive pressure sensor using an optical fibre Bragg grating embedded in a polymer patch layer: modelling and experimental validation

4.1 Introduction

The response of the reflection spectrum of an FBG sensor embedded into a patch to an applied transverse load depends on the longitudinal elongation of the grating. The quantity of the elongation of the grating is determined by the stress and strain fields acting along the grating. The working principle of the FBG sensor embedded in polymer patch is explained in detail in chapter 2. The need for a mathematical model and FBG simulation algorithm was explained in detail in section 2.13. In this chapter, the algorithm and the flow diagram of the developed simulation system based on ABAQUS and Matlab software are explained along with the obtained results. Experimental validation of the simulation results is also provided.

4.2 Mathematical modelling of an FBG embedded in polymer patch

As was discussed in chapter 2 section 2.3, although a FBG is sensitive to strain and temperature, it is less sensitive to pressure. The pressure sensitivity of a bare FBG is 0.00304 nm/MPa [173]. Typically the range of interest for contact pressure measurement is up to 1 MPa in a healthcare application such as prosthetics. Hence this sensitivity is not suitable for these applications. As was explained in chapter 2 section 2.3.7, there are different approaches on how to enhance the sensitivity of an FBG towards pressure. This project focused on the embedding of an FBG in a polymer patch, which allows the translation of the transverse load into an axial strain. However, the sensitivity of the FBG embedded in a polymer patch is heavily dependent on the physical properties of the patch, such as its shape, dimensions and its mechanical properties such as its Young's modulus. Therefore, in order to achieve the required sensitivity

it is important to optimise the design parameters described above. Hence a mathematical model for the FBG sensor embedded in polymer is very important. The model of the FBG embedded in polymer patch consists of two main calculations. The stress/strain experienced by the FBG due to the transverse pressure is modelled with the aid of a finite element analysis (FEA) software. The stress and strain values are then extracted and imported to Matlab for the transfer matrix formulism. The flow diagram in section 4.3 describes this in detail. There are number of FEA software packages available, such as ANSYS, RFEM, ABAQUS, FreeCAD.

ABAQUS has many advantages over the other FEA packages including its nonlinear performance, contact modelling capabilities, efficient substructures, and extreme deformation simulations [212]. The core foundation of ABAQUS omits linear assumptions and simplification and enables the ABAQUS developers to create much more realistic FEA tools to simulate virtually any form of complex real world physics, for example, the FBG pressure sensor comprised of a polymer patch and an optical fibre. ABAQUS provides the best contact algorithm when handling these different types of contacts between different assemblies. Especially in complex situations such as where the user would not know what kind of contact to be used, ABAQUS will decide the best type of contact by investigating the properties of each assembly.

Thus, with these many advantages, the mathematical modelling of the FBG sensor was developed using ABAQUS/CAE finite element software. The finite element modelling of the sensor consists of several steps.

1. Creation of the parts (fibre, patch and base) and assigning them material properties (Young's modulus, poison ratio, density)
2. Optimising mesh size
3. Creation of assembly and selection of contact algorithm and boundary conditions
4. Selection of geometric non linearity

These steps are described in detail in section 4.2.1

4.2.1. Creation of the parts and selection of material properties

The basic model of the sensor system is comprised of the fibre and a polymer patch. This is shown in figure 4.1. This figure shows the patch with the size of 6mm x 6mm x 1mm. The optical fibre is 8 mm in length.

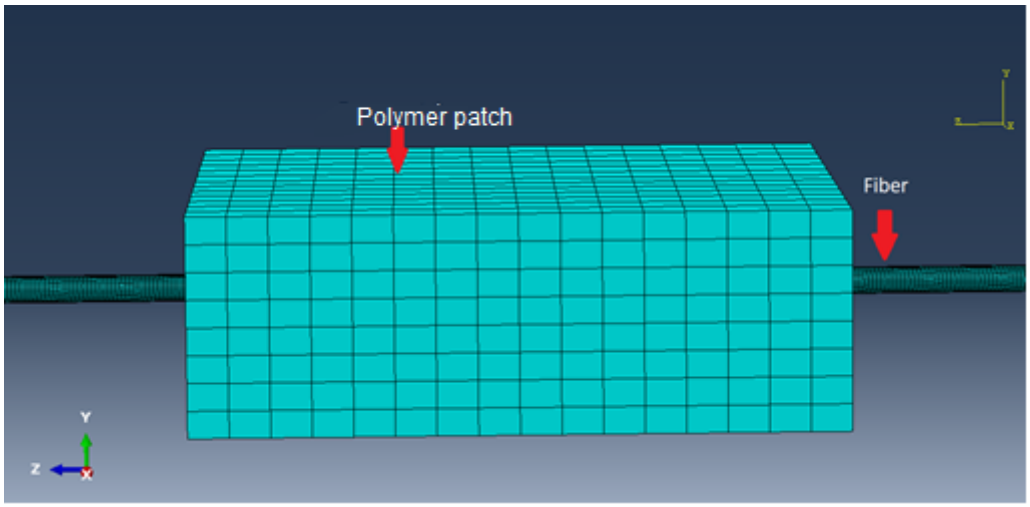

Figure 4.1: Finite Element model of the FBG sensor embedded in 6mmx6mmx1mm cuboid shape patch

Realistically, for compression bandage pressure measurements, the FBG sensor within the patch should be kept between the skin and the bandage layers in order to measure the contact pressure experienced by the skin. Therefore, another part is added to the model which provides the base representing the square block of material. The Young's modulus and Poisson ratio for each part are assigned separately. The fibre is assigned with 72 GPa and Young's modulus of 0.4 [213] as these are the standard values for silica fibre. The values used for each simulation are tabulated separately in the relevant section of the thesis. Figures 4.2 and 4.3 show the cross section of the mesh of the optical fibre and a side view of the meshed model respectively.

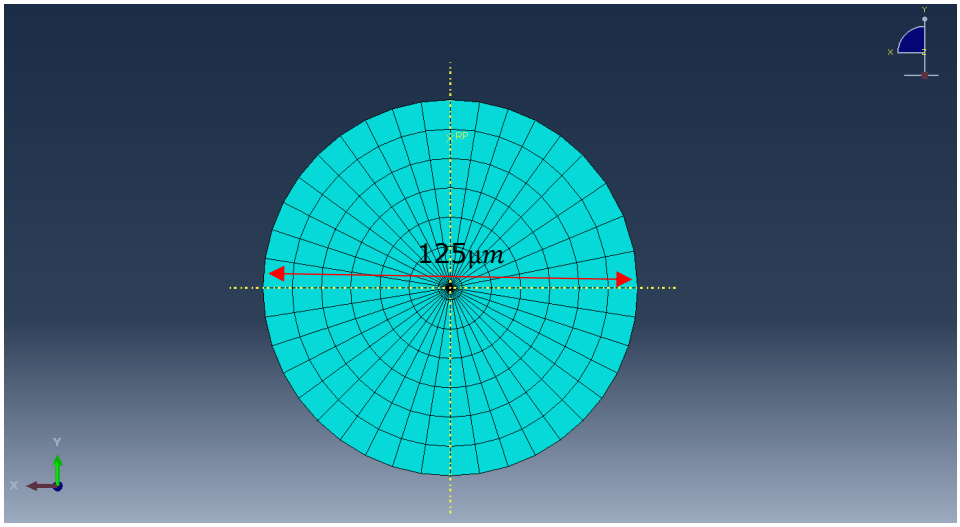

Figure 4.2: Cross section of the FEM mesh of the single mode fibre (diameter 125 μm)

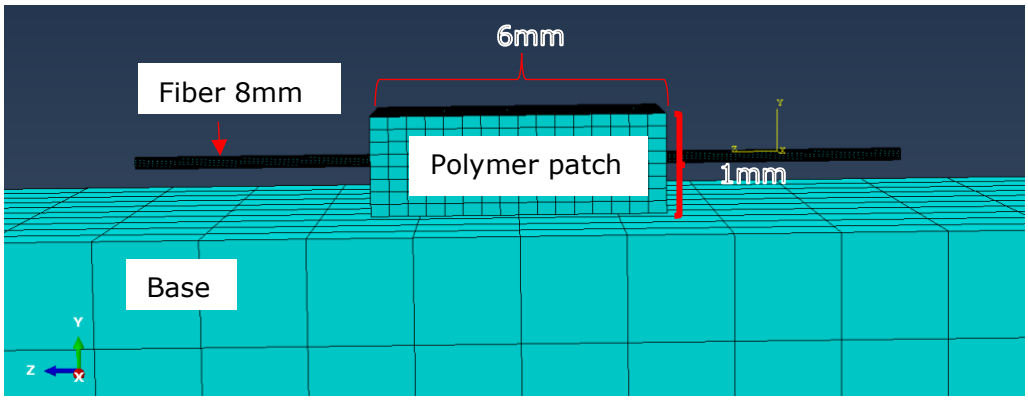

Figure 4.3: FE model of the FBG sensor with a base (polymer patch dimensions 6mmx6mmx1mm)

4.2.2 Optimising mesh parameters of the FBG

The quality of the mesh is very important in finite element analysis to produce accurate results. Mesh density is a significant quantity that is used to control the accuracy. A highly dense mesh will produce more accurate results. However, if a mesh is too dense it may require a large amount of computer memory and long running times, especially in nonlinear analyses. Therefore, it is crucial to select the optimum mesh parameters in order to save the memory and time while producing acceptable, accurate results.

The most common way to evaluate the mesh quality is by mesh refinement and interpretations of results discontinuities. In this method, the mesh is refined until a critical result is achieved. In this situation, the longitudinal strain along

the fibre central axis was observed on a specific location (maximum strain value, at the centre of the fibre) of the FBG until it converged to one value. For a transverse loading of 5MPa, the longitudinal strain was plotted along the axis of the fibre (figure 4.4) for each mesh refinement. Five different mesh sizes were considered. The global sizes of tested meshes are 1 mm, 0.5 mm, 0.1 mm, 0.05 mm and 0.01 mm. The number of total mesh elements are 960, 1920, 9600, 19200 and 128000, respectively.

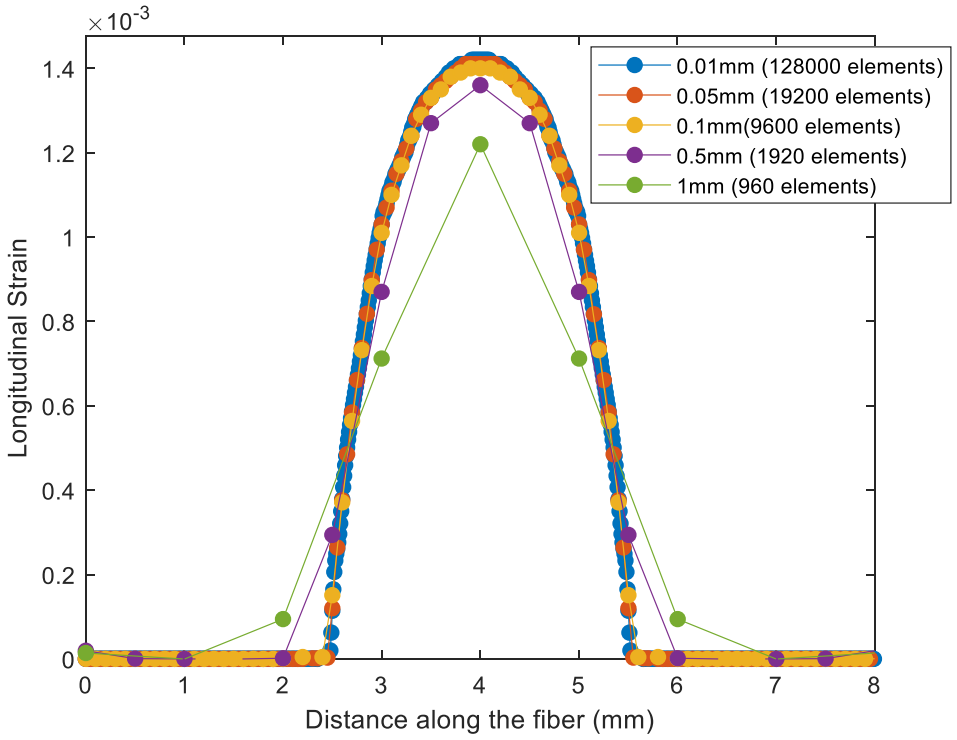

Figure 4.4: Longitudinal strain profile for a transverse loading of 5MPa along the fibre for different mesh profiles

Figure 4.5 shows the longitudinal strain plotted for a specific point (middle of fibre) on the FBG, for the different mesh densities explained above. As the mesh density increases, the longitudinal strain also increases and after 19200 elements mesh density further produces only minor increase (<0.0005) in longitudinal strain. Although it is reasonable to select 19200 elements, the optimum mesh global size was selected as 0.01mm (which is the finest among the meshes,) resulting in a total number of elements of 128000 . The reason to select the 128000 element mesh is that it allows 300 FBG sections, whereas the

19200 element mesh only provides 60 FBG sections for transfer matrix method. The time for a simulation was 20 minutes.

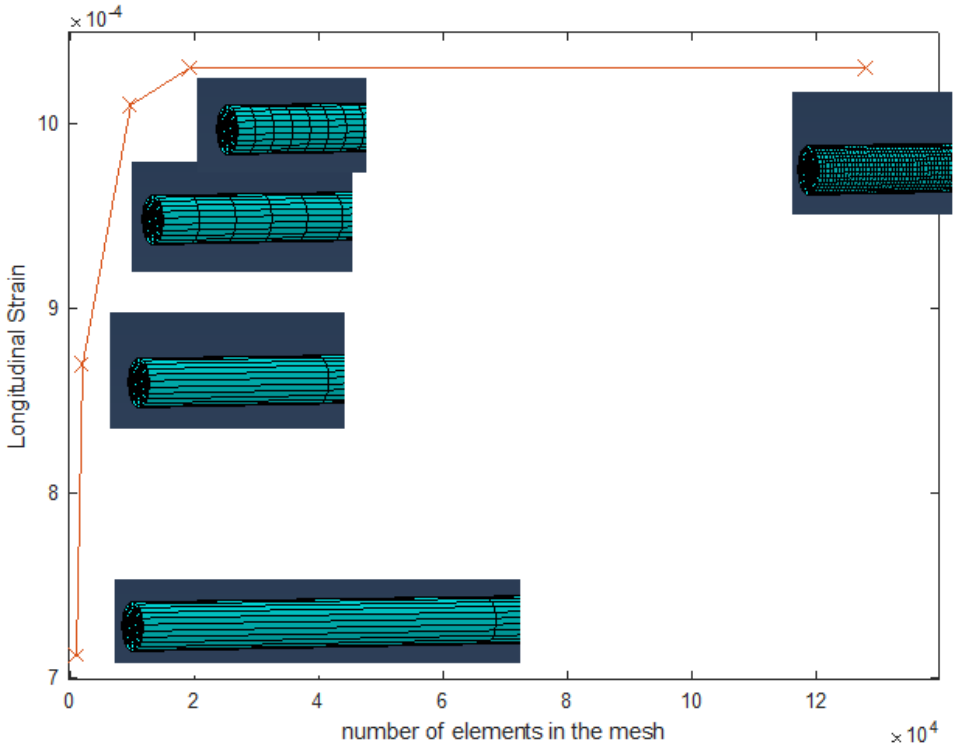

Figure 4.5: Longitudinal strain sensitivity to mesh density

4.2.3. Selection of contact algorithm and interaction properties

In order to make the parts (fibre, patch and base) to contact each other and produce accurate results for the loading conditions, it is important to define the types of interaction between the parts.

ABAQUS provides two different contact algorithms, namely general contact and contact pairs. A contact simulation using contact pairs or general contact is defined by specifying surface definitions, contact interactions, surface properties, contact properties and numerical controls. In many situations, it is not necessary to explicitly specify many of the aspects discussed above and the default settings are appropriate [214].

The general contact and contact pair algorithms' implementations share many underlying algorithms. General contact is a very quick and easy way of creating interactions, especially in complex contact problems. General contact acts as a

one single interaction, assuming that any surface can interact with any surface of the model. General contact uses tracking algorithms to ensure that contact conditions are effectively met. Additionally, this method can be used on both rigid and deformable bodies.

Considering all the advantages discussed above, in the finite element modelling reported in the thesis, the general contact algorithm was utilised for its convenience and accuracy.

It is expected that, in reality, there will be adhesive type bonding between the fibre and the patch. Therefore, a tie constraint was introduced between the outer surface of the fibre and the inner surface of the patch. The tie constraint will tie the outer surface of the fibre and the inner surface of the patch together so that there is no relative motion between them.

For the interaction between the polymer patch's bottom surface and the top surface of the base, tangential behaviour was selected with a friction penalty. This is because it is believed the surfaces are not perfectly smooth and a non zero friction coefficient exists between the patch and the base.

4.2.4 Extraction of stress and strain data to a text file

Abaqus generated stress and strain values along the fibre for each trasverse load are written to the text files for each FEM simulation as shown in figure 4.6. These files are later imported to MATLAB for the transfer matrix formulism.

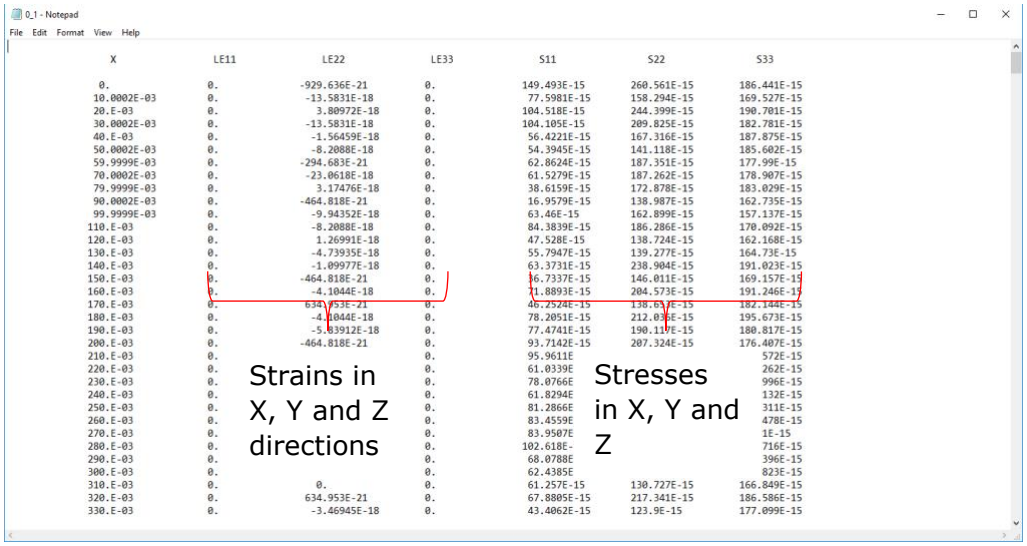

Figure 4.6: stress/strain file generated using LabVIEW, this contains three columns for stresses in X, Y and Z directions and three columns for strain in X, Y and Z direction

4.3 The FBG simulation algorithm structure

Figure 4.7 illustrates the flow chart of the algorithm structure used to simulate the FBG response. The detailed mathematical derivations are explained in chapter 2 section 2.3

When birefringence is present due to the transverse stresses, the FBG reflection spectrum presents two separate peaks and the total reflectance is calculated using the formula 2.37 given in chapter 2.

As is described in chapter 2 section 2.3.2, the number of sections (i.e. the number of uniform sections the FBG is divided into) used for the T-matrix calculations depends on the number of elements which was predefined in the mathematical FE model. Since the element size of the mesh was 0.01mm, the number of elements contains the FBG is equal to 300 elements (for a 3 mm long FBG). Hence the number of sections used for the t-matrix calculations is 300.

Table 4.1 shows the input parameters used for the T-matrix calculations.

Table 4.1: Input parameters for T-matrix calculations

Parameter	Value
Axes	x axis- direction perpendicular to transverse load y axis- direction transverse load applies z axis- fibre central axis
FBG length	3 mm
Design wavelength / Un-deformed wavelength	1534.75 nm
Initial effective refractive index	1.482[215]
Bandwidth limits	1530 -1550 nm
Resolution	1500 points
Strain optic tensor coefficients	P11 = 0.113 P12= 0.252
Poisson ratio of fibre	0.17[216]
Young's Modulus of fibre	75E9 Pa
Peak value of the dc effective index of refraction	2.5E-4[144]
Number of sections for T-matrix calculations	300
Power coupling coefficients	Px= 0.85[43] Py=0.15

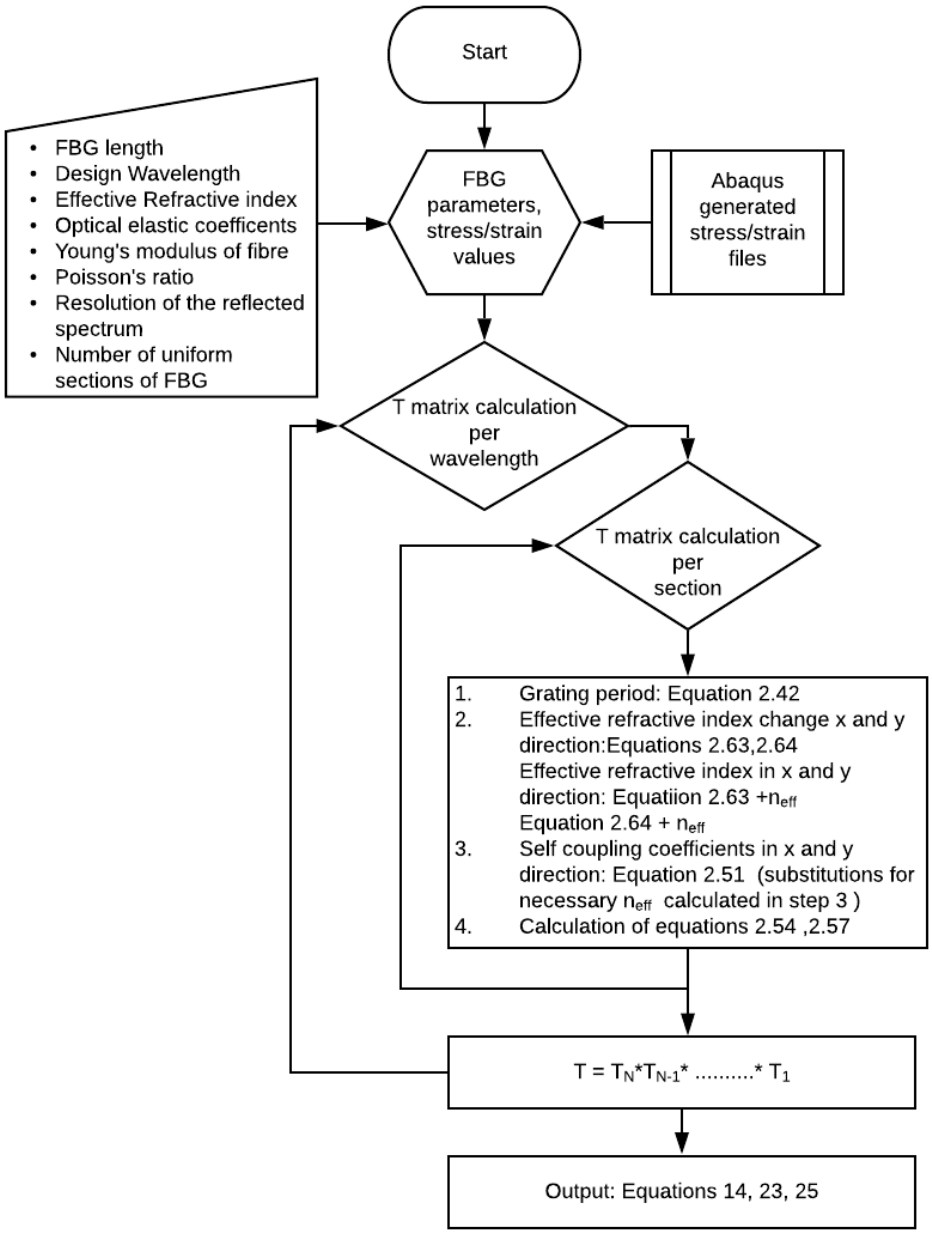

Figure 4.7: Flow diagram of the algorithm structure used to simulate the FBG response

4.4 Model validation based on previous experimental and simulation results

4.4.1 Simulated results obtained for longitudinal strain of a bare FBG

The first simulation was conducted for longitudinal strain applied to a bare 3mm long FBG. A typical germanosilicate fibre exhibits a 1.2 pm wavelength shift at 1550nm in the centre wavelength of a grating per applied $1\mu\varepsilon$ [141].

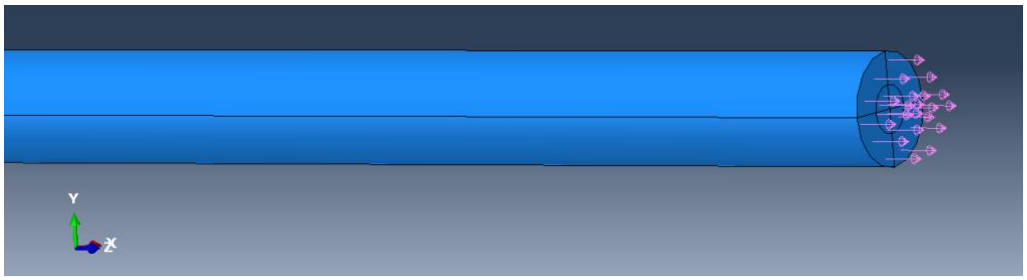

Figure 4.8: Application of longitudinal strain to the FBG (3 mm long), arrows representing longitudinal tensile forces acting on the fibre

Figure 4.8 shows the FE model of application of longitudinal strain to the FBG, while figure 4.9 illustrates the strain experienced by the FBG due to the applied longitudinal force.

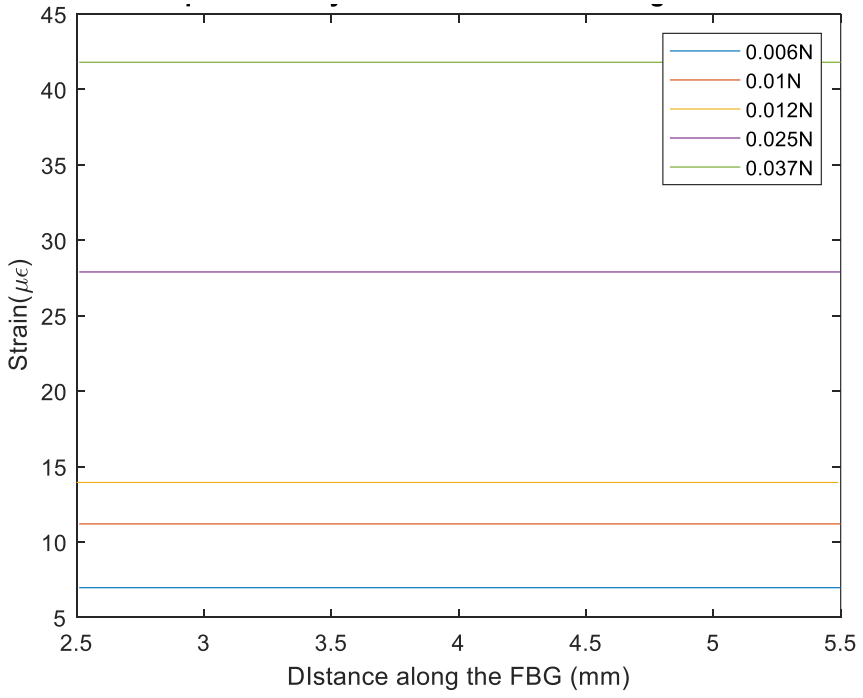

Figure 4.9: Strain experienced by the FBG for different longitudinal strain values

Figure 4.10 illustrates the simulated FBG reflection spectra for different longitudinal strain conditions. The calculated wavelength shift with respect to the unstrained conditions is plotted in figure 4.11. According to the figure 4.11, the strain sensitivity of the FBG is 1.2 pm/$\mu\varepsilon$, which agrees well with the theoretical value given in the literature [141].

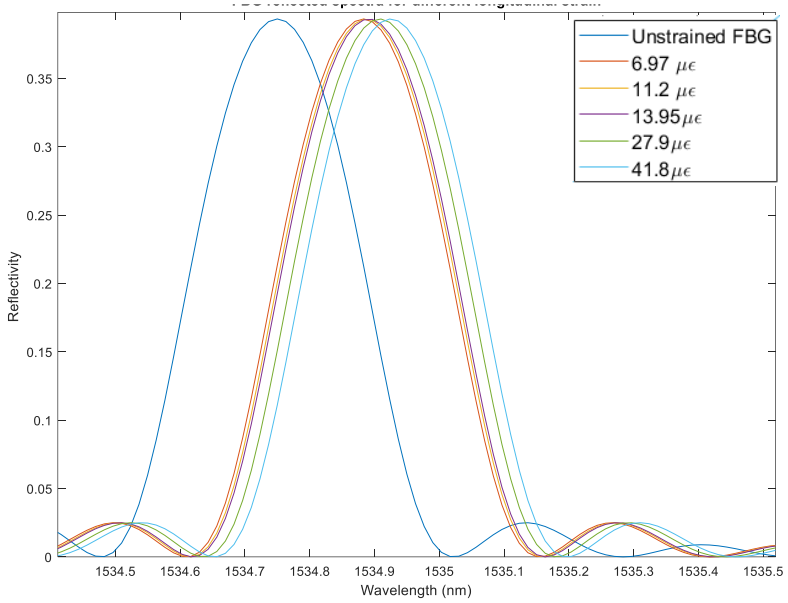

Figure 4.10: FE Simulated FBG reflection spectra for different applied longitudinal strain

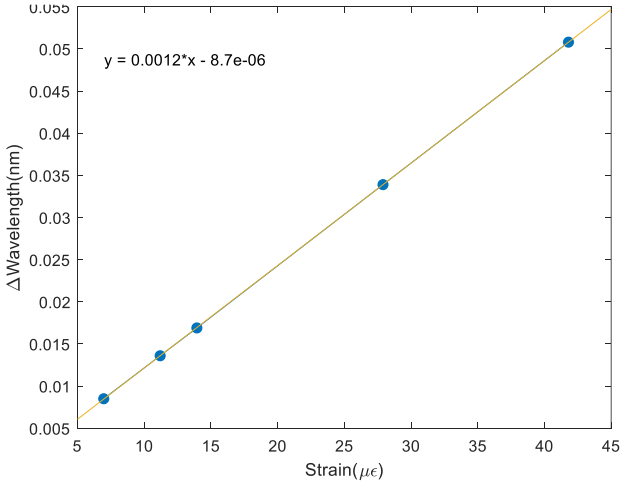

Figure 4.11: Simulated Bragg wavelength shift plotted as a function of longitudinal strain

4.4.2 Simulated results of bare FBG to transverse loading

The objective of this section of the thesis is to reproduce results reported in [217] to validate the mathematical FBG model. In their work they have presented the numerical and experimental results of a single mode fibre experiencing a diametric loading. The FEA model used for the simulations is shown in figure 4.12. In the model, the bottom surface of the FBG is fixed while the transverse line load is applied to the FBG as indicated by pink arrows in figure 4.12. The load is applied as load per length (N/mm). The length of the FBG is assumed to be 6mm and the design wavelength of the FBG is 1550 nm.

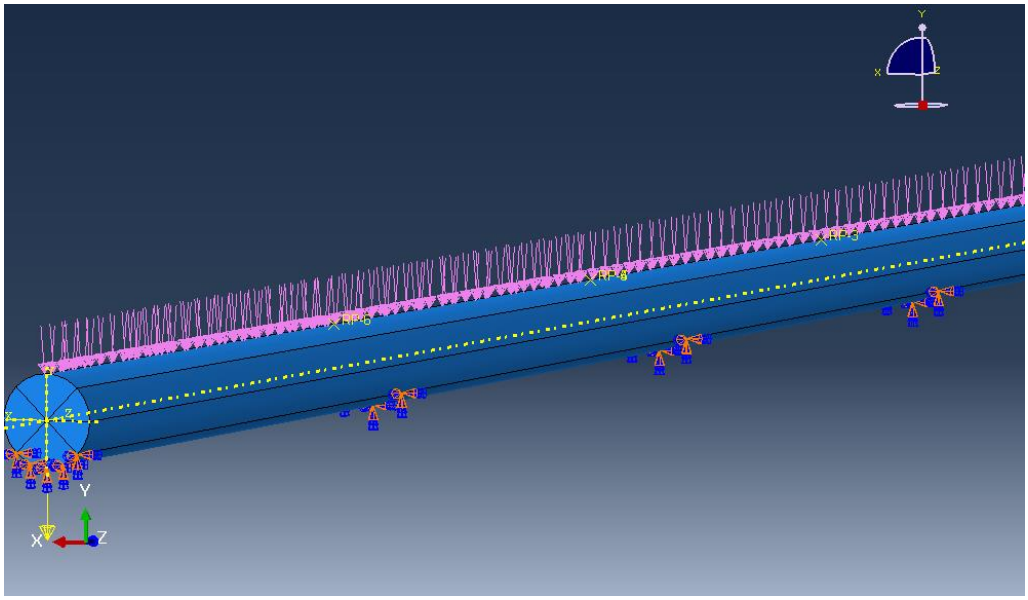

Figure 4.12: FE model for the transverse loading of a 6mm long FBG is (pink arrows indicate transverse load applied to the fibre. Boundary conditions applied to the bottom surface)

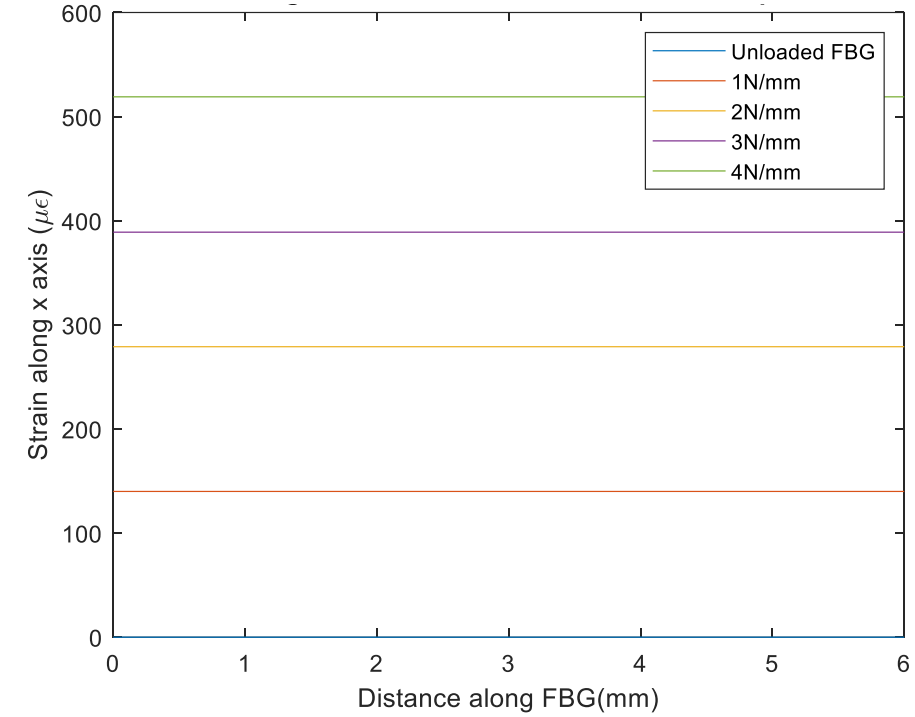

Figure 4.13: Strain experienced by the FBG along the x axis during transverse loading along z axis

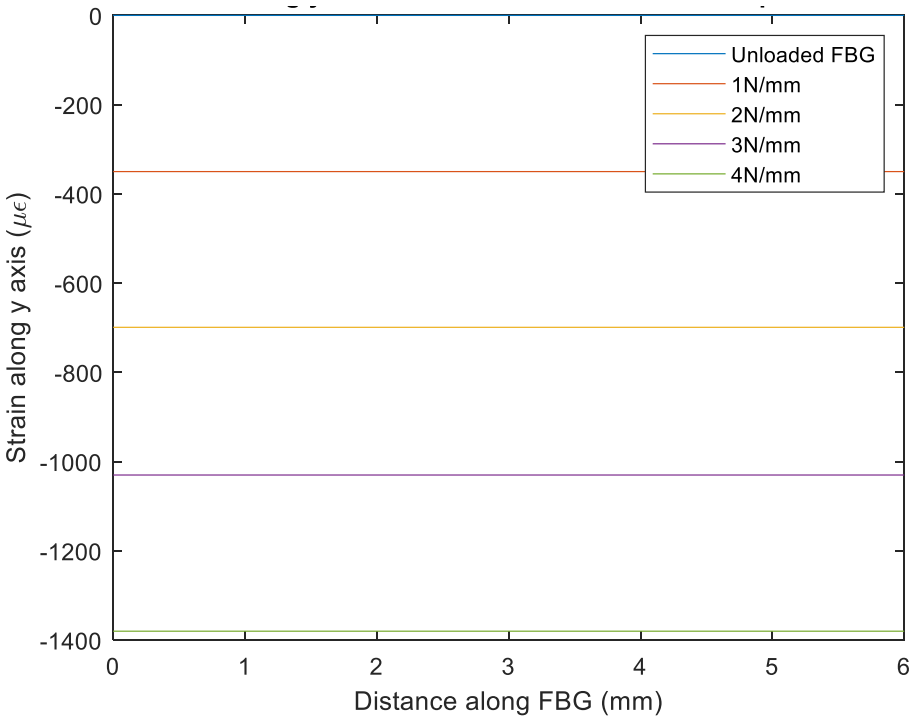

Figure 4.14: Strain experienced by the FBG along the y axis during transverse loading along z axis

Figures 4.13 and 4.14 illustrate the results of the simulation of the strain experienced by the FBG along the x-axis and y-axis, respectively, where the transverse load is applied along the y-axis. Figure 4.15 and figure 4.16 show the

spectral response for x and y direction, respectively. The wavelength shift of the FBG peak in the x-direction is more pronounced than in the y-direction. This is illustrated in figure 4.17.

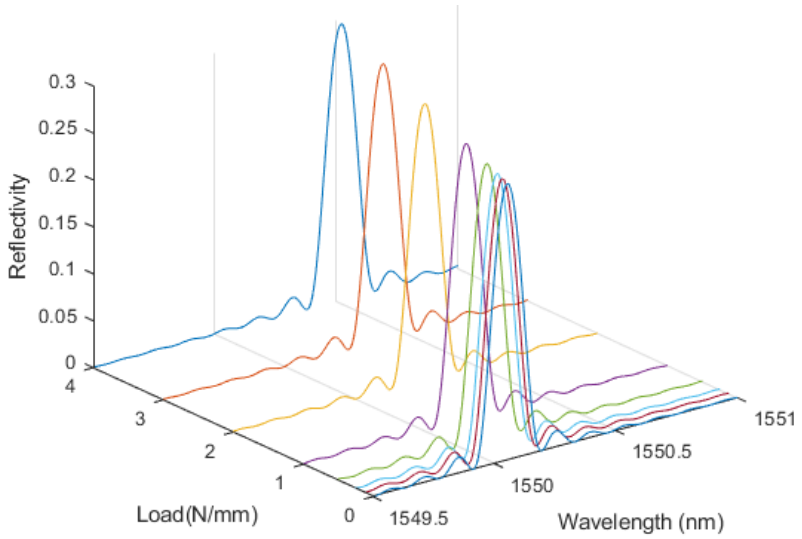

Figure 4.15: Evolution of the central wavelength of the FBG peak in x-direction for different transverse compression loading (N/mm) along z axis

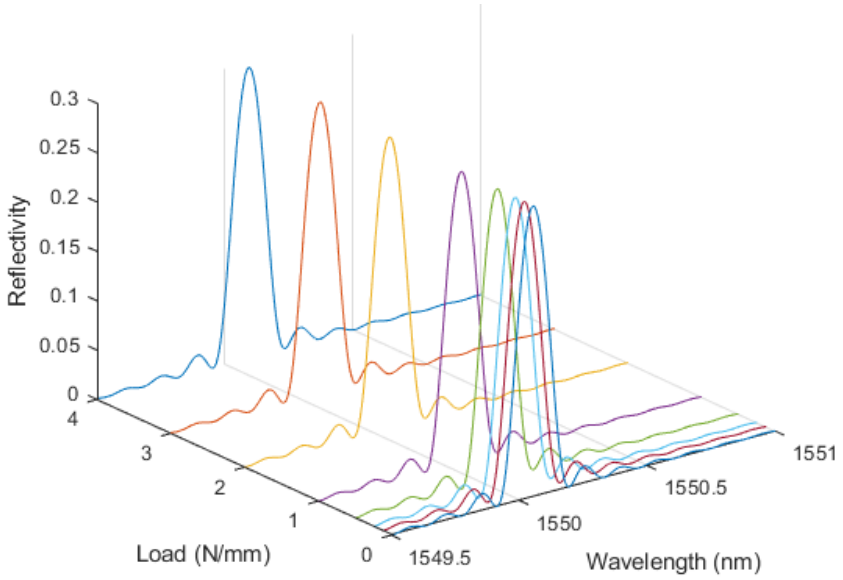

Figure 4.16: Evolution of central the wavelength of the FBG peak in y-direction for different transverse compression loading (N/mm) along z axis

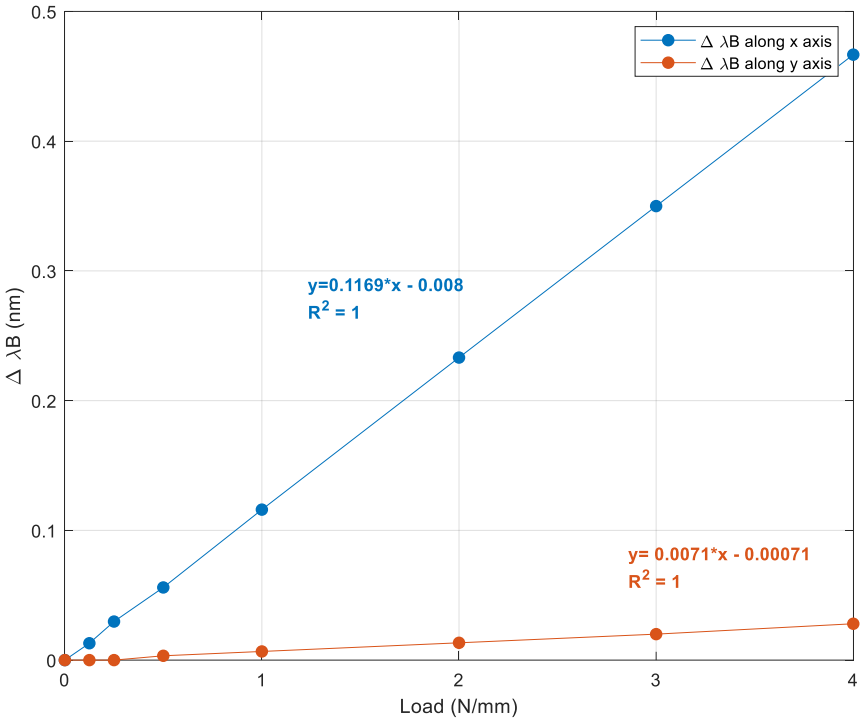

Figure 4.17: Graph of wavelength shift along x axis and y axis as a function of transverse load along z axis

A wavelength sensitivity of 0.116 nm/(Nmm^{-1}) is observed along the x-direction and a wavelength sensitivity of 0.0071 nm/(Nmm^{-1}) is observed along the y-direction. These results agree well with the results obtained by [217]. In Bosia's work the experimentally observed sensitivity along the x-axis is 0.1 nm/(Nmm^{-1}) and along the y-axis all the experimental data lies below 0.1nm. This shows the simulated results compare well with Bosia's experimental results.

4.4.3 Results obtained for the locally embedded FBG with polymer patch to transverse loading

The objective of this section of the thesis is to reproduce the experimental results reported in [175] to validate the mathematical FBG model. Correia R. et al. [175] reported the enhanced sensitivity of an FBG load sensor based on a subsection of a FBG embedded in a polymer resin. A 2mm long central section of the FBG is embedded within a 2mm x 2mm x 2mm polymer resin cube of a 6mm long FBG inscribed in a single mode fibre (figure 4.18). When the polymer cube is transversely loaded, it deforms and transfers the applied load as an axial

strain on to the fibre. Hence, a periodicity change is induced at the central section of the FBG. This will result in a phase defect in the FBG structure and hence a spectral dropout in the reflection spectra which is linearly dependent on the applied transverse load. Two resonant features (spectral holes) have been obtained and the experimentally determined sensitivity for the first and second order resonances were $2.93\pm0.01\times10^{-2}$ nmN^{-1} and $2.82\pm0.05\times10^{-2}$ nmN^{-1}.

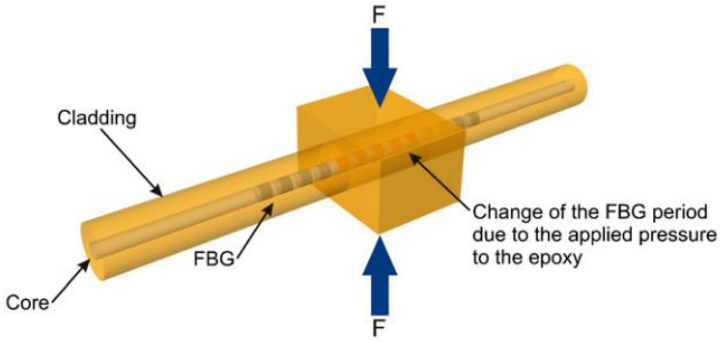

Figure 4.18: FBG embedded with polymer [175]

Rouard's method was used for the simulations and a uniform stress/strain distribution was assumed within the polymer patch. General hydrostatic stress-strain relationships were adopted and non-linearity and shear stresses were not taken into account.

4.4.3.1 Strain transfer efficiency and strain behaviour along the fibre axis for embedded FBGs

When the FBG is embedded in other materials the axial strain profile experienced by the FBG is heavily dependent on the efficiency of the strain transfer from the embedding material to the FBG [218]–[221]. During strain measurements in structural health monitoring and related civil engineering applications, FBGs are bonded to the measured structure directly or encapsulated into structures with adhesives. Therefore the accuracy of the strain measured is dependent on the bonding characteristics. As per Newton's third law, when strain in the host material causes deformations in the interlayer, the interlayer reacts, causing an opposite deformation in the host

material [222]. Due to the differences in the physical and mechanical properties of the embedded material, the strain transferred to the axis of the FBG is not always a uniform distribution. Ansari et al. [223] describe a theoretical model to investigate the actual strain transferred to the optical fibre. According to the results, strain transfer is highly dependent on the mechanical properties of a fibres' protective coating and bonded length. Zhou J et al. [218] reported a finite element method that investigated the strain transfer characteristics of FBG sensors. The axial strain distribution of each different outer layer of the fibre sensor has been studied along with the effects of Young's modulus of the adhesive, the bonding length and the thickness of the adhesive. The findings show that the axial strain experienced by the FBG is non uniform and the highest strain is experienced at the centre of the bonding. The strain gradually decreases to zero towards the furthest end of the bond.

The strain transfer rate from the bonding position can be defined as the ratio of the FBG sensor measured strain to the actual strain of the position and can be expressed as in equation 4.1 [219],[222],[224].

$$\alpha\,(x) = 1 - \frac{cosh(kx)}{cosh(kL)} \qquad (4.\ 1)$$

Where k is the shearing stress parameter which depends on the fibre's Young's modulus, the interlayer and host materials' shear moduli and the radius of the fibre, interlayer, and host material. 'x' is the position along the bonded length (x=0 at the midpoint of the bonding length), 'L' is the bonding length. According to equation 4.1 the maximum strain transfer is achieved when x=0. This is due to the symmetrical nature of the structure. Since the fibre is free from the axial stresses at both ends of the bonding, the strain transferred to the fibre goes to zero.

Moreover, as the bonded length increases, the strain transfer efficiency and the ratio of effective sensing length increases. As the stiffness of the adhesive increases, the sensing length also increases. These findings are illustrated in Figure 4.19.

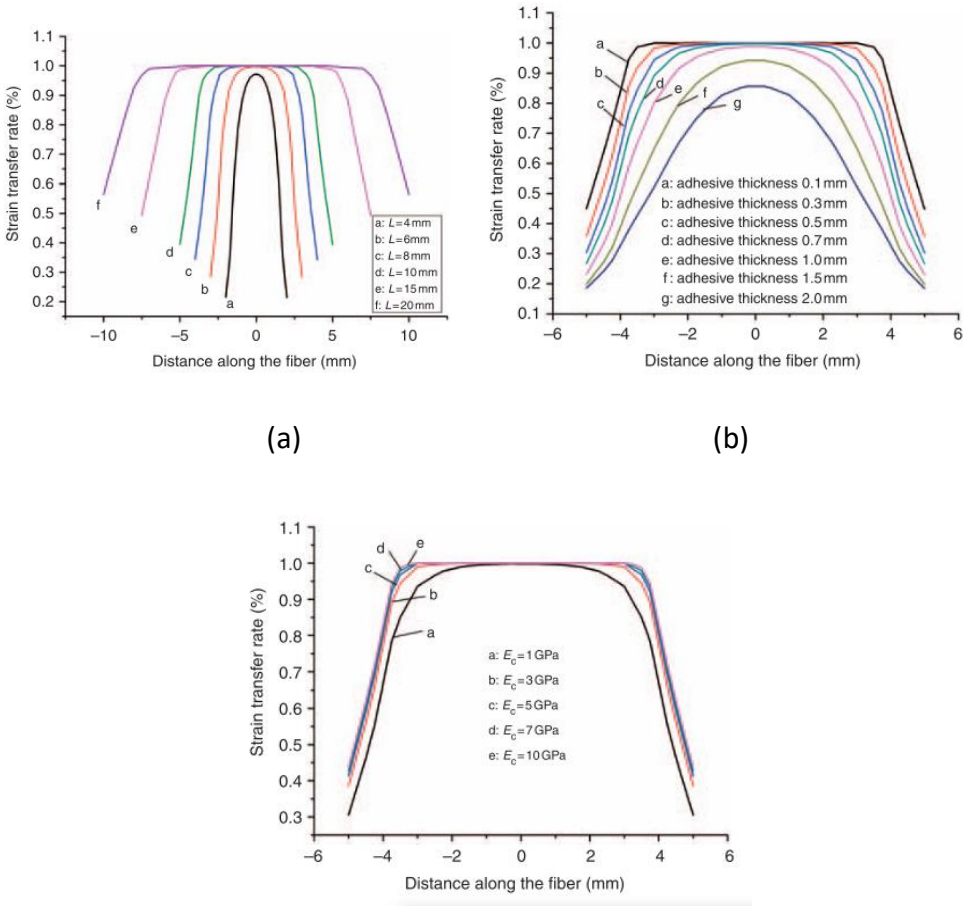

(a) (b)

(c)

Figure 4.19: Fibre axial strain profile along the length of the FBG (a) The strain transfer rate for different lengths of bonding (b)The strain transfer rate for different adhesive thickness (c)The strain transfer rate against different Young's modulus values of adhesives [218]

This behaviour of non-uniformity was observed in the simulations conducted in this project with FBGs embedded into polymer patches. Figure 4.20 shows the simulated axial stress experienced by an FBG of 6mm long embedded within the polymer patch of 2mm x 2mm x 2mm at the centre for a 14N load. At the centre of the fibre, more stress is experienced as discussed above. The strain experienced by the FBG embedded into the patch to different transverse loading is shown in Figure 4.21. As discussed above, at the centre of the FBG the maximum strain is observed. As the distance increases towards the end of the polymer patch the strain decreases gradually and reaches to zero at the two extremes of the polymer patch which is located at the 2mm and 4mm positions on the graph.

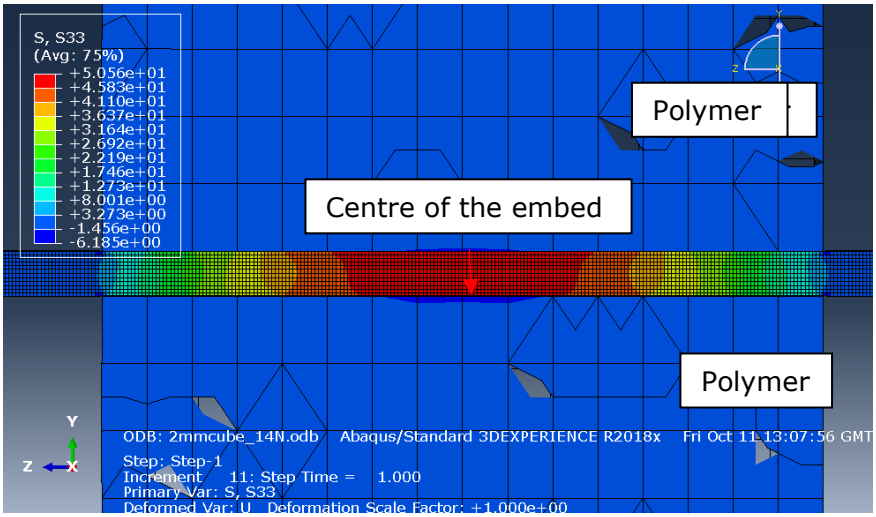

Figure 4.20: Axial stress profile along the length of the FBG

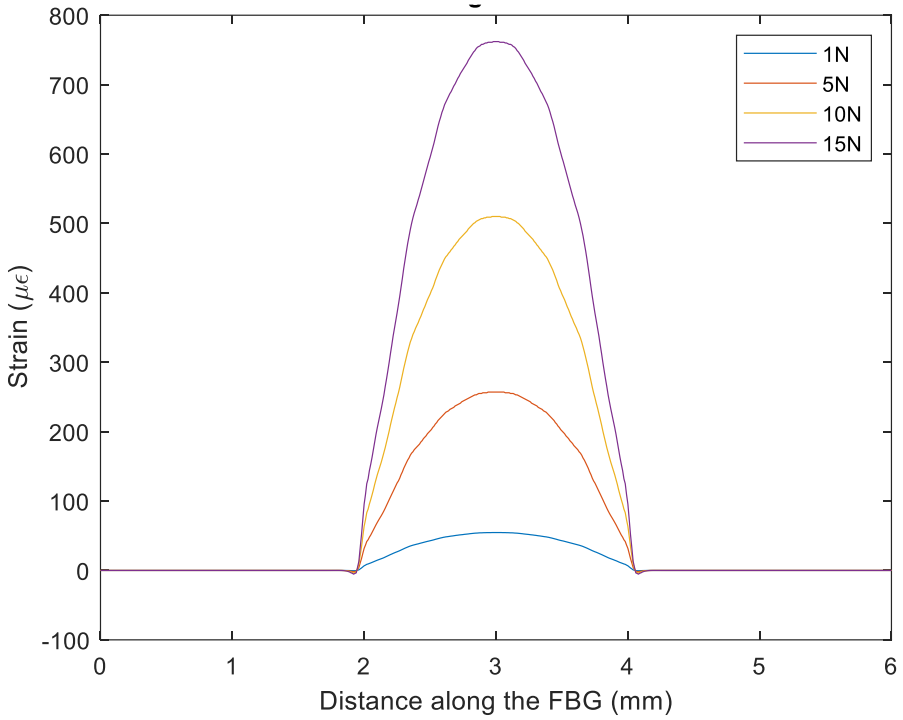

Figure 4.21: FE simulated axial strain along the distance of the FBG for different transverse loading conditions, FBG length is 6mm, cuboid patch 2mmx2mmx2mm

4.4.3.2 Analysis of spectral hole sensitivity of first and second order resonance to transverse loading

This section describes the results based on the simulations done for the FBG of 6mm, centrally embed in a polymer patch of 2mm x 2mm x 2mm. The parameters used for the mathematical modelling are described in table 4.2.

These values agree with the experimental and simulation results described in the paper [175].

Table 4.2: Parameters for the mathematical simulation

Parameter	Value
FBG length	6 mm
Design wavelength / Un-deformed wavelength	1553.1 nm
Initial effective refractive index	1.4465
Bandwidth limits	1548.1 -1558.1 nm
Resolution	1500 points
Strain optic tensor coefficients	P11 = 0.121 P12= 0.27
Poisson ratio of fibre	0.17
Young's Modulus of fibre	71.7E9 Pa
Young's Modulus of Polymer	689 MPa
Poisson ratio of Polymer	0.4
Peak value of the dc effective index of refraction	5E-5
Number of sections for T-matrix calculations	600
Power coupling coefficients	Px= 0.85 Py=0.15

Figure 4.22 shows the finite element model used for the simulations. As can be seen the fibre embedded with the polymer is sandwiched between two steel blocks. In this way, the transverse load can be applied uniformly to the patch. The uniform load is applied to the top surface of the top block as a distributed pressure load. The bottom surface of the bottom steel block is fixed. In this way the rotational and translational degrees of freedom are constrained for the bottom surface of the bottom steel block. A tie constraint has been used at the interface of the polymer block and the fibre.

The mesh of the FE model is shown in Figure 4.23.

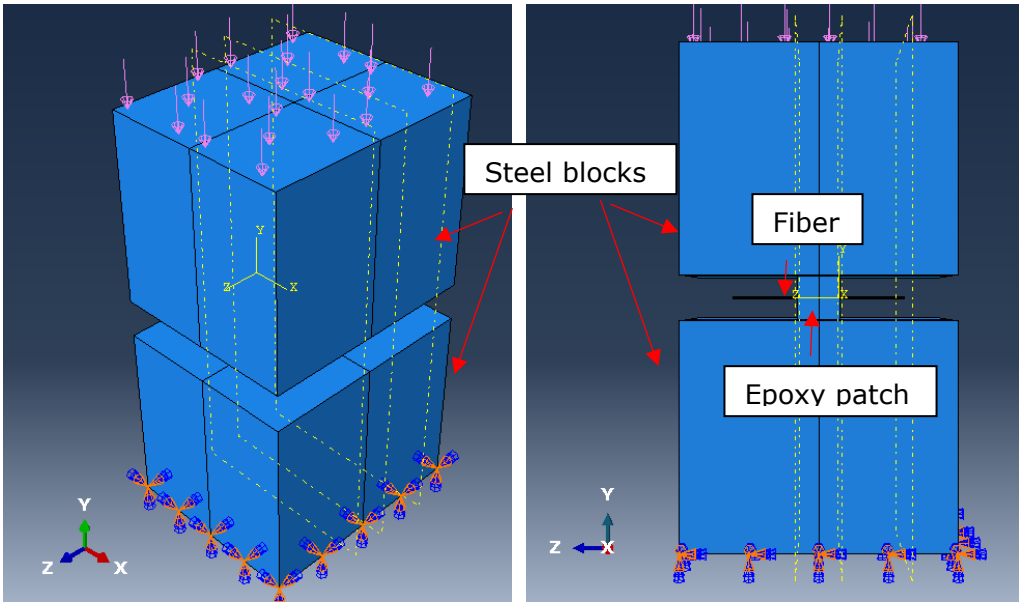

Figure 4.22: (a) Overview model (b) Side view of the model

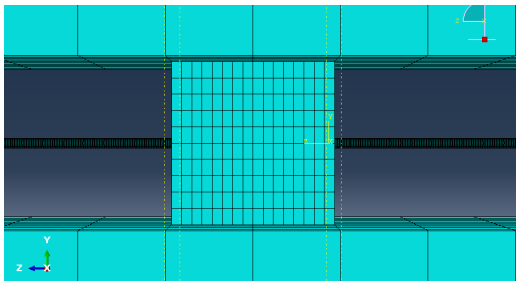

Figure 4.23: Mesh of the FEA model of the FBG embedded in polymer patch

Figure 4.24 depicts the evolution of the reflection spectrum of the FBG sensor. As it was observed experimentally in reference [175] two resonance features can be observed within the bandwidth of the reflection spectra.

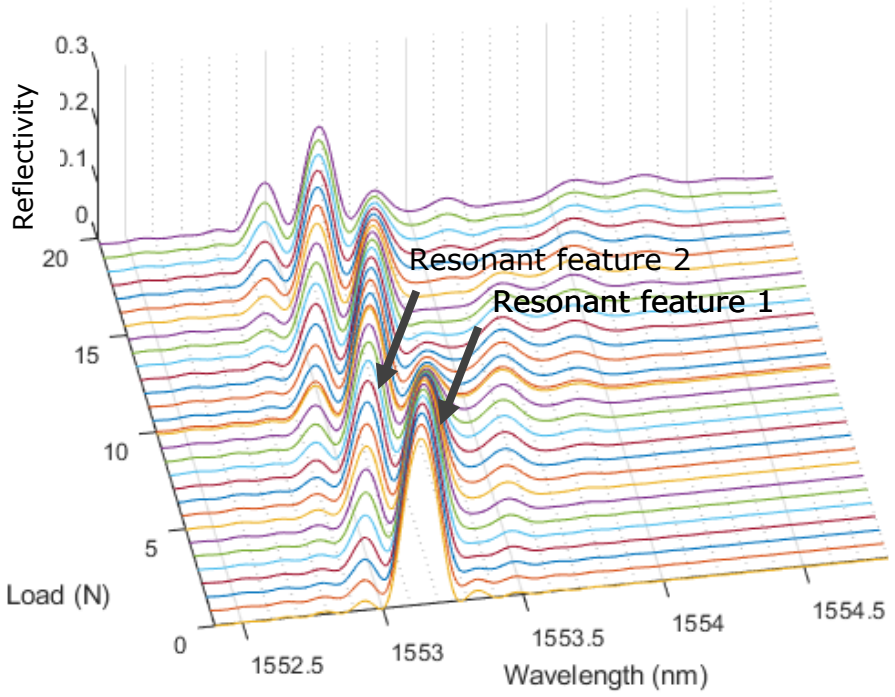

Figure 4.24: Evolution of the simulated reflection spectra (reproducing [175]*) of the FBG 6mm long embed with polymer 2mmx2mmx2mm cube at the centre under uniform transverse load*

Figure 4.25 shows the wavelength sensitivity of the first and second order resonance features, revealing that they show sensitivities of 2.88 $x10^{-2}$ nmN^{-1} and 2.78 $x10^{-2}$ nmN^{-1} respectively, which agree well with the experimental results obtained by Correia R. et al.

The absolute wavelength obtained in this work is very similar to the experimentally observed results [175]. The reflection spectrum obtained by the model is similar to the experimentally obtained reflection spectra discussed in the paper including the first and second order resonance features developed during the application of transverse load. This is because in this work the non uniform strain distribution along the fibre central axis (Z axis) was considered rather than taking the average strain. Thus, the developed mathematical model for the FBG simulation has a good agreement with the real world experimental results.

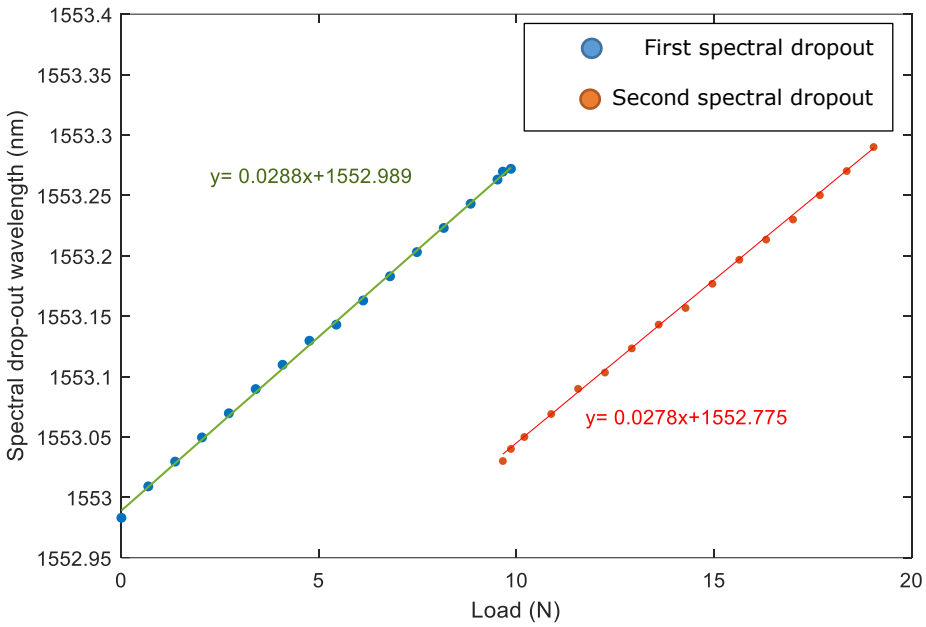

Figure 4.25: Dependence of simulated the central wavelengths of the first and second spectral dropout to the applied transverse load

4.5 Experimental validation of the results obtained for the mathematical modelling of the FBG of 6mmx6mmx1mm cuboid patch

This section describes an experimental validation of the simulated results obtained for an FBG of 3mm length embeded in a cuboid shaped polymer patch with dimensions of 6mm x 6mm x 1mm. The sensor configuration is shown in Figure 4.26. The FBG is assumed to be located at the centre of the polymer patch *i.e.* the FBG starts at position 2.5mm up to 5.5mm along the z axis of the fibre. Figure 4.27 shows the FEA model used for the simulations. The material properties of the polymer are selected for considering the data sheet for Loctite AA 3926 as this was used as the polymer material throughout the experimental validation. Parameters used for the simulations are listed in table 4.3.

Table 4.3: Material properties for the FEA model

Parameter	Value
FBG length	3 mm
Design wavelength / Un-deformed wavelength	1549.1 nm
Initial effective refractive index	1.4465
Bandwidth limits	1539.1 -1559.1 nm
Resolution	1500
Strain optic tensor coefficients	P11 = 0.121 P12= 0.27
Poisson ratio of fibre	0.17
Young's Modulus of fibre	71.7E9 Pa
Young's Modulus of Polymer	143MPa
Poisson ratio of Polymer	0.4
Peak value of the dc effective index of refraction	5E-5
Number of sections for T-matrix calculations	300
Power coupling coefficients	Px= 0.85 Py=0.15

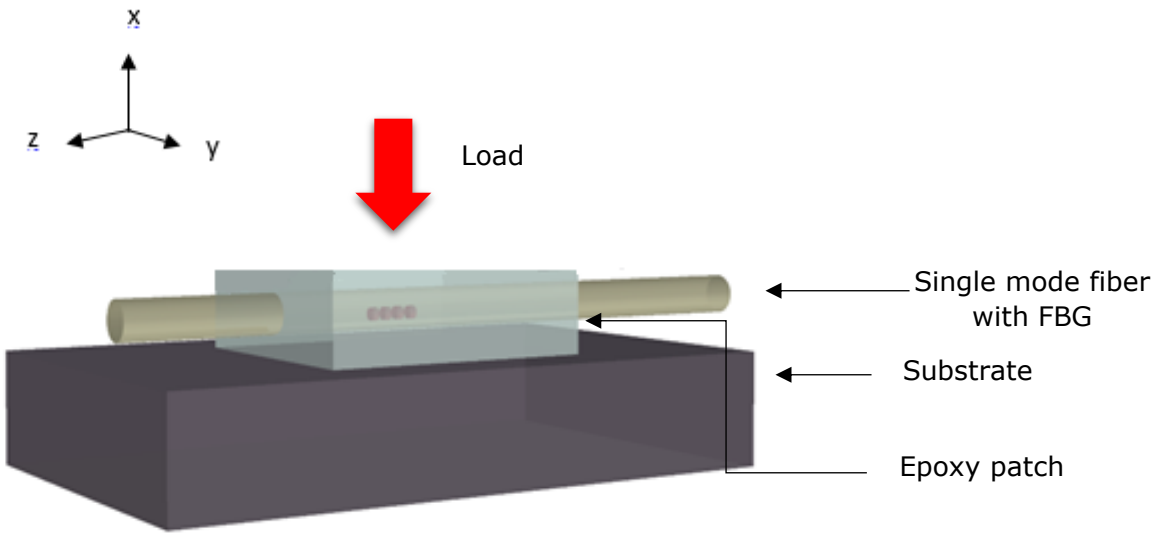

Figure 4.26: An FBG ebedded in a cuboid 6mmx6mmx1mm polymer patch

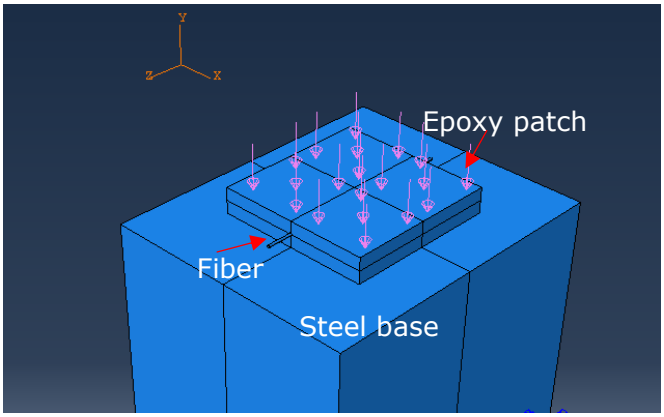

Figure 4.27: FEA model of an FBG with cuboid polymer patch (6mmx6mmx1mm)

4.5.1 The behaviour of the axial strain of the 6mmx6mmx1mm patch to the uniform transverse loading

As explained in section 4.4.3.1, the strain transfer to the optical fibre is heavily dependent on the mechanical and physical properties, such as shape, size and Young's modulus of the embedding material. The centre of the embedded section of the fibre experiences the maximum strain transfer from the embedding material. It is therefore important to position the FBG at the centre of the polymer patch to achieve a maximum strain transfer. Moreover, it is important to increase the length of the patch with respect to the FBG in order to obtain a maximum strain transfer between the polymer patch and the FBG. Consequently, it is expected to observe uniform and maximum strain transfer along the axis of the fibre by doubling the length of the polymer patch (6mm long) for the 3mm long FBG. The simulated strain distribution for the sensor for different transverse loading is plotted in figure 4.28.

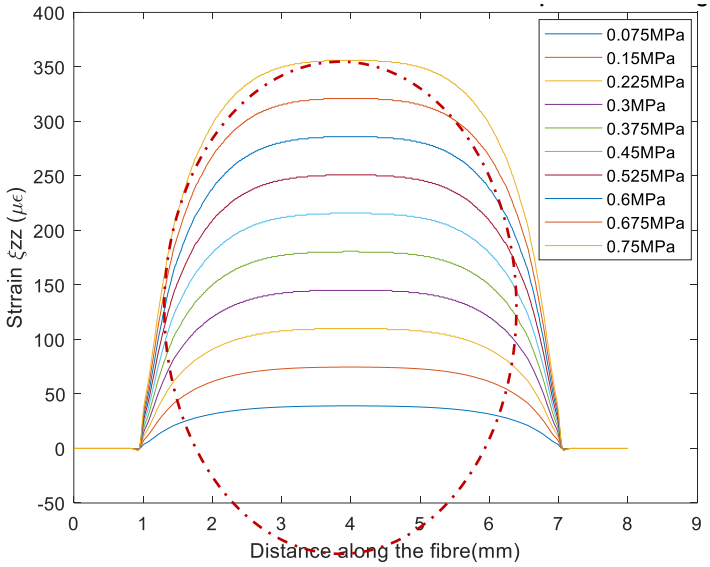

Figure 4.28: The strain transferred to the axis of the fibre from the uniform transverse loading plotted over the distance along the fibre. The FBG located between 2.5mm to 5.5mm section. This is indicated by a dashed circle.

The polymer patch lies in the 1mm to 7mm range along the z-axis of the graph and the FBG lies between 2.5mm and 5.5mm. As expected, the strain transfer efficiency and the uniformity have been increased by increasing the length of the polymer patch when compared to the strain experienced by the 2mm x 2mm x 2mm polymer patch described in section 4.4.3.1, figure 4.21. Figure 4.29 shows the axial strain plotted along the FBG length. Across the FBG region, a more uniform strain distribution has been observed compared to figure 4.21 for the 2mm x 2mm x 2mm square cube patch.

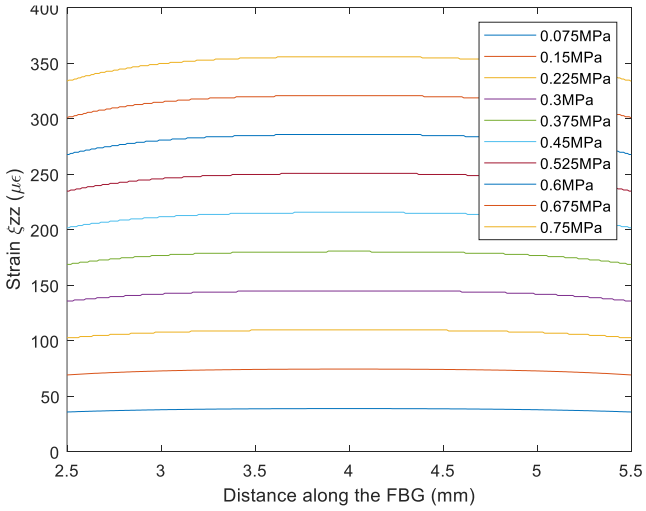

Figure 4.29: The strain experienced by the FBG is plotted along the length of the FBG

Figure 4.30 shows the evolution of the simulated reflection spectrum to uniform transverse pressure loading. The Bragg peak suffers a red shift with increasing transverse pressure load. The Bragg wavelength shift is plotted against the transverse pressure load and illustrated in figure 4.31. The simulated Bragg wavelength sensitivity of the sensor to the applied pressure is 0.565 nm/MPa. High positive linearity is observed with a correlation coefficient of 1. The next section of the thesis discusses the experimental validation of these simulation results.

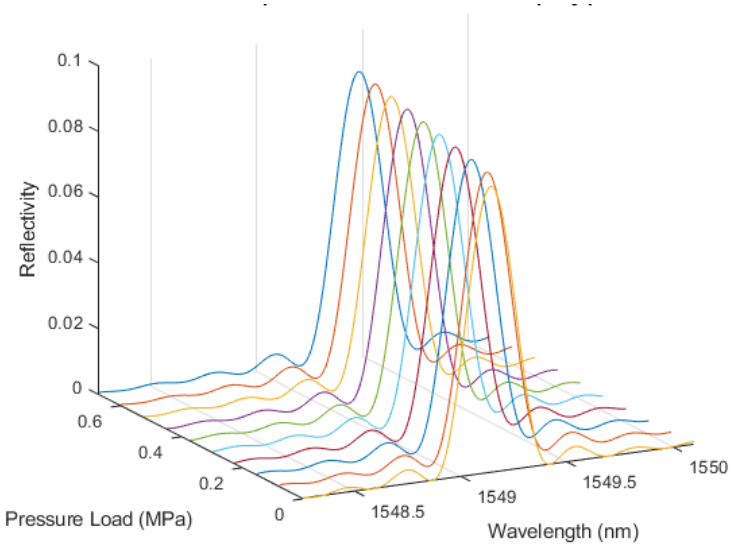

Figure 4.12: Evolution of the reflection spectra of the FBG (3mm) embedded in the centre of the cuboid 6mmx6mmx1mm patch

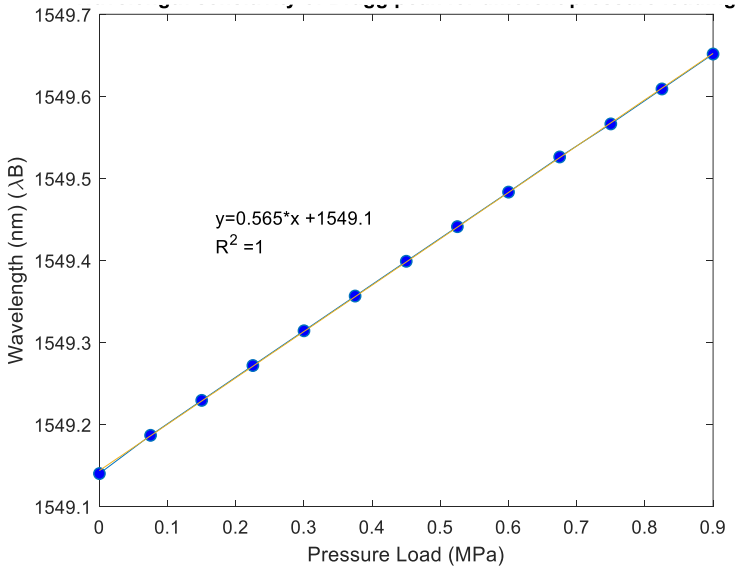

Figure 4.31: Simulated Bragg wavelength as a function of applied pressure

4.5.2 Experimental validation of the simulated results for the polymer patch of 6mm x 6mm x 1mm patch

The experimental validation setup consists of a customized cantilever which was built to apply a weight load to the FBG embedded in a polymer patch. The setup is illustrated in figure 4.32. The FBG is connected to an FBG interrogator, SmartScan, from Smart Fibres Ltd, Bracknell, UK. The interrogator can be controlled by the user interface software provided by the company. A load cell was placed under the FBG to monitor the pressure applied to the FBG. The signal of the load cell was amplified by an instrumentation amplifier and then converted to a digital signal. At the far free end of the cantilever, an empty bottle, connected with a water pump is placed. Load is applied to the FBG by adding water into the bottle using an Arduino controlled water pump. Load is applied to the sensor in 50ml steps, which corresponds to 50mg of weight increment. The data from the interrogator and the data from the load cell are recorded simultaneously. The whole measurement procedure was repeated three times. The voltage values obtained by the load cell were converted to load based on the calibration of the load cell.

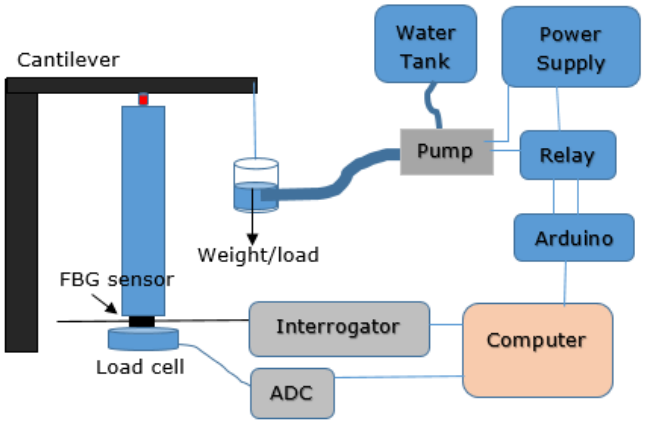

Figure 4.32: Experimental setup for the characterisation of the transverse load response of an FBG embedded in polymer patch

4.5.3 Embedment of the FBG in the polymer patch

Figure 4.33 (a) shows a picture of the mould used to fabricate the sensor. A channel was machined in the PTFE mould where the fibre is positioned so that

it sits in the middle of the patch. Although there are three wells in the mould only one mould is used for the sensor fabrication. This three well mould was used for another application initially and for this application centre well was used. The fibre is placed in the curing set up (shown in figure 4.33(b)), and secured at the two ends using magnets so that a pre-strain can be applied. This will make sure that bending of the fibre is avoided. Adjustments are made to the fibre to make sure the FBG is placed at the centre of the well by aligning the markers on the FBG and the centre of the well. Once the fibre is secured on the curing setup the polymer resin is poured into the well and cured for 5 minutes with a 5 W UV torch (wavelength range: 365 – 370 nm). After the patch is cured, the patch is polished to make sure its surface is flat. The polymer used was Loctite AA 3926, as discussed in section 4.5. The mechanical properties of this polymer are given in section 4.5.

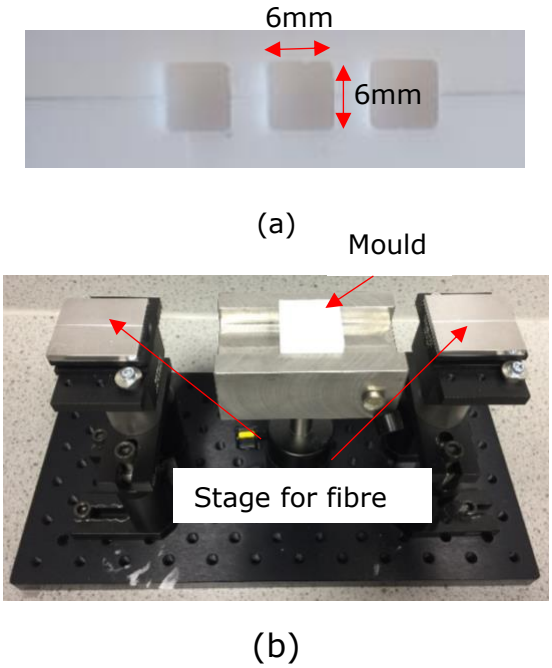

Figure 4.33: (a) picture of the 3D printed mould used to fabricate the sensor (b) the curing setup

The results obtained from the experimental validation have been plotted with the simulated result obtained on the same graph shown in figure 4.36. The experimentally obtained Bragg wavelength sensitivity is 0.595 nm/MPa and the

simulated results agree well. Moreover, the simulated results always lie within the error limits (standard deviation) of the experimentally obtained results.

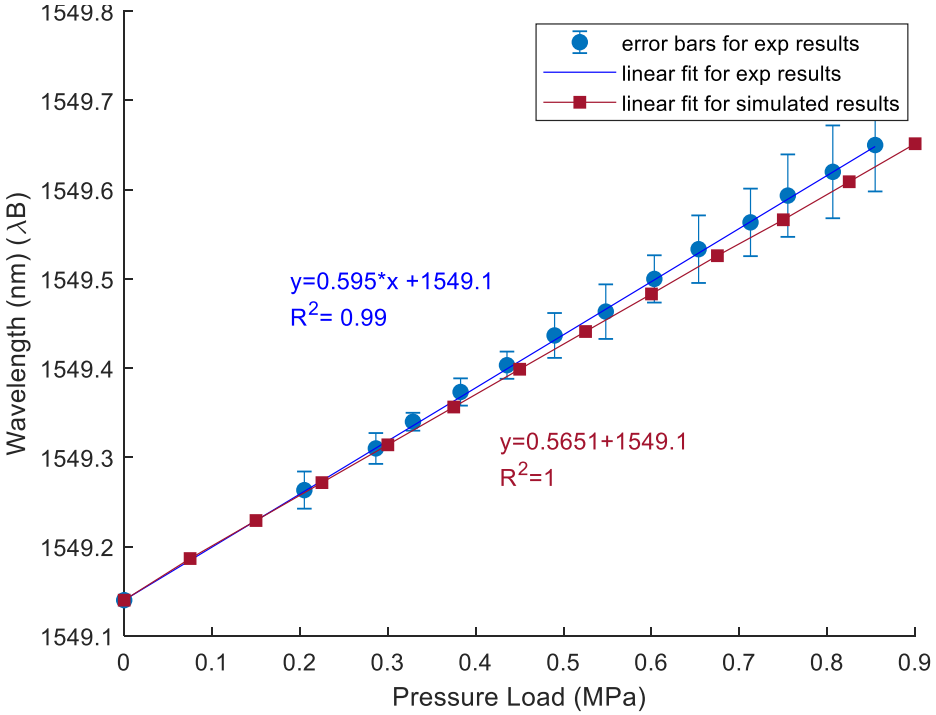

Figure 4.34: Experimentally obtained Bragg wavelength sensitivity to the applied transverse pressure load

4.6 Analysis of the simulated sensitivity of the FBG for different shapes of the polymer patch

In this section the aim is to compare and evaluate the sensitivity of the FBG embedded in different shapes of polymer patches. A comparison between 6mm x 6mm x 1mm cuboid patch, 6mm diameter disc patch and 6mm x 3mm x 1mm quasi rectangular shape have been simulated. The Young's modulus of the polymer patch has been kept constant at the same value (143 MPa) that was used for the above simulations in section 4.5.1 and section 4.5.2. The thickness was fixed at a value of 1mm throughout all the models. Moreover, strain optic coefficients, fibre parameters are kept constant throughout all the simulations.

4.6.1 The mathematical simulations of an FBG embedded centrally in a 6mm diameter disc

Figure 4.35 shows the FE model of an FBG embedded in 6mm diameter disc.

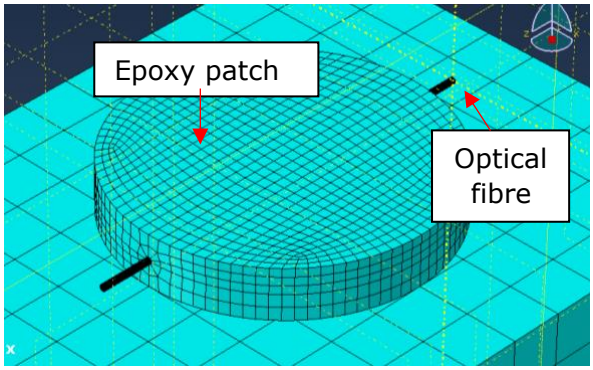

Figure 4.35: FEM mesh of the FBG (3mm) embedded in 6mm diameter, 1mm thickness polymer disc

Figure 4.36 shows the strain distribution along the axis of the FBG. Compared to the FBG embedded in the 6mm x 6mm x 1mm cuboid patch, the strain transferred to the FBG has been increased in the 6mm diameter disc patch. Although the bonded length is the same, the strain transferred to the FBG due to the transverse load is dependent on the shape of the patch. The reflection spectrum shifts a red shift with the increase of the transverse pressure load as shown in figure 4.37. Figure 4.38 shows the simulated wavelength versus applied pressure. The wavelength sensitivity of the sensor to the pressure is 0.6226 nm/MPa.

This value is higher than the sensitivity obtained for the cuboid shape patch. This is due to the fact that higher strain values are transferred to the FBG from the circular shaped disc patch when compared to the strain transferred to the FBG by the cuboid shape patch.

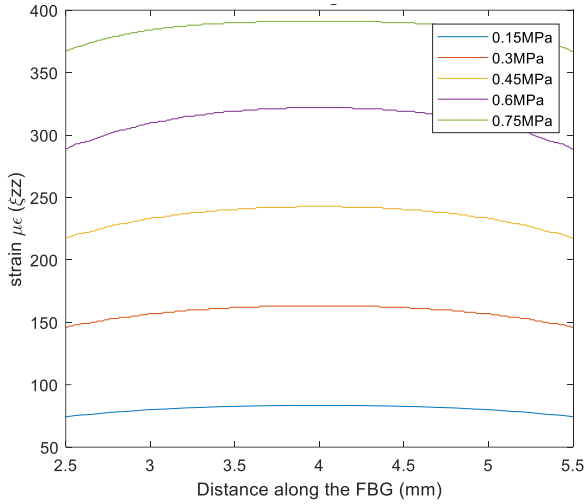

Figure 4.36: Strain distribution along the axis of the fibre for the FBG embedded in 6mm diameter patch

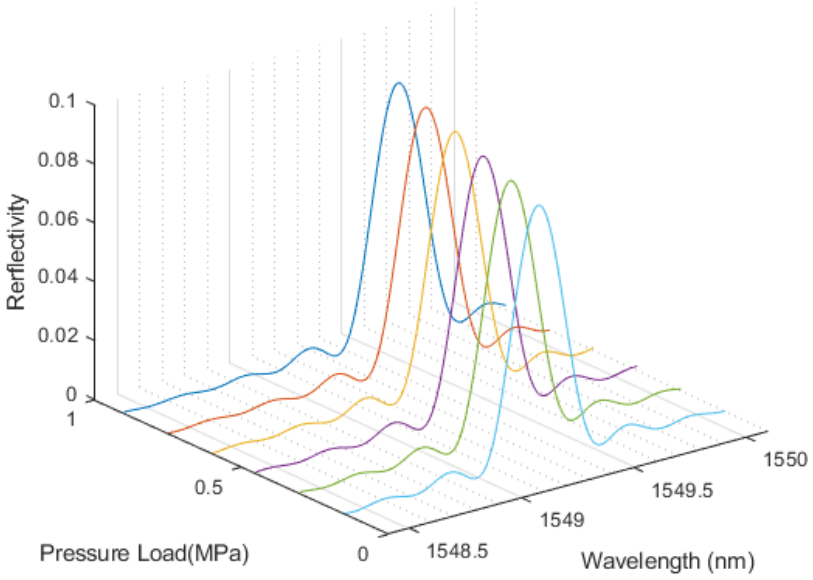

Figure 4.37: Evolution of the reflection spectra of the FBG embedded in 6mm diameter disc

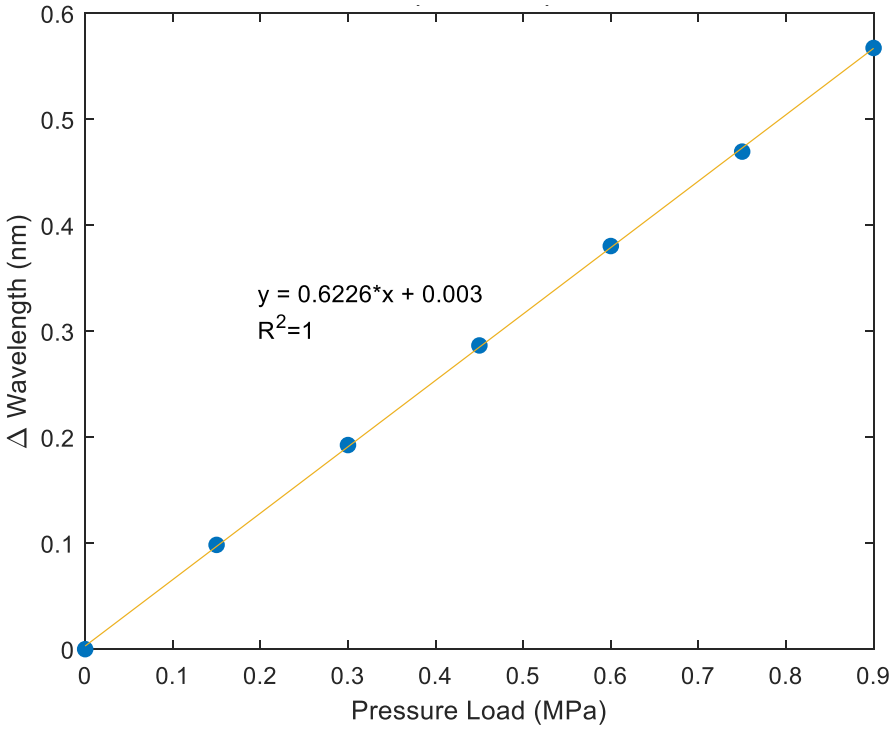

Figure 4.38: Simulated wavelength sensitivity of a 3mm long FBG embedded centrally in a 6mm diameter disc , 1mm thick circular disc to transverse pressure

4.6.2 The mathematical simulations of an FBG embedded centrally in a 6mm x 3mm x 1mm quasi rectangular shape patch

Figure 4.39 shows the FE model for the FBG embedded in a quasi-rectangular shaped patch. Figure 4.40 shows the strain distribution experienced by the FBG due to the transverse pressure loading on the quasi rectangular patch. The strain values show more or less uniform strain transfer along the length of the FBG. However, the strain transferred to the FBG is much lower than on the 6mm diameter disc and the 6mm x 6mm x 1mm square shaped patch.

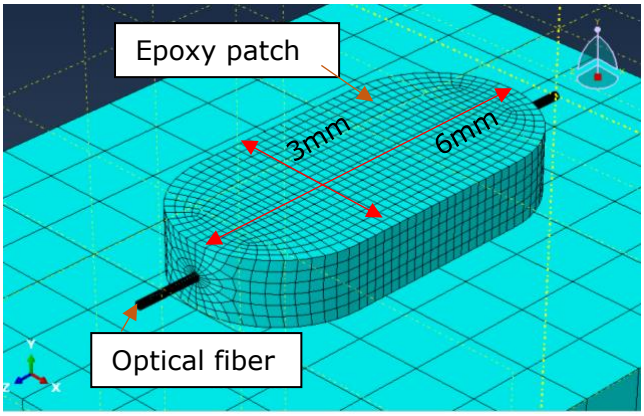

Figure 4.39: FEM mesh for the FBG (3mm) embedded in a quasi-rectangular shape patch (6mmx3mmx1mm)

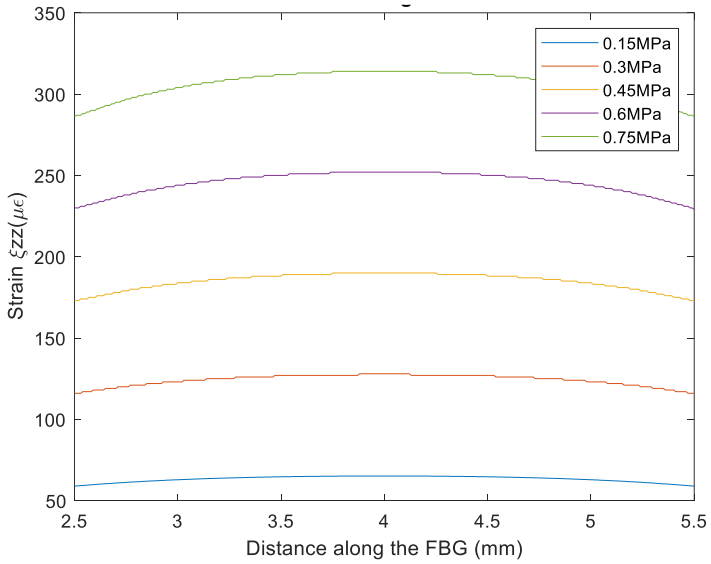

Figure 4.40: Strain distribution along the axis of the fibre for the FBG embedded in a quasi rectangular patch

Figure 4.41 demonstrates the evolution of the reflection spectra to different transverse loads. There is a shift towards the red end of the spectrum with the increment of the transverse load.

The simulated sensitivity shows a value of 0.49 nm/MPa which is lower when compared to the cuboid shape and the circular disc shape. This is due to the fact that the strain transferred to the FBG from the quasi rectangular patch is lower compared to the other two patch shapes mentioned above.

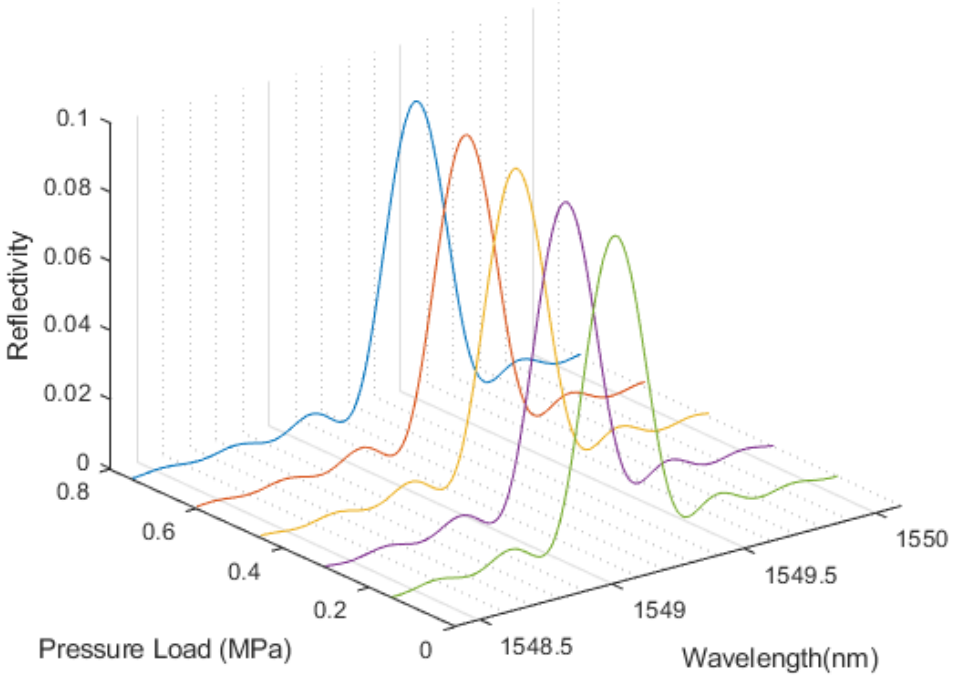

Figure 4.41: Evolution of the simulated reflection spectrum of the FBG (3mm) embedded in quasi rectangular patch to different transverse pressure loading

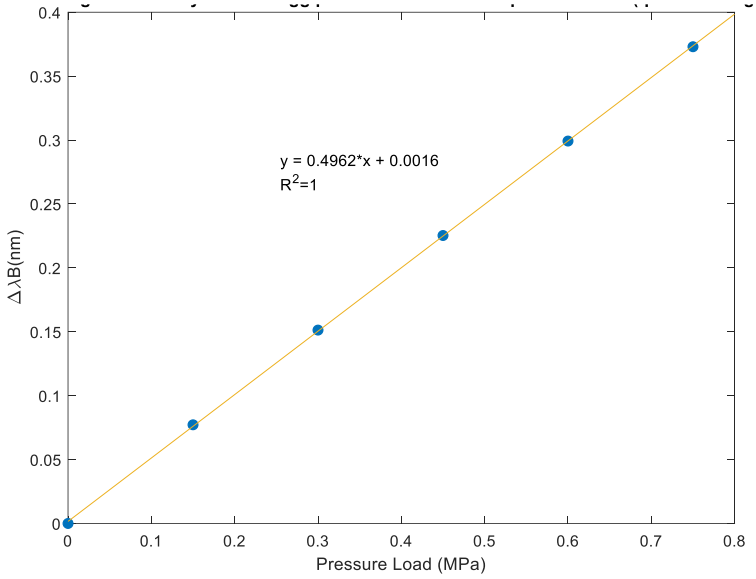

Figure 4.42: : Simulated wavelength sensitivity of a 3mm long FBG embedded centrally in a 6mm x 3mm x 1mm quasi rectangular shape patch to transverse pressure load for

The highest sensitivity achieved was for the circular shaped disc patch. The next section of this chapter will compare the sensitivities of the FBG when embedded in three different diameter patches.

4.6.3 Investigation of the pressure sensitivity of the FBG when embedded into different discs diameters

Since the circular disc has the highest sensitivity among all the shapes, it is necessary to compare how diameter effects the sensitivity of the sensor. Three different diameters discussed and compared (5mm, 6mm and 7mm). The 6mm disc patch is already discussed in section 4.6.1. However, for comparison purposes some of the results are illustrated again in this section.

Figure 4.43 illustrates the FEM mesh used for the simulations of FBG embedded in a 5 mm disc patch and 7 mm disc patch.

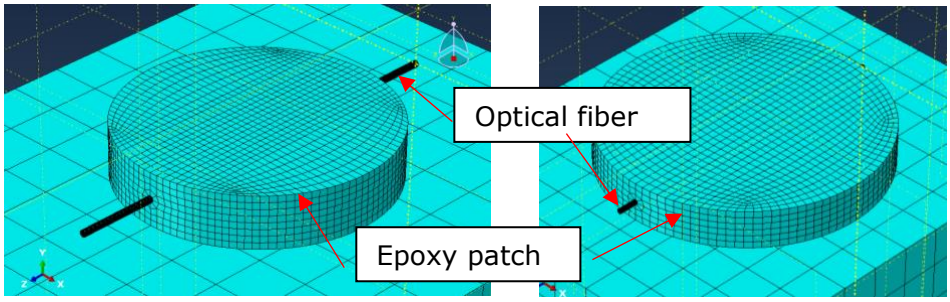

(a) (b)

Figure 4.43: FEM mesh of the FBG (3 mm) embedded in (a) 5 mm diameter 1 mm thickness polymer disc (b)7 mm diameter 1 mm thickness polymer patch

Figure 4.44 depicts the simulated strain distribution obtained along the axis of the FBG. In contrast to the strain profile obtained by the FBG with 5 mm disc and 6mm disc; the strain profile of the FBG with 7 mm disc is more uniform throughout the length of the FBG.

The wavelength sensitivities of the three different patches with different diameters are illustrated in figure 4.45.

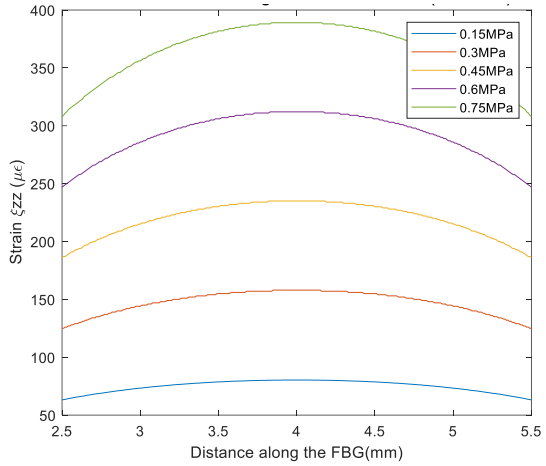

(a)

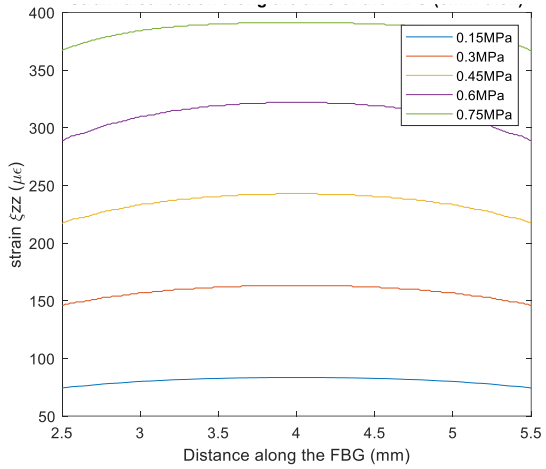

(b)

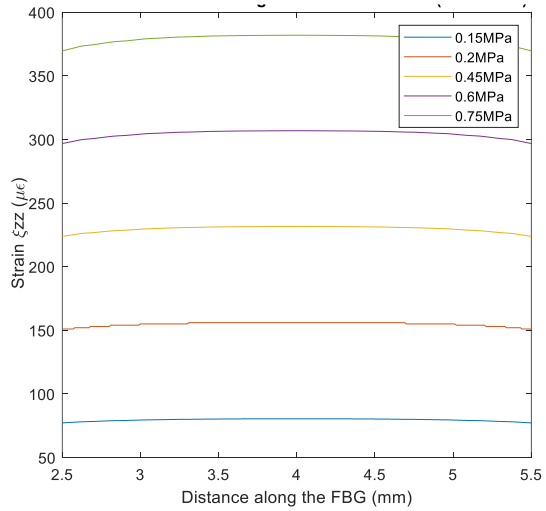

(c)

Figure 4.44: axial strain profile of the FBG embedded in (a) a 5 mm disc patch (b) a 6mm disc patch (c) a 7 mm disc patch

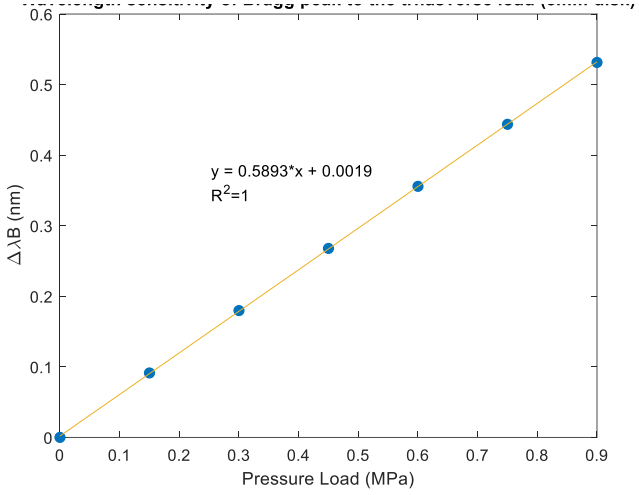

(a)

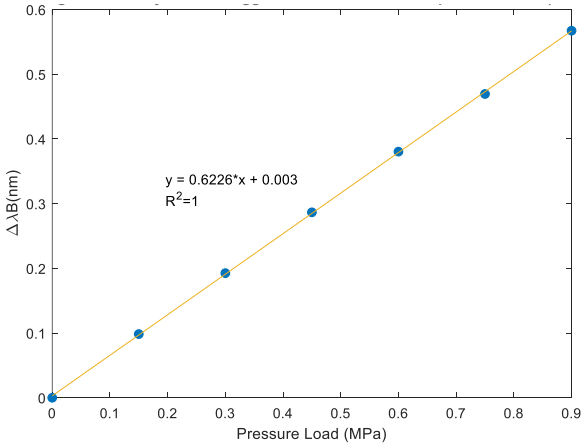

(b)

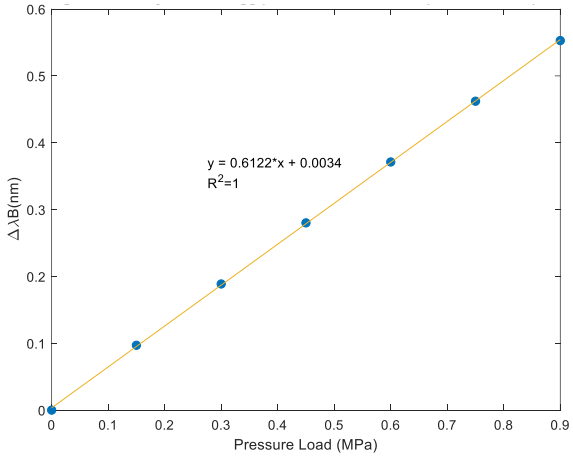

(c)

Figure 4.45: Wavelength shift of the Bragg Peak as a function of transverse pressure for different diameter discs (a) a 5 mm disc (b) a 6 mm disc (c) a 7 mm disc patches

By observing the three graphs it can be seen that the highest sensitivity is for the 6 mm diameter patch. This observation encourages investigating the stress and strain distributions more closely for different diameters and in order to decide the optimum disc diameter to achieve a maximum strain transfer to the axis of the FBG.

Figure 4.46 shows the axial strain along the FBG for patches with different diameters for a pressure load of 0.9 MPa.

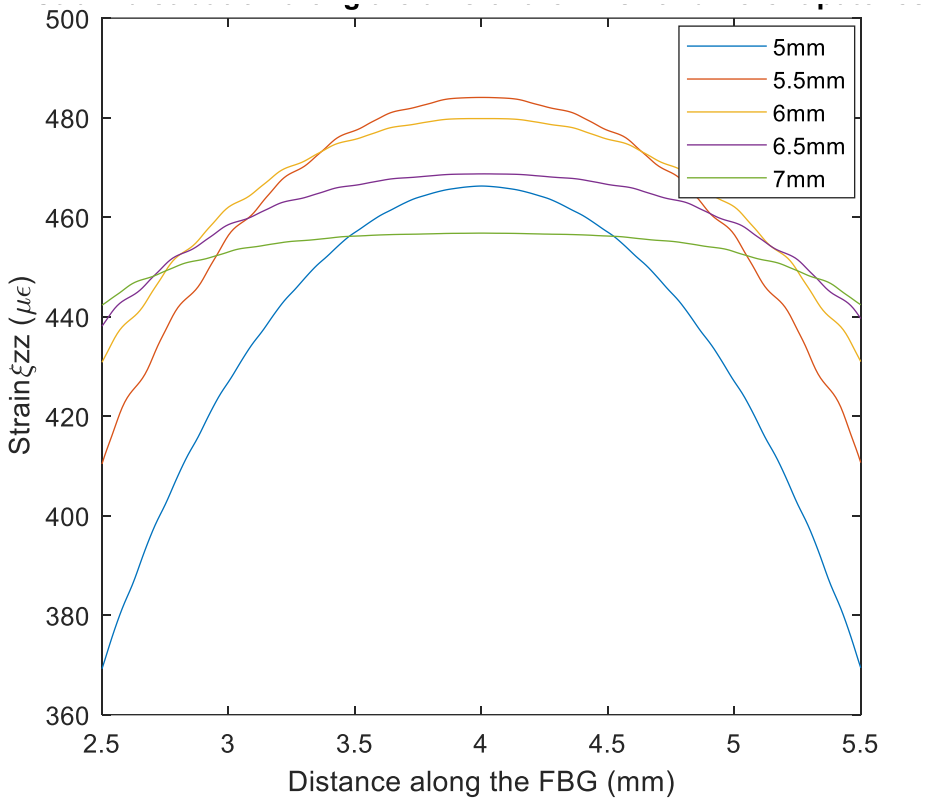

Figure 4.46: Longitudinal strain along the FBG for different diameter patches for 0.9 MPa transverse loading

According to the figure it can be observe that the maximum strain experienced at the centre of the FBG is dependent on the diameter of the disc patch. The maximum strain is transferred to the middle of the FBG is for 5.5mm diameter disc patch and the diameters less than that or higher than that experience a lower strain transfer.

The deformation of the polymer patch due to the transverse load produces reaction forces on the fibre that in return produce longitudinal stresses. The longitudinal strain caused by the longitudinal stresses is due to the longitudinal

forces acting on the fibre. This can be explained by observing figure 4.47. These reaction forces increase with the increase in the diameter of the polymer patch, whichi is due to the increase in the bonded length between the patch and the fibre. When the diameter is below 5.5mm, the increment of the reaction forces are dominant when compared to the increase in the area of the patch (due to the diameter increase) and hence the net longitudinal stresses are increased with the diameter. After a diameter of 5.5 mm the area increment due to the increase of diameter is dominant when compared to the reaction forces and hence the stresses starts to reduce. The net longitudinal strain also starts to reduce. The maximum strain due to the transverse load is observed at 5.5 mm disc diameter.

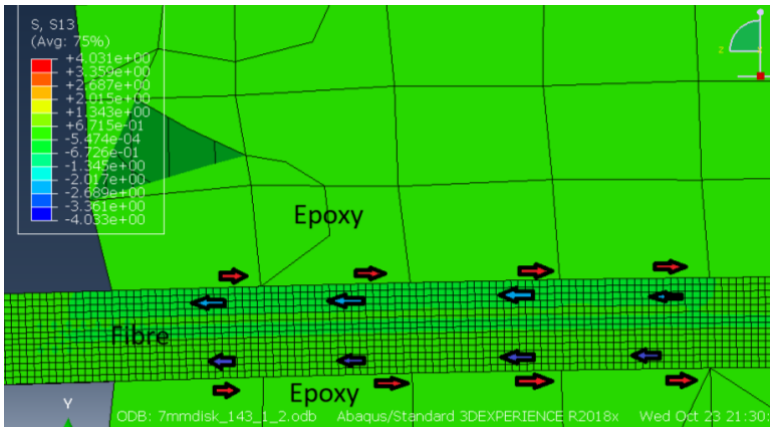

Figure 4.47: The reaction forces acting on the fibre due to the deformation of the polymer (red arrows: forces acting on the polymer patch, blue arrows: forces acting on the fibre)

Figure 4.48 shows the wavelength sensitivity of the FBG due to the transverse loading when embedded in the 5.5 mm diameter patch. As expected, the highest sensitivity of 0.6244 nm/MPa was achieved for a 5.5 mm diameter disc.

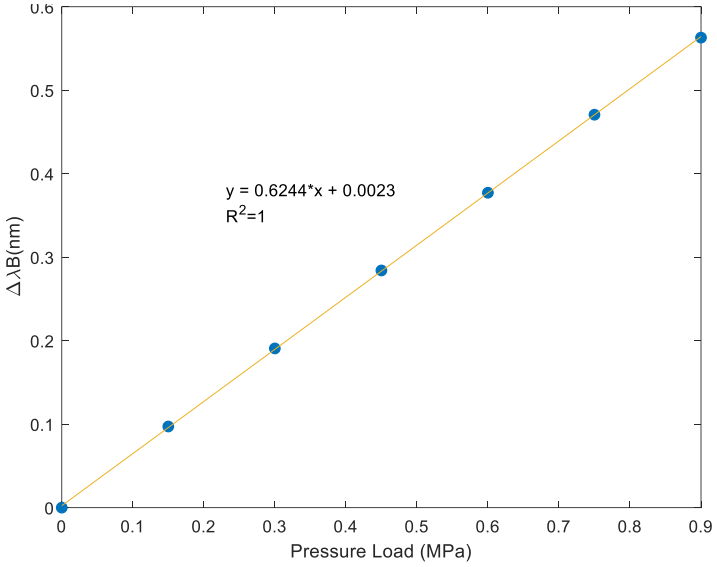

Figure 4.48: Wavelength shift of the Bragg Peak as a function of transverse pressure for 5.5mm diameter disc

4.6.4 Comparison of the sensitivity of the FBG to different Young's modulus of the polymer

This section investigates the influence of the Young's modulus of the polymer upon the FBG's sensitivity to transverse load. The Young's moduli of three commercially available polymers were considered: Loctite AA 3926, with a Young's modulus of 143MPa, Panacol Vitralit 1655 adhesive with a Young's modulus of 44MPa and Loctite AA 3921 with a Young's modulus of 20 MPa. Since the highest sensitivity was achieved for the 5.5 mm diameter disc with 1 mm thickness, this shape has been used for the simulations.

Figure 4.49 shows the evolution of the reflection spectra for the 5.5mm disc with a Young's modulus of 44 MPa. Figure 4.50 shows the wavelength sensitivity of the Bragg peak to the transverse loading. The observed sensitivity is 0.786 nm/MPa and this is a 1.25 times increment of the sensitivity when compared with the polymer patch with 143 Young's modulus.

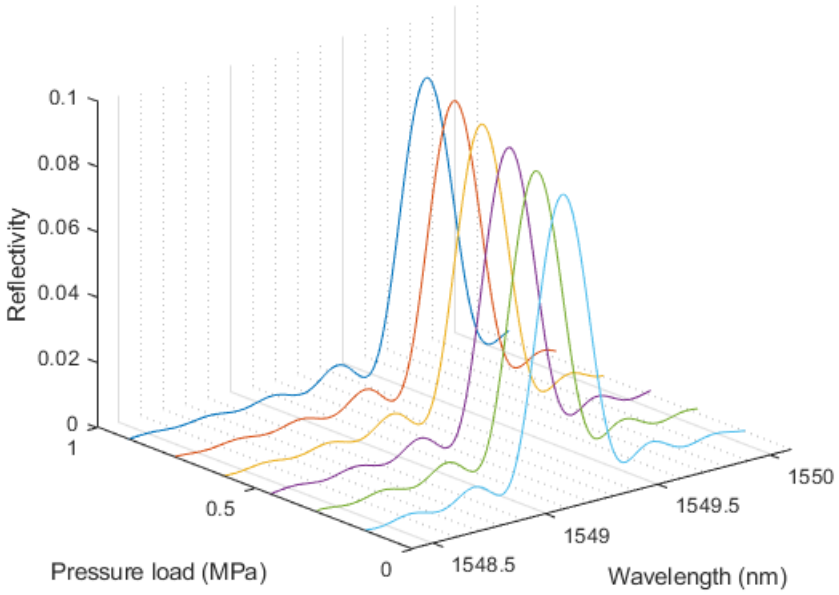

Figure 4.49: Evolution of the simulated reflection spectrum of the FBG(3mm) embedded in a 5.5mm diameter disc patch with a Young's modulus of 44 MPa, to different transverse pressure loading

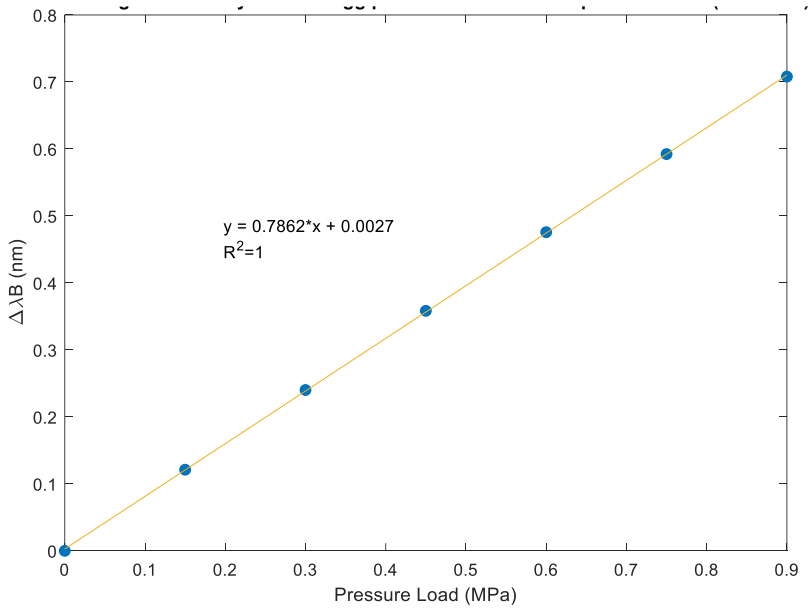

Figure 4.50: Wavelength shift of the Bragg Peak as a function of transverse pressure for 5.5 mm diameter disc with Young's modulus of 44 MPa

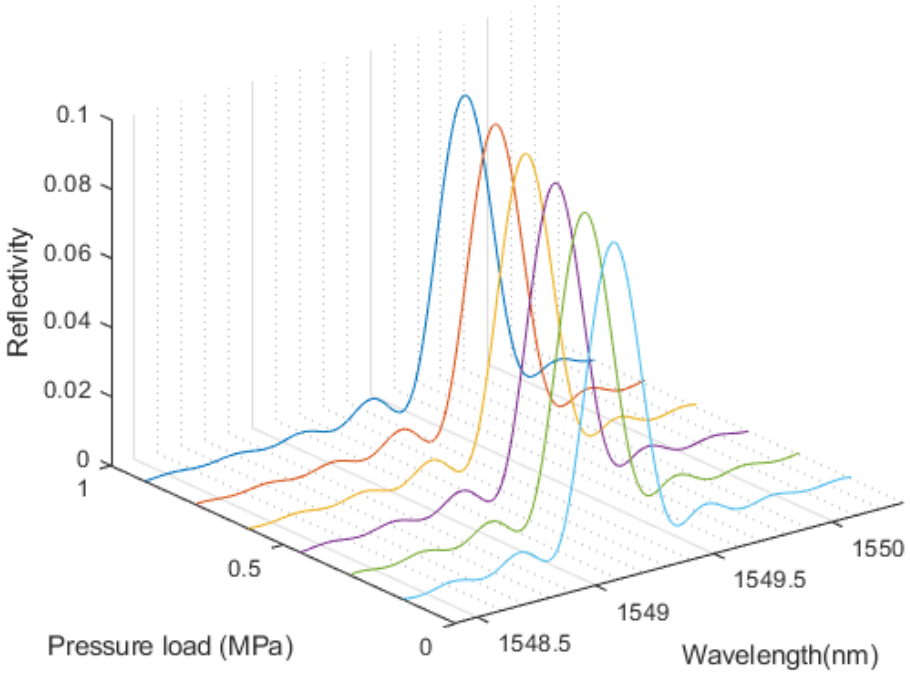

Figure 4.51: Evolution of the simulated reflection spectrum of the FBG embedded in 5.5mm diameter disc patch with a Young's modulus of 20 MPa, to different transverse pressure loading

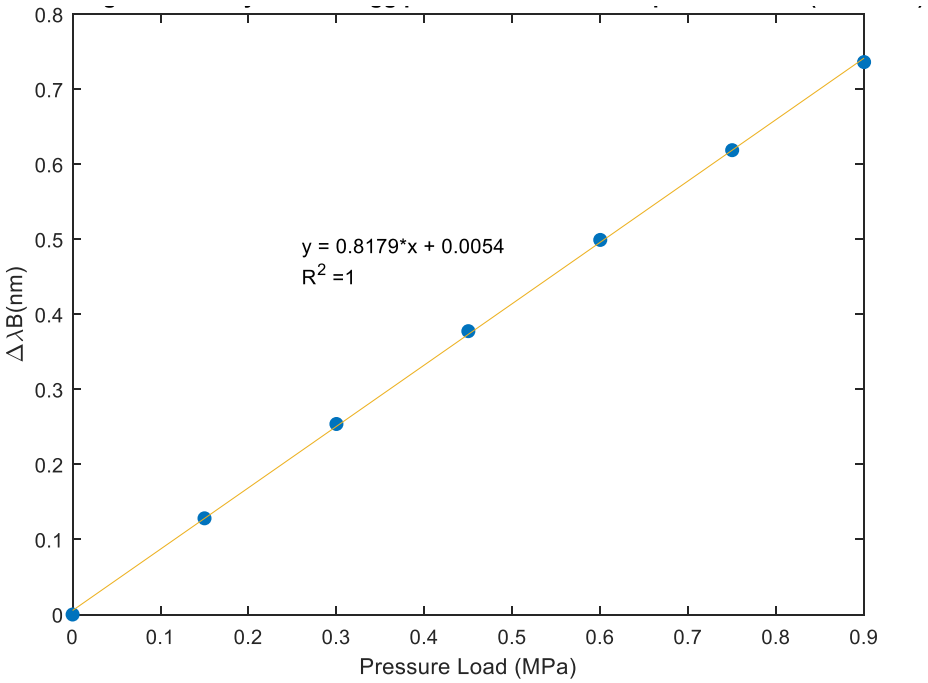

Figure 4.52: Wavelength shift of the Bragg Peak as a function of transverse pressure for 5.5 mm diameter disc with Young's modulus of 20 MPa

Figure 4.51 shows the evolution of the reflection spectrum for the 5.5mm diameter disc with a Young's modulus of 20 MPa. Figure 4.52 shows the wavelength sensitivity of the Bragg peak to the transverse loading. The observed sensitivity is 0.8179 nm/MPa where this is a 1.04 times increment of the sensitivity when compared to the polymer patch with 44 MPa Young's modulus and a 1.31 times increment when compared to the polymer patch with 143 MPa Young's modulus. A summary of the results is included in table 4.4

Table 4.4 Summary of the results for the FE simulated FBG

Shape	Dimensions	Young's modulus (MPa)	Sensitivity (nm/MPa)
cuboid	6mmx6mmx1mm	143	0.565
Quasi rectangle	6mmx3mmx1mm	143	0.4962
Disc	5mm diameter, 1mm thickness	143	0.5893
Disc	6mm diameter, 1mm thickness	143	0.6226
Disc	7mm diameter, 1mm thickness	143	0.6122
Disc	5.5mm diameter, 1mm thickness	143	0.6244
Disc	5.5mm diameter, 1mm thickness	44	0.7862
Disc	5.5mm diameter, 1mm thickness	20	0.8179

4.6.5 Birefringence effects for the patch sensor

The work discussed above does not show any birefringence or nonlinear effects due to the fact that the pressure range discussed in healthcare (0-1MPa) is too low to observe birefringence. However, it is important to see at what ranges

the sensor starts to show birefringence. Therefore the initial design cuboid patch sensor of dimensions 6mm x 6mm x 1mm with 143 MPa Young's modulus has been simulated to observe these effects.

Table 4.5: Splitting of the FBG signal into two waves due to the birefringence for cube patch of 6mm x 6mm x 1mm with a Young's modulus 143 MPa, X wave is representing the fast-axis and Y wave is representing the slow-axis.

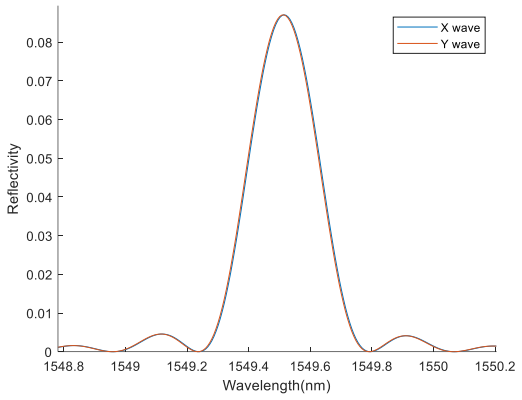	Load = 0.75 MPa
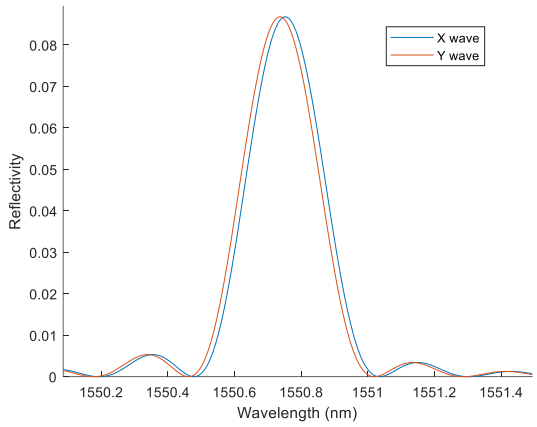	Load = 3.75 MPa
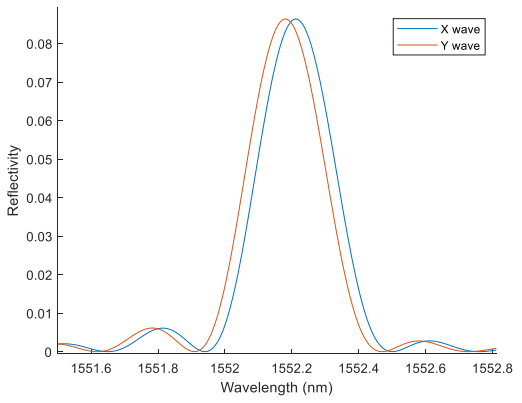	Load = 7.5 MPa

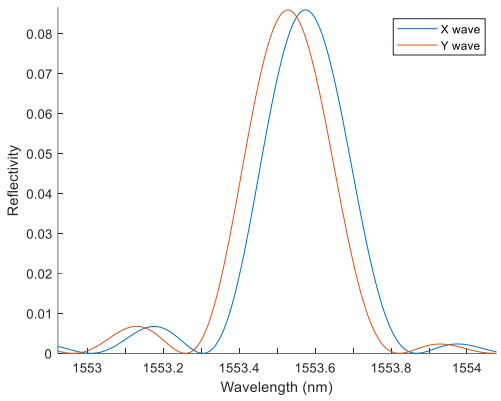	Load = 11.25 MPa
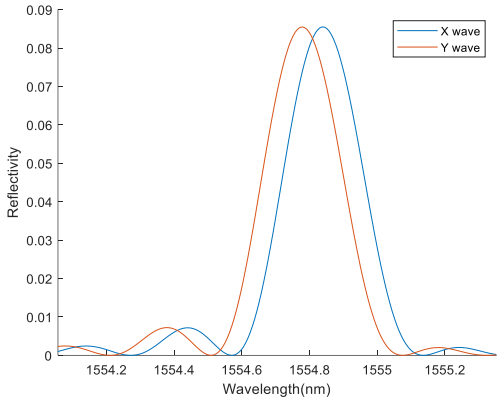	Load = 15 MPa
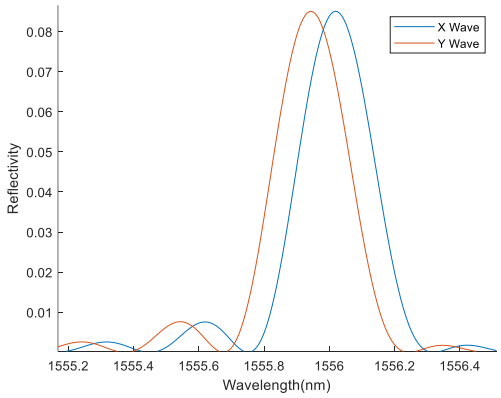	Load = 18.75 MPa

According to the results included in table 4.5 it clearly can be seen when the load is less than 1 MPa, the cube patch does not show birefringence. Birefringence starts to show after 3.75 MPa.

Table 4.6: Splitting of the FBG signal into two waves due to the birefringence for disk patch of diameter 5.5mm with a Young's modulus 20 MPa

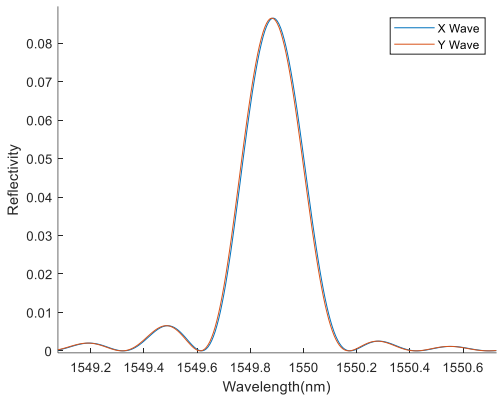	Load= 1.1 MPa
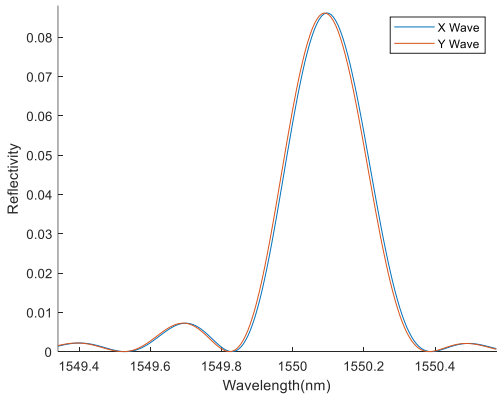	Load= 1.5 MPa
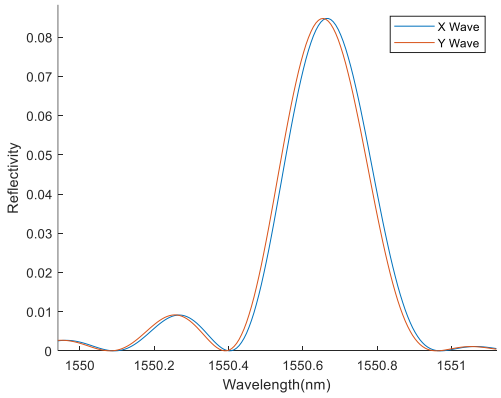	Load= 2.6 MPa

According to table 4.6 the birefringence effects start to show after about 2.6 MPa for a 5.5mm diameter disk with Young's modulus of 20MP. Loads beyond these could not be applied to the FEA model due to the high distortion of the patch. However, these results give a good insight at what levels the nonlinear effects could begin to be observed.

4.7 Conclusions

A mathematical model of an optical fibre Bragg grating embedded in a polymer patch for contact pressure measurement in healthcare has been presented. The model has been validated for previous obtained experimental results reported in the literature. The mathematical model is validated experimentally for a 3mm long FBG embedded in a 6mm x 6mm x 1mm polymer cuboid patch.

According to the strain transfer characteristics of an FBG, the strain transfer rate from the embedded layer to the axis of the fibre is a complex function which depends on many variables and attributes, including the number of layers of the material bonded to the FBG, the bonding length of the embedment, the thickness of the embedded layer, the material properties of the embedded layer and the shape of the embedded layers. However, a maximum strain transfer is achieved at the centre of the fibre/centre of the patch, due to its symmetry. Therefore, by embedding the FBG in the centre of the patch a maximum strain transfer could be acheived.

Three different shapes including cuboid, quasi rectangular and circular disc have been simulated to obtain the optimum shape and size for the sensor. According to the simulation results, the circular disc shape shows the highest sensitivity. The optimum diameter observed was 5.5mm achieving a highest sensitivity of 0.6244 nm/MPa for a Young's modulus of 143 MPa. This is an increment of 0.064 nm/MPa when compared to the initial cuboid shape of 6mm x 6mm x 1mm patch. However, by increasing the diameter, a more uniform strain distribution along the length of the FBG could be observed by compromising the sensitivity.

The effect of the Young's modulus of the patch on the sensitivity of the FBG was investigated. For this purpose, three commercially available polymer material properties were used. Young's modulli that have been investigated are 143 MPa, 44 MPa and 20 MPa. As the Young's modulus decreases the sensitivity of the FBG sensor is increased. The highest sensitivity of 0.8179 nm/MPa was observed for the 5.5 mm disc with 1 mm thickness with a Young's

modulus of 20 MPa. As the Young's modulus of the material decreases the polymer becomes more deformable and hence the reaction forces applied on the fibre are significant. As a result of the longitudinal strain increases, the Bragg wavelength shift is greater for the same pressure, when compared to higher Young's modulus (less deformable) polymer.

The reflection spectra of all the simulated FBGs showed no birefringence within the pressure range of 0 - 1MPa. The application of the pressure sensor is within this pressure range and the effects out of this range are less important and out of the scope of this study. This is due to the fact that transverse stresses are negligible compared to the longitudinal strain within the considered pressure range. The refractive index is uniform about the axis of the fibre and hence the reflected peak does not separate along x-axis and y-axis.

However, the T effects with peak splitting along the x-axis and y-axis were observed for the 5.5 mm diameter patch with a Young's modulus of 20MPa after 2.6 MPa, whereas for the 6mm x 6mm x 1mm with a Young's modulus 143MPa splitting was observed after 3.75MPa.

The initial design was a polymer patch with a cuboid shape of 6mm x 6mm x 1mm and a Young's modulus of 143 MPa. This resulted in a sensitivity of 0.56 nm/MPa. Overall the sensitivity has been increased by 1.5 times from the initial design by changing its shape and the Young's modulus of the polymer. Moreover, R Correia et al. [175] obtained a wavelength sensitivity of 0.029 nm/N (0.116 nm/MPa) for a 6 mm FBG embedded centrally in a 2mm x 2mm x 2mm cube patch with a Young's modulus of 689 MPa, to the transverse loading. As per the simulated results obtained in this work, this sensitivity could be improved 7 times by fabricating an FBG sensor of a length of 3mm, embedded centrally in a disc shaped polymer patch of 20 MPa Young's modulus with a diameter of 5.5 mm and a thickness of 1 mm.

Chapter 5

Development of a compact Fibre Bragg Grating (FBG) interrogator

5.1 Introduction

This chapter discuss the work related to the development of a compact FBG interrogator for the compression bandage pressure measurement application in healthcare. The main objective is to build a compact optical transducer for the FBG contact pressure sensor discussed in chapter 4. Development of the FBG interrogator is based on a three section DBR tuneable laser. In section 5.2 an extensive review on currently available FBG interrogation techniques both commercially and in literature is presented. This is followed by a detailed discussion of the background information related to the physics and working principles of tuneable lasers. It is very important to understand the tuning mechanism of a tuneable laser in order to achieve a continuous wavelength sweep. This is followed by a detailed explanation of software and hardware development of the miniature FBG interrogator system. Section 5.5 includes the conclusions and future work.

5.2 Review on the available FBG interrogation systems

Although there are many advantages of FBG sensors, as discussed in chapters 2 and 4 their commercial usage is affected by the size, availability and the cost of the FBG interrogation techniques. Many FBG interrogation techniques have been researched and developed and these can be broadly categorised into six main types [58], [225].

1. Spectroscopic
2. Interferometric
3. Edge filters
4. Tuneable filters
5. FBG interrogators based on photonics integrated circuits (PICs)
6. Tuneable laser sources

In the early stages of development, FBG sensor technology used a broadband light source and an optical spectrum analyser (OSA) as the wavelength identifying method by means of plotting the spectral distribution of the reflected or transmitted light from the FBG. However, OSAs are very expensive and bulky devices and hence not suitable for deployment in healthcare applications where a lightweight and compact sensor system is required.

In interferometry, two light beams and their relative path/phase difference can be used to determine the wavelength shift of FBGs. Light reflected from a grating is directed through the interferometer which has unbalanced paths and the Bragg wavelength is converted into a phase shift where the phase of an unbalanced interferometer depends on the input wavelength. References [1], [226]–[229] report FBG interrogation techniques based on the Mach-Zehnder interferometric method.

Edge filters provide a linear relationship between the Bragg wavelength and the output intensity of the edge filter. By measuring the intensity change, the wavelength change induced by the measurand could be obtained. The measurement range is inversely proportional to the resolution and hence this method is not suitable for multiplexed FBGs. Alfonso et al. [230] describe the initial development of an optical FBG interrogator using an edge filter scheme. A wavelength resolution of 7 pm was reported with a data acquisition rate of 2.5 kHz. A recent development of a wireless portable FBG interrogation system using an optical edge filter is reported [231] for application in healthcare, in particular plethysmograph monitoring. The accuracy in terms of standard deviation is given as 0.1 pm for the system. Stan et al. [232] described a method of increasing the dynamic range of FBG interrogation techniques based on edge-filtering by using a microcontroller in a control loop. The purpose of the control loop is to keep the filter tuned to the wavelength at the mid reflection point as dynamic strain is applied. Similar work on FBG interrogation using edge filters is also reported in references [233]–[235].

The tuneable filter uses the convolution of both the spectrum of the tuneable filter and the FBG to measure the wavelength shift of the FBG. When the

spectrum of the tuneable filter matches the FBG output the convolution equals 1 which means the maximum achieved output. By identifying this maximum point and the wavelength difference of the tuneable filter, the wavelength shift could be identified. The resolution of this technique is highly dependent on the linewidth of the tuneable filter and the FBG. Different types of filters used in the literature include Fabry-Perot filters [236]–[238], acousto-optic filters [239],[240] and FBG based filters [241]. A portable FBG interrogator for dynamic monitoring in wearable applications is reported in the literature based on a white light source and the spectral convolution between sensor and a tunable filter [242]. The resolution of this interrogator is 3.82pm for a sweeping range of 15.64nm.

Recent advances in photonic integration introduces novel FBG interrogators based on photonic integrated circuits which are available commercially [243],[244]. These interrogators allow low cost, miniaturized FBG readout units with light weight, repeatability, low power consumption, thermal and vibration stability and wide ranges of wavelength[245]. PICs can contain tens to hundreds of optical components. Electronic ICs consist of transistors, capacitors and resistors whereas in PICs, lasers, modulators, photodetectors and filters all are integrated into a single substrate. These methods have some draw backs such as the number of FBGs that can be simultaneously integrated and dynamic capabilities of the readout unit [246]. A sensing chip with 1mm thickness based on a single Vertical Cavity Surface Emitting Laser (VCSEL) is report in the literature [247]. The resolution of the system dependent on the driving frequency and demonstrated range is 1.5 pm- 4 pm.

FBG interrogation based on tuneable lasers is a very attractive alternative to the above discussed interrogation methods allowing orders of magnitude improvement in the output power as well as reduction in the signal linewidth and hence higher resolution. Moreover, tuneable lasers provide wavelength division multiplexing capabilities. Various tuneable lasers have been researched and studied for the use of FBG interrogation. Coroy et al. [248] demonstrated the first FBG interrogation system using a distributed feedback

laser. Ball et al. [249] reported the use of a tuneable Erbium fibre laser to interrogate a FBG multipoint temperature sensor. The use of tuneable distributed feedback lasers and a Mach-Zehnder interferometer is reported in reference [250]. A miniature (110x50x40mm) low cost FBG interrogator based on a tuneable Vertical Cavity Surface Emitting Laser (VCSEL) has been reported [251] which allows a wavelength sweep of 7nm. FAZ Technology [252] reported a tuneable laser (SG-DBR or MG-Y) and photonic integrated circuit based FBG interrogator [253].

Wavelength tuning in tunable lasers is done by controlling the input current for each of the tuning sections of the laser. Therefore, precise, stable current controllers are crucial for a tunable laser circuit. There are commercially available, fully integrated current controlling options available for lasers. However, the prices of these controllers are very high and most of these are bulky benchtop devices as they come up with all the available options for general purpose use. A review of commercially available interrogation systems is summarised in table 5.1

It is clear from table 5.1 that the average price of an FBG interrogator is around 5000 GBP. Additionally the size and the weight of the commercially available interrogators are too large for the FBG interrogation required for the contact pressure measurement applications in healthcare, where a wearable solution would be beneficial, as discussed in chapter 4.

Table 5.1: Summary of commercially available FBG interrogators

Manufacturer	Size and weight	Wavelength range	Max no.of sensors/ channels	Resolution	Price
Micron optics SM130	122 mm x 267 mm x 135 mm 2.5 kg	1510-1590 nm	Up to 500	1nm	~ 2000 GBP
Micron optics si255	307 mm x 274 mm x 69 mm 4.9 kg	1500-1600 nm	16 channels	1pm	
Micron optics si155	206 mm x 274 mm x 79 mm 3.0 kg	1500-1600 nm	4 channels	1 pm	
Smart fibres SmartScan	140 mm x 115 mm x 85 mm 0.9 kg	1528 -1568 nm	64 sensors		> 5,000 GBP
Smart fibres SmartScan Aero Mini	45 mm x 135 mm x 203 mm 1.4 kg	1528 -1568 nm	64 sensors	< 1pm	
Technobis Switch gator	110 mm x130 mm x47 mm 0.54 kg	1515 -1585 nm	64 sensors	1 pm	~ 5,000 GBP
Ibsen photonics I-MON 256	110 mm x94 mm x49 mm	1525-1570 nm	37 sensors	<0.5 pm	~ 3,000 GBP
Ibsen photonics I-MON 512	110mm x94 mmx 49 mm	1510-1595 or 1275-1345 nm	70 sensors	<0.5 pm	~ 3,415 GBP
HBM FS42PI	155 mm x 125 mm x 275 mm 6kg	1500 - 1600 nm	4 channels	1 pm	
Welltech FBG 210-4	225 mm x205 mm x95 mm	1525 - 1565 nm	64 x4 sensors	1 pm	
Welltech FBG3000	295 mm x291 mm x123 mm	1525 - 1565 nm	64 x8 sensors	10 pm	
Bayspec FBGA	96 mm x 68 mmx 15.8 mm	1510-1590 nm		1 pm	
Fibrepro IS7000	364 mmx 363 mm x 147 mm	1530 - 1565 nm	16 x 8 sensors	1 pm	~ 8,000 GBP
FBGs FBG-Scan 700	260 mm x 230 mm x 60 mm	1525–1565 nm	40 sensors	0.4 nm	
FBGs FBG-Scan 800	260 mm x 230 mm x 60 mm	1510–1590 nm	40 sensors	0.8 nm	

5.3 Background Information on Tuneable lasers

5.3.1 Basic concepts of Tuneable lasers

In order to understand the tuning concept of lasers, a simplified equivalent circuit is illustrated in figure 5.1

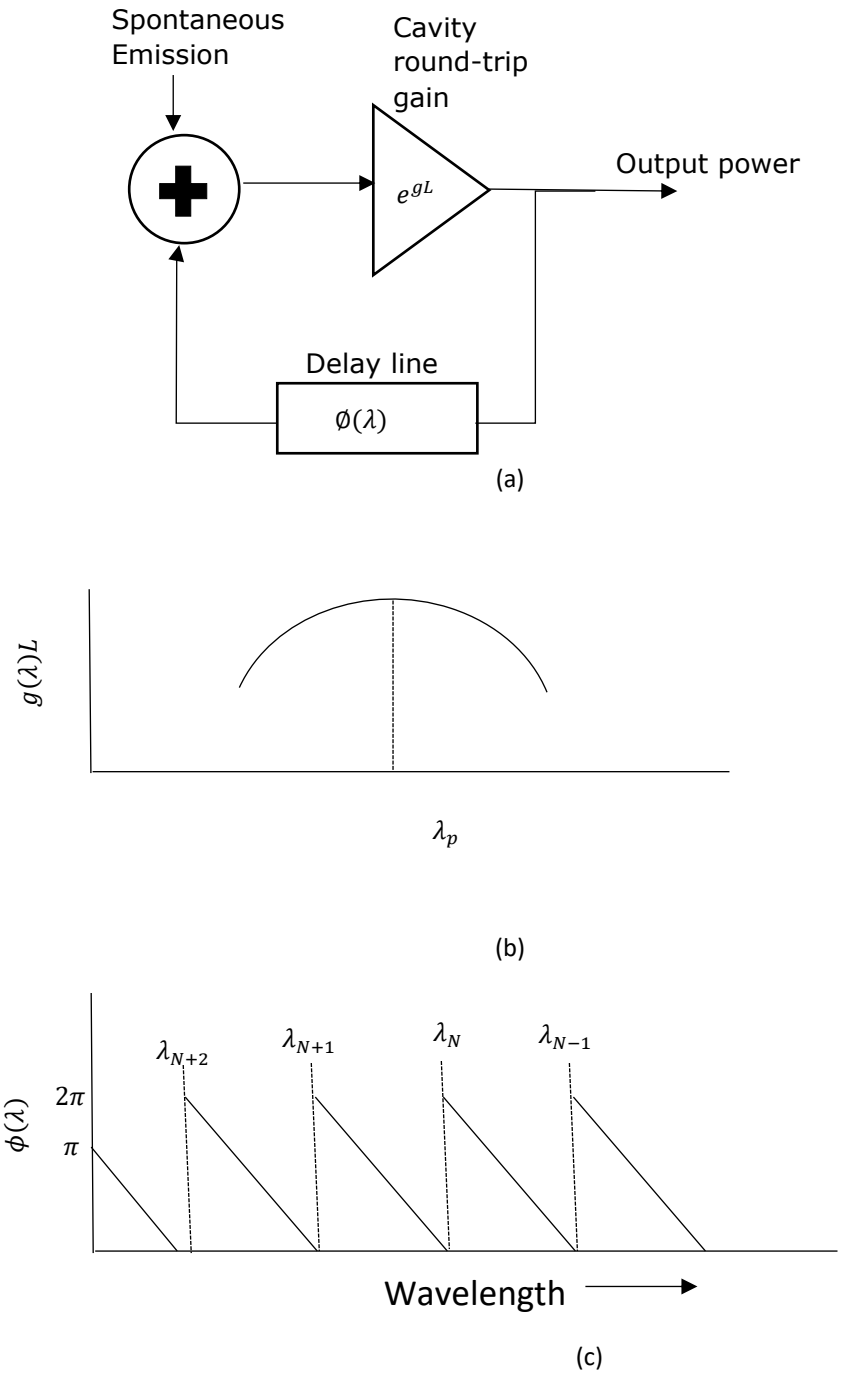

Figure 5.1: (a) Simplified equivalent circuit of a laser oscillator (b) plot of normalised cavity gain (c) phase shift [254]

Figure 5.1 (a) shows the simplified equivalent circuit of the laser oscillator. A gain characteristic is plotted in figure 5.1 (b) and the phase condition is plotted in figure 5.1 (c).

According to the figure 5.1 (b) the gain peak is at λ_p. The precise laser wavelength is defined by the phase condition. The dominant mode for this example is the Nth mode as the maximum of the gain overlaps with the Nth mode.

Tuning of the laser can be done either by adjusting the cavity gain characteristic (λ_p), by adjusting the cavity phase ($\phi(\lambda)$) or by changing both of these.

Depending on the way the tuning is performed or, the structure of the device, the tuning of a laser can be divided in to three main tuning schemes. These are continuous, discontinuous and quasi continuous.

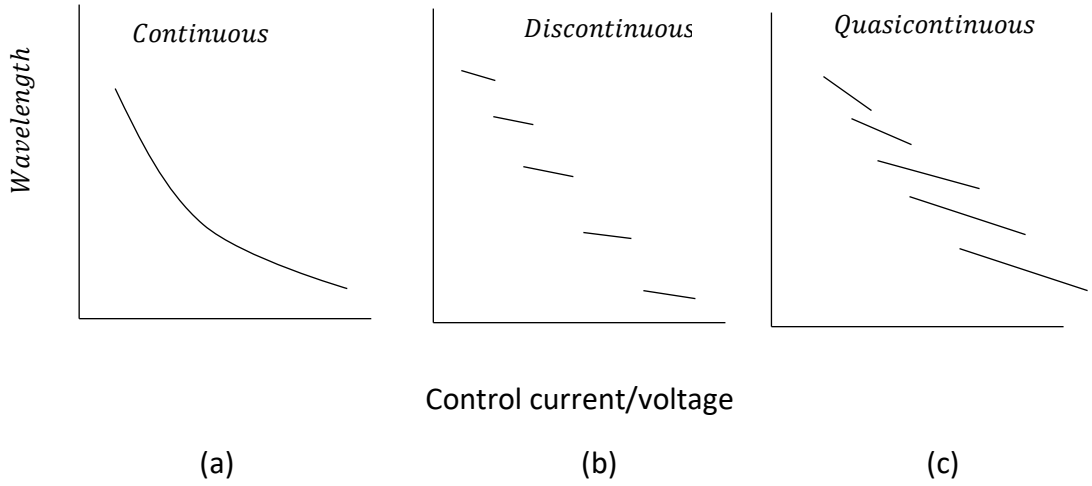

Figure 5.2: Representation of three different tuning schemes of tuneable lasers (a) continuous (b) discontinuous (c) quasi-continuous plotted for emission wavelength versus the control current/wavelength [254]

In a continuous scheme, the wavelength is tuned smoothly in arbitrarily small steps and no mode change occurs. All the other laser parameters are kept constant. Most importantly, a continuous scheme allows single mode stable operation throughout the entire tuning range. Continuous tuning requires simultaneous mutual adjustments of cavity gain peak and comb mode

spectrum [255] and practically this is very difficult to achieve with laser structures [256].

A discontinuous scheme permits a larger tuning range by allowing the longitudinal mode to change during tuning. At 1550 nm wavelength, a tuning range of 100nm is achievable [257]. However, in the discontinuous scheme, it is impossible to achieve emission of all the wavelengths within the tuning range.

A quasi-continuous tuning scheme offers intermediate tuning when compared with the other two methods. This is accomplished by overlapping small continuous tuning regimes of single longitudinal modes to achieve a large tuning range. The total tuning range is limited by the tunability of the cavity gain characteristic.

5.3.1.1 Tuning of cavity gain characteristic

Tuning of the gain characteristic is done by shifting the gain peak wavelength (λ_p) by varying the wavelength dependence of the active medium gain $g(\lambda)$ or else by using wavelength selective mirror losses.

Tuning of the cavity gain characteristic is explained in figure 5.13.

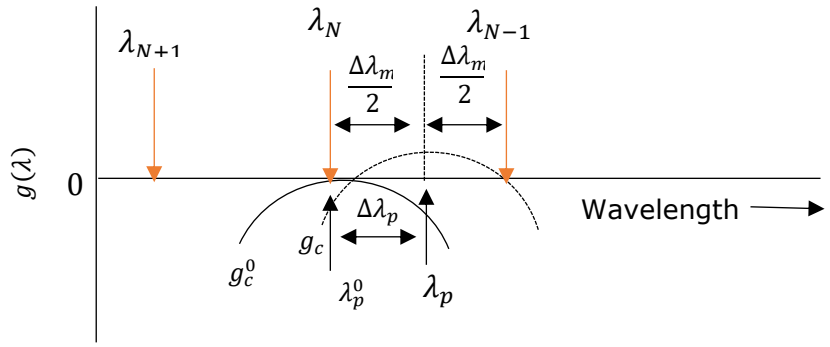

Figure 5.3: Wavelength tuning by shifting the gain peak wavelength. g_c^0 is the gain curve before tuning and g_c is the gain curve after tuning [254].

The change of the λ_p can be described as $\lambda_p = \lambda_p^0 + \Delta\lambda_p$

where, λ_p^0 denotes the cavity gain peak before tuning and λ_p is the cavity gain peak after tuning. Depending on the mode spacing, the gain characteristic of the laser undergoes an amplitude change during tuning and hence the gain-clamping mechanism as shown in figure 5.3. Therefore, $g_c = 0$ (essential lasing condition of gain-saturation point where total loss is equal to the total mode gain hence cavity round trip gain is equal to zero [254]) is achieved only at the dominant laser modes, but not at λ_p. It can be noted that lasing wavelength remains constant at λ_N mode as long as $\lambda_p < \lambda_N + \frac{\Delta\lambda_m}{2}$ and at $\lambda_p = \lambda_N + \frac{\Delta\lambda_m}{2}$, λ_{N-1} begins to dominate and again this remains constant until $\lambda_p = \lambda_{N-1} + \frac{\Delta\lambda_m}{2}$ and the dominant lasing mode will change to λ_{N-2}. Hence it can be clearly noted that, using this method, the wavelength is tuned in a discontinuous way although the cavity gain peak (λ_p) could be varied smoothly. Therefore, this tuning scheme will not facilitate access to all the wavelengths within the tuning range.

5.3.1.2 Tuning of comb-mode spectrum

In this tuning scheme λ_p is kept constant while shifting the comb mode spectrum. The shift of the comb mode spectrum can be described as $\lambda_i = \lambda_i^0 + \Delta\lambda_i$ (for the ith mode), where, λ_i^0 is the initial position before tuning. The behaviour of the tuning mechanism is illustrated in figure 5.14.

According to equation 5.5, the shifting of the comb mode spectrum should be done by changing the optical length which is $n_{eff}L$. The cavity length is practically difficult to change, hence it is the refractive index of the cavity that is changed. As a result of the tuning mechanism the total gain characteristic undergoes an amplitude change as shown in figure 5.4. Again, lasing occurs for mode i if $|\lambda_p - \lambda_i| < \frac{\Delta\lambda_m}{2}$. Although the longitudinal number will not change in this tuning scheme, the mode wavelength changes linearly with $\Delta\lambda_c$. Stepwise continuous regimes are obtained until a mode hop to the next higher mode by yielding a downward wavelength jump at the borders of these continuous regimes (e.g. $\Delta\lambda_c = \frac{\Delta\lambda_m}{2}, \frac{3\Delta\lambda_m}{2}$ ….).

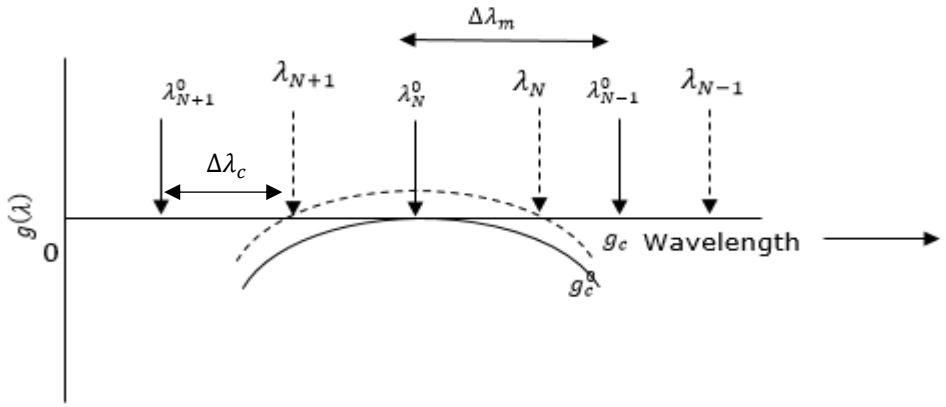

Figure 5.4: Wavelength tuning of a laser by shifting comb-mode spectrum [254]

During both tuning schemes discussed above, a discrete behaviour of the obtained wavelengths is observed. However, by performing both tuning schemes simultaneously, a considerably improved tuning performance could be achieved.

Wavelength tuning of laser diodes requires electronic control of the gain peak wavelength or the comb mode positions. Electronic wavelength tuning involves controlling the refractive index of the cavity medium using three different methods: (1) carrier injection which is related to the free-carrier plasma effect [258], [259]; (2) application of an electric field which is related to the quantum confined stark effect [260], [261]; (3) by temperature control related to the thermal tuning effect [262], [263].

A complete tuneable laser diode consists of an integrated optoelectronic circuit, compromised of an active region, a wavelength selective tuneable reflector and/or tuneable phase shifter. The integration of tuning sections and the active region could be arranged in two directions - either in the longitudinal/horizontal direction or the transverse/vertical direction. The transverse integration leads to DFB type tuneable lasers, whereas longitudinal integration results in DBR type tuneable lasers.

The tuneable laser used for this project is a three section DBR laser due to its less complex tuning mechanism when compared with a four section tuneable laser and the availability within the research group. Therefore, the discussion

that follows will focus mainly on DBR tuneable laser structures. DBR type lasers use longitudinal integration of the active region and tuning elements and can be represented as shown in figure 5.5. According to figure 5.5, tuning section 1 allows the electronic control of cavity gain characteristic λ_p and tuning section2 allows phase control or the comb mode spectrum tuning.

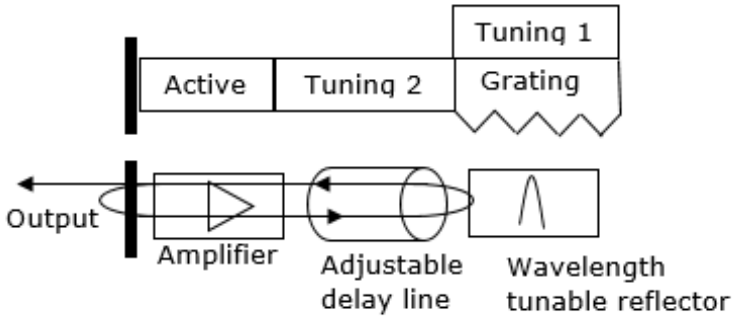

Figure 5.5: Longitudinal integration of active region and tuning elements in a DBR wavelength tuneable laser structure [264]

5.3.2 Wavelength Tuneable Two section DBR laser

A two section DBR laser is made by longitudinally integrating a tuneable Bragg reflector with an amplifying section. There are two available configurations as shown in figure 5.6 - one with a passive DBR structure (5.6 (a)) and the other with an active DBR structure (5.6 (b)). On both structures the P-electrode is divided into two and the n-electrode provides an electronic common [264]. Current I_a controls the length L_a of the active region and hence controls the optical gain and power. Current I_B controls the length of Bragg section L_B and hence controls the laser emission wavelength.

An active DBR region structure provides simpler fabrication and good light coupling over the alternative passive structure.

A typical tuning characteristic curve for a two section DBR laser is shown in figure 5.7. In figure 5.7, the longer active length device has 17 successive longitudinal modes, while the shorter active length device has 9. Therefore the tuning between mode hops are more pronounced for the shorter active length

device. A two section DBR laser only allows tuning of the spectral shape of the cavity gain by tuning of the Bragg wavelength. Due to lacking the option for comb-mode spectrum tuning [264], discontinuous tuning behaviour could be observed with mode hops in the tuning characteristic curve.

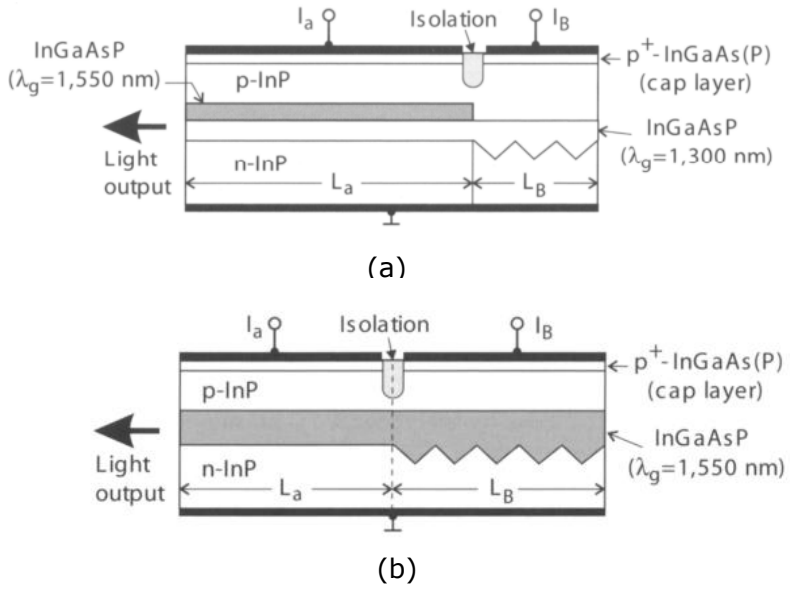

Figure 5.6: Tuneable DBR structure with (a) active-passive structure (b) active-active structure [254]

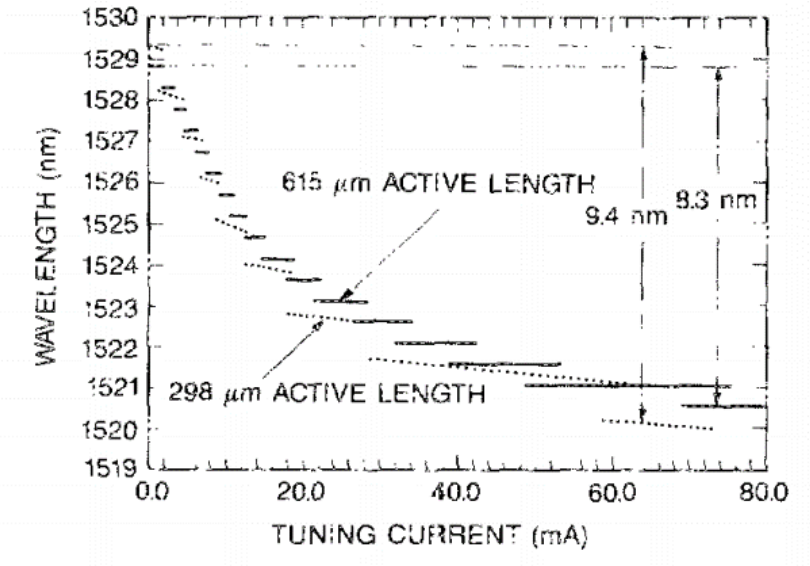

Figure 5.7: Bragg tuning current of two section DBR laser [265] *at two different active lengths(L_a) solid curve is for 615 μm length and dashed line curve is for 298 μm length.*

5.3.3 Wavelength Tuneable Three section DBR laser

The limitation with the two section tuneable DBR laser is the lack of continuous wavelength tuning. Therefore, the three section DBR laser provides improvement to the two section laser by allowing continuous tuning done by the addition of a phase tuning section. Figure 5.8 illustrates a structure of three section tuneable DBR laser. The phase shifter acts as an adjustable delay line and this will control the comb mode spectrum. This structure, with three different electrodes, provides three independent controls. Optical gain and power are controled through the control of current I_a, shifting the comb mode spectrum through tuning of current I_p and the cavity gain peak wavelength is selected by the Bragg wavelength (tuning the Bragg current (I_B)) of the passive Bragg reflector.

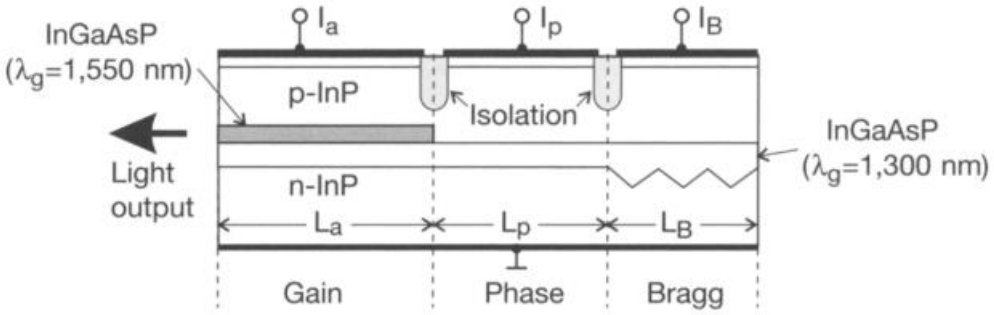

Figure 5.8: Three section wavelength tuneable DBR laser structure [254]

In a three section DBR laser, the wavelength can also be changed by controlling the current I_B. Hence, the lasing wavelength of a three section tuneable DBR laser is a function of all three currents. This was demonstrated experimentally by Koch et al. [265] and is illustrated in figure 5.9. In figure 5.9 I_d is the Bragg current. One current is always varied keeping the other two currents are fixed for each plot. As can be seen, 5.8 nm of discontinuous tuning has been achieved. Moreover, during this experiment it was also noticed that by tuning two currents I_a and one of the other two currents and by keeping the ratio I_B/I_p constant, a continuous, smooth wavelength tuning was achieved for a tuning range of about 3 nm.

The theoretical studies [266],[267] and the experimental studies [268]–[270] which involve optimization of the tuning of 3 section DBR lasers suggest a maximum continuous tuning range of the order of 6.5 nm while a discontinuous tuning range can go more than 10nm.

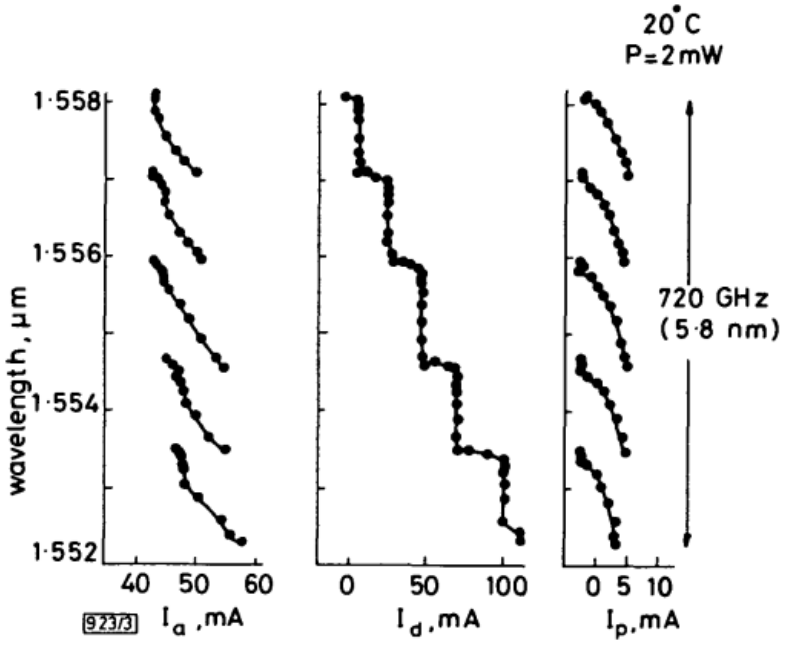

Figure 5.9: Laser range tuning by controlling three currents [265]. *I_d is equal to the Bragg current (I_B) in the discussion*

The wavelengths which are not accessible during such a discontinuous scheme could be tuned using quasi-continuous tuning in a three section tuneable DBR laser. Figure 5.10 shows an experimentally obtained quasi-continuous tuning curve for a three section tuneable DBR laser, demonstrating 10nm of tuning.

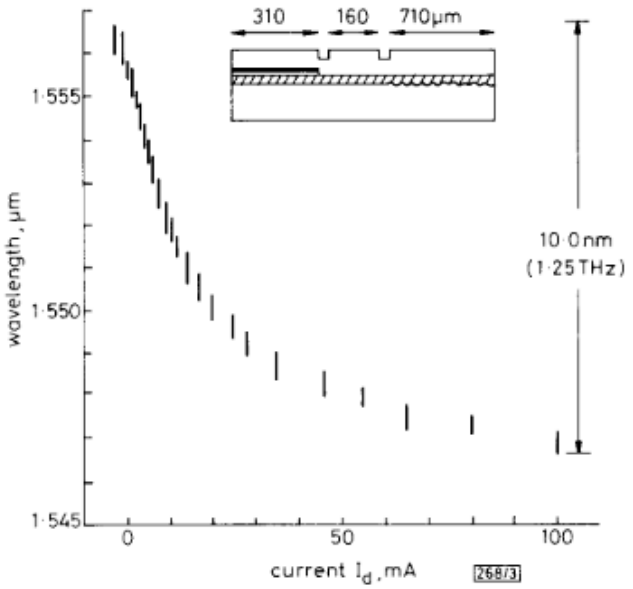

Figure 5.10: Quasi-continuous tuning of a three section tuneable DBR laser [271]

The vertical lines represent the continuous regimes achieved by tuning I_p for a fixed I_B.

By having the right combination of I_B and I_p, all continuous wavelength tuning could be achieved for a particular laser gain. For that reason, it is crucial to have a calibration map of the laser and saved database of wavelengths and currents, as well as a computer aided system to control and access the required currents and hence the necessary wavelengths.

5.4 Development of a miniature FBG interrogator for an FBG patch contact pressure sensor for healthcare applications

As explained in chapters 2 and 4, the measurement of sub-bandage pressure in healthcare environments is important in the treatment of pressure ulcers and similar conditions. The FBG contact pressure sensor detailed in chapter 4 is an ideal solution for this. However, this requires a miniaturised and wearable FBG interrogation system.

As discussed in section 5.2, FBG interrogation using a tuneable laser provides advantages, such as high output power and better resolution, over the other FBG interrogation techniques. Tunable lasers are also compact devices (a tunable laser with a butterfly package has a footprint size of 12.7 mm x 30 mm). The factors mentioned above are the main motivation to use the wavelength

swept tuneable laser FBG interrogation technique for the design and development.

5.4.1 Proposed FBG Interrogation method

The proposed FBG interrogation system consists of tuneable laser, current driver, photo detection circuit and a control circuit. A three section tuneable DBR laser, XM0167 from Xeston Technologies Ltd, is used as the light source. This tuneable laser typically produces a very narrow bandwidth of light and the central wavelength of the emission light can be tuned over a range of 9nm (1535-1544 nm). The proposed FBG interrogation technique uses the wavelength sweep method. The spectrum of wavelengths (~ 9 nm) illuminated the FBG by tuning the DBR laser. The FBG reflection spectrum is then detected using a photo detection circuit. For continuous and smooth tuning, a look-up table, where the relationship between tuning current and wavelengths is stored and implemented, is required. The reflected light from the FBG sensor will be guided into the photo detection circuit. The reflected signal is plotted using a LabVIEW interface. In the initial stages of this project, an Arduino board was expected to be used as the control unit. The plan was to develop a more sophisticated microcontroller unit in the later stages. A block diagram of the FBG interrogation system is shown in figure 5.11.

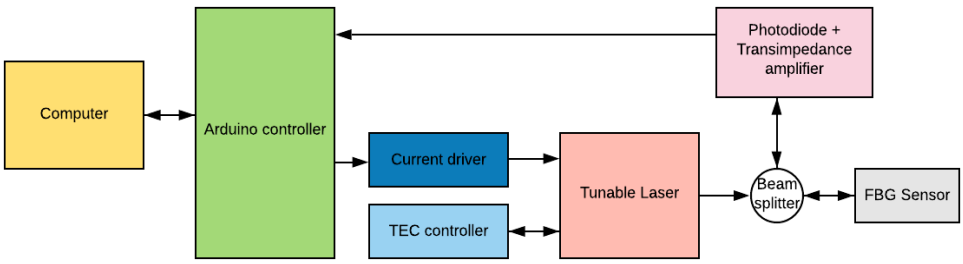

Figure 5.11: Block diagram of proposed FBG interrogation system

In the following sections, each part of the bock diagram is explained in more detail.

5.4.1.1 Three section DBR laser module

In this project, a three section DBR tuneable laser (figure 5.22) was used for development of a miniature FBG interrogator. Table 5.1 shows the maximum current ratings for the laser module. According to figure 5.22, pins 13 and 11 are for the optical gain and power control and provide the functionality of I_a as described in section 5.3.2. Pin 14 provides the control of the comb-mode spectrum enabling the functionality of I_p and pin 12 (rear current pin) provides the functionality of I_B by controlling the lasing wavelength.

An image of the three section laser with its butterfly package and fibre pigtail output is shown in figure 5.12 (b). Butterfly packaging provides safe and easy connection for the fibre sensors. Moreover, the butterfly package comes with a Thermal Electric Cooler (TEC)/ Peltier module, a thermistor and a monitor photodiode in addition to the three section DBR laser module. The heat accumulated during the laser operation should be dissipated well in order to prevent any wavelength shift or degradation of the laser. The thermistor within the packaging is able to detect the temperature. By connecting the thermistor to a TEC controller, the voltage /current required by the Peltier element for cooling is determined. The TEC controller is directly connected to the integrated Peltier element of the tuneable laser and hence the temperature of the laser module is controlled. Moreover, using the integrated monitoring photodetector the power produced by the laser module is monitored. The photo monitoring circuit is completely independent of the laser output and can be used to provide feedback to regulate the power of the laser output.

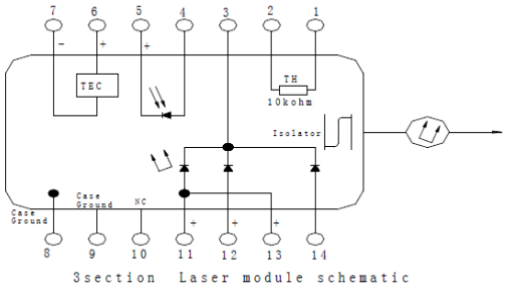

(a) (b)

Pin Assignments			
Pin	**Function**	**Pin**	**Function**
1	Thermistor	8	Case Ground
2	Thermistor	9	Case Ground
3	LD Cathode (-)	10	NC
4	MPD Anode	11	I gain
5	MPD Cathode	12	I rear
6	TEC (+)	13	I gain
7	TEC (-)	14	I phase

(c)

Figure 5.12: (a) Electric schematic (b) picture of the 3 section DBR laser module in the 14 pin butterfly package (c) pin assignment of the three section DBR laser

Table 5.2: Electrical ratings of the three section DBR tuneable laser module

Section	Range	Max limit
Gain	100 mA – 250 mA Threshold (35-40 mA)	300 mA
Rear	0-90 mA	120 mA
Phase	0-5 mA	10 mA

5.4.1.2 Current driver module

The LTC 2662 (figure 5.13) from Analogue devices was selected as the most suitable current driver for the project. This chip was selected as it provides all the requirements (current ranges and voltages, number of channels) needed for the project. This chip is a five channel 12/16 bit current source with a maximum of 300 mA per channel. Since we require three tuning currents and the maximum current required is 300mA (gain current) this provides more than the required number of channels on a single chip.

There are eight programmable current ranges of 300 mA, 200 mA, 100 mA, 50 mA, 25 mA, 12.5 mA, 6.25 mA and 3.125 mA. This is advantageous as the

current resolution per channel can be increased for each current section by selecting only the necessary current range for the section. For example, the gain section requires the range of 300 mA and for 12 bit scheme the current resolution that can be achieved is $\frac{300}{2^{12}} = \sim 0.07\, mA$ while, for the phase section which requires the range of 6.25 mA, using a 12 bit scheme the current resolution that can be achieved is $\frac{6.25}{2^{12}} = \sim 0.0015\, mA$. This chip requires the use of the SPI programming protocol, which is facilitated by any microcontroller programming platform. Additionally, the size of this chip is 5mm × 5 mm which is ideal for the project when considering the size aspect.

Figure 5.13: LTC 2662 chip

For the initial stages of the development it was decided to use the evaluation board DC2692 of the LTC 2662 chip by Analogue devices. The reason is this is a quick and easy way to evaluate the performance of the chip before going to further development. This has pin-outs (turrets) for the SPI communication, power and each channel separately.

Figure 5.14: DC2692 evaluation board for the LTC chip 2662

5.4.1.3 Thermoelectric cooler (TEC) controller

Thermoelectric cooling plays an important role in tuneable laser devices. As explained in section 5.4.1.1, if not controlled properly the temperature built up during the laser module operation may damage or degrade the performance of

the laser. In order to control the temperature within the laser, a thermoelectric cooling controller is connected with the integrated thermistor and the Peltier element. Depending on the temperature measured by the thermistor, the TEC controller alters the voltage across the two junctions of the Peltier element and hence stabilizes the temperature within the laser module. In the initial stages of the development of the miniature FBG interrogator, a commercially available TEC controller by the Thorlabs (ITC 110) was used. In the subsequent stages of development, a high efficiency TEC controller chip LTC1923, Analogue Devices (figure 5.15 (a)), was used with the dimensions of 5 mm x 5 mm which is ideal for the realisation of a miniaturised interrogator. Again, in the first stages of development of the miniature FBG interrogator, the evaluation board (figure 5.15 (b)) of the LTC1923 chip by Analogue devices was used.

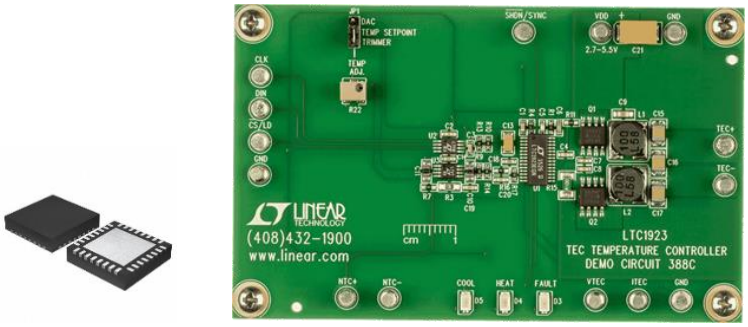

(a) (b)

Figure 5.15: (a) LTC1923 TEC controller chip (b) Development board of LTC 1923

5.4.1.4 Photo detection Circuit

The reflected light from the FBG is directed to a photo detection circuit in order to identify the wavelength. This photo detector will produce an electric current for each wavelength throughout the wavelength sweep of the tuneable laser diode. Using a transimpedance amplifier this current is converted to a voltage. During the development stages, a PDA10CS (EC) simplified photodetector by Thorlabs was used for photo detection.

5.4.1.5 Arduino controller

The Arduino UNO Wi-Fi programmable circuit board consists of Atmega 328P microcontroller and ESP8266 Wi-Fi module. This was considered for use in the

early stages of development because this provides a quick start to the project without the need to design a microcontroller circuit. This device comes with 20 digital I/O pins and 6 Analog I/O pins. The digital I/O pins are important for controlling the current driver through the SPI communication protocol and Analog pins are important to analyse the current signals received by the photo detection circuit. It also provides simple connection to the computer with a USB cable. Moreover, the Integrated Development Environment (IDE) provided by the Arduino is open source and comes with all the standard and specific libraries needed for the programming.

5.4.1.6 Computer Interface

LabVIEW (Laboratory Virtual Instrument Engineering Workbench) is a graphical programming language developed by National Instruments. This is a sophisticated programme environment ideal for applications that require testing, measuring and control of the processes with the rapid access to hardware and data. LabVIEW was selected as the main programming language because it can be used to program an Arduino using the LINX open source software and at the same time can be used to provide a graphical interface for controlling the system, analysing the data and plotting results all within a single interface. LINX by LabVIEW is an open source software which provides easy to use LabVIEW VIs for interacting with common embedded platforms like Arduino, chipKIT and myRIO. LINX is a hardware abstraction layer that allows the user to have a single LabVIEW interface with a variety of different hardware devices. Therefore, LINX helps to bridge the gap between the physical Arduino and the LabVIEW software.

5.4.2 Current control and calibration system

As discussed in section 5.2.1, in order to achieve a continuous wavelength sweep over the wavelength tuning range of the tuneable laser, a look-up table is required. Therefore, in this section of the thesis the calibration work of the laser is described.

5.4.2.1 Software development

The integrated circuit chip of the current driver has a SPI interface for receiving the current values. The communication protocol is shown in figure 5.16. When the chip select line is low, the data on the SDI pin is loaded into the shift register on the rising edge of the clock pin. First, the 4 bit command (C3-C0) is loaded followed by the 4 bit DAC address (A3-A0) and then 16 bit data word in binary format. The data word comprises a 16 bit input code ordered with the most significant bit first (MSB). The data is transferred to the LTC2662 when the chip select is low. The rising edge of the chip select line ends the data transfer.

The developed front panel and block diagram are illustrated in figure 5.17. The LTC2662 includes a high voltage multiplexer for monitoring the voltage and current at the output pins, which was included in the LabVIEW user interface to enable independent current monitoring. The options for selecting the preferred current channel with the preferred current range were included in the User interface. Moreover, options for the user to control the clock frequency and display the current written to the channels are included in the user interface.

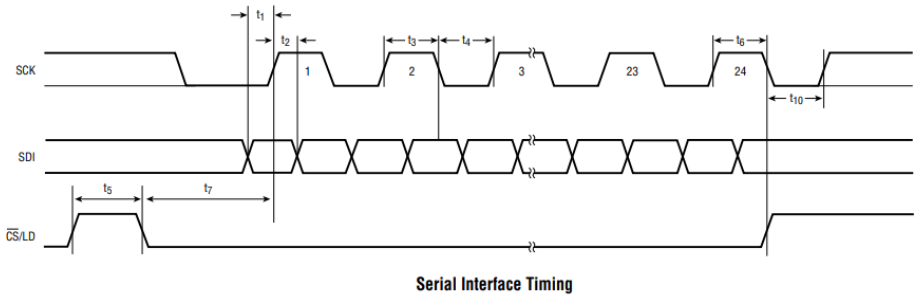

Serial Interface Timing

(a)

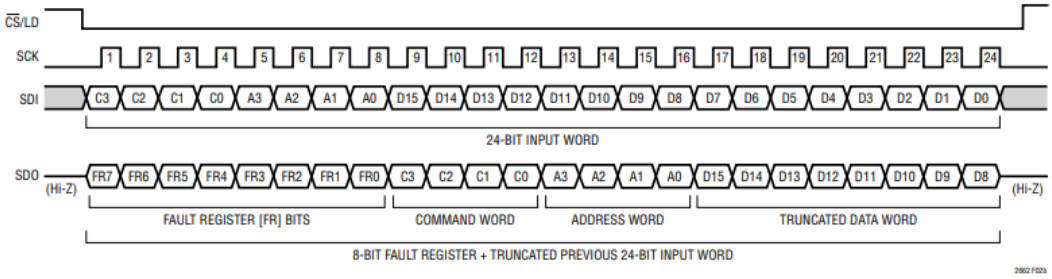

24-Bit Load Sequence

(b)

Figure 5.16: (a) Timing diagram for the current driver chip (b) 24 bit sequence

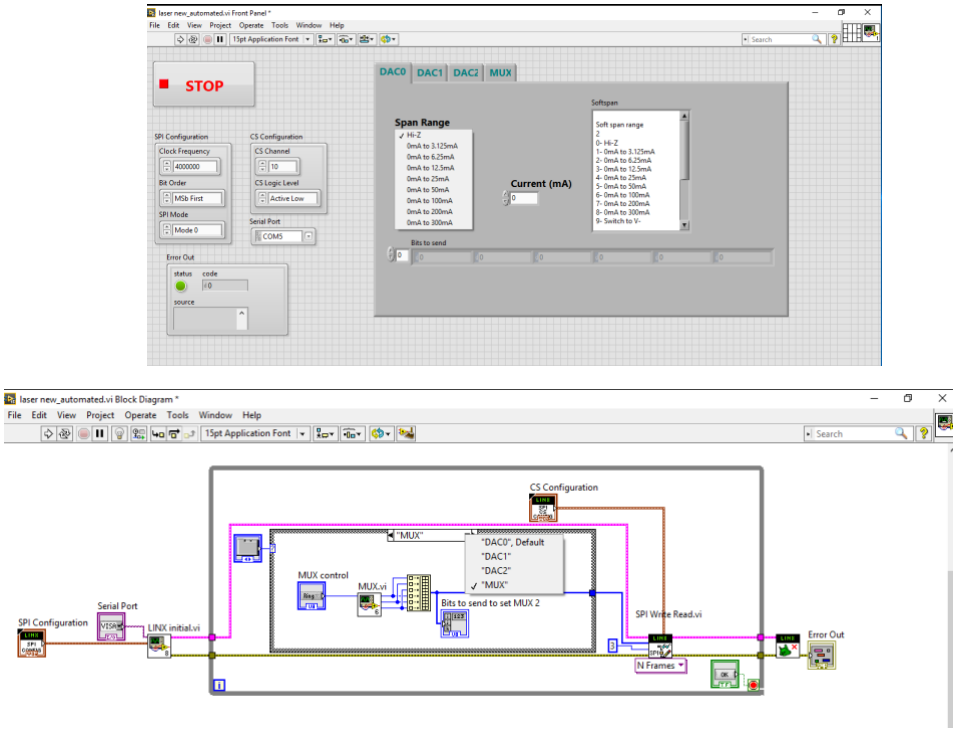

Figure 5.17: LabVIEW current control user interface(top) and block diagram (bottom)

5.4.2.2 Testing the current driver

According to the discussion in section 5.2.4 it was clear that for the tuning and characterization of a three section tuneable laser it is important to provide an accurate constant current for each tuning section of the laser to achieve and maintain a specific wavelength. Any fluctuations of the current will cause a change of the wavelength. Therefore, one important aspect is to maintain a stable output current during the operation of the tuneable laser. The current stability of the current driver was first tested by connecting a resistor load to the current driver followed by connecting the tuneable laser directly to the current driver. The results showed stable current during the operation of the laser over a duration of 30 minutes. This can be seen in figure 5.18, which depicts testing the current stability at different current levels by promptly changing the current levels.

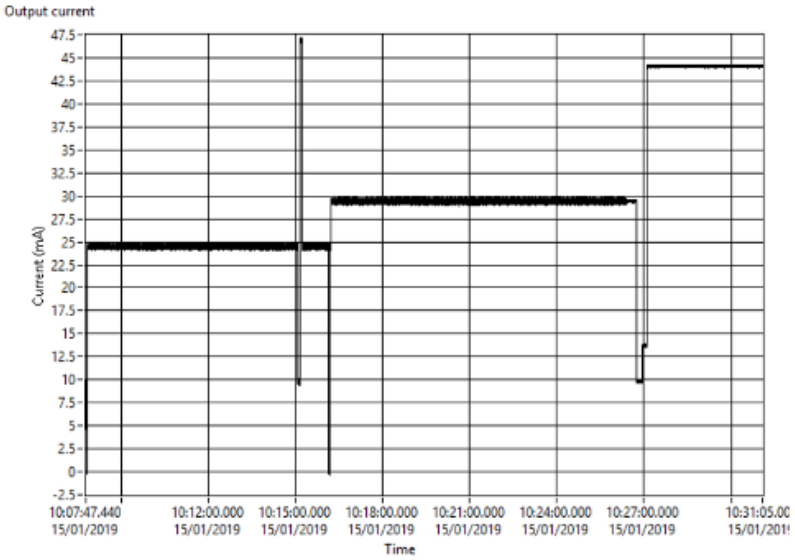

(a)

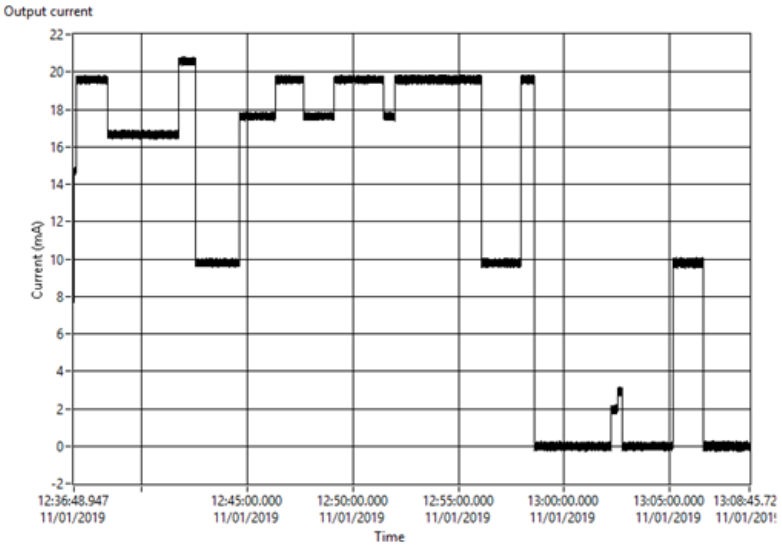

(b)

Figure 5.18: plots of MUX measured output current vs time for two channels (a) and (b)

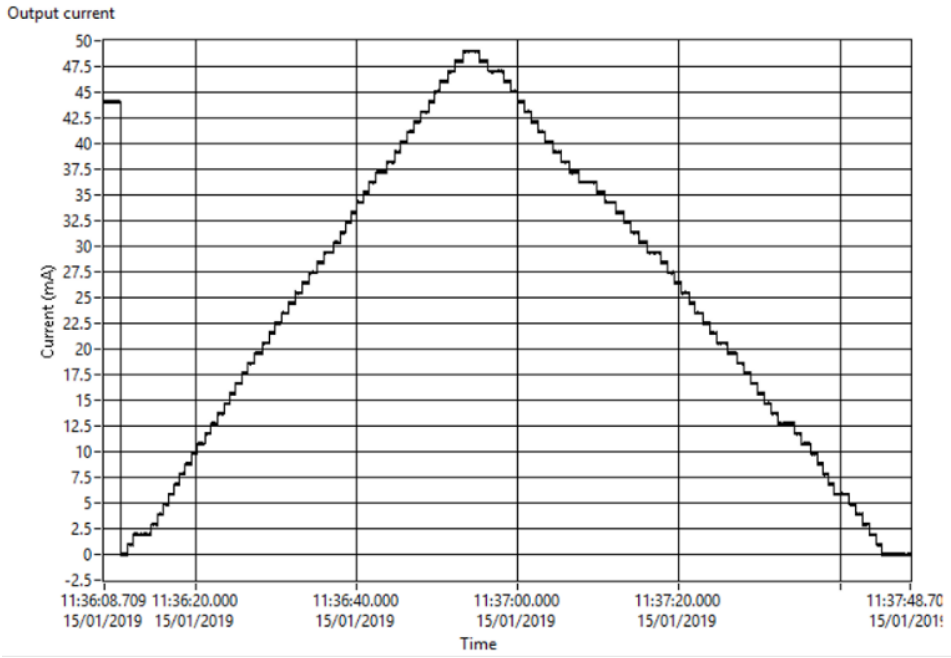

Figure 5.19: plot of MUX measured output current vs time, current has changed in 1 mA steps over a range of 0-49 mA

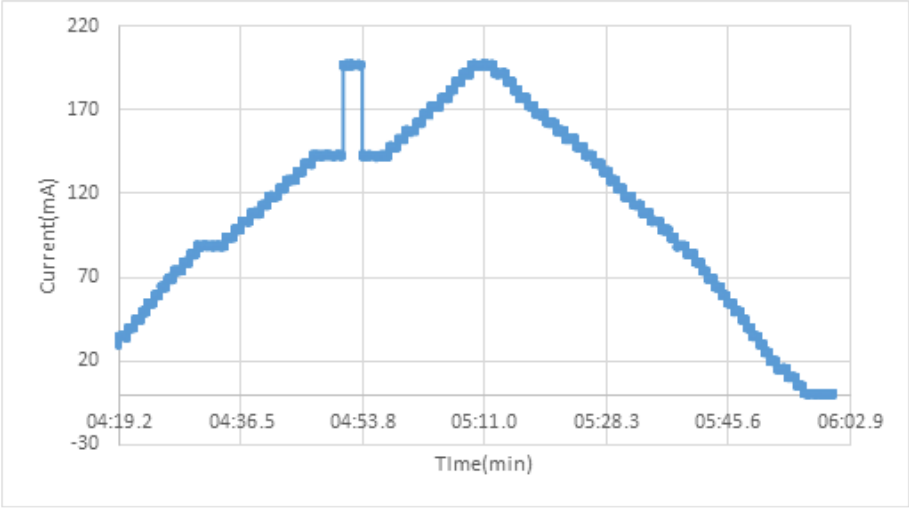

Figure 5.20: plot of measured output current for current sweep from 0-200mA in steps of 5 mA. At time 04:53 tested for an abrupt change (140mA to 200mA) in the current

The output current was monitored using MUX. Figure 5.19 shows the output current change in steps of 1 mA over a range of 0-49 mA. Figure 5.20 shows the output current for control of the current in the range of 0-200mA with 5mA steps. The whole current range could be achieved with good resolution during this tuning.

5.4.2.3 Tuneable laser calibration system

Figure 5.31 illustrates the experimental setup used for the wavelength calibration. The software control interface was developed using LabVIEW. An optical spectrum analyser (OSA) (Anritsu MS9710C) was used for the monitoring of the FBG wavelength spectrum. A LabVIEW compatible measurement interface was created for the OSA. After each scan of the spectrum, the FBG peak wavelength and power were extracted and plotted against the tuning current.

Figure 5.32 shows the discontinuous tuning scheme performed by keeping the gain section current fixed at 150 mA, the phase section current fixed at 0 mA and tuning rear current from 0-90 mA in 0.1 mA steps. The typical discontinuous behaviour expected from a three section tuneable laser is observed. The total achievable tuning range for discontinuous tuning was ~9 nm. Power fluctuations within a range of 4mW during the tuning are also observed (see figure 5.23). It is clear that as a result of tuning the power fluctuates in a periodic pattern and the overall power reduces. This behaviour could be explained by considering the side mode suppression ratio (SMSR) of a tunable DBR laser [272]. SMSR is the power ratio at the lasing fundamental mode/wavelength to its nearest allowed mode [273]. The wavelength of the main mode changes with tuning and a weaker side mode starts to become stronger and the main mode moves away from the centre of the Bragg band. At this point, SMSR is highest. Both modes experience equal loss when they are symmetric about the FBG wavelength. Any further tuning contributes to a laser mode hop and then the stronger peak will dominate over the other. Therefore, at each mode hop the output power reaches a local maximum during the tuning. This contributes to the periodic pattern observed in the output power during tuning. This agrees well with the datasheet (see the appendix B) of the tunable laser which stated that during the wavelength scanning of 1535-1544 nm the power varies in a periodic pattern within a range of 9.8 dBm- 7.4 dBm which is equal to 4.1 mW.

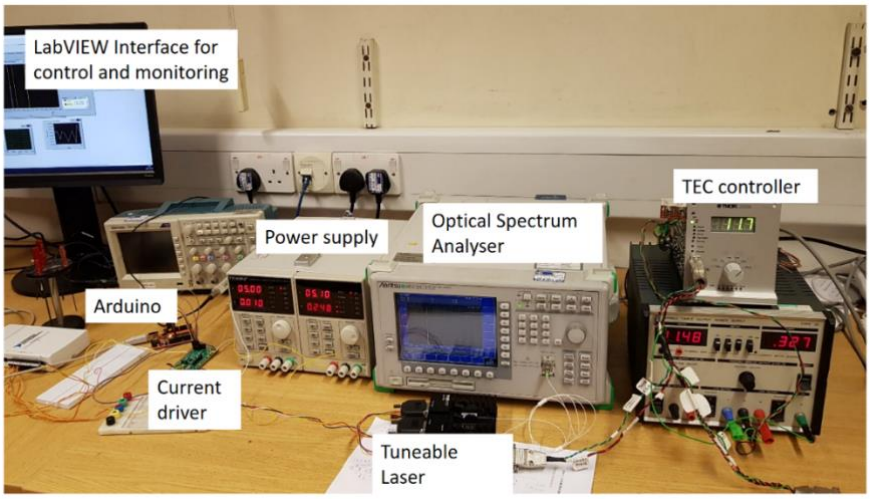

Figure 5.21: Tuneable laser calibration system

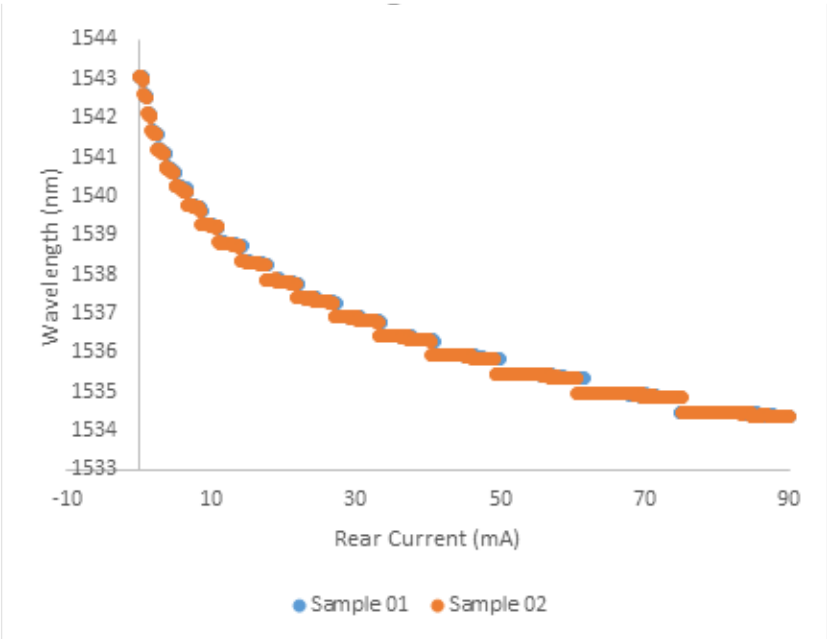

Figure 5.22: Wavelength obtained for the rear current tuning over 0-90 mA range with gain =150 mA and phase =0mA. This is an example for discontinuous tuning scheme of a tuneable laser.

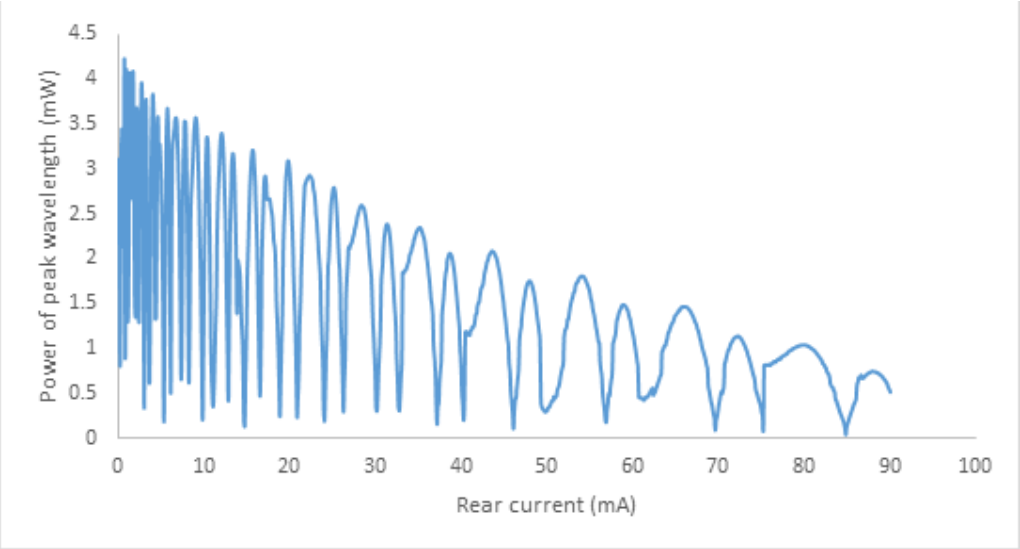

Figure 5.23: Power fluctuations during the discontinuous tuning of the tuneable laser

Another important aspect checked during the initial stages of the experiments was the wavelength stability of the tuneable laser during its operation. In order to check the stability, a particular current value was fixed and a measurement per minute was taken up to a total of 100 minutes. Then, the standard deviation of these measurements was calculated. For example, the gain current was fixed at 150 mA, the phase current at 0mA and the rear current was fixed to 2 mA, 10 mA, 50 mA, 70 mA and 90 mA for different tests. Figure 5.24 shows the results obtained.

According to results obtained it is clear that the wavelength is stable during the time of its operation and shows a small standard deviation value in the order of 0.01 pm.

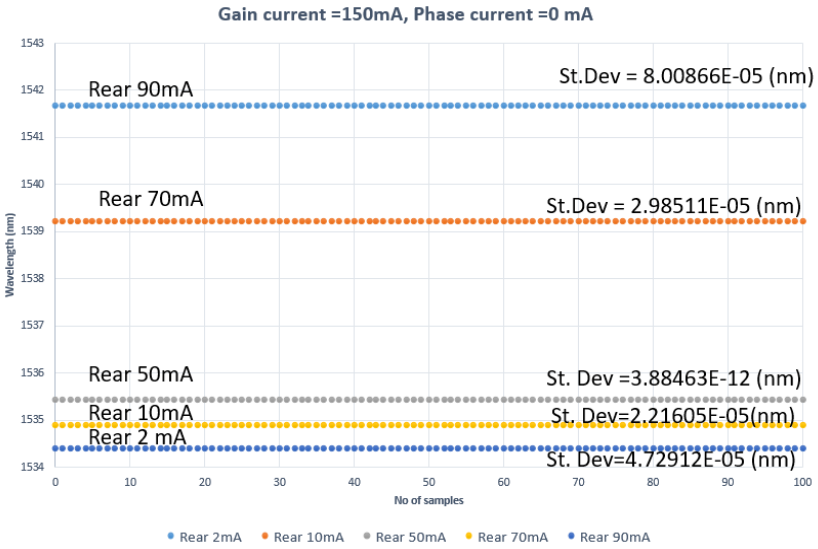

Figure 5.24: Plot of determining the stability of the FBG measured wavelength during tuneable laser operation.

5.4.2.4 Automated Measurement system

In order to achieve a continuous wavelength sweep, it is crucial to obtain the corresponding current combination. According to the table 5.1, the rear current range is 0-90 mA and phase current range is 0-5 mA. If the rear current tuned in 1mA steps and the phase current tuned in 1 mA steps, the total combinations of measurements is 546. However, in order to achieve a discontinuous behaviour during the wavelength sweep allows a fine tuning and achieve all the accessible wavelength measurements. For example if the rear current is tuned in 0.1 mA steps and phase is tuned in 0.1 mA steps the total number of measurements will be equivalent to 54600. Recording this number of measurements is not easy with manual tuning and therefore an automated measurement system was developed. Since the sampling frequency of the OSA is low and takes 0.5 seconds for a single spectrum it was replaced with an Ibsen 256USB FBG interrogator which allows a 3 kHz sampling rate per single spectrum. This Interrogator is provided with the LabVIEW compatible source codes and hence it was easy to develop the measurement and recording LabVIEW interface.

A global variable was created for both FBG interrogator measurements and current control. Sequential programming methods (flat sequences) are used in

the timed data logged measurement operation. This way there is no data loss. While the measurement is made, the global variable is turned off and on the next available sequence where the measurement is saved and appended into a text file, the global variable will be turned on. Turning on/off the global variable initiates a current step change in the current control. In this way the current and wavelength data were recorded without any data loss. When all the available current combinations have been tested, the tuneable laser will automatically turn off by putting the output current terminals to high impedance mode.

Figure 5.25 shows the demonstrated wavelength tuning curve for the gain current fixed at 100 mA, the rear current tuned with 1 mA steps and the phase current tuned with 1 mA steps. When compared with the discontinuous scheme there is a slight reduction in the total tuning range. Although the total achievable range is 8.4nm there is a comparatively large wavelength discontinuity that occurred from 1541.63 – 1542.19 nm and hence the effective tuning range is considered to be ~ 7 nm.

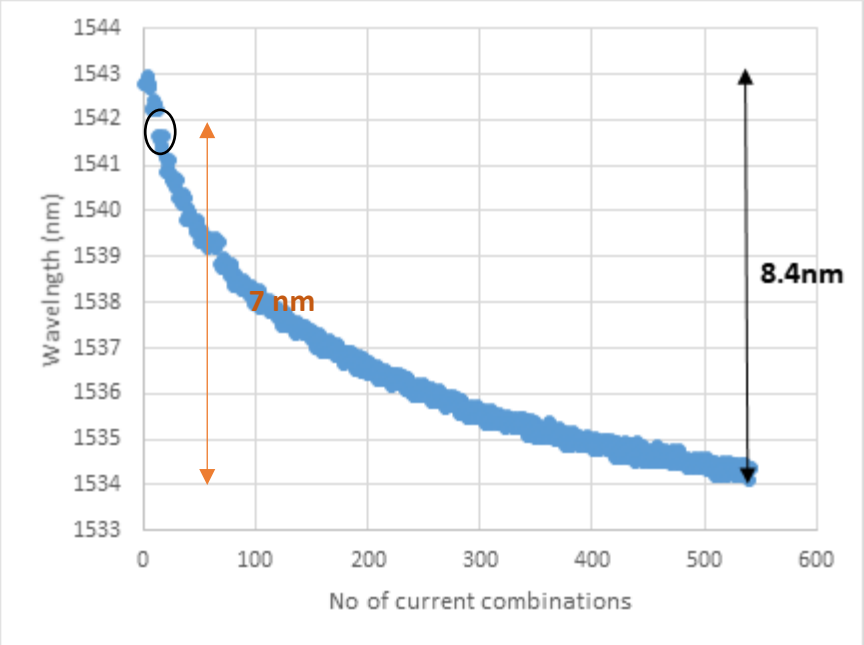

Figure 5.25: Wavelength tuning with Phase current (1mA step), rear current (1 mA step), Gain is fixed at 150 mA, total wavelength range of 8.4 nm and 7 nm of effective continuous tuning range was achieved

Figure 5.26 shows the wavelength tuning curve for the gain current fixed at 100 mA, the rear current tuned in 0.1 mA steps and the phase current tuned in 0.5 mA steps. It can be clearly seen that a continuous wavelength tuning for a tuning range of 9nm could be achieved with a wavelength resolution of 0.01 nm.

Using these measurements, three lookup tables were created which have wavelength resolutions of 0.01 nm, 0.1 nm and 1 nm. This is an important factor in the FBG interrogation system as the resolution of the wavelength sweep affects the system measurement speed. For example, the lookup table with resolution 0.01nm will create $\frac{9\ nm}{0.01nm} = 900$ sample points, which means that in order to achieve a single measurement using the proposed setup 900 current combinations should be accessed. On the other hand, the lookup table with resolution 0.1 nm will create 90 sample points and hence increases the scanning speed by a factor of 10 for a single measurement.

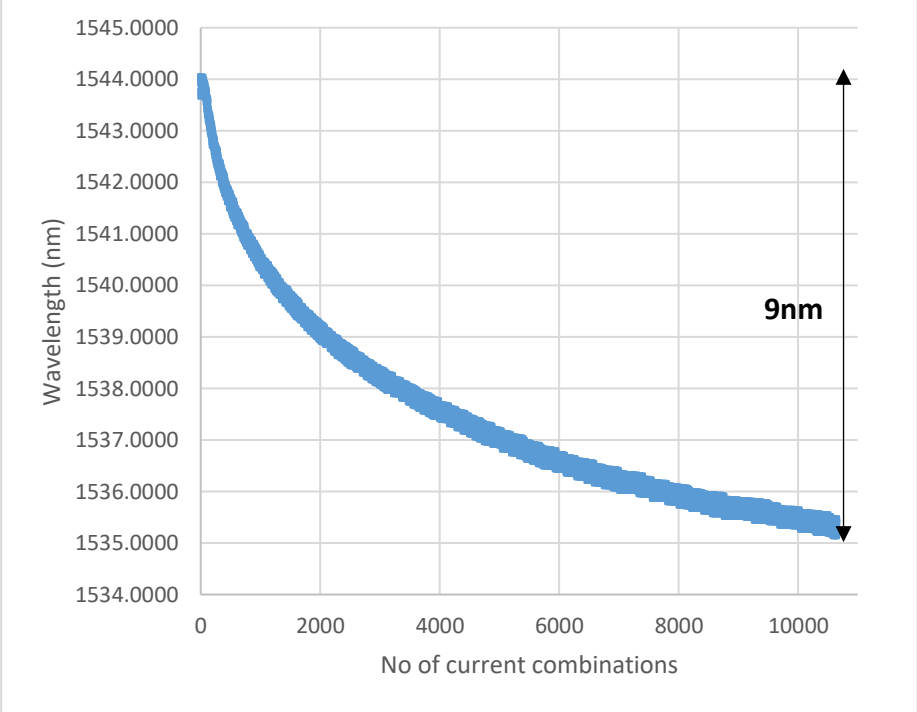

Figure 5.26: Wavelength tuning with Phase current (0.1 mA step), rear current (0.5 mA step), gain current is fixed at 100 mA. A continuous wavelength range of 9 nm was achieved

5.4.3 FBG Interrogation system

The FBG integration system is illustrated in figure 5.27. The system was powered using an external power supply while the Arduino was powered by the computer using USB cable. The output from the photodetector was directly fed to the Analogue pins of the Arduino.

The Arduino microcontroller has access to the lookup tables and therefore access to the current combinations required for driving the tuneable laser in order to perform a wavelength sweep across the tuning range. The Arduino controls the current driver while receiving the data from the photo detector and these data are then passed to the computer. The computer then plots the amplitude of the photodetector signal versus the wavelength data in order to produce the wavelength spectrum.

In this kind of data acquisition, where two parallel operations (wavelength sweeping and collecting the data from photodetector) take place, it is important to retrieve all the values from the photodetector without losing any data. Hence, a producer/consumer design pattern is ideal for the LabVIEW programming. As with the standard Master/Slave design pattern, the Producer/Consumer pattern is used to decouple processes that produce and consume data at different rates. The Producer/Consumer pattern's parallel loops are broken down into two categories; those that produce data, and those that consume the data produced. Data queues are used to communicate data between loops in the Producer/Consumer design pattern. These queues offer the advantage of data buffering between producer and consumer loops. The block diagram of such a Producer/Consumer design is illustrated in figure 5.28. In the user interface, the FBG spectrum, the raw data and also the FBG spectrum using Gaussian fitted data are plotted (Figure 5.30). Three photographs taken while performing a simple strain test are also included.

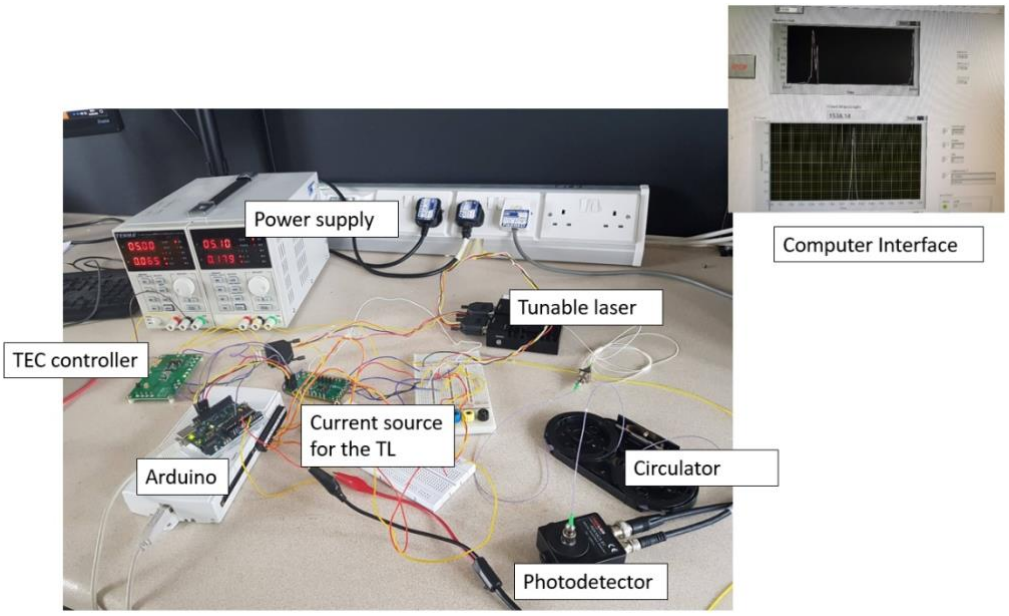

Figure 5.27: FBG interrogation system

A 3mm long FBG with a central wavelength of 1538.1 nm written in the University of Nottingham optics laboratory was used for the testing of the system. This FBG was first checked using a commercial interrogator, SmartScope FBG interrogator from SmartFibres. The observed spectrum is shown in figure 5.29. Figure 5.30 shows the same FBG sensor tested using the developed system. The side small peak feature observed in the SmartScope was observed in FBG spectrum obtained using the developed system. Moreover, the SmartScope showed a peak wavelength of 1538.1484 nm while the developed system showed a peak wavelength of 1538.14 nm. This indicates the built system was producing reliable results when compared with the commercial one.

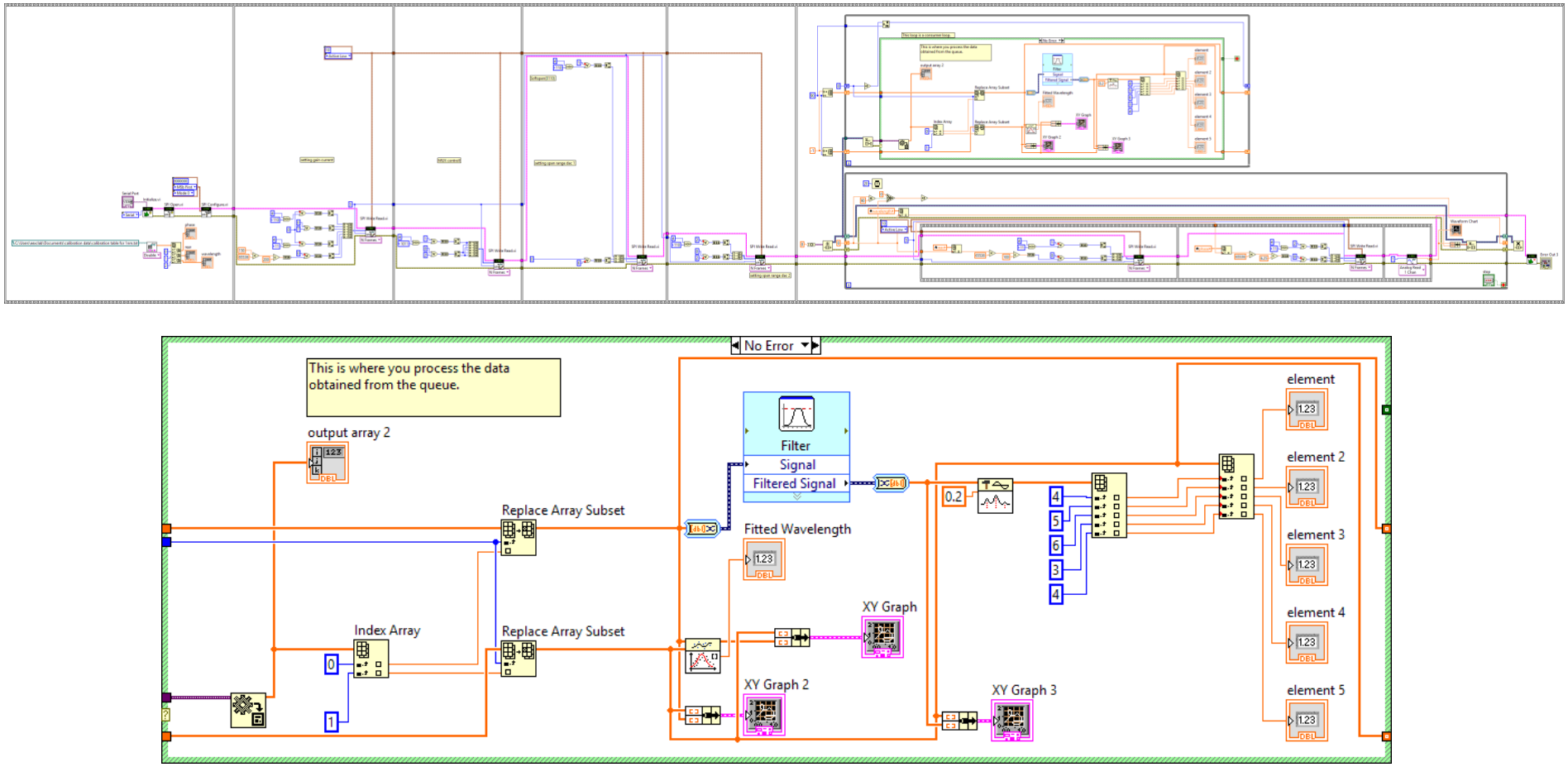

Figure 5.28: LabVIEW block diagram (producer/consumer loop) of the data acquisition and control interface for the FBG interrogator

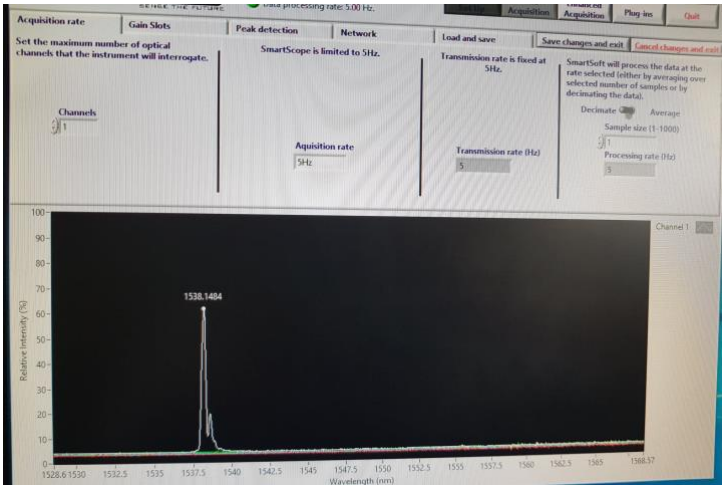

Figure 5.29: FBG spectrum tested from SmartScope, Observed wavelength is 1538.1484 nm

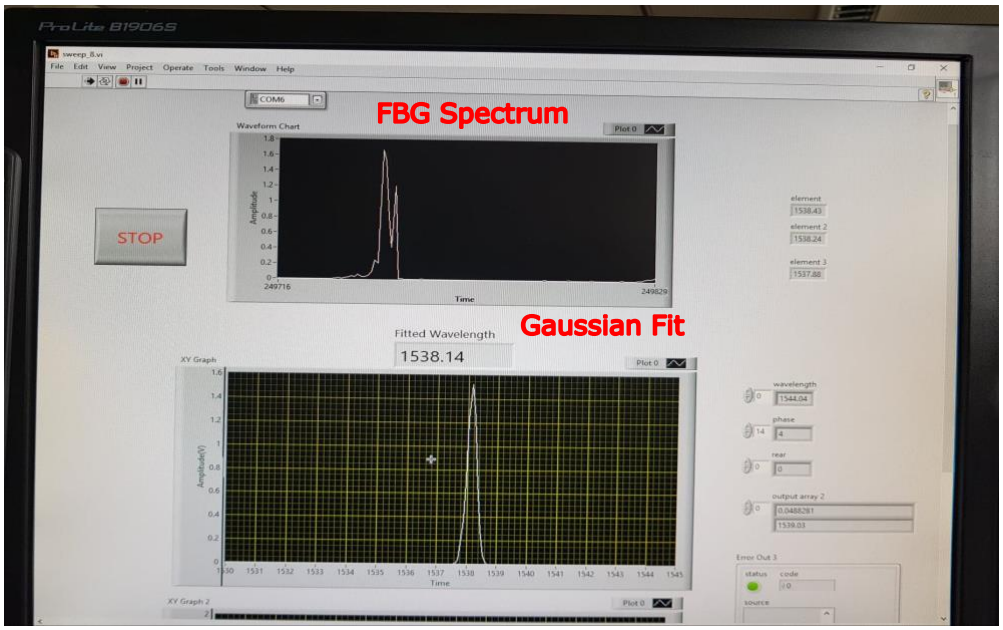

Figure 5.30: FBG spectrum observed from the FBG interrogator

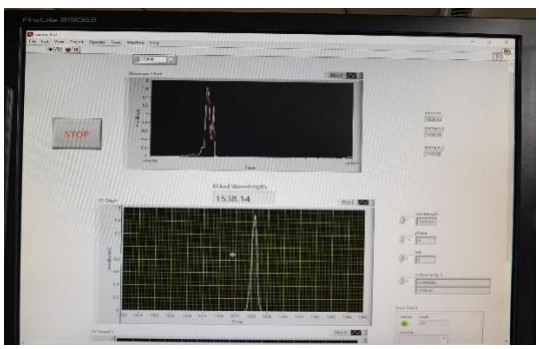

1538.14 nm

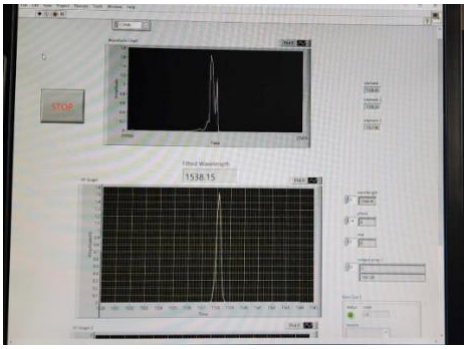

1538.15 nm

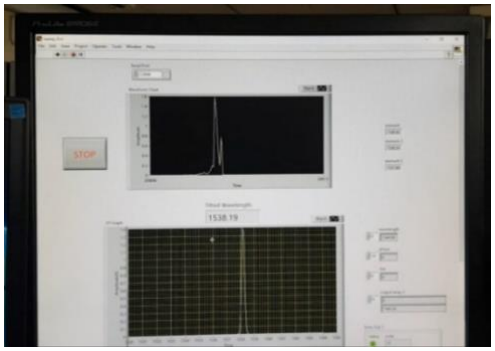

1538.19 nm

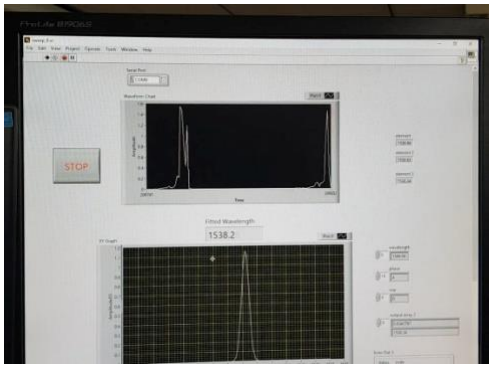

1538.2 nm

Figure 5.31: Testing the FBG interrogator with a applying straining to the FBG sensor

Figure 5.31 shows four images that were taken while performing a simple strain test. As the FBG is straining a wavelength increase was observed.

Table 5.3: Bill of material for the FBG interrogator system

Item	Qty	Unit price(£)	Total (£)
3 section tuneable laser	1	800.00	800.00
Digital to Analog Converters - DAC 16-Bit 5-Channel 300mA Current Source DAC	1	33.19	33.19
LTC1923 1923f High Efficiency Thermoelectric Cooler Controller	1	33.66	33.66
Micro controller unit	1	20.40	20.40
FDS100 - Si Photodiode, 10 ns Rise Time, 350 - 1100 nm, 3.6 mm x 3.6 mm Active Area	1	11.21	11.21
Miscellaneous			200.00
			1098.46

Table 5.3 includes the bill of materials for the FBG interrogator. Approximately the FBG interrogator costs £1100.

5.5 Conclusion and Future Work

Successful first steps in the implementation of a miniaturised FBG interrogator based on a 3 section tuneable DBR laser were accomplished. However, further work is still required on the hardware development and characterisation in order to develop a truly wearable system.

A circuit diagram including the current drive chip, thermoelectric cooler, and tuneable laser including the necessary electronics was designed and illustrated in figure 5.32. The KiCad open source software was used for the development of the schematic and also for the PCB design. The KiCad generated 3D view of the expected PCB board is shown in figure 5.43. The size of the board is 80 mm x 60 mm.

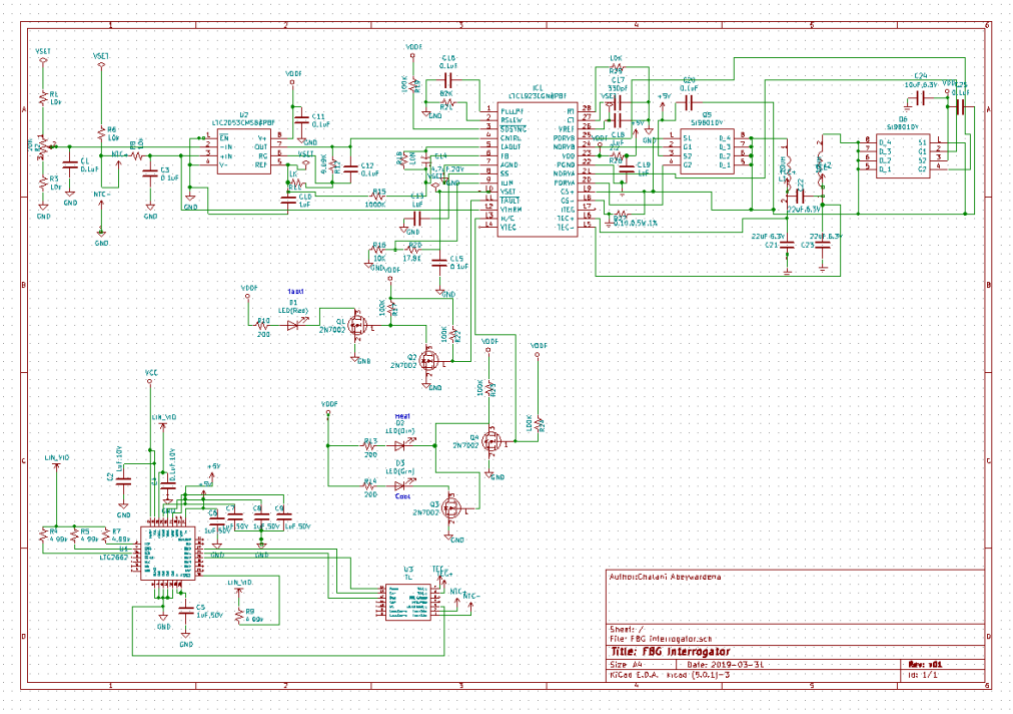

Figure 5.32: Circuit diagram of Tuneable laser + Current Driver +TEC controller

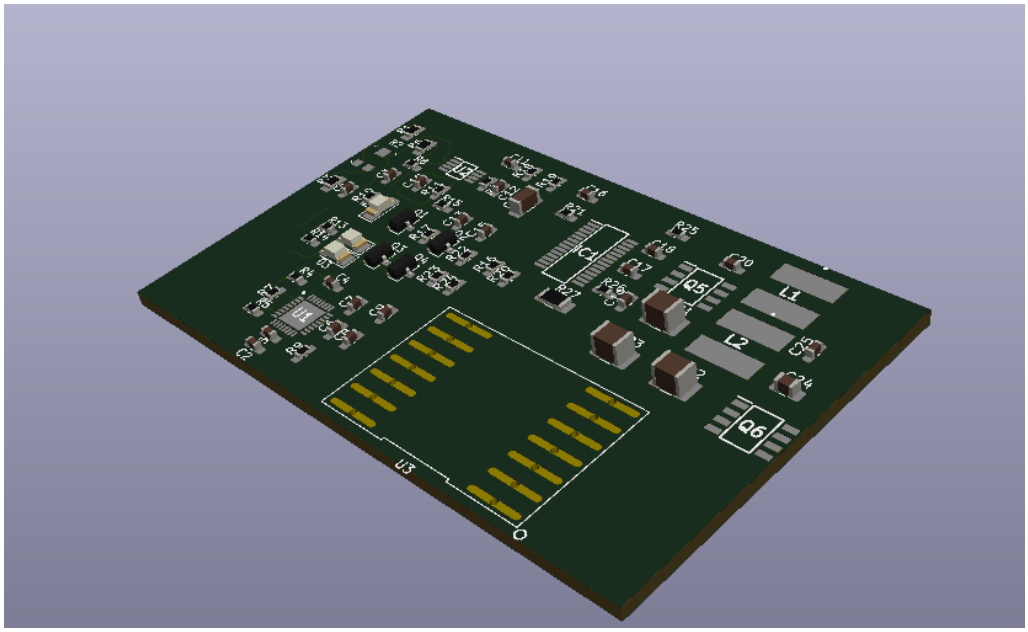

Figure 5.33: 3D view of the PCB design

Currently, the circuit was run using the USB cable connected to the computer. Nevertheless, a power supply and microcontroller unit should be added to the PCB design.

According to the table 5.3, the cost will be not more than £1100 and this can be sold with a 30% mark-up around £1400-£1450. This is a low price for an FBG interrogator when compared with the commercial products available in the market that cost £3000 or upwards (Table 5.1).

One main aspect should be considered when designing the power supply is considering the devices using 5 V power and the devices using 3.3 V separately. Some of the commercial microcontrollers are operated at 3.3 V and some of them operate at 5 V. Depending on the microcontroller used the power regulators should be added to the circuit.

One important matter that requires investigation before designing the power supply is the power consumption of the whole system. An Arduino-Uno, when run by the USB cable, draws a maximum of 400 mA, but when it is run by a dc adapter it could draw up to maximum of 1 A. However, the current consumption per digital I/O pin is 40 mA. 5 pins are used during the operation

which means the maximum current consumption is 200 mA. Current consumption from the microcontroller is 50 mA. Hence the total estimated power for the microcontroller circuit should be 250 mA. The maximum current used by the current driver+ tuneable circuit obtained by the power supply is ~ 180 mA and the TEC controller required maximum current of ~65 mA. The total power consumption ~500 mA. However, there are other factors that should be considered like the power dissipation of the voltage regulator circuits, power capacity of the battery and battery discharging rate. Thus, one potential option is a 12 V battery to power up the circuit with a capacity of 1.2 Ah. This would allow to run the device for approximately two hours. Wi-Fi data communication would also be possible by integrating a commercially available Wi-Fi module such as the ESP 8266.

Another important factor to consider is maintaining a constant output power of the tunable laser during its operation (Figure 5.23). In order to achieve this the monitoring photodiode of the tuneable laser could be used. The current produced in the monitoring photodiode is proportional to the output power as discussed in section 5.4.1.1. Hence this current from the photodiode can be used as a feedback signal for the laser driver circuit in order to maintain a stable power during its operation by changing the gain current. This will be a future enhancement of the system.

The initial steps for a potential miniature single channel FBG interrogator are developed for the application of FBG based contact pressure measurements as discussed in chapter 4. Future potential features that could be added to the system include WiFi data transfer and powering the system by battery for a truly portable device.

Chapter 6

Conclusions and Future Work

6.1 Introduction

This chapter of the thesis presents the main conclusions of the conducted research project and outlines future directions. This chapter also discusses the achievements of the objectives discussed initially in the project aims and objectives (Chapter 1, section 1.2).

6.2 Summary of current research work

There were three main objectives to achieve in this PhD research. The conclusion and the future work for each objective is discussed below.

6.2.1 Miniature fibre optic pressure sensor using Fabry-Perot interferometer

One of the main objectives of this research is to investigate the potential of a miniature fibre optic pressure sensor using Fabry-Perot interferometric technique for invasive medical applications. Targeted applications with the required specifications are included table 2.1. Due to the biocompatiability, small size and flexibility, FP sensors provide an ideal sensing technique for invasive pressure measurements such as arterial blood pressure monitoring, intracranial pressure monitoring, in ophthalmology and gastroenterology applications. The pressure ranges from 0- 40 kPa for these applications and can be provided by the FP sensor.

The sensor consists of single mode silica fibre to carry the light and a Parylene-C pressure sensitive diaphragm. The diameter of the sensor head is 125 μm. Nevertheless with the necessary fibre protections such as fibre jackets the diameter would be 250 μm. Two methods of cavity formation have been identified as: focused Ion beam (FIB) micromachining technique and splicing with a capillary tubing. Additionally, two ways of film deposition have been identified. One method involves using the self-attachment bonding properties

of the Parylene-C film. The second method involves enclosing the fibre tip with a wet film and allowing it to dry so that it attaches to the tip of the fibre. Three sensors have been tested using combinations of these methods. The first sensor was developed by using the FIB technique for cavity inscribing at the tip of the fibre. Then the Parylene-C film of 200 nm was attached to the tip of the cavity by simply launching the fibre towards the film which was supported by a holder. The cavity length of the sensor is 8.7 μm and diameter is 21 μm as confirmed by the SEM measurements. The average achieved sensitivity was around 0.6 nm/kPa with an averaged root mean square error of 2.91 nm/kPa, for a pressure range of 0-70kPa. However, this method suffers from several limitations. The re-deposition caused by the milling process causes poor surface quality of the cavity (this is shown in chapter 3 figure 3.44). This then leads to light scattering. By using a low milling current the amount of re-deposition can be reduced, and this could help to achieve better surface quality. However, there is a compromise between the cavity milling time and the FIB milling current as described in chapter 3. As the milling current reduces, the milling time increases. Therefore, the quality of the cavity could be achieved at the expense of cost and time required per sensor. The second sensor was developed by splicing a fibre capillary to a single mode fibre and cleaving to achieve a micro air cavity. The pressure sensitive Parylene- C diaphragm is attached to the tip using the same method used for the first sensor. This sensor has a fibre cavity length of 26 μm and a diameter of 70 μm. The average sensitivity was 1.03 nm/kPa with an average root mean square error of 0.65 nm/kPa for a pressure range of 0-12 kPa range. The third sensor was created very similar to the second sensor, except for the film attachment technique. The film was attached to the tip of the fibre by using the second method described. This has an average sensitivity of 0.12 nm/kPa with an average root mean square error of 0.107 nm/kPa for a pressure range of 0- 18 kPa with a cavity of diameter of 70 μm and cavity length of 87 μm.

All the sensors showed hysteresis. The calculated hysteresis obtained for the first sensor is 32%, second sensor 12.5% and the third sensor 12%. As the time

of the measurement cycle increases, the hysteresis behaviour started to appear. This was supposed to be an effect of the air permeability of the Parylene-C as discussed in chapter 3, section 3.5.

However the performance of the sensor is limited by the wavelength drift, cross sensitivity to temperature (0.084 nm/Celsius) and longer time response (3 seconds) to be able to use in the targeted application area.

6.2.2 Contact pressure sensing using optical fibre Bragg gratings

Contact pressure measurement is an important aspect in healthcare applications in areas such as pressure ulcers, compression bandage therapy and prosthetics. Due to their flexibility, small sizes, and biocompatibility, FBG sensors are an attractive solution for contact pressure measurement in healthcare. Advantages of FBGs are extensively discussed in chapter 2, section 2.5.5. A successful mathematical model for a highly sensitive FBG contact pressure sensor was developed using finite element analysis (FEA) and transfer matrix technique. This model uses two software packages: ABAQUS CAE FEA tool for the stress/strain simulation due to the pressure applied and MATLAB to simulate the FBG response due to the stress/strain experienced by the FBG. The developed mathematical model is able to identify birefringence of the fibre that may undergo during transverse pressure loadings. The simulated results were verified experimentally and compared to the previously published research in the literature [141], [175], [217]. This mathematical model is useful in engineering the sensor, for optimisation of the designing parameters. The mathematical model was also validated experimentally using an in-house built experimental setup (described in chapter 4, section 4.5.1) for a 3mm long FBG embedded centrally in a 6mm x 6mm x 1mm polymer cuboid patch and the Young's modulus of 143MPa. The experimentally obtained sensitivity of the sensor was 0.595 nm/MPa and the simulated results achieved a sensitivity of 0.565 nm/MPa. These results show very good agreement between the mathematical model and the experimentally obtained results. When embedding the FBG sensor it is important to place it in the horizontal centre of

the patch. This is because, the maximum strain transfer, from the patch to the FBG occurs at the horizontal centre of the patch. This was observed throughout all the simulated strain results of the sensor. Not only the position; the strain transferred from the polymer bonded to the FBG is affected by many parameters such as the thickness of the polymer, material properties of the polymer, bonding length and the number of layers. Simulations were used to obtain the maximum sensitivity based on optimising the shape, size, and Yong's modulus of the patch. Three different shapes were simulated, a cuboid (6mm x 6mm x 1mm), a quasi-rectangular shape (6mm x 3mm x 1mm), and a disc (6mm diameter, 1mm thickness). During these simulations the Young's modulus of the polymer was kept as 143 MPa. The sensitivities achieved for each shape are 0.5651 nm/MPa, 0.4962 nm/MPa, and 0.6226nm/MPa, respectively. The highest sensitivity was achieved for the disc shape and this may be due to the radial symmetry of the disc and hence the radial stresses contribute towards the axial strain experienced by the FBG. The next sets of simulations were conducted to optimise the size of the disc shape. The optimum diameter achieved was 5.5 mm for a Young's modulus of 143 MPa resulting in a sensitivity of 0.6244 nm/MPa. The deformation of the polymer layer due to the transverse load produced reaction forces on the fibre and hence produced longitudinal stresses. This reaction forces increase with the increase of the diameter of the polymer layer as the bonded length increases. When the diameter is less than 5.5mm the reaction forces are dominant when compared to the increase in area of the layer, and hence, the net longitudinal stress increases. Above the optimum diameter (5.5 mm) the area increase due to the increase of diameter is dominant when compared to the reaction forces and hence the stresses and the net longitudinal strain starts to reduce. The effect of the Young's modulus on the sensitivity of the FBG was investigated. For this purpose, three different commercially available polymer material properties were used. The values of the Young's modulus values are 143 MPa, 44 MPa and 20 MPa respectively. The obtained sensitivities for each Young's modulus values are 0.6244 nm/MPa, 0.7862 nm/MPa, and 0.8719 nm/MPa respectively. For the 5.5 mm diameter, 1 mm thickness patch; maximum

sensitivity of 0.8719 nm/MPa was obtained for the Young's modulus of 20 MPa. As the Young's modulus of the material decreases the polymer becomes more deformable and hence the reaction forces applied on the fibre are greater. As a result of the longitudinal strain increases, the Bragg wavelength shift is greater for the same pressure load, when compared to a higher Young's modulus (less deformable) of polymer. Therefore, the wavelength sensitivity to the transverse load increases. According to the simulation results, the pressure sensitivity of a bare FBG (~ $3x10^{-3}$ nm/MPa) can be increased ~270 times (0.8179 nm/MPa) by selecting an FBG of 3 mm length, embedding it at the horizontal centre of a polymer layer of Young's modulus of 20 MPa, in the shape of a circular disc with a diameter 5.5 mm and thickness of 1 mm. Birefringence effects with peak splitting along fast axis and slow axis were observed for the 5.5 mm diameter patch with a Young's modulus of 20MPa after 2.6 MPa, whereas for the 6mm x 6mm x 1mm with a Young's modulus 143MPa after 3.75MPa. As discussed in chapter 2, section 2.5.4, birefringence effect starts to appear as a result of the splitting of the refraction index along the fast and slow axes after the pressure mentioned above.

6.2.3 Towards miniaturised FBG interrogator

Although FBGs are an ideal candidate for contact pressure sensing in healthcare, its use is limited by the size and the cost of the FBG techniques available commercially. For the highly sensitive FBG contact pressure sensor described above, it is very important to have a compact FBG interrogator. A successful initial step towards a compact FBG interrogator in healthcare applications was achieved using a three section DBR tuneable laser, wavelength swept FBG demodulation technique. As a part of the research, an automated compact current calibration and measurement system for the three sectional tunable laser with a LabVIEW interface, was developed using the Arduino development environment. The wavelength stability due to the current stability of the system was investigated. The wavelength stability was tested and resulted in a standard deviation of ~0.01pm. The FBG interrogator consists of a LabVIEW interface for the user to visualise the FBG spectrum.

Three wavelength scanning resolutions were achieved by obtaining three current lookup tables for each resolution values at 1 nm, 0.1 nm and 0.01 nm. The developed FBG interrogator was tested with an FBG sensor prepared at the University laboratory and compared the spectrum with the commercial SmartScope FBG interrogator. The spectrum of both system results in the same FBG peak wavelengths. However further characterisation and experimental tests needed to be done to evaluate the performance of the FBG interrogator. A circuit diagram including the current drive chip, thermoelectric cooler, and tuneable laser including the necessary electronics was designed and illustrated in figure 5.42. KiCad open source was used for the development of the electric schematic and for the PCB. KiCad generated 3D view of the expected PCB board as shown in figure 5.43. The size of the board is 80 mm x 60 mm. According to the table 5.3, the cost will be not more than £1100 and this can be sell with a 30% mark-up around £1400-£1450.

6.3 Future work

Overall, a miniature fibre-optic Fabry- Perot pressure sensor for invasive medical applications has been investigated and developed. However, to achieve its full potential a few gaps needed to be addressed. These gaps and the future work are identified below. The sensor fabrication method is very promising and yet the air permeability observed in Parylene-C should be addressed in order to eliminate the air leakage to the sensor and hence the hysteresis over the long-time measurements. This is an important factor for the application in invasive pressure measurements, where the measurement could be air, blood or other fluid. According to Choudhury R. et al. [274] a material that is permeable to air is usually permeable to water, in either the vapour or the liquid phase. Gas permeability is given in the reference [200]. As the thickness of the membrane increases the amount of gas leak decreases. Therefore, a thicker film will decrease the air leaking through the film. However, thicker film will decrease the sensitivity significantly (chapter 2, equation 2.34). To make the sensor impermeable to air or any liquid, protective bio-compatible metal foils could be laminated on to the polymer films or thin

films may be metalized by vacuum sputtering or other techniques [203]. Also the techniques used by the food packaging industry to make the food packaging air impermeable could be adopted such as deposition of silicon oxide and other ceramics, or nanocomposites on polymer films [204]. Another great way to address the air permeability is to make the film thicker. Moreover, temperature sensitivity is an interfering parameter and hence this fact should be considered while taking measurements. This can be done by allowing time for the sensor to become thermally stable before making any pressure measurement. However, in a temperature dynamic changing system this measuring pressure is quite challenging. Introducing two cascade cavities using the same techniques described above, temperature can be compensated [207], [208]. With these future enhancements a successful miniature Fabry-Perot fibre optic pressure sensor could be obtained for the invasive medical applications as it was expected in the objective.

A successful mathematical model has been developed for a highly sensitive FBG contact pressure. As future improvement to the model it can be suggested to investigate the effect of the thickness of the polymer layer to the model. Moreover, it is also important to look for the artefact that may result during sensor manufacturing process such as bending or straining which may lead to reduce/increase the sensitivity. The mathematical model was experimentally validated for hard contacts. This may be very much likely to occur in an application such as prosthetics where the interface pressure is measured between stump and the prosthetic socket. However, in applications such as compression therapy, sensors will be deployed in a more complex environment than this. The sensor may sit in between skin and the compression bandage, or it may sit in between two layers of bandage. However, for future work it is important to validate in a complex environment to optimise the model and increase its robustness.

The proposed PCB design which includes the required circuitry of tunable laser, current driver IC, and the TEC controller IC has dimensions of 8 cm x 6 cm. However in order to fulfil the objectives described in chapter 1, section 1.2

further work should be carried out in hardware development. The power supply design, microcontroller unit, and the power stabilisation circuitry should be added in order to achieve the initial objectives. It is important to test the power consumption of the whole system. When Arduino-Uno runs, the USB cable draws maximum of 400 mA and when it is run by a DC adapter, it can draw up to max of 1 A. However, the current draw per digital I/O pin is 40 mA. 5 pins are used during the operation which means the maximum current draw is 200 mA. Current draw from the microcontroller is 50 mA. Hence, the total estimated power for the microcontroller circuit should be 250 mA. The maximum current used by the current driver as well as the tuneable laser circuit obtained by the power supply is ~ 180 mA and the TEC controller required maximum current of ~65mA. Therefore, the total power consumption ~500mA. However, there are other factors that should be considered like the power dissipation of the voltage regulator circuits, power capacity of the battery, and battery discharging rate. Therefore, a potential solution is to use a 12 V battery to power up the circuit with a capacity of 1.2 Ah would allow to run the device approximately for two hours. Wi-Fi data communication would also be possible by integrating a commercially available Wi-Fi module such as ESP8266. Another important enhancement to the interrogator is to remove output power fluctuations by using the monitoring photodiode of the tuneable laser diode module. The current produced in the monitoring photodiode is analogue to the output power. This means the current from the photodiode can be used as a feedback source of the laser driver circuit in order to maintain a stable power during its operation by changing the gain current. By addressing all the suggestions described above, a compact, lightweight, standalone FBG interrogator could be achieved by fulfilling the underlying objective.

References

[1] B. Culshaw and A. Kersey, “Fiber-optic sensing: A historical perspective,” *J. Light. Technol.*, vol. 26, no. 9, pp. 1064–1078, May 2008, doi: 10.1109/JLT.0082.921915.

[2] U. White, “Surgical Robotics: The Next 25 Years Successes, Challenges, and the Road Ahead,” *UK-RAS White Pap.*, 2018, Accessed: Oct. 29, 2019. [Online]. Available: www.ukras.org.

[3] M. Engin, A. Demirel, E. Z. Engin, and M. Fedakar, “Recent developments and trends in biomedical sensors,” *Meas. J. Int. Meas. Confed.*, 2005, doi: 10.1016/j.measurement.2004.11.002.

[4] F. Taffoni, D. Formica, P. Saccomandi, G. Di Pino, and E. Schena, “Optical fiber-based MR-compatible sensors for medical applications: An overview,” *Sensors (Switzerland)*, vol. 13, no. 10. MDPI AG, pp. 14105–14120, Oct. 18, 2013, doi: 10.3390/s131014105.

[5] A. Méndez, “Optics in medicine,” in *Optics in Our Time*, Cham: Springer International Publishing, 2016, pp. 299–333.

[6] A. Mendez, “Biomedical fiber optic sensor applications,” in *Conference on Optical Fiber Communication, Technical Digest Series*, 2015, vol. 2015-June, doi: 10.1364/ofc.2015.th1c.1.

[7] P. Rolfe, F. Scopesi, and G. Serra, “Biomedical instruments for fetal and neonatal surveillance,” *J. Phys. Conf. Ser.*, vol. 48, no. 1, pp. 1131–1136, Oct. 2006, doi: 10.1088/1742-6596/48/1/210.

[8] W. V. Gonzales, A. T. Mobashsher, and A. Abbosh, “The progress of glucose monitoring—A review of invasive to minimally and non-invasive techniques, devices and sensors,” *Sensors (Switzerland)*, vol. 19, no. 4. MDPI AG, Feb. 02, 2019, doi: 10.3390/s19040800.

[9] S. Pasche, S. Angeloni, R. Ischer, M. Liley, J. Luprano, and G. Voirin, “Wearable biosensors for monitoring wound healing,” in *CIMTEC 2008 -*

Proceedings of the 3rd International Conference on Smart Materials, Structures and Systems - Biomedical Applications of Smart Materials, Nanotechnology and Micro/Nano Engineering, 2008, vol. 57, pp. 80–87, doi: 10.4028/www.scientific.net/AST.57.80.

[10] "How to Measure Body Temperature Using the Health Sensor Platform." https://www.maximintegrated.com/en/design/technical-documents/app-notes/6/6502.html (accessed Feb. 02, 2020).

[11] W. M. Osman, A. B. Al Nabi, and K. H. Billal, "Optical Fiber Review," *J. Electr. Electron. Syst.*, vol. 07, no. 01, p. 249, 2018, doi: 10.4172/2332-0796.1000249.

[12] J. A. C. Heijmans, L. K. Cheng, and F. P. Wieringa, "Optical fiber sensors for medical applications — Practical engineering considerations," in *Fourth focused workshop on electronic recognition of bio-molecules*, vol. 22, no. January, J. Vander Sloten, P. Verdonck, M. Nyssen, and J. Haueisen, Eds. Berlin, Heidelberg: Springer Berlin Heidelberg, 2009, pp. 2330–2334.

[13] P. Roriz, O. Frazão, A. B. Lobo-Ribeiro, J. L. Santos, and J. A. Simões, "Review of fiber-optic pressure sensors for biomedical and biomechanical applications," *J. Biomed. Opt.*, vol. 18, no. 5, p. 050903, 2013, doi: 10.1117/1.jbo.18.5.050903.

[14] D. J. Monk, D. S. Soane, and R. T. Howe, "Determination of the Etching Kinetics for the Hydrofluoric Acid/Silicon Dioxide System," 1993.

[15] J. Bühler, F.-P. Steiner, and H. Baltes, "Silicon dioxide sacrificial layer etching in surface micromachining," *J. Micromechanics Microengineering*, vol. 7, no. 1, pp. R1–R13, Mar. 1997, doi: 10.1088/0960-1317/7/1/001.

[16] T. Fresvig, P. Ludvigsen, H. Steen, and O. Reikerås, "Fibre optic Bragg grating sensors: An alternative method to strain gauges for measuring deformation in bone," *Med. Eng. Phys.*, vol. 30, no. 1, pp. 104–108,

2008, doi: 10.1016/j.medengphy.2007.01.006.

[17] E. Udd, “Review of multi-parameter fiber grating sensors,” in *Fiber Optic Sensors and Applications V*, Sep. 2007, vol. 6770, p. 677002, doi: 10.1117/12.753525.

[18] S. Pevec and D. Donlagić, “Multiparameter fiber-optic sensors: a review,” *Opt. Eng.*, vol. 58, no. 07, p. 1, Mar. 2019, doi: 10.1117/1.OE.58.7.072009.

[19] H. Partsch, “Compression therapy of the Legs,” *J Dermatol Surg Oncol*, vol. 17, pp. 799–805, 1991, doi: 10.1046/j.1524-4725.2002.01181.x.

[20] E. A. Drynan, M. Schier, and A. L. Raisis, “Comparison of invasive and noninvasive blood pressure measurements in anaesthetized horses using the Surgivet V9203,” *Vet. Anaesth. Analg.*, vol. 43, no. 3, pp. 301–308, May 2016, doi: 10.1111/vaa.12297.

[21] M. Ward and J. A. Langton, “Blood pressure measurement,” *Contin. Educ. Anaesth. Crit. Care Pain*, vol. 7, no. 4, pp. 122–126, Aug. 2007, doi: 10.1093/bjaceaccp/mkm022.

[22] E. Al-Fakih, N. Abu Osman, and F. Mahmad Adikan, “Techniques for Interface Stress Measurements within Prosthetic Sockets of Transtibial Amputees: A Review of the Past 50 Years of Research,” *Sensors*, vol. 16, no. 7, p. 1119, Jul. 2016, doi: 10.3390/s16071119.

[23] I. Clausen and T. Glott, “Development of Clinically Relevant Implantable Pressure Sensors: Perspectives and Challenges,” *Sensors*, vol. 14, no. 9, pp. 17686–17702, Sep. 2014, doi: 10.3390/s140917686.

[24] T. Tagawa, T. Tamura, and P. A. Oberg, “Biomedical Sensors and Instruments,” in *Biomedical Sensors and Instruments*, CRC Press, 2011, p. 20.

[25] F. J. He and G. A. MacGregor, “Blood pressure is the most important cause of death and disability in the world,” *Eur. Hear. Journal, Suppl.*,

vol. 9, no. B, pp. B23–B28, May 2007, doi: 10.1093/eurheartj/sum005.

[26] M. Walsh *et al.*, “Relationship between intraoperative mean arterial pressure and clinical outcomes after noncardiac surgery: Toward an empirical definition of hypotension,” *Anesthesiology*, vol. 119, no. 3, pp. 507–515, 2013, doi: 10.1097/ALN.0b013e3182a10e26.

[27] Z. Roth and M. M. Brown, “The seventh report of the Joint National Committee on Prevention, Detection, Evaluation, and Treatment of High Blood Pressure: The JNC report,” *Evidence-Based Ophthalmology*, vol. 7, no. 4. pp. 170–171, 2006, doi: 10.1097/01.ieb.0000212051.70761.83.

[28] G. D. Baura, “Blood Pressure Monitors,” in *Medical Device Technologies*, vol. 68, no. 6, Elsevier, 2012, pp. 147–164.

[29] G. Ogedegbe and T. Pickering, “Principles and techniques of blood pressure measurement,” *Cardiol Clin*, vol. 28, no. 4, pp. 571–586, 2010, doi: 10.1016/j.ccl.2010.07.006.

[30] K. Lakhal, S. Ehrmann, and T. Boulain, “Noninvasive BP Monitoring in the Critically Ill: Time to Abandon the Arterial Catheter?,” *Chest*. 2018, doi: 10.1016/j.chest.2017.10.030.

[31] A. Mirdamadi and M. Etebari, “Comparison of manual versus automated blood pressure measurement in intensive care unit, coronary care unit, and emergency room,” *ARYA Atheroscler*, vol. 13, p. 29, 2017, Accessed: Jan. 10, 2020. [Online]. Available: www.mui.ac.ir.

[32] I. Pour-Ghaz *et al.*, “Accuracy of non-invasive and minimally invasive hemodynamic monitoring: where do we stand?,” *Ann Transl Med*, vol. 7, no. 17, p. 421, 2019, doi: 10.21037/atm.2019.07.06.

[33] D. C. Evans *et al.*, “Complications associated with pulmonary artery catheters: a comprehensive clinical review.,” *Scand. J. Surg.*, vol. 98, no. 4, pp. 199–208, 2009, doi: 10.1177/145749690909800402.

[34] A. Ranaweera, “American Thoracic Society,” *Int. J. Pharm. Med.*, vol. 19, no. 3, pp. 173–177, 2005, doi: 10.2165/00124363-200519030-00005.

[35] N. Kizilova, “Review of emerging methods and techniques for arterial pressure and flow waves acquisition and analyses,” *Int. J. Biosens. Bioelectron.*, vol. 4, no. 4, 2018, doi: 10.15406/ijbsbe.2018.04.00122.

[36] “MEMSCAP | Invasive blood pressure.” http://www.memscap.com/applications-and-market-segments/medical-and-biomedical/invasive-blood-pressure (accessed Feb. 02, 2020).

[37] A. M. Jagadeesh, N. G. Singh, and S. Mahankali, “A comparison of a continuous noninvasive arterial pressure (CNAP^{TM}) monitor with an invasive arterial blood pressure monitor in the cardiac surgical ICU,” *Ann. Card. Anaesth.*, vol. 15, no. 3, pp. 180–184, 2012, doi: 10.4103/0971-9784.97973.

[38] R. M. Gardner, “Direct blood pressure measurement - Dynamic response requirements,” *Anesthesiology*, vol. 54, no. 3, pp. 227–236, 1981, doi: 10.1097/00000542-198103000-00010.

[39] Chris Nickson, “Arterial line and Pressure Transducer,” *Vocortex*, pp. 1–14, 2015, Accessed: Feb. 07, 2020. [Online]. Available: https://litfl.com/arterial-line-and-pressure-transducer/.

[40] A. Jones and O. Pratt, “Physical Principles of Intra arterial Blood Pressure Measurement,” *Atotw*, no. June, pp. 1–8, 2009.

[41] E. Cibula, D. Donlagic, and C. Stropnik, “Miniature Fiber Optic Pressure Sensor for Medical Applications,” in *Proceedings of IEEE Sensors*, 2002, vol. 1, no. 1, pp. 711–714, doi: 10.1109/icsens.2002.1037190.

[42] H. Matsumoto, M. Saegusa, K. Saito, and K. Mizoi, “The Development of a Fibre Optic Catheter Tip Pressure Transducer,” *J. Med. Eng. Technol.*, vol. 2, no. 5, pp. 239–242, Jan. 1978, doi:

10.3109/03091907809161807.

[43] L. H. Lindstrom, “Miniaturized Pressure Transducer Intended for Intravascular Use,” *IEEE Trans. Biomed. Eng.*, vol. BME-17, no. 3, pp. 207–219, Jul. 1970, doi: 10.1109/TBME.1970.4502735.

[44] A. Lekholm and L. Lindström, “Optoelectronic transducer for intravascular measurements of pressure variations,” *Med. Biol. Eng.*, vol. 7, no. 3, pp. 333–335, May 1969, doi: 10.1007/BF02474776.

[45] C. Dealey, J. Posnett, and A. Walker, “The cost of pressure ulcers in the United Kingdom,” *J. Wound Care*, vol. 21, no. 6, pp. 261–266, 2012, doi: 10.12968/jowc.2012.21.6.261.

[46] D. J. Margolis, W. Bilker, J. Santanna, and M. Baumgarten, “Venous leg ulcer: Incidence and prevalence in the elderly,” *J. Am. Acad. Dermatol.*, vol. 46, no. 3, pp. 381–386, 2002, doi: 10.1067/mjd.2002.121739.

[47] J. F. Guest, G. W. Fuller, and P. Vowden, “Venous leg ulcer management in clinical practice in the UK: costs and outcomes,” *Int. Wound J.*, vol. 15, no. 1, pp. 29–37, Feb. 2018, doi: 10.1111/iwj.12814.

[48] L. Pfisterer, G. König, M. Hecker, and T. Korf, “Pathogenese der varizenbildung - Lehren aus der biomechanik,” *Vasa - Journal of Vascular Diseases*, vol. 43, no. 2. Verlag Hans Huber AG, pp. 88–99, 2014, doi: 10.1024/0301-1526/a000335.

[49] B. R. Meyerowitz and A. Crook, “ELASTIC-STOCKING COMPRESSION AND VENOUS BLOOD-FLOW. EFFECT IN THE LOWER LIMB,” *Lancet*, vol. 276, no. 7142, pp. 122–124, Jul. 1960, doi: 10.1016/S0140-6736(60)91265-4.

[50] J. C. Barbenel, “Pressure management,” *Prosthet. Orthot. Int.*, vol. 15, no. 3, pp. 225–231, 1991, doi: 10.3109/03093649109164292.

[51] H. Partsch *et al.*, “Measurement of lower leg compression in vivo: Recommendations for the performance of measurements of interface

pressure and stiffness," *Dermatologic Surg.*, vol. 32, no. 2, pp. 224–233, 2006, doi: 10.1111/j.1524-4725.2006.32039.x.

[52] R. Correia *et al.*, "Highly sensitive contact pressure measurements using FBG patch in endotracheal tube cuff," *Sixth Eur. Work. Opt. Fibre Sensors*, vol. 9916, p. 99161F, 2016, doi: 10.1117/12.2236859.

[53] R. Correia, E. Chehura, S. W. James, and R. P. Tatam, "A pressure sensor based upon the transverse loading of a sub-section of an optical fibre Bragg grating," *Meas. Sci. Technol.*, vol. 18, no. 10, pp. 3103–3110, 2007, doi: 10.1088/0957-0233/18/10/S09.

[54] H. Hu, S. Li, J. Wang, Y. Wang, and L. Zu, "FBG-based real-time evaluation of transverse cracking in cross-ply laminates," *Compos. Struct.*, vol. 138, pp. 151–160, 2016, doi: 10.1016/j.compstruct.2015.11.037.

[55] O. Hassoon, M. Tarfoui, and a El Malk, "Numerical Simulation of Fiber Bragg Grating Spectrum for Mode-I Delamination Detection," *Int. J. Mech. Aerospace, Ind. Mechatronics Eng.*, vol. 9, no. 1, pp. 144–149, 2015.

[56] G. Pereira, M. McGugan, and L. P. Mikkelsen, "FBG_SiMul V1.0: Fibre Bragg grating signal simulation tool for finite element method models," *SoftwareX*, vol. 5, pp. 163–170, 2016, doi: 10.1016/j.softx.2016.08.001.

[57] L. A. Ferreira, E. V. Diatzikis, J. L. Santos, and F. Farahi, "Demodulation of fiber Bragg grating sensors based on dynamic tuning of a multimode laser diode," *Appl. Opt.*, vol. 38, no. 22, p. 4751, 1999, doi: 10.1364/ao.38.004751.

[58] J. C. C. Chan, "Interrogation of fiber Bragg grating sensors with a tunable laser source," The Hong Kong Polytechnic University, 2010.

[59] G. Keiser, "Optical Fibers for Biophotonics Applications," *Biophotonics*, pp. 53–89, 2016, doi: 10.1007/978-981-10-0945-7_3.

[60] J. A. Stratton, *Electromagnetic Theory*, vol. 33, no. 12. Hoboken, NJ, USA: John Wiley & Sons, Inc., 2015.

[61] D. A. Fleisch, *A student's guide to Maxwell's equations*, 16th ed. Cambridge: Cambridge University Press, 2016.

[62] J. A. Buck, *Fundamentals of optical fibers*. John Wiley & Sons, 2004.

[63] T. Okoshi, *Optical Fibers.* Elsevier Science, 1982.

[64] M. S. Kumar, *Fundamentals of optical fibre communication*. PHI Learning, 2014.

[65] G. Lifante, *Integrated Photonics*, vol. 90. Boston, MA: Springer US, 2004.

[66] K. Iizuka, *Elements of Photonics, Volume II*, vol. 2. New York, USA: John Wiley & Sons, Inc., 2002.

[67] D. Gloge, "Weakly Guiding Fibers," *Appl. Opt.*, vol. 10, no. 10, p. 2252, Oct. 1971, doi: 10.1364/ao.10.002252.

[68] I. Gómez-Castellanos, "Intensity distributions and cutoff frequencies of linearly polarized modes for a step-index elliptical optical fiber," *Opt. Eng.*, vol. 46, no. 4, p. 045003, 2007, doi: 10.1117/1.2719698.

[69] A. Kumar and A. Ghatak, *Polarization of light with applications in optical fibers*. SPIE, 2011.

[70] T. R. Woliński, "Polarization in optical fibers," *Acta Phys. Pol. A*, vol. 95, no. 5, pp. 749–760, 1999, doi: 10.12693/APhysPolA.95.749.

[71] P. Hariharan, *Basics of Interferometry*. Elsevier Inc., 2007.

[72] L. Wang and N. Fang, "Applications of Fiber-Optic Interferometry Technology in Sensor Fields," in *Optical Interferometry*, InTech, 2017.

[73] B. Culshaw, "Fiber optics in sensing and measurement," *IEEE J. Sel. Top. Quantum Electron.*, vol. 6, no. 6, pp. 1014–1021, Nov. 2000, doi: 10.1109/2944.902150.

[74] L. B. Yuan, L. M. Zhou, and J. S. Wu, “Fiber optic temperature sensor with duplex Michelson interferometric technique,” *Sensors Actuators, A Phys.*, vol. 86, no. 1–2, pp. 2–7, Oct. 2000, doi: 10.1016/S0924-4247(00)00357-5.

[75] C. T. Ma, C. L. Lee, and Y. W. You, “Design and implementation of a novel measuring scheme for fiber interferometer based sensors,” *Sensors (Switzerland)*, vol. 19, no. 19, 2019, doi: 10.3390/s19194080.

[76] M. Yu and B. Balachandran, “Acoustic measurements using a fiber optic sensor system,” in *Journal of Intelligent Material Systems and Structures*, 2003, vol. 14, no. 7, pp. 409–414, doi: 10.1177/1045389X03034058.

[77] “BASIC STRUCTURE OF AN OPTICAL FIBER,” 2554. https://www.tpub.com/ceb/82.htm.

[78] P. A. Flournoy, R. W. McClure, and G. Wyntjes, “White-Light Interferometric Thickness Gauge,” *Appl. Opt.*, vol. 11, no. 9, p. 1907, Sep. 1972, doi: 10.1364/AO.11.001907.

[79] U. Sharma and X. Wei, “Fiber optic interferometric devices,” in *Fiber Optic Sensing and Imaging*, vol. 9781461474, 2013, pp. 29–53.

[80] M. P. Boyce, *Gas Turbine Engineering Handbook*. Elsevier Inc., 2012.

[81] B. Gupta, “Monitoring in the ICU Anaesthesia Update in,” pp. 37–42.

[82] C. Prescott and S. Ruff, “The shocked patient,” *Medicine (United Kingdom)*, vol. 45, no. 2. pp. 81–85, 2017, doi: 10.1016/j.mpmed.2016.11.007.

[83] “Cardiac Catheterization | American Heart Association.” https://www.heart.org/en/health-topics/heart-attack/diagnosing-a-heart-attack/cardiac-catheterization (accessed Sep. 18, 2019).

[84] “Cardiac catheterisation measurements | PHA.” https://www.phauk.org/what-is-ph/tests-you-might-have/cardiac-

catheterisation/cardiac-catheterisation-measurements/ (accessed Sep. 18, 2019).

[85] R. K. Tandon and N. Saikia, “Measuring intravariceal pressure,” *Gastrointestinal Endoscopy*, vol. 70, no. 3. pp. 414–416, Sep. 2009, doi: 10.1016/j.gie.2009.03.038.

[86] “The Role of Pressure Sensors in Medical Devices.” https://www.ecnmag.com/article/2009/10/role-pressure-sensors-medical-devices (accessed Sep. 18, 2019).

[87] I. Clausen, L. G. W. Tvedt, and T. Glott, “Measurement of urinary bladder pressure: A comparison of methods,” *Sensors (Switzerland)*, vol. 18, no. 7, pp. 1–2, Jul. 2018, doi: 10.3390/s18072128.

[88] “Advantages of Minimally Invasive Surgery - Mount Sinai Medical Center - ORTHOREHAB.” https://www.msmc.com/orthorehab/advantages-of-minimally-invasive-surgery/ (accessed Sep. 18, 2019).

[89] F. Zhao, “Nonlinear solutions for circular membranes and thin plates,” in *Modeling, Signal Processing, and Control for Smart Structures 2008*, Mar. 2008, vol. 6926, p. 69260W, doi: 10.1117/12.775511.

[90] D. Chairman Rowant, E. D. James, A. E. J. L. Kramer, A. M. Sterling, and P. F. Suhel, “Urodynamic equipment: Technical aspects: Produced by the international continence society working party on urodynamic equipment,” *J. Med. Eng. Technol.*, vol. 11, no. 2, pp. 57–64, 1987, doi: 10.3109/03091908709062796.

[91] D. Griffiths, K. Hofner, R. Van Mastrigt, H. J. Rollema, A. Spangberg, and D. Gleason, “Standardization of terminology of lower urinary tract function: Pressure-flow studies of voiding, urethral resistance, and urethral obstruction,” *Neurourol. Urodyn.*, vol. 16, no. 1, pp. 1–18, 1997, doi: 10.1002/(SICI)1520-6777(1997)16:1<1::AID-NAU1>3.0.CO;2-I.

[92] W. Schäfer *et al.*, “Good urodynamic practices: Uroflowmetry, filling cystometry, and pressure-flow studies,” *Neurourol. Urodyn.*, vol. 21, no. 3, pp. 261–274, 2002, doi: 10.1002/nau.10066.

[93] P. J. D. Andrews, G. Citerio, L. Longhi, K. Polderman, J. Sahuquillo, and P. Vajkoczy, “NICEM consensus on neurological monitoring in acute neurological disease,” in *Intensive Care Medicine*, Aug. 2008, vol. 34, no. 8, pp. 1362–1370, doi: 10.1007/s00134-008-1103-y.

[94] ANSI/AAMI, “ANSI/AAMI NS28:1988 (R 2010) - Intracranial pressure monitoring devices,” Arlington, VA, USA, 2010. Accessed: Dec. 30, 2020. [Online]. Available: https://webstore.ansi.org/standards/aami/ansiaamins2819882010.

[95] E. Coss-Adame, S. S. C. Rao, J. Valestin, A. Ali-Azamar, and J. M. Remes-Troche, “Accuracy and Reproducibility of High-definition Anorectal Manometry and Pressure Topography Analyses in Healthy Subjects,” *Clin. Gastroenterol. Hepatol.*, vol. 13, no. 6, pp. 1143-1150.e1, Jun. 2015, doi: 10.1016/j.cgh.2014.12.034.

[96] S. S. C. Rao, F. Azpiroz, N. Diamant, P. Enck, G. Tougas, and A. Wald, “Minimum standards of anorectal manometry,” *Neurogastroenterol. Motil.*, vol. 14, no. 5, pp. 553–559, 2002, doi: 10.1046/j.1365-2982.2002.00352.x.

[97] ISO, “ISO-8612:Ophthalmic instruments-Tonometers,” Geneva, Switzerland, 2009., 2009. Accessed: Dec. 30, 2020. [Online]. Available: https://www.sis.se/std-911552.

[98] R. N. Weinreb, J. D. Brandt, D. Garway-Heath, and F. Medeiros, *Intraocular Pressure Intraocular Pressure World Glaucoma Association Consensus Series 4*. Fort Lauderdale, FL: Kugler Publications, 2007.

[99] A. G. Mignani and F. Baldini, “Biomedical sensors using optical fibres,” *Reports Prog. Phys.*, vol. 59, no. 1, pp. 1–28, 1996, doi: 10.1088/0034-4885/59/1/001.

[100] G. Voskerician *et al.*, “Biocompatibility and biofouling of MEMS drug delivery devices,” *Biomaterials*, vol. 24, no. 11, pp. 1959–1967, 2003, doi: 10.1016/S0142-9612(02)00565-3.

[101] N. Sabir and V. Ramachandra, “Decontamination of anaesthetic equipment,” *Contin. Educ. Anaesthesia, Crit. Care Pain*, vol. 4, no. 4, pp. 103–106, Aug. 2004, doi: 10.1093/bjaceaccp/mkh029.

[102] “FIBER OPTICS/BIOMEDICAL DEVICE ENGINEERING: Sterilization for success: Applying optical fiber in biomedicine | Bio Optics World.” https://www.bioopticsworld.com/biophotonics-tools/article/16429954/fiber-opticsbiomedical-device-engineering-sterilization-for-success-applying-optical-fiber-in-biomedicine (accessed Sep. 19, 2019).

[103] D. R. Biswas, “Optical fiber coatings for biomedical applications,” *Opt. Eng.*, vol. 31, no. 7, p. 1400, 1992, doi: 10.1117/12.57701.

[104] É. Pinet, “Pressure measurement with fiber-optic sensors: commercial technologies and applications,” *21st Int. Conf. Opt. Fiber Sensors*, vol. 7753, no. May 2011, p. 775304, 2011, doi: 10.1117/12.895536.

[105] Y. J. Rao, Z. L. Ran, and Y. Gong, *Fiber-optic fabry-perot sensors: An introduction*. CRC Press, 2017.

[106] H. Hencky, “On the stress state in circular plates with vanishing bending stiffness,” *Zeitschrift für Math. und Phys.*, vol. 63, pp. 311–317, 1915.

[107] F. Zhao, “Nonlinear solutions for circular membranes and thin plates,” *Model. Signal Process. Control Smart Struct. 2008*, vol. 6926, no. April 2008, p. 69260W, 2008, doi: 10.1117/12.775511.

[108] J. D. Campbell, “On the theory of initially tensioned circular membranes subjected to uniform pressure,” *Q. J. Mech. Appl. Math.*, vol. 9, no. 1, pp. 84–93, 1956, doi: 10.1093/qjmam/9.1.84.

[109] “FISO Medical Pressure Monitoring.” https://fiso.com/wp-

content/uploads/2018/10/MC-00263_-Medical-Pressure-Monitoring-Product-Datasheet_R7.pdf.

[110] É. Pinet, “Fabry-pérot fiber-optic sensors for physical parameters measurement in challenging conditions,” *J. Sensors*, vol. 2009, 2009, doi: 10.1155/2009/720980.

[111] O. Engström, Hindås, R. Hans, and Partille, “Method of Manufacturing a Measuring Device,” 5619046, 1997.

[112] D. Donlagic, E. Cibula, and E. Pinet, “Fabry-Perot Optical Sensor and Method of Manufacturing,” US 8559770 B2, 2013.

[113] R. A. Wolthuis, G. L. Mitchell, E. Saaski, J. C. Hartl, and M. A. Afromowitz, “Development of Medical Pressure and Temperature Sensors Employing Optical Spectrum Modulation,” *IEEE Trans. Biomed. Eng.*, vol. 38, no. 10, pp. 974–981, 1991, doi: 10.1109/10.88443.

[114] Y. Zhu and A. Wang, “Miniature fiber-optic pressure sensor,” *IEEE Photonics Technol. Lett.*, vol. 17, no. 2, pp. 447–449, 2005, doi: 10.1109/LPT.2004.839002.

[115] X. Wang *et al.*, “An optical fiber tip pressure sensor for medical applications,” *Quantum Electron. Laser Sci. Conf.*, vol. 2, pp. 916–918, 2005.

[116] L. H. Chen, C. C. Chan, S. K. Goh, and J. Sun, “Chitosan diaphragm-based fiber optic pressure sensor,” in *2009 Conference on Lasers & Electro Optics & The Pacific Rim Conference on Lasers and Electro-Optics*, Aug. 2009, pp. 1–2, doi: 10.1109/CLEOPR.2009.5292697.

[117] “OPP-M fiber optic pressure sensor, probe and transducer.” https://opsens-solutions.com/products/fiber-optic-pressure-sensors/opp-m/ (accessed Sep. 19, 2019).

[118] “Medical | Fiso.” https://fiso.com/en/service/medical/ (accessed Sep. 19, 2019).

[119] “Endosense.” https://www.cardiovascular.abbott/us/en/home.html (accessed Sep. 19, 2019).

[120] “RJC Enterprises, LLC - Current fiber optic sensor users.” http://www.rjcenterprises.net/users.html (accessed Sep. 19, 2019).

[121] J. Wu, M. Yao, F. Xiong, A. Ping Zhang, H. Y. Tam, and P. K. A. Wai, “Optical Fiber-Tip Fabry-Pérot Interferometric Pressure Sensor Based on an in Situ μ-Printed Air Cavity,” *J. Light. Technol.*, vol. 36, no. 17, pp. 3618–3623, Sep. 2018, doi: 10.1109/JLT.2018.2843885.

[122] G. C. Hill *et al.*, “SU-8 MEMS Fabry-Perot pressure sensor,” *Sensors Actuators, A Phys.*, vol. 138, no. 1, pp. 52–62, 2007, doi: 10.1016/j.sna.2007.04.047.

[123] T. Katsumata, Y. Haga, K. Minami, and M. Esashi, “MICROMACHINED 125μm DIAMETER ULTRA MINIATURE FIBER-OPTIC PRESSURE SENSOR FOR CATHETER,” *IEEJ Trans. Sensors Micromachines*, vol. 120, no. 2, pp. 58–63, 2000, doi: 10.1541/ieejsmas.120.58.

[124] M. Da Zhou, C. Yang, Z. Liu, J. P. Cysyk, and S. Y. Zheng, “An implantable Fabry-Pérot pressure sensor fabricated on left ventricular assist device for heart failure,” *Biomed. Microdevices*, vol. 14, no. 1, pp. 235–245, Feb. 2012, doi: 10.1007/s10544-011-9601-z.

[125] D. C. Abeysinghe, S. Dasgupta, J. T. Boyd, and H. E. Jackson, “A novel MEMS pressure sensor fabricated on an optical fiber,” *IEEE Photonics Technol. Lett.*, vol. 13, no. 9, pp. 993–995, Sep. 2001, doi: 10.1109/68.942671.

[126] E. Cibula, D. Donlagic, and C. Stropnik, “Miniature fiber optic pressure sensor for medical applications,” in *Proceedings of IEEE Sensors*, vol. 1, pp. 711–714, doi: 10.1109/ICSENS.2002.1037190.

[127] E. Cibula and D. Donlagić, “Miniature fiber-optic pressure sensor with a polymer diaphragm,” *Appl. Opt.*, vol. 44, no. 14, pp. 2736–2744, May 2005, doi: 10.1364/AO.44.002736.

[128] Y. Wang, D. N. Wang, C. Wang, and T. Hu, “Compressible fiber optic micro-Fabry-Pérot cavity with ultra-high pressure sensitivity,” *Opt. Express*, vol. 21, no. 12, p. 14084, Jun. 2013, doi: 10.1364/oe.21.014084.

[129] E. Cibula, S. Pevec, B. Lenardic, E. Pinet, and D. Donlagic, “Miniature all-glass robust pressure sensor,” *Opt. Express*, vol. 17, no. 7, p. 5098, 2009, doi: 10.1364/oe.17.005098.

[130] D. Donlagic and E. Cibula, “All-fiber high-sensitivity pressure sensor with SiO_2 diaphragm,” *Opt. Lett.*, vol. 30, no. 16, p. 2071, 2005, doi: 10.1364/ol.30.002071.

[131] C. Hassler, R. P. Von Metzen, P. Ruther, and T. Stieglitz, “Characterization of parylene C as an encapsulation material for implanted neural prostheses,” *J. Biomed. Mater. Res. - Part B Appl. Biomater.*, vol. 93, no. 1, pp. 266–274, 2010, doi: 10.1002/jbm.b.31584.

[132] F. T. Tsai, C. T. Chuang, T. C. Li, and P. C. Yu, “Study of Parylene-C thin film Deposited on Flat Substrates,” 2012, doi: 10.4028/www.scientific.net/AMM.217-219.1077.

[133] “Literature Review: Biological Safety of Parylene C | MDDI Online.” https://www.mddionline.com/literature-review-biological-safety-parylene-c (accessed Sep. 23, 2019).

[134] M. S. Taylor II and J. L. Williams, “Barrier coating on blood contacting devices,” Nov. 26, 1991.

[135] S. Kuppusami and R. H. Oskouei, “Parylene Coatings in Medical Devices and Implants: A Review,” *Univers. J. Biomed. Eng.*, vol. 3, no. 2, pp. 9–14, 2015, doi: 10.13189/ujbe.2015.030201.

[136] P. J. Chen, D. C. Rodger, M. S. Humayun, and Y. C. Tai, “Unpowered spiral-tube parylene pressure sensor for intraocular pressure sensing,” *Sensors Actuators, A Phys.*, vol. 127, no. 2, pp. 276–282, Mar. 2006, doi: 10.1016/j.sna.2005.08.027.

[137] R. P. Von Metzen and T. Stieglitz, “The effects of annealing on mechanical, chemical, and physical properties and structural stability of Parylene C,” *Biomed. Microdevices*, vol. 15, no. 5, pp. 727–735, Oct. 2013, doi: 10.1007/s10544-013-9758-8.

[138] S. C. Systems, “SCS Parylene Properties,” *SCS Parylene Dimer*. p. 12, 2007, Accessed: Sep. 23, 2019. [Online]. Available: https://scscoatings.com/wp-content/uploads/2017/09/02-SCS-Parylene-Properties-1016.pdf.

[139] P. Cosseddu, A. Piras, and A. Bonfiglio, “Fully deformable organic thin-film transistors with moderate operation voltage,” *IEEE Trans. Electron Devices*, vol. 58, no. 10, pp. 3416–3421, Oct. 2011, doi: 10.1109/TED.2011.2161763.

[140] “How is Parylene Coating Applied? | VSi PARYLENE.” https://vsiparylene.com/parylene-advantages/process/#1549224059856-788be9e6-b2a2 (accessed Jan. 18, 2020).

[141] A. Othonos, K. Kalli, D. Pureur, and A. Mugnier, “Fibre Bragg gratings,” *Springer Ser. Opt. Sci.*, vol. 123, pp. 189–269, 2006, doi: 10.1007/3-540-31770-8_6.

[142] K. J. Peters and D. Inaudi, “Fiber optic sensors for assessing and monitoring civil infrastructures,” in *Sensor Technologies for Civil Infrastructures*, vol. 1, Elsevier, 2014, pp. 121–158.

[143] G. Meltz and W. W. Morey, “Bragg grating formation and germanosilicate fiber photosensitivity,” Dec. 1991, p. 185, doi: 10.1117/12.51164.

[144] M. Prabhugoud and K. Peters, “Modified Transfer Matrix Formulation for Bragg Grating Strain Sensors,” *J. Light. Technol.*, vol. 22, no. 10, pp. 2302–2309, Oct. 2004, doi: 10.1109/JLT.2004.833281.

[145] J.-J. Liau *et al.*, “A NEW LOOK AT NUMERICAL ANALYSIS OF UNIFORM

FIBER BRAGG GRATINGS USING COUPLED MODE THEORY," *Prog. Electromagn. Res.*, vol. 93, pp. 385–401, 2009, doi: 10.2528/PIER09031102.

[146] T. Erdogan, "Fiber grating spectra," *J. Light. Technol.*, vol. 15, no. 8, pp. 1277–1294, 1997, doi: 10.1109/50.618322.

[147] A. Ikhlef, R. Hedara, and M. Chikh-bled, "Uniform Fiber Bragg Grating modeling and simulation used matrix transfer method," *Int. J. Comput. Sci. Issues*, vol. 9, no. 1, pp. 368–374, 2012.

[148] K. Peters, M. Studer, J. Botsis, A. Iocco, H. Limberger, and R. Salathé, "Embedded optical fiber bragg grating sensor in a nonuniform strain field: Measurements and simulations," *Exp. Mech.*, vol. 41, no. 1, pp. 19–28, 2001, doi: 10.1007/BF02323100.

[149] H. Y. Ling, K. T. Lau, W. Jin, and K. C. Chan, "Characterization of dynamic strain measurement using reflection spectrum from a fiber Bragg grating," *Opt. Commun.*, vol. 270, no. 1, pp. 25–30, 2007, doi: 10.1016/j.optcom.2006.08.032.

[150] Y. Chen, J. Li, Y. Yang, M. Chen, J. Li, and H. Luo, "Numerical modeling and design of mid-infrared FBG with high reflectivity," *Optik (Stuttg).*, vol. 124, no. 16, pp. 2565–2568, Aug. 2013, doi: 10.1016/j.ijleo.2012.07.016.

[151] I. Bennion, J. A. R. Williams, L. Zhang, K. Sugden, and N. J. Doran, "UV-written in-fibre Bragg gratings," *Opt. Quantum Electron.*, vol. 28, no. 2, pp. 93–135, 1996, doi: 10.1007/BF00278281.

[152] G. F. Pereira, L. P. Mikkelsen, and M. McGugan, "Crack detection in fibre reinforced plastic structures using embedded fibre bragg grating sensors: Theory, model development and experimental validation," *PLoS One*, vol. 10, no. 10, pp. 1–36, 2015, doi: 10.1371/journal.pone.0141495.

[153] R. Gafsi and M. A. El-Sherif, "Analysis of Induced-Birefringence Effects

on Fiber Bragg Gratings," *Opt. Fiber Technol.*, vol. 6, no. 3, pp. 299–323, 2000, doi: 10.1006/ofte.2000.0333.

[154] S. Mastero, "Optomechanical behavior of embedded fiber Bragg grating strain sensors," Drexel University, 2005.

[155] S. Mastero, "Optomechanical behavior of embedded fiber Bragg grating strain sensors," *Microscope*, no. July, 2005.

[156] L. Michaille, M. W. McCall, Y. C. Lai, and J. A. R. Williams, "Analysis of single and multiple, non-permanent, tunable, birefringent spectral holes in a fibre-Bragg grating stop-band produced via uniaxial pressure," *Opt. Commun.*, vol. 222, no. 1–6, pp. 1–8, 2003, doi: 10.1016/S0030-4018(03)01452-4.

[157] "Compression in venous leg ulcers a WUWHS consensus document - Wounds International." https://www.woundsinternational.com/resources/details/compression-venous-leg-ulcers-wuwhs-consensus-document (accessed Jan. 21, 2020).

[158] "Venous leg ulcer - Treatment - NHS." https://www.nhs.uk/conditions/leg-ulcer/treatment/ (accessed Nov. 01, 2019).

[159] "Effective compression therapy - Wounds UK." https://www.wounds-uk.com/resources/details/effective-compression-therapy (accessed Nov. 01, 2019).

[160] J. C. Barbenel and S. Sockalingham, "Device for measuring soft tissue interface pressures," *J. Biomed. Eng.*, vol. 12, no. 6, pp. 519–522, Nov. 1990, doi: 10.1016/0141-5425(90)90062-R.

[161] S. Thomas, "Compression bandaging in the treatment of venous leg ulcers," *World Wide Wounds*, vol. 1998, 1998, Accessed: Aug. 30, 2019. [Online]. Available: http://www.worldwidewounds.com/1997/september/Thomas-

Bandaging/bandage-paper.html.

[162] I. Anderson, “Understanding Chronic Venous Hypertension,” *Wound Essentials*, vol. 3, pp. 20–32, 2008.

[163] M. D. Steinberg and E. D. Cooke, “Design and evaluation of a device for measurement of interface pressure,” *J. Biomed. Eng.*, vol. 15, no. 6, pp. 464–468, 1993, doi: 10.1016/0141-5425(93)90059-8.

[164] Z. Moore, “Compression bandaging: are practitioners achieving the ideal sub-bandage pressures?,” *J. Wound Care*, vol. 11, no. 7, pp. 265–268, 2002, doi: 10.12968/jowc.2002.11.7.26423.

[165] J. Pellicer, V. García-Morales, and M. J. Hernández, “On the demonstration of the Young-Laplace equation in introductory physics courses,” *Phys. Educ.*, vol. 35, no. 2, pp. 126–129, 2000, doi: 10.1088/0031-9120/35/2/309.

[166] S. Thomas, “The use of the Laplace equation in the calculation of sub-bandage pressure,” *World Wide Wounds*, vol. 2002, 2002, Accessed: Aug. 30, 2019. [Online]. Available: http://www.worldwidewounds.com/2003/june/Thomas/Laplace-Bandages.html.

[167] D. H.-C. Wang, N. Blenman, S. Maunder, V. Patton, and J. Arkwright, “An optical fiber Bragg grating force sensor for monitoring sub-bandage pressure during compression therapy,” *Opt. Express*, vol. 21, no. 17, p. 19799, 2013, doi: 10.1364/oe.21.019799.

[168] J. Schuren and K. Mohr, “The efficacy of Laplace’s equation in calculating bandage pressure in venous leg ulcers,” *Wounds UK*, vol. 4, no. 2, pp. 38–47, 2008.

[169] A. W. P. Buis and P. Convery, “Calibration problems encountered while monitoring stump/socket interface pressures with force sensing resistors: Techniques adopted to minimise inaccuracies,” *Prosthet. Orthot. Int.*, vol. 21, no. 3, pp. 179–182, 1997, doi:

10.3109/03093649709164552.

[170] G. Pirouzi, N. A. Abu Osman, A. Eshraghi, S. Ali, H. Gholizadeh, and W. A. B. Wan Abas, “Review of the socket design and interface pressure measurement for transtibial prosthesis,” *Scientific World Journal*, vol. 2014. Hindawi Publishing Corporation, 2014, doi: 10.1155/2014/849073.

[171] E. K. Moo, N. A. Abu Osman, B. Pingguan-Murphy, W. A. B. Wan Abas, W. D. Spence, and S. E. Solomonidis, “Interface pressure profile analysis for patellar tendon-bearing socket and hydrostatic socket,” *Acta Bioeng. Biomech.*, vol. 11, no. 4, pp. 37–43, 2009.

[172] P. Quesada and H. B. Skinner, “Department of Veterans Affairs Analysis of a below-knee patellar tendon-bearing prosthesis: A finite element study,” *J. Rehabil. Res. Dev.*, vol. 28, no. 3, pp. 1–12, 1991, doi: 10.1682/JRRD.1991.07.0001.

[173] M. G. Xu, L. Reekie, Y. T. Chow, and J. P. Dakin, “Optical in-fibre grating high pressure sensor,” *Electron. Lett.*, vol. 29, no. 4, pp. 398–399, 1993, doi: 10.1049/el:19930267.

[174] M. Ferguson-Pell, S. Hagisawa, and D. Bain, “Evaluation of a sensor for low interface pressure applications,” *Med. Eng. Phys.*, vol. 22, no. 9, pp. 657–663, 2000, doi: 10.1016/S1350-4533(00)00080-1.

[175] R. Correia, E. Chehura, J. Li, S. W. James, and R. P. Tatam, “Enhanced sensitivity fibre Bragg grating (FBG) load sensor,” *Meas. Sci. Technol.*, vol. 21, 2010, doi: 10.1088/0957-0233/21/9/094006.

[176] N. S. Rajput and X. Luo, *FIB Micro-/Nano-fabrication*, Second Edi. Yi Qin, 2015.

[177] N.-T. Nguyen, “Fabrication technologies,” in *Micromixers*, Elsevier, 2012, pp. 113–161.

[178] N. S. Rajput and X. Luo, “FIB Micro-/Nano-fabrication,” in

Micromanufacturing Engineering and Technology: Second Edition, Elsevier Inc., 2015, pp. 61–80.

[179] M. Yeakub Ali, W. Hung, and F. Yongqi, "A Review of Focused Ion Beam Sputtering," *Int. J. Precis. Eng. Manuf.*, vol. 11, no. 1, pp. 157–170, 2010, doi: 10.1007/s12541-010-0019-y.

[180] C. Martelli *et al.*, "Micromachining long period gratings in optical fibres using focused ion beam," 2007, doi: 10.1364/bgpp.2007.btuc6.

[181] J. Huang, A. Alqahtani, J. Viegas, and M. S. Dahlem, "Fabrication of optical fiber gratings through focused ion beam techniques for sensing applications," 2012, doi: 10.1109/PGC.2012.6458009.

[182] B. C. Gibson *et al.*, "Exposure and characterization of nano-structured hole arrays in tapered photonic crystal fibers using a combined FIB/SEM technique," *Opt. Express*, vol. 13, no. 22, p. 9023, 2005, doi: 10.1364/opex.13.009023.

[183] C. Martelli, P. Olivero, J. Canning, N. Groothoff, B. Gibson, and S. Huntington, "Micromachining structured optical fibers using focused ion beam milling," *Opt. Lett.*, vol. 32, no. 11, p. 1575, Jun. 2007, doi: 10.1364/ol.32.001575.

[184] W. Yuan, F. Wang, and O. Bang, "Optical fiber sensors fabricated by the focused ion beam technique," in *OFS2012 22nd International Conference on Optical Fiber Sensors*, Oct. 2012, vol. 8421, pp. 842173-842173–4, doi: 10.1117/12.974932.

[185] R. M. André *et al.*, "Tapered optical fiber tip probes based on focused ion beam-milled Fabry-Perot microcavities," *Nanoeng. Fabr. Prop. Opt. Devices XIII*, vol. 9927, p. 99270R, 2016, doi: 10.1117/12.2236321.

[186] "The Quanta 200 3D Simplified Operation Manual." https://www.mri.psu.edu/sites/default/files/file_attach/fib_sop.pdf (accessed Jan. 17, 2020).

[187] M. W. Martynowycz, W. Zhao, J. Hattne, G. J. Jensen, and T. Gonen, "Qualitative Analyses of Polishing and Precoating FIB Milled Crystals for MicroED," *Structure*, vol. 27, no. 10, pp. 1594-1600.e2, Apr. 2019, doi: 10.1016/j.str.2019.07.004.

[188] "The Quanta 200 3D Simplified Operation Manual." https://www.mri.psu.edu/sites/default/files/file_attach/fib_sop.pdf.

[189] A. Goswami, K. Singh, S. Aravindan, and P. V. Rao, "Optimizing FIB milling process parameters for silicon and its use in nanoreplication," *Mater. Manuf. Process.*, vol. 32, no. 10, pp. 1052–1058, 2017, doi: 10.1080/10426914.2016.1257127.

[190] S. N. Bhavsar, S. Aravindan, and P. V. Rao, "Experimental investigation of redeposition during focused ion beam milling of high speed steel," *Precis. Eng.*, 2012, doi: 10.1016/j.precisioneng.2011.12.005.

[191] B. G. Lipták, *Instrument engineers' handbook*. CRC Press, 2003.

[192] "IEC 61987-1, Industrial process measurement and control. Data structures and elements in process equipment catalogues . Part 1: Measuring equipment with analogue and digital output," 2006, Accessed: Jan. 20, 2020. [Online]. Available: www.iec.ch/searchpub.

[193] "IEC 61298-2:2008 , Estonian Centre for Standardisation." https://www.evs.ee/products/iec-61298-2-2008 (accessed Jan. 20, 2020).

[194] "Understanding Pressure Sensor Accuracy | Building Automation Systems | Industry Articles | Dwyer Instruments." https://www.dwyer-inst.co.uk/articles/industry/powderbulk/understanding-pressure-sensor-accuracy/understanding-pressure-sensor-accuracy.cfm (accessed Jan. 20, 2020).

[195] D. Tandeske, *Pressure Sensors: Selection and Application*. Hong Kong: Taylor & Francis, 1990.

[196] “What are Hysteresis Errors?” https://appmeas.co.uk/resources/pressure-measurement-notes/what-are-hysteresis-errors/ (accessed Jan. 20, 2020).

[197] W. Sui, M. S. Duvieusart, J. Zhao, Y.-C. Tai, and Y.-K. Lee, “Comparative study of the viscoelasticity of parylene thin films for MEMS using Nano-DMA and Molecular Dynamics,” in *2017 IEEE 30th International Conference on Micro Electro Mechanical Systems (MEMS)*, Jan. 2017, no. July, pp. 468–471, doi: 10.1109/MEMSYS.2017.7863444.

[198] S. A. Sharifian and D. R. Buttsworth, “Reducing the mechanical hysteresis problem in optically addressed diaphragm pressure sensors,” in *Fifth International Conference on Vibration Measurements by Laser Techniques: Advances and Applications*, May 2002, vol. 4827, pp. 234–244, doi: 10.1117/12.468141.

[199] “Explanation of hysteresis calculation.” https://web.mst.edu/~cottrell/ME240/Resources/Calibration/Explanation of Hysteresis calculation.doc.

[200] H. Yasuda, “Units of gas permeability constants,” *J. Appl. Polym. Sci.*, vol. 19, no. 9, pp. 2529–2536, Sep. 1975, doi: 10.1002/app.1975.070190915.

[201] “ISO 15105-1. Plastics film and sheeting. Determination of gas transmission rate.,” 2007.

[202] “Everything You Need To Know About Parylene | VSi PARYLENE.” https://vsiparylene.com/parylene-advantages/properties/ (accessed Jan. 20, 2020).

[203] W. Prins and J. J. Hermans, “Theory of Permeation through Metal Coated Polymer Films,” *J. Phys. Chem.*, vol. 63, no. 5, pp. 716–720, May 1959, doi: 10.1021/j150575a017.

[204] V. Siracusa, “Food packaging permeability behaviour: A report,” *International Journal of Polymer Science*, vol. 2012. 2012, doi:

10.1155/2012/302029.

[205] A. K. Roy Choudhury, P. K. Majumdar, and C. Datta, “Factors affecting comfort: human physiology and the role of clothing,” in *Improving Comfort in Clothing*, Elsevier, 2011, pp. 3–60.

[206] W. Wang, X. Jiang, and Q. Yu, “Temperature self-compensation fiber-optic pressure sensor based on fiber Bragg grating and Fabry-Perot interference multiplexing,” *Opt. Commun.*, vol. 285, no. 16, pp. 3466–3470, Jul. 2012, doi: 10.1016/j.optcom.2012.04.001.

[207] H. Bae, D. Yun, H. Liu, D. A. Olson, and M. Yu, “Hybrid miniature fabry-perot sensor with dual optical cavities for simultaneous pressure and temperature measurements,” *J. Light. Technol.*, vol. 32, no. 8, pp. 1585–1593, Apr. 2014, doi: 10.1109/JLT.2014.2308060.

[208] Z. Li, J. Tian, Y. Jiao, Y. Sun, and Y. Yao, “Simultaneous measurement of air pressure and temperature using fiber-optic cascaded Fabry-Perot interferometer,” *IEEE Photonics J.*, vol. 11, no. 1, Feb. 2019, doi: 10.1109/JPHOT.2018.2884776.

[209] D. S. Nag, S. Sahu, A. Swain, and S. Kant, “Intracranial pressure monitoring: Gold standard and recent innovations,” *World J. Clin. Cases*, vol. 7, no. 13, pp. 1535–1553, 2019, doi: 10.12998/wjcc.v7.i13.1535.

[210] B. H. McGhee and E. J. Bridges, “Monitoring arterial blood pressure: what you may not know.,” *Crit. Care Nurse*, vol. 22, no. 2, pp. 60–64, 66, 2002.

[211] G. Obloluk Darovic, “Hemodynamic monitoring: Invasive and noninvasive clinical application,” *Nursing*, vol. 17, no. 11. W.B. Saunders Co, p. 88, 1987, doi: 10.1016/0266-612x(88)90048-x.

[212] F. E. A. S. Llc, “‘The real world is nonlinear’... 7 main Advantages using Abaqus,” 2019. http://www.feaservices.net/Seven-Reasons.pdf.

[213] S. C. Her and W. N. Lin, “Simultaneous measurement of temperature and mechanical strain using a fiber bragg grating sensor,” *Sensors (Switzerland)*, vol. 20, no. 15, pp. 1–12, 2020, doi: 10.3390/s20154223.

[214] MIT, “About Contact,” *About contact Interact.*, pp. 8–10, Accessed: Sep. 12, 2019. [Online]. Available: https://abaqus-docs.mit.edu/2017/English/SIMACAEITNRefMap/simaitn-c-contactoverview.htm.

[215] D. Kinet, P. Mégret, K. W. Goossen, L. Qiu, D. Heider, and C. Caucheteur, “Fiber Bragg grating sensors toward structural health monitoring in composite materials: Challenges and solutions,” *Sensors (Switzerland)*, vol. 14, no. 4, pp. 7394–7419, 2014, doi: 10.3390/s140407394.

[216] P. Wierzba and B. B. Kosmowski, “Application of polarisation-maintaining side-hole fibres to direct force measurement,” *Opto-electronics Rev.*, vol. 11, no. 4, pp. 305–311, 2003.

[217] F. Bosia, P. Giaccari, J. Botsis, M. Facchini, H. G. Limberger, and R. P. Salathé, “Characterization of the response of fibre Bragg grating sensors subjected to a two-dimensional strain field,” *Smart Mater. Struct.*, vol. 12, no. 6, pp. 925–934, 2003, doi: 10.1088/0964-1726/12/6/009.

[218] J. Zhou, Z. Zhou, and D. Zhang, “Study on strain transfer characteristics of fiber Bragg grating sensors,” *J. Intell. Mater. Syst. Struct.*, vol. 21, no. 11, pp. 1117–1122, Jul. 2010, doi: 10.1177/1045389X10375997.

[219] L. Sun, H. Hao, B. Zhang, X. Ren, and J. Li, “Strain Transfer Analysis of Embedded Fiber Bragg Grating Strain Sensor,” *J. Test. Eval.*, vol. 44, no. 6, p. 20140388, 2016, doi: 10.1520/jte20140388.

[220] Y. E. Pak, “Longitudinal shear transfer in fiber optic sensors,” *Smart Mater. Struct.*, vol. 1, no. 1, pp. 57–62, 1992, doi: 10.1088/0964-1726/1/1/008.

[221] L. Sun, D. Liang, H. Zhang, H. Li, and X. Wang, “Comparison of several strain transfer theory calculation methods of the embedded FBG strain sensors,” in *International Conference on Smart Materials and Nanotechnology in Engineering*, Jul. 2007, vol. 6423, p. 64233Z, doi: 10.1117/12.779629.

[222] H. N. Li, G. D. Zhou, L. Ren, and D. S. Li, “Strain transfer coefficient analyses for embedded fiber bragg grating sensors in different host materials,” *J. Eng. Mech.*, vol. 135, no. 12, pp. 1343–1353, 2009, doi: 10.1061/(ASCE)0733-9399(2009)135:12(1343).

[223] F. Ansari and Y. Libo, “Mechanics of bond and interface shear transfer in optical fiber sensors,” *J. Eng. Mech.*, vol. 124, no. 4, pp. 385–394, 1998, doi: 10.1061/(ASCE)0733-9399(1998)124:4(385).

[224] Q. Wang, Y. Qiu, H. Zhao, J. Chen, Y. Wang, and Z. Fan, “Analysis of strain transfer of six-layer surface-bonded fiber Bragg gratings,” *Appl. Opt.*, vol. 51, no. 18, p. 4129, Jun. 2012, doi: 10.1364/AO.51.004129.

[225] G. Rajan and K. K. Iniewski, “Optical fiber sensors: Advanced techniques and applications,” *Opt. Fiber Sensors Adv. Tech. Appl.*, pp. 1–559, 2017, doi: 10.1201/b18074.

[226] M. A. Davis and A. D. Kersey, “All-fibre Bragg grating strain-sensor demodulation technique using a wavelength division coupler,” *Electron. Lett.*, vol. 30, no. 1, pp. 75–77, Jun. 1994, doi: 10.1049/el:19940059.

[227] B. Das and V. Chandra, “Fiber-MZI-based FBG sensor interrogation: comparative study with a CCD spectrometer,” *Appl. Opt.*, vol. 55, no. 29, p. 8287, Oct. 2016, doi: 10.1364/ao.55.008287.

[228] M. D. Todd, G. A. Johnson, and B. L. Althouse, “A novel Bragg grating sensor interrogation system utilizing a scanning filter, a Mach-Zehnder interferometer and a 3 x 3 coupler,” *Meas. Sci. Technol.*, vol. 12, no. 7, pp. 771–777, 2001, doi: 10.1088/0957-0233/12/7/303.

[229] M. Song, S. Yin, and P. B. Ruffin, “Fiber Bragg grating strain sensor demodulation with quadrature sampling of a Mach–Zehnder interferometer,” *Appl. Opt.*, vol. 39, no. 7, p. 1106, Mar. 2000, doi: 10.1364/ao.39.001106.

[230] J. E. Alfonso, L. G. Cardenas, C. A. Triana, and M. V. Duran, “Design of an optical sensing interrogator using an edge filter scheme,” 2013, doi: 10.1109/IMOC.2013.6646509.

[231] K. Ogawa, S. Koyama, Y. Haseda, K. Fujita, H. Ishizawa, and K. Fujimoto, “Wireless, portable fiber bragg grating interrogation system employing optical edge filter,” *Sensors (Switzerland)*, vol. 19, no. 14, 2019, doi: 10.3390/s19143222.

[232] N. Stan *et al.*, “Increasing dynamic range of a fibre Bragg grating edge-filtering interrogator with a proportional control loop,” *Meas. Sci. Technol.*, vol. 25, no. 6, 2014, doi: 10.1088/0957-0233/25/6/065206.

[233] P. André *et al.*, “A cost-effective edge-filter-based FBG strain interrogator using catastrophic fuse effect microcavity interferometers,” in *Optical Components and Materials XV*, Feb. 2018, p. 71, doi: 10.1117/12.2291042.

[234] C. Florida *et al.*, “FBG interrogator based on spectral edge optical source,” in *Optics InfoBase Conference Papers*, 2018, vol. Part F124-, doi: 10.1364/ofs.2018.wf81.

[235] S. M. Melle, K. Liu, and R. M. Measures, “Practical fiber-optic Bragg grating strain gauge system,” *Appl. Opt.*, vol. 32, no. 19, p. 3601, Jul. 1993, doi: 10.1364/ao.32.003601.

[236] Y. Ma, C. Wang, Y. Yang, S. Yan, and J. Li, “High resolution and wide scale fiber Bragg grating sensor interrogation system,” *Opt. Laser Technol.*, vol. 50, pp. 107–111, 2013, doi: 10.1016/j.optlastec.2013.02.018.

[237] A. D. Kersey, T. A. Berkoff, and W. W. Morey, “Multiplexed fiber Bragg

grating strain-sensor system with a fiber Fabry–Perot wavelength filter," *Opt. Lett.*, vol. 18, no. 16, p. 1370, Aug. 1993, doi: 10.1364/ol.18.001370.

[238] S. Y. Jeong, S. J. Choi, and J. K. Pan, "An implementation of FBG interrogator with a tunable fabry-perot filter," in *Optics InfoBase Conference Papers*, 2017, vol. Part F52-IPRSN 2017, doi: 10.1364/IPRSN.2017.JTu4A.16.

[239] M. G. Xu, H. Geiger, J. L. Archambault, L. Reekie, and J. P. Dakin, "Novel interrogating system for fibre Bragg grating sensors using an acousto-optic tunable filter," *Electron. Lett.*, vol. 29, no. 17, pp. 1510–1511, 1993, doi: 10.1049/el:19931006.

[240] M. G. Xu, H. Geiger, and J. P. Dakin, "Modeling and performance analysis of a fiber bragg grating interrogation system using an acousto-optic tunable filter," *J. Light. Technol.*, vol. 14, no. 3, pp. 391–396, Mar. 1996, doi: 10.1109/50.485598.

[241] D. A. Jackson, L. Reekie, J. L. Archambault, and A. B. Lobo Ribeiro, "Simple multiplexing scheme for a fiber-optic grating sensor network," *Opt. Lett.*, vol. 18, no. 14, p. 1192, Jul. 1993, doi: 10.1364/ol.18.001192.

[242] C. A. R. Diaz *et al.*, "Perrogator: A Portable Energy-Efficient Interrogator for Dynamic Monitoring of Wavelength-Based Sensors in Wearable Applications," *Sensors*, vol. 19, no. 13, p. 2962, Jul. 2019, doi: 10.3390/s19132962.

[243] F. Grillot, "Photonic Integrated Circuits for Fiber Bragg Grating Based Sensing." http://www.pics4all.jeppix.eu/public/downloads/AN/PICs4ALL_Application_Note_FBG_Sensing.pdf.

[244] "Fiber sensing solutions based on integrated photonics." https://www.technobis.com/products/fiber-sensing-solutions/.

[245] Y. E. Marin, T. Nannipieri, C. J. Oton, and F. Di Pasquale, "Current Status

and Future Trends of Photonic-Integrated FBG Interrogators," *J. Light. Technol.*, vol. 36, no. 4, pp. 946–953, Feb. 2018, doi: 10.1109/JLT.2017.2779848.

[246] Y. E. Marin, T. Nannipieri, C. J. Oton, and F. Di Pasquale, "Integrated FBG Sensors Interrogation Using Active Phase Demodulation on a Silicon Photonic Platform," *J. Light. Technol.*, vol. 35, no. 16, pp. 3374–3379, 2017, doi: 10.1109/JLT.2016.2598395.

[247] B. Van Hoe *et al.*, "Ultra Small Integrated Optical Fiber Sensing System," *Sensors*, vol. 12, no. 9, pp. 12052–12069, Sep. 2012, doi: 10.3390/s120912052.

[248] T. Coroy, L. M. Chappell, N. J. Guillermo, S. Y. Huang, R. M. Measures, and K. D. Chik, "Peak Detection Demodulation of a Bragg Fiber Optic Sensor using a Gain-Coupled Distributed Feedback Tunable Laser," vol. 16, p. OWC17, 2015, doi: 10.1364/ofs.1997.owc17.

[249] G. A. Ball, W. W. Morey, and P. K. Cheo, "Fiber Laser Source/Analyzer for Bragg Grating Sensor Array Interrogation," *J. Light. Technol.*, vol. 12, no. 4, pp. 700–703, 1994, doi: 10.1109/50.285367.

[250] A. Roy, A. L. Chakraborty, and C. K. Jha, "Fiber Bragg grating interrogation using wavelength modulated tunable distributed feedback lasers and a fiber-optic Mach–Zehnder interferometer," *Appl. Opt.*, vol. 56, no. 12, p. 3562, Apr. 2017, doi: 10.1364/AO.56.003562.

[251] P. M. Toet, M. P. Maniscalco, R. A. J. Hagen, H. C. Hakkesteegt, and J. Lugtenburg, "Miniature and low cost fiber Bragg grating interrogator for structural monitoring in nano-satellites," in *International Conference on Space Optics — ICSO 2014*, Nov. 2017, p. 190, doi: 10.1117/12.2304250.

[252] S. K. Ibrahim, M. Farnan, D. M. Karabacak, and J. M. Singer, "Enabling technologies for fiber optic sensing," *Opt. Sens. Detect. IV*, vol. 9899, no. April, p. 98990Z, 2016, doi: 10.1117/12.2234975.

[253] A. W. Koch, M. Plattner, A. Hurni, M. Manhart, and P. Putzer, “Design of a fiber-optic interrogator module for telecommunication satellites,” Nov. 2017, p. 26, doi: 10.1117/12.2309040.

[254] J. Buus, M. C. Amann, and D. J. Blumenthal, *Tunable laser diodes and related optical sources, second edition*. Wiley-IEEE Press, 2005.

[255] L. A. Coldren and S. W. Corzine, “Continuously-Tunable Single-Frequency Semiconductor Lasers,” *IEEE J. Quantum Electron.*, vol. 23, no. 6, pp. 903–908, 1987, doi: 10.1109/JQE.1987.1073446.

[256] M. C. Amann and W. Thulke, “Continuously Tunable Laser Diodes: Longitudinal Versus Transverse Tuning Scheme,” *IEEE J. Sel. Areas Commun.*, vol. 8, no. 6, pp. 1169–1177, 1990, doi: 10.1109/49.57823.

[257] R. C. Alferness, “Widely tunable semiconductor lasers,” in *Conference on Optical Fiber Communication/International Conference on Integrated Optics and Optical Fiber Communication*, 1993, p. TuC5, doi: 10.1364/OFC.1993.TuC5.

[258] M. Okuda, K. Murata, and K. Oonaka, “Tunability of Distributed Bragg-Reflector Laser by Modulating Refractive Index in Corrugated Waveguide,” 1977.

[259] B. R. Bennett, R. A. Soref, and J. A. Del Alamo, “Carrier-Induced Change in Refractive Index of InP, GaAs, and InGaAsP,” *IEEE J. Quantum Electron.*, vol. 26, no. 1, pp. 113–122, 1990, doi: 10.1109/3.44924.

[260] D. A. B. Miller *et al.*, “Band-edge electroabsorption in quantum well structures: The quantum-confined stark effect,” *Phys. Rev. Lett.*, vol. 53, no. 22, pp. 2173–2176, 1984, doi: 10.1103/PhysRevLett.53.2173.

[261] N. Susa and T. Nakahara, “Enhancement of change in the refractive index in an asymmetric quantum well,” *Appl. Phys. Lett.*, vol. 60, no. 20, pp. 2457–2459, May 1992, doi: 10.1063/1.106932.

[262] S. L. Woodward, C. A. Burrus, U. Koren, B. I. Miller, M. G. Young, and M.

A. Newkirk, “A DBR Laser Tunable by Resistive Heating,” *IEEE Photonics Technol. Lett.*, vol. 4, no. 12, pp. 1330–1332, 1992, doi: 10.1109/68.180566.

[263] T. Kameda *et al.*, “A DBR Laser Employing Passive-Section Heaters, with 10. 8 nm Tuning Range and 1.6 MHz Linewidth,” *IEEE Photonics Technol. Lett.*, vol. 5, no. 6, pp. 608–610, 1993, doi: 10.1109/68.219684.

[264] M.-C. Amann and J. Buus, *Tunable laser diodes*. Artech House, 1998.

[265] T. L. Koch, U. Koren, and B. I. Miller, “High performance tunable 1.5 μm InGaAs/InGaAsP multiple quantum well distributed Bragg reflector lasers,” *Appl. Phys. Lett.*, vol. 53, no. 12, pp. 1036–1038, 1988, doi: 10.1063/1.100057.

[266] X. Pan, H. Olesen, and B. Tromborg, “A Theoretical Model of Multielectrode DBR Lasers,” *IEEE J. Quantum Electron.*, vol. 24, no. 12, pp. 2423–2432, 1988, doi: 10.1109/3.14372.

[267] N. P. Caponio *et al.*, “Analysis and Design Criteria of Three-Section DBR Tunable Lasers,” *IEEE J. Sel. Areas Commun.*, vol. 8, no. 6, pp. 1203–1213, 1990, doi: 10.1109/49.57827.

[268] B. Stoltz, M. Dasler, and O. Sahlén, “Low threshold-current, wide tuning-range, butt-joint DBR laser grown with four MOVPE steps,” *Electron. Lett.*, vol. 29, no. 8, pp. 700–702, Apr. 1993, doi: 10.1049/el:19930469.

[269] T. J. Reid, C. A. Park, P. J. Williams, A. K. Wood, and J. Buus, “3.8nm continuous tuning range of a low threshold distributed bragg reflector laser,” in *12th IEEE International Conference on Semiconductor Laser*, Aug. 2005, pp. 242–243, doi: 10.1109/islc.1990.764510.

[270] Y. Kotaki, M. Matsuda, H. Ishikawa, and H. Imai, “Tunable DBR laser with wide tuning range,” *Electron. Lett.*, vol. 24, no. 8, pp. 503–505, 1988, doi: 10.1049/el:19880342.

[271] S. Murata, I. Mito, and K. Kobayashi, “Tuning ranges for 1.5 μm wavelength tunable DBR lasers,” *Electron. Lett.*, vol. 24, no. 10, pp. 577–579, May 1988, doi: 10.1049/el:19880392.

[272] S. L. Woodward, I. M. I. Habbab, T. L. Koch, and U. Koren, “The Sidemode-Suppression Ratio of a Tunable DBR Laser,” *IEEE Photonics Technol. Lett.*, vol. 2, no. 12, pp. 854–856, 1990, doi: 10.1109/68.62008.

[273] N. Maluf and K. Williams, *Introduction to microelectromechanical systems engineering*. Artech House, 2004.

[274] A. K. Roy Choudhury, P. K. Majumdar, and C. Datta, *Factors affecting comfort: human physiology and the role of clothing*, no. 1985. Elsevier Masson SAS., 2011.

Appendix A: Transfer matrix matlab code

```
clear
clc
neff= 1.482;%effective refractive index
L=3e-3; %length of Fbg
dn=1.2e-4;%peak value of the dc effective index of refraction
change
lambda_D=1550e-9; %Designed Bragg wavelength

res=1500;%wavelength resolution
lambda=1e-9*linspace(1540,1560,res);%spectrum with resolution
given in res
nom_per=lambda_D./(2*neff);

sr=600; %number of sections
l_i= L/sr; %length of a section
avg_index =dn;
sum_index=0;

E=75e9
%%Strain calculation
p11=0.113;
p12=0.252;
v=0.17;
pe=((neff^2)/2)*(p12-v*(p11+p12));


filename =  'D:\Finite element modeling\Fibre
strain\squarepatch 3mm\44n.txt';
[C1,
strain1,strain2,strain3,stress1,stress2,stress3]=textread(filen
ame, '%f %f %f %f %f %f %f','delimiter', ',', 'headerlines',
3);%ignore the first 3 lines
strainx=strain1(302:501);
strainy=strain2(302:501);
strainz=strain3(302:501);
stressx=stress1(302:501)*1e6;
```

```
stressy=stress2(302:501)*1e6;
stressz=stress3(302:501)*1e6;

M= mean(strainz);

for j=1:res

    k=pi*dn/lambda_D;%coupling coefficient

delta1=2*neff*pi*(1./lambda-1./lambda_D) + 0*2*pi*dn./lambda;
%differential propagation constant

q1=sqrt(k.^2-delta1.^2);

f11(j,1)=(cosh(q1(j)*L))-1i*delta1 (j)/q1(j)*sinh(q1(j)*L);
f12(j,1)=-(1i*k/q1(j)*sinh(q1(j)*L));
f21(j,1)=(1i*k/q1(j)*sinh(q1(j)*L));
f22(j,1)=(cosh(q1(j)*L)+1i*delta1 (j)/q1(j)*sinh(q1(j)*L));
F1=[f11(j,1) f12(j,1);f21(j,1) f22(j,1)];
R1(j)=(abs(-F1(2,1)/F1(1,1)))^2;

end

figure (2)
plot(lambda*1000000000,R1)
hold on;

x=0;%initialising x

for r=1:res

for n=1:sr

    tempwave(n)= lambda_D*(1+(1-pe)*M);

 %calculation of bragg period per section
gratingperiod(n)= tempwave(n)/ (2* neff);

%effective refractive index change per section
dnx(n)=(-(neff^3)*((p11-2*v*p12)*stressx(n)+((1-v)*p12-
v*p11)*(stressy(n)+stressz(n)))/(2*E));
dny(n)=-((neff^3)*((p11-2*v*p12)*stressy(n)+((1-v)*p12-
v*p11)*(stressx(n)+stressz(n)))/(2*E));


%effective refractive index per section
neffx(n)=neff+dnx(n);
neffy(n)=neff+dny(n);


%self coupling coefficient per section
deltax(n)=(2*(neffx(n))*pi*((1./lambda(r))-
1./(2*neffx(n)*gratingperiod(n))))+ (2*pi*dn./lambda(r));
%differential propagation constant
deltay(n)=(2*(neffy(n))*pi*(1./lambda(r)-
1./(2*neffy(n)*gratingperiod(n))))+ (2*pi*dn./lambda(r));
```

```
k=pi*dn/lambda(r);

qx(r,n)=sqrt(k.^2-deltax(n).^2);  %calculation of self coupling
coefficient

qy(r,n)=sqrt(k.^2-deltay(n).^2);

% q(r,n)=sqrt(k(n).^2-delta(n).^2);  %calculation of self
coupling coefficient
%
% f11(r,n)=(cosh(q(r,n)*l_i)-(i*(delta
(n)/q(r,n))*sinh(q(r,n)*l_i)));
% f12(r,n)=-(i*(k(n)/q(r,n))*sinh(q(r,n)*l_i));
% f21(r,n)=(i*(k(n)/q(r,n))*sinh(q(r,n)*l_i));
% f22(r,n)=(cosh(q(r,n)*l_i)+i*(delta
(n)/q(r,n))*sinh(q(r,n)*l_i));

f11x(r,n)=(cosh(qx(r,n)*l_i)-
(i*(deltax(n)/qx(r,n))*sinh(qx(r,n)*l_i)));
f12x(r,n)=-(i*(k/qx(r,n))*sinh(qx(r,n)*l_i));
f21x(r,n)=(i*(k/qx(r,n))*sinh(qx(r,n)*l_i));
f22x(r,n)=(cosh(qx(r,n)*l_i)+i*(deltax(n)/qx(r,n))*sinh(qx(r,n)
*l_i));

f11y(r,n)=(cosh(qy(r,n)*l_i)-
(i*(deltay(n)/qy(r,n))*sinh(qy(r,n)*l_i)));
f12y(r,n)=-(i*(k/qy(r,n))*sinh(qy(r,n)*l_i));
f21y(r,n)=(i*(k/qy(r,n))*sinh(qy(r,n)*l_i));
f22y(r,n)=(cosh(qy(r,n)*l_i)+i*(deltay(n)/qy(r,n))*sinh(qy(r,n)
*l_i));

if n<2

F1x=[f11x(r,n) f12x(r,n);f21x(r,n) f22x(r,n)];
f1x=F1x;
F1y=[f11y(r,n) f12y(r,n);f21y(r,n) f22y(r,n)];
else
Fnewx=[f11x(r,n) f12x(r,n);f21x(r,n) f22x(r,n)];
F1x=Fnewx*F1x;
Fnewy=[f11y(r,n) f12y(r,n);f21y(r,n) f22y(r,n)];
F1y=Fnewy*F1y;
end
x=(x+l_i);
sum_index= sum_index+dnx(n);
end


R2x(r)=(abs(-F1x(2,1)/F1x(1,1)))^2;
R2y(r)=(abs(-F1y(2,1)/F1y(1,1)))^2;

R2(r)=(abs(-F1(2,1)/F1(1,1)))^2;
R2(r) = 0.5*R2x(r)+0.5*R2y(r);

end

 plot(lambda* 1000000000,R2)
```

```
plot(lambda* 1000000000,R2x)
plot(lambda* 1000000000,R2y)
```

```
wavelegthshift= (1-pe)*mean(strainz)*lambda_D*10^9
lambda_wv1= 2*neff*(max(gratingperiod)-min(gratingperiod));
lambda_wv2= (neff^3)*nom_per*((1+v)*p12-
(1+v)*p11*abs(stressy(n)+stressx(n)))/(E);
lambda_wv= (lambda_wv1+lambda_wv2)*10^9
```

Appendix B: Data sheet of tunable laser

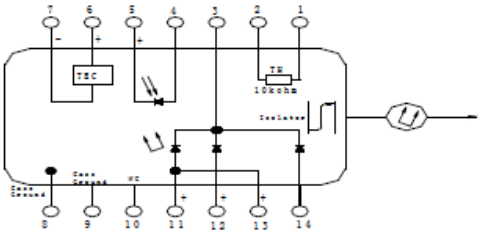

Section Laser module schematic

Connection

Pin Assignments			
Pin	**Function**	**Pin**	**Function**
1	Thermistor	8	Case Ground
2	Thermistor	9	Case Ground
3	LD Cathode (-)	10	NC
4	MPD Anode	11	I gain
5	MPD Cathode	12	I rear
6	TEC (+)	13	I gain
7	TEC (-)	14	I phase

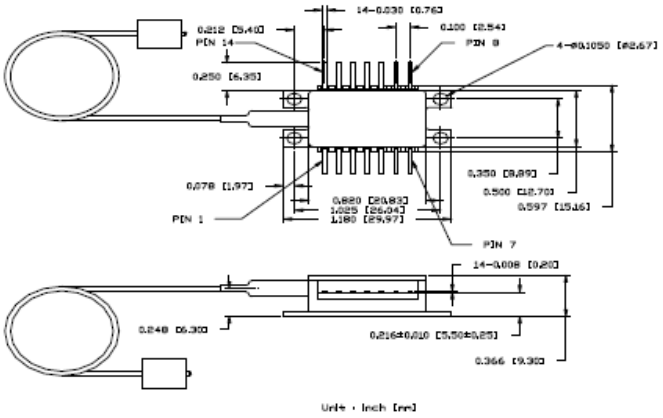

Xeston Technologies Ltd.

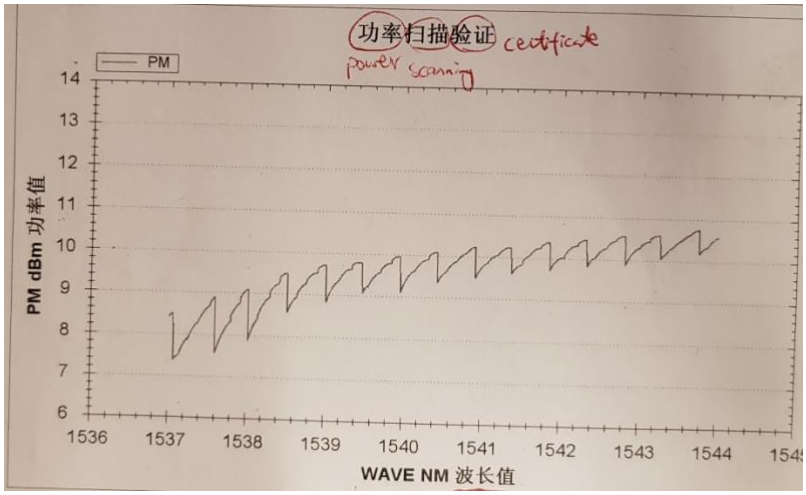
功率扫描验证 certificate
power scanning
PM
PM dBm 功率值
14
13
12
11
10
9
8
7
6
1536
1537
1538
1539
1540
1541
1542
1543
1544
WAVE NM 波长值